Modeling, Parameter Identification, and Degradation-Conscious Control of Polymer Electrolyte Membrane (PEM) Fuel Cells

by

Alireza Goshtasbi

A dissertation submitted in partial fulfillment
of the requirements for the degree of
Doctor of Philosophy
(Mechanical Engineering)
in the University of Michigan
2020

Doctoral Committee:

Associate Research Scientist Tulga Ersal, Co-Chair
Professor Jing Sun, Co-Chair
Professor Ilya Kolmanovsky
Associate Research Scientist Jason Siegel
Professor Anna Stefanopoulou

Alireza Goshtasbi

goshtasb@umich.edu

ORCID iD: 0000-0002-9575-6091

©Alireza Goshtasbi 2020

To Zeinab.

Acknowledgments

First and foremost, I would like to extend my sincerest gratitude and appreciation to my advisor, Dr. Tulga Ersal, without whose guidance this dissertation would not have been possible. Tulga has taught me a great deal over the past five years, on both professional and personal fronts. It was his endless patience that allowed me to work on many different problems throughout my PhD. His wisdom will continue to be a guiding light for my future endeavors and I will be forever grateful for the great many things that he has taught me. I would also like to thank all members of my dissertation committee, Prof. Jing Sun, Prof. Anna Stefanopoulou, Prof. Ilya Kolmanovsky, and Dr. Jason Siegel for their constructive feedback on this work and highlighting a number of critical problems that I had to address in this dissertation. I am specially thankful to Dr. Siegel for his guidance with my research very early on. I have to thank all our incredible ME staff members, as well. In particular, Lisa Rogers, Adam Mael, and Rachel Casanova have helped me greatly in navigating all the rules and requirements of my degree.

I would like to acknowledge the financial and technical support by Ford. Most of my graduate studies were funded by Ford and I was fortunate to collaborate with many amazing people in their Fuel Cell Department. I am particularly thankful to Ben Pence and Valerie Nelson for their remarkable patience with me as I learned the fuel cell fundamentals. They also provided very valuable feedback on my work that helped me improve it. I am also grateful for the many fruitful discussions I have had with Jixin Chen and Jim Waldecker, both of whom have contributed immensely to my graduate work with

their valuable input. Overall, our collaboration with Ford has been a notably successful one and I look forward to continuing this work with them.

Furthermore, I acknowledge the Rackham Graduate School for the two Rackham Research Grants that I received during my PhD. These funds allowed me to use the high performance computational resources that were needed to run some of the simulations and optimizations presented in this dissertation.

I am also grateful to all our lab members, past and present, for they have provided me with critical feedback on numerous occasions. I have to specially thank Xin Zhou, since the main idea for solving one of the most critical pieces of my model was formed after one of our casual conversations. I am also thankful to all my great friends in Ann Arbor, without whom I could not have survived the past few years. Most notably, I am thankful to Navid Alamti, for all the memories we have shared. I also have to thank him for kindly granting me access to the much coveted *Alamati Cloud* that helped me pace up putting the last pieces of this dissertation together.

I owe the greatest debt of gratitude to my parents, Fereshteh and Bahman, who have always supported me despite all the reservations they have had about my ways. I could not have possibly gotten to the point where I am today without their unwavering love and support throughout the years. The sacrifices they have made to make sure I succeed in realizing my dreams is beyond my comprehension and I am forever thankful to them. Finally, I am grateful to my lovely wife, Negin, for her love, kindness, and exemplary patience that has allowed me to continue chasing my goals as we navigate through the difficult phase of life that living apart has brought upon us. Her motivating brilliance shines a light on my day despite the physical distance and helps me carry on.

Table of Contents

List of Tables

List of Figures

Nomenclature

This nomenclature contains a list of abbreviations, parameters, and variables used in the dissertation. Only the parameters and variables of the fuel cell system models are described here. The variables used in describing the sensitivity analysis and model parameterization procedures and the control formulation follow the conventions in the literature and are described in the text. Throughout the dissertation, bold italic and bold typefaces are used for vectors and matrices, respectively, whereas a regular typeface is reserved for scalar values. The choice of units shown in this nomenclature is made for convenience and is used throughout the dissertation, unless noted otherwise.

Abbreviations

ACL	Anode catalyst layer
ADMM	Alternating direction method of multipliers
BV	Butler-Volmer
CCL	Cathode catalyst layer
CCM	Catalyst coated membrane
CH	Channel
CL	Catalyst layer
CV	Control volume

CW	Cold wet
DAE	Differential algebraic equation
DARE	Discrete algebraic Riccati equation
DEA	Dead-ended anode
DM	Diffusion media
DT	Double-trap
DVS	Dynamic vapor sorption
ECSA	Electrochemical surface area
EOD	Electro-osmotic drag
FIM	Fisher information matrix
GA	Genetic algorithm
GDL	Gas diffusion layer
HD	Hot dry
HFR	High frequency resistance
HOR	Hydrogen oxidation reaction
IP	In-plane
LHS	Latin hypercube sampling
LN	Land
LTV	Linear time varying

MB	Membrane
MEA	Membrane electode assembly
MPC	Model predictive control
MPL	Microporous layer
MRI	Magnetic resonance imaging
NSTF	Nano-structured thin film
OCV	Open circuit voltage
ODE	Ordinary differential equation
OED	Optimal experimental design
ORR	Oxygen reduction reaction
P2D	Pseudo 2-dimensional
PCI	Phase change induced
PDE	Partial differential equation
PEM	Polymer electrolyte membrane
PI	Proportional-integral
PSO	Particle swarm optimization
Pt	Platinum
PTFE	Polytetrafluoroethylene
QP	Quadratic program

RAE	Relative absolute error
REV	Representative elementary volume
RH	Relative humidity
SANS	Small angle neutron scattering
SAXS	Small angle X-ray scattering
TO	Thermo-osmosis
TP	Through-plane

Roman

A_{cool}	Available cooling area, [cm^2]
A_{fc}	Single cell active area, [cm^2]
A_{T}	Cathode outlet throttle area, [cm^2]
$A_{\text{Pt}}^{\text{eff}}$	Effective Pt surface area, [cm^2]
$A_{\text{ion}}^{\text{eff}}$	Effective ionomer surface area, [cm^2]
a_c	Volumetric surface area of ionomer, [cm^2/cm^3]
a_{Pt}	Volumetric surface area of Pt, [cm^2/cm^3]
C_{D}	Cathode outlet discharge coefficient, [$-$]
c_{v}	Water vapor concentration, [mol/cm^3]
c_{rct}	Reactant concentration, [mol/cm^3]
c_{H_2}	H_2 concentration, [mol/cm^3]

$c_{H_2,\mathrm{CH}}$ H_2 concentration in channel, [mol/cm^3]

$c_{H_2,\mathrm{Pt}}$ H_2 concentration at Pt surface, [mol/cm^3]

$c_{H_2}^{\mathrm{ref}}$ Reference H_2 concentration, [mol/cm^3]

c_{O_2} O_2 concentration, [mol/cm^3]

$c_{O_2,\mathrm{CH}}$ O_2 concentration in channel, [mol/cm^3]

$c_{O_2,\mathrm{Pt}}$ O_2 concentration at Pt surface, [mol/cm^3]

$c_{O_2}^{\mathrm{ref}}$ Reference O_2 concentration, [mol/cm^3]

c_{sat} Saturated vapor concentration, [mol/cm^3]

D_{h} Channel hydraulic diameter, [cm]

D_i Diffusivity of species i, [cm^2/s]

$D_{i,j}$ Binary diffusivity of species i in species j, [cm^2/s]

D_i^{eff} Effective diffusivity of species i, [cm^2/s]

$D_{\mathrm{Kn,i}}$ Knudsen diffusivity of species i, [cm^2/s]

$D_{\mathrm{w,mb}}^{\mathrm{eff}}$ Effective membrane water diffusivity, [cm^2/s]

$D_{T,\mathrm{mb}}^{\mathrm{eff}}$ Effective membrane thermal water diffusivity, [mol/(cm $\cdot$ K)]

d_{c} Compressor blade diameter, [cm]

$d_{\mathrm{transport}}$ Total transport path length, [cm]

$ECSA$ Electrochemically active surface area, [(m^2/g)$_{\mathrm{Pt}}$]

E_{cell} Cell voltage, [V]

$E_{\text{act,mb}}$ Activation energy for ionomer conductivity, [kJ/mol]

E_{OCV} Open-circuit voltage, [V]

$E_{\text{act,an}}$ HOR activation energy, [kJ/mol]

$E_{\text{act,ca}}$ ORR activation energy, [kJ/mol]

$E_{\text{rev,PtO}}$ Reversible potential for PtO formation, [V]

E_{PtO} Interaction energy for PtO formation, [kJ/mol]

EW Ionomer equivalent weight, [g/mol]

e_V Voltage prediction error, [V]

e_R Resistance prediction error, [$\text{m}\Omega \cdot \text{cm}^2$]

$e_{\max}$ Maximum allowable voltage prediction error, [V]

F Faraday's constant, [C/mol]

f_j Molar flow rate of species j per unit length, [$\text{mol}/(\text{cm} \cdot \text{s})$]

f_v Water volume fraction in ionomer, [$-$]

$f(\varepsilon)$ Porosity correction factor for diffusivity, [$-$]

f_{RH} RH dependency factor for ORR, [$-$]

$f_{RH,a}$ Fitting parameter for f_{RH}, [$-$]

$f_{RH,b}$ Fitting parameter for f_{RH}, [$-$]

$f_{RH,c}$ Fitting parameter for f_{RH}, [$-$]

$g(s)$ Saturation correction factor for diffusivity, [$-$]

H_{HOR} Heat of reaction for HOR, [J/mol]

H_{ORR} Heat of reaction for ORR, [J/mol]

H_{ad} Heat of sorption, [J/mol]

H_{pc} Enthalpy of phase change, [kJ/g]

H_{H_2} Henry's Law constant for H_2, [$\text{atm} \cdot \text{m}^3/\text{mol}$]

h_{CH} Channel height, [cm]

h_{conv} Heat convection coefficient, [$\text{W}/(\text{cm}^2 \cdot \text{K})$]

IC Ionomer to carbon ratio, [$-$]

i_{dens} Current density, [A/cm^2]

$i_{0,\text{an}}^{\text{ref}}$ Reference HOR exchange current density, [A/cm^2]

$i_{0,\text{ca}}^{\text{ref}}$ Reference ORR exchange current density, [A/cm^2]

i_x Crossover (leak) current density, [A/cm^2]

J_{cp} Compressor inertia, [$\text{kg} \cdot \text{m}^2$]

J Optimization cost for parameterization, [$-$]

$K_{\text{abs,CL}}$ CL absolute permeability, [cm^2]

$K_{\text{abs,MPL}}$ MPL absolute permeability, [cm^2]

$K_{\text{abs,GDL}}$ GDL absolute permeability, [cm^2]

$K_{\text{l,rel}}$ Liquid relative permeability, [$-$]

$K_{\text{l}}^{\text{eff}}$ Liquid effective permeability, [cm^2]

$K_{p,\mathrm{mb}}$ Membrane water permeability, [cm^2]

k_{ad} Interfacial water transfer coefficient, [cm/s]

$k_{\mathrm{ca,in}}$ Cathode orifice constant, [$\mathrm{kg}/(\mathrm{s}\cdot\mathrm{Pa})$]

k_{cross} Scaling factor for membrane gas permeability, [−]

$k_{\mathrm{evp/cnd}}$ Phase change rate constant, [1/s]

k_{PtO} Rate constant for PtO formation, [1/s]

k_T^{eff} Effective thermal conductivity, [$\mathrm{W}/(\mathrm{m}\cdot\mathrm{K})$]

$k_{T,\mathrm{CL}}$ CL thermal conductivity, [$\mathrm{W}/(\mathrm{m}\cdot\mathrm{K})$]

$k_{T,\mathrm{MPL}}$ MPL thermal conductivity, [$\mathrm{W}/(\mathrm{m}\cdot\mathrm{K})$]

$k_{T,\mathrm{GDL}}$ GDL thermal conductivity, [$\mathrm{W}/(\mathrm{m}\cdot\mathrm{K})$]

$k_{T,\mathrm{mb}}$ Membrane thermal conductivity, [$\mathrm{W}/(\mathrm{m}\cdot\mathrm{K})$]

k_t Motor constant, [$\mathrm{N}\cdot\mathrm{m}/\mathrm{A}$]

k_v Motor constant, [$\mathrm{V}/(\mathrm{rad/s})$]

k_1 Interfacial transport resistance parameter, [−]

k_2 Interfacial transport resistance parameter, [−]

k_3 Interfacial transport resistance parameter, [−]

L_{c} Carbon loading, [$\mathrm{mg}/\mathrm{cm}^2$]

L_{Pt} Pt loading, [$\mathrm{mg}/\mathrm{cm}^2$]

$\dot{M}_j$ Molar flow rate of species j in the flow channel, [mol/s]

M_{H_2} Molar mass of H_2, [g/mol]

M_{H_2O} Molar mass of water, [g/mol]

M_{N_2} Molar mass of N_2, [g/mol]

M_{O_2} Molar mass of O_2, [g/mol]

$\dot{m}_{\text{cool}}$ Coolant mass flow rate, [kg/s]

$N_{j,\text{mb}}$ Molar flux of species j through the membrane, [mol/(cm$^2 \cdot$ s)]

$N_{H_2,\text{mb}}$ Molar H_2 membrane crossover flux, [mol/(cm$^2 \cdot$ s)]

$N_{N_2,\text{mb}}$ Molar N_2 membrane crossover flux, [mol/(cm$^2 \cdot$ s)]

$N_{O_2,\text{mb}}$ Molar O_2 membrane crossover flux, [mol/(cm$^2 \cdot$ s)]

$N_{\text{w,mb}}$ Water flux in ionomer phase, [mol/(cm$^2 \cdot$ s)]

N_{H_2} H_2 molar flux in anode, [mol/(cm$^2 \cdot$ s)]

N_{O_2} O_2 molar flux in cathode, [mol/(cm$^2 \cdot$ s)]

$N_{\text{l,GDL}}$ Molar liquid water flux at the GDL-CH boundary, [mol/(cm$^2 \cdot$ s)]

$N_{\text{v,GDL}}$ Molar vapor flux at the GDL-CH boundary, [mol/(cm$^2 \cdot$ s)]

n_{Brugg} Bruggeman coefficient, [$-$]

n_{cell} Number of cells in the stack, [$-$]

n_d Electro-osmotic drag coefficient, [$-$]

n_e Fitting parameter for $f(\varepsilon)$, [$-$]

n_R Number of elements in resistance prediction error vector, [$-$]

n_V	Number of elements in voltage prediction error vector, [−]
n_v	Fitting parameter for $g(s)$, [−]
n_{Pt}	Number of Pt particles on a carbon particle, [−]
P_{aux}	Power consumed by auxiliary equipment, [kW]
P_{cm}	Power consumed by compressor, [kW]
P_{fc}	Power generated by the fuel cell stack, [kW]
P_{net}	Net power generated by the fuel cell system, [kW]
p_{atm}	Ambient atmospheric pressure, [bar]
p_c	Capillary pressure, [bar]
p_{ch}	Channel pressure, [bar]
p_{ca}	Cathode channel pressure, [bar]
p_{g}	Gas pressure, [bar]
p_{l}	Liquid pressure, [bar]
p_{in}	Inlet channel pressure, [bar]
$p_{\mathrm{H_2,Pt}}$	H_2 partial pressure at Pt surface, [bar]
$p_{\mathrm{O_2,Pt}}$	O_2 partial pressure at Pt surface, [bar]
$p_{\mathrm{l,CH}}$	Liquid pressure in the channel (for boundary condition), [bar]
p_{sat}	Saturated vapor pressure, [bar]
p_{sm}	Supply manifold pressure, [bar]

R	Universal gas constant, $[\mathrm{J}/(\mathrm{mol}\cdot\mathrm{K})]$
R_{mb}	Membrane ionic resistance, $[\Omega\cdot\mathrm{cm}^2]$
$R_{\mathrm{CL}}^{\mathrm{eff,ca}}$	Cathode CL effective ionic resistance, $[\Omega\cdot\mathrm{cm}^2]$
R_{elec}	Total electronic resistance, $[\Omega\cdot\mathrm{cm}^2]$
$\mathcal{R}_{i,j}$	Transport resistance of gas species i in layer j, [s/cm]
$\mathcal{R}_{O_2}$	Total O_2 transport resistance in cathode, [s/cm]
$\mathcal{R}_{H_2}$	Total H_2 transport resistance in anode, [s/cm]
$\mathcal{R}_{\mathrm{v}}$	Total vapor transport resistance, [s/cm]
$\mathcal{R}_{O_2}^{\mathrm{micro}}$	Local O_2 transport resistance in the cathode CL, [s/cm]
$\mathcal{R}_{\mathrm{ion,int}}$	O_2 transport resistance at ionomer-water interface, [s/cm]
$\mathcal{R}_{\mathrm{Pt,int}}$	O_2 transport resistance at Pt-ionomer interface, [s/cm]
$\mathcal{R}_{\mathrm{w,int}}$	O_2 transport resistance at water-pore interface, [s/cm]
$\mathcal{R}_T$	Total heat transport resistance, $[\mathrm{cm}^2\cdot\mathrm{K/W}]$
$\mathcal{R}_{\mathrm{v}}$	Total vapor transport resistance, [s/cm]
R_{cm}	Motor constant, $[\Omega]$
RH	Relative humidity, $[-]$
r_{c}	Carbon particle radius, [nm]
r_{Pt}	Pt particle radius, [nm]
S_i	Source term for reaction, i

S_{l}	Source term for liquid water accumulation, [g/(cm$^3 \cdot$ s)]
S_{λ}	Source term for ionomer water content, [mol/(cm$^3 \cdot$ s)]
S_i	Source term for gas species i, [mol/(cm$^3 \cdot$ s)]
S_T	Source term for heat equation, [W/cm^3]
S_{pc}	Source term for phase change, [mol/(cm$^3 \cdot$ s)]
S_{ad}	Source term for water absorption/desorption, [mol/(cm$^3 \cdot$ s)]
s	Liquid saturation, [−]
s_{relax}	Ionomer relaxation variable, [−]
Sh	Sherwood number, [−]
St_{H_2}	H_2 stoichiometry, [−]
St_{O_2}	O_2 stoichiometry, [−]
T	Temperature, [K]
T_{atm}	Ambient temperature, [K]
T_{cp}	Compressor outlet temperature, [K]
$T_{\mathrm{cool,in}}$	Coolant inlet temperature, [K]
T_{s}	Sampling time, [s]
U_{c}	Compressor blade tip speed, [m/s]
V_{ca}	Cathode volume, [m^3]
v_{cm}	Compressor motor voltage, [V]

V_{sm} Supply manifold volume, [m^3]

$W_{i,\text{in}}$ Mass flow rate of i into the cathode, [kg/s]

$W_{i,\text{out}}$ Mass flow rate of i out of the cathode, [kg/s]

$W_{i,\text{rct}}$ Mass flow rate of i reacting in the cathode, [kg/s]

w_{CH} Channel width, [cm]

w_{LN} Land width, [cm]

$wt\%$ Pt/C weight fraction, [−]

x Through-the-membrane location, [cm]

x_{O_2} O_2 mass fraction in dry air, [−]

x_{Pt} Number fraction of Pt particles, [−]

y Along-the-channel location, [cm]

z In-plane location, [cm]

Greek

α_{an} Transfer coefficient for HOR, [−]

α_{ca} Transfer coefficient for ORR, [−]

α_{PtO} Transfer coefficient for PtO formation, [−]

β Normalized membrane water flux, [−]

χ Cathode CL utilization, [−]

ΔT_{cool} Coolant temperature change, [°C]

$\Delta p_{\mathrm{an/ca}}$	Channel pressure drop, [mbar]
δ_{ion}	Ionomer film thickness on carbon-supported Pt, [cm]
δ_{w}	Water film thickness on carbon-supported Pt, [cm]
δ	Layer thickness, [μm]
δ_{DM}	Total thickness of porous layers, [μm]
δ_{mb}	Membrane thickness, [μm]
δ_{CL}	CL thickness, [μm]
δ_{MPL}	MPL thickness, [μm]
δ_{GDL}	GDL thickness, [μm]
ε	Porosity/volume fraction, [$-$]
ε_{α}	Volume fraction of phase α, [$-$]
ε_{c}	Carbon volume fraction in the CL, [$-$]
$\varepsilon_{\mathrm{Pt}}$	Pt volume fraction in the CL, [$-$]
$\varepsilon_{\mathrm{ion}}$	Ionomer volume fraction, [$-$]
ε_{g}	Volume fraction of gas phase, [$-$]
ε_{l}	Volume fraction of liquid phase, [$-$]
$\varepsilon_{\mathrm{CL}}$	CL porosity, [$-$]
$\varepsilon_{\mathrm{MPL}}$	MPL porosity, [$-$]
$\varepsilon_{\mathrm{GDL}}$	GDL porosity, [$-$]

η_{cm} Motor mechanical efficiency, [−]

η_{cp} Compressor efficiency, [V]

η_{HOR} HOR activation overpotential, [V]

η_{ORR} ORR activation overpotential, [V]

γ Ratio of specific heats for air, [−]

γ_{an} Reaction order for HOR, [−]

γ_{ca} Reaction order for ORR, [−]

κ_{ion} Effective ionic conductivity, [S/cm]

κ_{res} Residual ionic conductivity, [S/cm]

κ_0 Reference ionic conductivity, [S/cm]

λ Ionomer water content, [−]

λ_{eq} Equilibrium water content, [−]

λ_{th} Threshold ionomer water content for conductivity, [−]

λ^* Quasi-equilibrium water content, [−]

μ_{l} Liquid water viscosity, [Pa $\cdot$ s]

$\omega_{\text{ca,in}}$ Humidity ratio for cathode inlet, [−]

Π_{HOR} HOR Peltier coefficient, [V]

Π_{ORR} ORR Peltier coefficient, [V]

Φ Normalized compressor flow rate, [−]

φ	Ionomer relaxation parameter, [−]
ρ_{l}	Liquid phase density, [g/cm^3]
ρ_{c}	Carbon density, [g/cm^3]
ρ_{Pt}	Pt density, [g/cm^3]
ρ_{ion}	Ionomer density, [g/cm^3]
ρc_p	Volumetric heat capacity, [J/(cm$^3 \cdot$ K)]
Ψ	Membrane gas permeability, [mol/(cm $\cdot$ bar $\cdot$ s)]
σ_{l}	Liquid water surface tension, [N/m]
τ	Tortuosity factor for porous layer, [−]
τ_{cm}	Compressor motor torque, [N $\cdot$ m]
τ_{cp}	Torque required to drive the compressor, [N $\cdot$ m]
τ_{relax}	Ionomer relaxation time constant, [s]
θ	Generic model parameter [−]
$\bar{\theta}$	Generic normalized model parameter [−]
θ_{PtO}	PtO coverage [−]
θ_{CL}	Contact angle for CL, [−]
θ_{MPL}	Contact angle for MPL, [−]
θ_{GDL}	Contact angle for GDL, [−]
ω	Energy parameter for Temkin isotherm, [kJ/mol]

$\xi_{\text{diff,mb}}$ Fitting parameter for membrane water diffusivity, [−]

Subscripts and Superscripts

abs Absolute

act Activation

ad Absorption/desorption

an Anode

aux Auxiliary

c Capillary/Carbon

ca Cathode

CH Channel

cm Compressor motor

cnd Condensation

cool Coolant

cp Compressor

diff Diffusion

eff Effective

elec Electronic

eq Equilibrium

evp Evaporation

fc	Fuel cell
g	Gas phase
h	Hydraulic
hcd	High current density
in	Inlet
int	Interfacial
ion	Ionomer
IP	In-plane
Kn	Knudsen
l	Liquid phase
lcd	Low current density
mb	Membrane
out	Outlet
pc	Phase change
rct	Reaction
ref	Reference
rel	Relative
relax	Relaxation
res	Residual

rev	Reversible
sat	Saturation
sm	Supply manifold
T	Thermal
th	Threshold
v	Vapor phase
w	Water

Abstract

Polymer electrolyte membrane (PEM) fuel cells are touted as zero-emission alternatives to internal combustion engines for automotive applications. However, high cost and durability issues have hindered their commercialization. Therefore, significant research efforts are underway to better understand the scientific aspects of PEM fuel cell operation and engineer its components for improved lifetime and reduced cost. Most of the research in this area has been focused on material development. However, as demonstrated by Toyota's fuel cell vehicle, intelligent control strategies may lead to significantly improved durability of the fuel cell stack even with existing materials. Therefore, it seems that the outstanding issues can be better resolved through a combination of improved materials and effective control strategies.

Accordingly, this dissertation aims to develop a model-based control strategy to improve performance and durability of PEM fuel cell systems for automotive applications. To this end, the dissertation first develops a physics-based and computationally efficient model for online estimation purposes. The need for such a model arises from the fact that detailed information about the internal states of the cell is required to develop effective control strategies for improved performance and durability, and such information is rarely available from direct measurements. Therefore, a software sensor must be developed to provide the required signals for a control system. To this end, this work utilizes spatio-temporal decoupling of the underlying problem to develop a model that can estimate water and temperature distributions throughout an operating fuel cell in a computationally ef-

ficient manner. The model is shown to capture a variety of complex physical phenomena, while running at least an order of magnitude faster than real time for dynamically changing conditions. The model is also validated with extensive experimental measurements under different operating conditions that are of interest for automotive applications.

Furthermore, the dissertation extensively explores the sensitivity of the model predictions to a variety of parameters. The sensitivity results are used to study the parameter identifiability problem in detail. The challenges associated with parameter identification in such a large-scale physics-based model are highlighted and a model parameterization framework is proposed to address them. The proposed framework consists of three main components: (1) selecting a subset of model parameters for identification, (2) optimally designing experiments that are maximally informative for parameter identification, and (3) designing a multi-step identification algorithm that ensures sufficient regularization of the inverse problem. These considerations are shown to lead to effective model parameterization with limited experimental measurements.

Finally, the dissertation uses a version of the proposed model to develop a degradation-conscious model-predictive control (MPC) framework to enhance the performance and durability of PEM fuel cell systems. In particular, a reduced-order model is developed for control design, which is then successively linearized about the current operating point to enable use of linear control design techniques that offer significant computational advantages. A variety of constraints on system safety and durability are considered and simulation case studies are conducted to evaluate the framework's utility in maximizing performance while respecting the durability constraints. It is also shown that the linear MPC framework employed here can generate the optimal control commands faster than real time. Therefore, the proposed framework is expected to be implementable in practical applications and contribute to extending the lifetime of fuel cell systems.

Chapter 1

Introduction

1.1 Motivation

A PEM fuel cell is an electrochemical energy conversion device in which hydrogen is electrochemically combusted to produce electricity, water, and heat. The high energy density, relatively fast transients, and zero tailpipe emissions make PEM fuel cells a suitable candidate for automotive applications [1]. However, despite the fact that the technology has matured significantly over the past two decades, remaining roadblocks still inhibit widespread use in the automotive industry. High cost of production and limited lifetime are among such hurdles that have to be overcome for mass market penetration [2].

Enhancing performance and durability of PEM fuel cells requires a thorough understanding of transport phenomena and various degradation mechanisms that limit the stack's lifetime. Mathematical models have been invaluable towards achieving this goal, as they have shed light on some of the important aspects of fuel cell performance and durability [3–5]. Nevertheless, there is still a need for physics-based and quantitatively predictive models that enable real-time monitoring of unmeasurable variables critical to system performance and lifetime. Accurate model parameterization and effective control strategies to mitigate degradation are among other areas that require more attention from

the fuel cell research community. Fortunately, these problems have been considered extensively in the battery research community and their results can be utilized to accelerate similar efforts in fuel cell development.

The overarching goal of this study is to create a model-based framework for degradation-conscious control of PEM fuel cells, so that the performance and durability trade-offs can be effectively explored and controlled. Successful implementation of such a control strategy can also lead to considerable balance of plant cost reductions. The system-level approach to enhancing performance and durability and reducing the system cost is motivated by the fact that innovative system design and control solutions play a significant role and have great potential in addressing the challenges faced by automotive PEM fuel cells, as has been demonstrated by the commercialized fuel cell vehicles, such as the Toyota Mirai [6]. This approach is also expected to be a valuable addition to the material-based solutions that are commonly sought in the fuel cell research community [7].

To achieve the above-mentioned goal, we first develop a physics-based model of the PEM fuel cell to act as an online sensor and provide information about the critical variables inside an operating fuel cell. This is in part necessitated by the fact that sensor measurement of these variables are difficult, costly, and in many cases impossible to obtain in an automotive application. We further consider effective parameterization of the developed model to enable quantitatively predictive modeling of physical phenomena. Lastly, the developed model is utilized to propose a degradation-conscious control framework that seeks to enhance performance and durability of the fuel cell system, while exploring opportunities for system-level cost savings.

To allow an in-depth investigation of the above-mentioned issues and the proposed framework, the following section takes a closer look at the components of a PEM fuel cell and their role in the cell's performance and lifetime. Critical aspects of fuel cell development are briefly reviewed and the role of mathematical models in improving the understanding of underlying phenomena and enabling further performance and durability

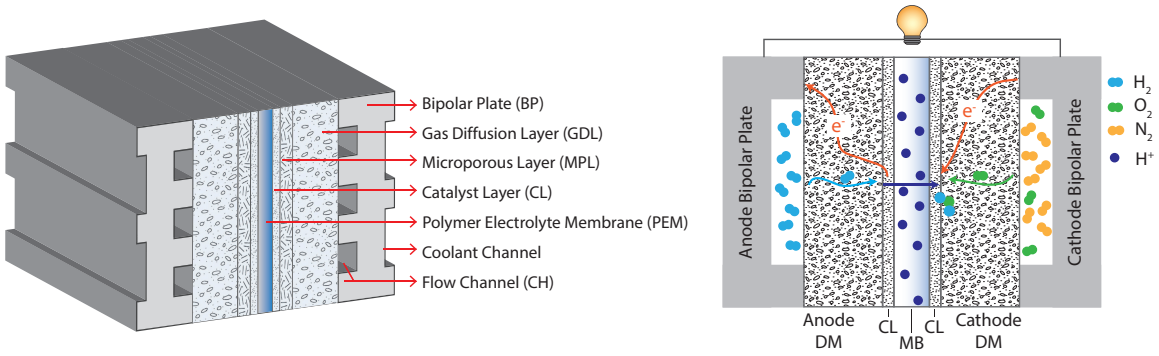

(a) (b)

Figure 1.1: PEM fuel cell schematics: (a) single cell structure and (b) operational principle.

enhancement is emphasized. This is then followed by a review of the relevant literature on modeling and control of fuel cell systems.

1.2 PEM Fuel Cell Structure and Operating Principles

A schematic of a PEM fuel cell is shown in Fig. 1.1. As illustrated in the figure, a single cell consists of a polymer electrolyte membrane (PEM), catalyst layers (CLs) on the anode and cathode sides, diffusion media (DM), and two bipolar plates that clamp the cell together. Each DM consists of a gas diffusion layer (GDL) and an optional microporous layer (MPL), which is typically found in state-of-the-art DM. The bipolar plates include machined grooves that provide channels for reactant and coolant transport. The combination of PEM, CLs, and the DM is sometimes referred to as the membrane electrode assembly (MEA). Furthermore, in state-of-the-art fuel cells, the catalyst layers are typically coated on the membrane through a variety of processes. This results in what is usually known as the catalyst coated membrane (CCM) [8, 9].

In a PEM fuel cell hydrogen is fed into the anode channel, whereas air or pure oxygen is fed into the cathode channel. Hydrogen participates in the hydrogen oxidation reaction

(HOR) in the anode CL, releasing protons and electrons. The electrons are transported across the external circuit, while the protons go through the PEM. They are recombined in the cathode CL during the oxygen reduction reaction (ORR) that generates water and heat (see Fig. 1.1(b)). The HOR and ORR half reactions are as follows:

$$\text{HOR} : 2H_2 \rightarrow 4H^+ + 4e^-,$$
$$\text{ORR} : O_2 + 4H^+ + 4e^- \rightarrow 2H_2O.$$

The overall reaction is the electrochemical combustion of hydrogen:

$$2H_2 + O_2 \rightarrow 2H_2O.$$

The fuel cell components are designed to facilitate the above electrochemical reactions in order to generate electrical power with highest possible efficiency. Different cell layers and their functionalities are described in detail in the following subsections.

1.2.1 Polymer Electrolyte Membrane (PEM)

At the heart of the fuel cell, the PEM enables selective transport of species, thereby creating the *interfaces* required for the electrochemical reactions. In particular, the PEM is conductive to protons released through the HOR, while it inhibits electron and reactant transport. The hydration state of the PEM determines its proton conductivity; a humidified PEM has a high proton conductivity and small ohmic resistance, whereas a dry PEM incurs a large ohmic loss due to lowered proton conductivity. As is explained below, this also creates a dilemma for water management in the cell: the PEM has to be hydrated to lower the ohmic resistance, but too much water can be detrimental to performance by flooding the DM and causing mass transport losses.

The water transport properties of the PEM affect its hydration state and should be well understood. Specifically, four major transport mechanisms have been identified: (1)

electro-osmotic drag (EOD), in which water molecules are carried with the ionic current passing through the PEM [10], (2) diffusion, where water is transported along a concentration gradient [11], (3) hydraulic permeation, where water is transported due to a difference in hydraulic pressure across the membrane [12], and (4) thermo-osmosis (TO), where water is transported due to a temperature gradient across the PEM to result in a more thermodynamically favorable state [13]. Each of these transport mechanisms have been characterized extensively in the literature. However, consensus about the magnitude of each mechanism's contribution to the overall water transport has not been reached. Therefore, both modeling and experimental efforts continue to focus on resolving outstanding issues regarding water transport in the PEM. In a recent work, Kusoglu et al. provide an extensive review of the topics relevant to PEM [14], which can be consulted for further insight into PEM operation.

Another important aspect of the PEM's utility is its selective transport property, which is crucial to fuel cell operation and also poses one of the main challenges in designing durable fuel cell stacks. In particular, even the smallest pinholes in the PEM create a shortcut for gas transport and lead to the exothermic combustion due to the direct contact between the reactants [15]. Once this shortcut is established, the electrochemical interfaces will no longer participate in the reaction. Therefore, PEM degradation, which can be in the form of chemical [16], mechanical [17, 18], and thermal degradation [19,20] as well as synergistic degradation mechanisms [21–23], results in catastrophic performance deterioration and must be minimized. While a complete understanding of all possible degradation modes is not available, literature points to hydration, voltage, and temperature cycling as culprits in PEM degradation [4, 24–26]. For instance, hydration and dehydration of the PEM result in repeated compressive and tensile stress cycles that may initiate cracks and pinholes or cause the existing ones to propagate through the membrane's thickness [17,27]. Similarly, attacks by radical species formed through electro-

chemical reactions may compromise the PEM's chemical composition. To mitigate such degradation, the fuel cell community has traditionally resorted to material-based solutions, such as reinforcements for mechanical durability [28–30] or different additives [31–33] for chemical stability. However, such effects may also be mitigated, to some extent, by effectively controlling the internal conditions of the fuel cell. For example, the hydration state of the PEM can be maintained within some specified bounds in order to avoid excessive stresses on the membrane. Such applications require mathematical models [34, 35], first to define the degradation constraints that ensure target lifetimes are met, and then to be used in a model-based control framework that respects the identified constraints.

1.2.2 Catalyst Layer (CL)

Catalyst layers are where the electrochemical reactions take place and are arguably the most complicated components of a PEM fuel cell. Specifically, they provide *three-phase boundaries* that allow for electrons, protons, and reactant gases to participate in the reaction. In conventional PEM fuel cells, catalyst layers typically consist of Platinum (Pt) particles dispersed on primary carbon particles and (partially) covered by ionomer (see Fig. 1.2). The Pt particle size is in the range of 2-15 nm, while the primary carbon particles may have sizes of up to 80 nm based on the type of carbon support used. The Pt improves reaction kinetics. The carbon support provides an electronically conductive phase, while allowing a high electrochemically active surface area (ECSA) to be achieved. The Pt decorated carbon particles are typically bound by an ion-conducting polymer, which in many cases is the same as that in the PEM. This ionomer phase provides pathways for proton transport in the catalyst layers. The pore space in the catalyst layer allows gaseous reactant to reach the reaction site (see Fig. 1.2). It is worth mentioning that more recent developments such as the nano-structured thin film (NSTF) catalyst layers do not necessarily conform to this description [36]. However, such catalysts are

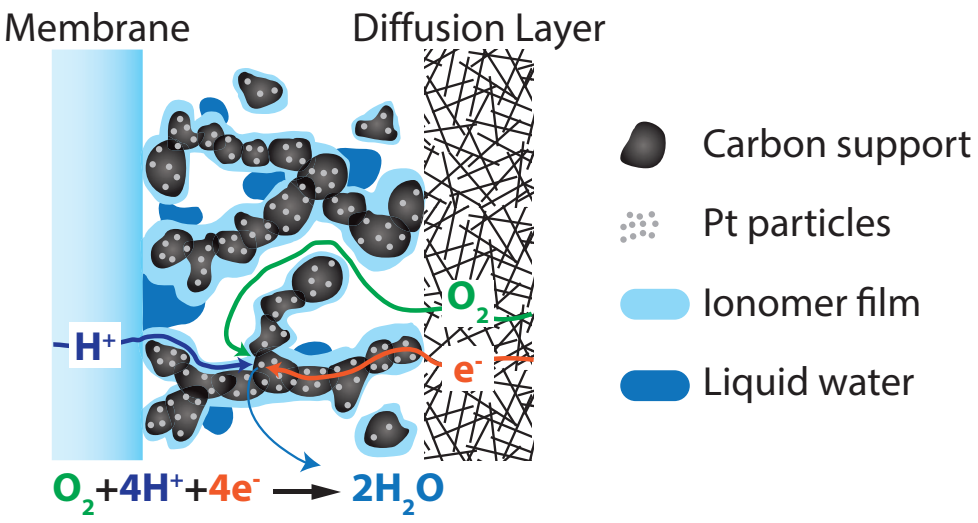

Figure 1.2: Schematic of gas and charged species transport in the cathode catalyst layer.

beyond the scope of this work and are not considered in this discussion.

Effective performance of the CLs depend on the electron, ion, and reactant gas' ability to reach the reaction site. High electronic conductivity of carbon ensures efficient electron transport. Therefore, the performance of the CL is determined by the balance between proton and gas transport resistances. In the anode CL, HOR occurs close to the membrane due to high diffusivity of hydrogen and facile HOR kinetics. Therefore, there is minimal resistance to proton transport in the anode CL and only a small mass transport resistance. In the cathode CL, however, the trade-off is quite significant due to sluggish ORR kinetics and the propensity of the cathode side to flooding by product water. Under dry conditions, the ionomer has low conductivity, which results in considerable proton transport resistance, and minimal macroscopic mass transport resistance as oxygen can get to the ionomer surface in the cathode catalyst layer without being blocked by liquid water. Nonetheless, excessive ionomer drying may lead to mass transport limitations due to depressed oxygen permeability in the dry ionomer thin film [37, 38]. On the other hand, the ionomer's high conductivity under wet conditions results in minimal protonic resistance. However, liquid water may accumulate in the pore space in the CL and DM and block oxygen pathways to the active sites. Therefore, such trade-offs have to be

understood to enable the highest catalyst utilization and optimal performance. Significant experimental developments in recent years have helped elucidate the distribution of different phases in the CL [39–43] and improve the understanding of the factors limiting its performance. Nevertheless, mathematical models that capture the local transport resistances in the CL continue to be of special interest for further catalyst development.

A major focus in catalyst research is the reduction of Pt loading. Such reductions are necessitated by the cost and scarcity of Pt [44]. Extensive research in this area has led to significant improvements. In particular, state-of-the-art cathode CLs have Pt loadings on the order of 0.15 mg/cm^2 while the loading in the anode CLs is as low as 0.05 mg/cm^2 [44, 45]. The higher loading on the cathode is due to the sluggish ORR kinetics. Unfortunately, cathode Pt loading below 0.15 mg/cm^2 results in increased performance loss at higher current densities [44, 46]. This issue has received considerable attention in the literature in recent years, as researchers have tried to identify the root causes of the observed behavior. Mathematical models have been an indispensable tool in this endeavor. Nevertheless, they may have led the community astray in some cases [47]. The debate seems far from settled and further model development is necessary for a better understanding of the limiting factors.

Catalyst degradation is also of profound significance, as it can dramatically limit the lifetime of the cell [4]. Corrosion of the carbon support [48–50] and Pt dissolution and migration [51–54] are among major degradation effects. Various causes of such phenomena are documented in the literature [4]. However, similar to the PEM degradation, a complete picture of the synergistic effects has remained elusive. Here again, the mitigation strategies typically involve material-based solutions, such as adding a catalyst to promote oxygen evolution reaction over carbon corrosion [55,56]. Nonetheless, system-level strategies have proven useful in enhancing catalyst durability [57] and model-based control techniques can potentially extend the durability of the state-of-the-art catalysts even further.

1.2.3 Diffusion Media (GDL and MPL)

The porous diffusion media consists of GDL and in most cases an MPL. Its role is to provide pathways for reactant gas transport from the channels to the active sites in the CLs and transport the product water and heat away from the CLs. The DM must also provide electronic connection to the backing plates and mechanical support for the PEM and the CLs. The porous structure of the DM means that the transport pathways are typically tortuous, which increases the transport resistance. Another important aspect of the DM design is its propensity to flooding. If the DM cannot effectively remove the product water, liquid water may build up in the pores and block pathways for gas transport, thereby increasing the mass transport resistance and incurring performance losses. As such, many state-of-the-art diffusion layers are coated with a hydrophobic coating (in most cases PTFE) to repel liquid water.

Heat transfer properties of the DM can play a significant role in water transport, as well. In particular, a small heat conductivity of the DM results in a considerable temperature gradient across its thickness. This temperature gradient can promote water removal in vapor phase, which is known as phase-change-induced (PCI) flow [3, 58, 59]. In PCI flow, water evaporates at the high temperature location near the CL, moves across the DM's thickness along the vapor pressure gradient, and condenses at the location with lower temperature near the channel [3]. At higher operating temperatures, this mechanism is shown to be the dominant mode of water transport. This can be advantageous as PCI flow minimizes liquid buildup in the pores of the DM, and therefore, mass transport losses due to flooding will be minimal. However, it induces another type of mass transport loss due to the fact that the incoming reactant gas has to move in the opposite direction of the outgoing vapor flux. The degree to which the performance is improved or degraded due to the PCI flow depends on the properties of the DM as well as the particular operating conditions under investigation [3]. Overall, the effectiveness of the DM depends on the

choice of materials, such as the binder and hydrophobic coatings used, as well as its microstructure [60, 61]. This is another area where mathematical models have proven useful in improving the understanding of the underlying phenomena and optimizing the choice of materials and design of the DM [62].

As mentioned above, the DM is typically made up of two layers: a GDL and an MPL. The GDL has pore sizes on the order of 1-100 microns, whereas the MPL has smaller pore size on the order of 10-1000 nanometers. In addition to the smaller pore size, the MPL is typically made to be more hydrophobic than the GDL to drive the water away from the CL. Experimental results indicate an improvement in performance when using the MPL [63]. The cause of this improvement is still under debate [62]. Some of the main mechanisms for performance improvement due to the MPL suggested in the literature include [62, 64]: (1) improved contact between the layers and lowered ohmic loss, (2) increased temperature in the CL due to lower thermal conductivity of the MPL, which enhances water removal in vapor form, (3) forcing more water removal through the anode and reducing cathode flooding, and (4) providing selected pathways for liquid water removal through the GDL. Some of these proposed improvements continue to be contested, and transport models are constantly used to support or rebut such hypotheses.

As for the degradation of the DM, several effects have been discussed in the literature that result in loss of PTFE content, change in water retention capabilities, and change in thermal and mass transport properties [25,26]. Nevertheless, such degradation phenomena are secondary to PEM and CL degradation and are not considered to be the major limiting factor for PEM fuel cell lifetime. Therefore, they are not considered in this dissertation.

1.2.4 Bipolar Plates and Gas Flow Channels

The bipolar plates serve as current collectors as well as backing layers providing mechanical support to the cell structure. Therefore, they should be made out of highly conductive

material with enough mechanical strength that can withstand clamping pressures on the order of 1-5 MPa [1, 65]. They should also be chemically stable and corrosion resistant [1, 65]. The choice of material for the bipolar plates is a topic that is beyond the scope of this dissertation and is not further elaborated on.

Another important feature of the bipolar plates is the layout of the gas flow channels. The size, shape and pattern of the channels can have a significant impact on the performance of the cell. These parameters can affect pressure drop along the channel, uniformity of reactant distribution, and water removal capability, all of which affect the cell performance [1]. In particular, various flow channel patterns have been proposed and investigated in the literature, ranging from parallel to serpentine and interdigitated flow channels. While all these configurations have been used in prototypes with some degree of success, it appears that most high volume production stacks have simple parallel flow designs to minimize cross-flow effects and liquid accumulation at the bends. The mesh design in Toyota Mirai is a notable exception [66]. Nevertheless, parallel flow channels are quite prevalent and are used in this dissertation when a channel model is to be developed.

1.2.5 Modes of Operation

The flow direction in the gas channels is an important operational variable that can have a profound impact on the performance, especially under drier conditions. In particular, anode and cathode gas streams may flow in the same direction, *i.e.*, co-flow operation, or in the opposite direction, *i.e.*, counter-flow operation (see Fig. 1.3). In some cases the streams flow perpendicular to each other, which is called cross-flow. The models of PEM fuel cells should have the flexibility to represent these variations in the operation mode. This dissertation considers co-flow and counter-flow cases, since they are the main modes of operation for most state-of-the-art fuel cell stacks. It is worth mentioning that the Toyota Mirai's design does not conform to this categorization [66] and is beyond the

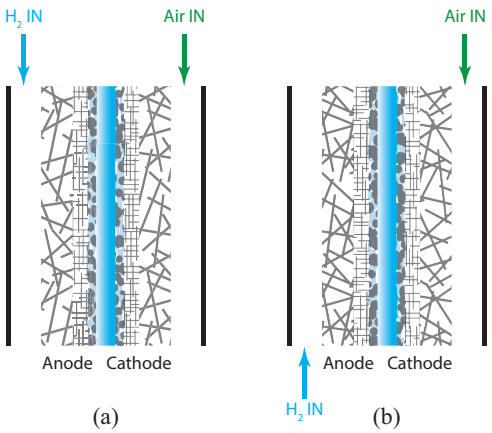

Figure 1.3: Common fuel cell flow configurations: (a) Co-flow and (b) Counter-flow.

scope of this work.

Another important operational variable is the fuel utilization scheme. More specifically, the cell may be operated in dead-ended anode (DEA) configuration [67, 68] or a recirculation system may be used to maximize fuel utilization [69]. Such configurations can also have an impact on uniformity of current and reactant distributions. Data from stack suppliers seem to suggest that most of the state-of-the-art fuel cell stacks are now operated with anode recirculation. Accordingly, the model that is developed in this dissertation is readily applicable to this configuration. DEA operation may be simulated with some modifications to the proposed model, but is out of the scope of this work.

Having described the components of a PEM fuel cell, we now turn our attention to the background relevant to the scope of this dissertation. Particularly, we review the relevant literature on fuel cell modeling, model parameterization, and fuel cell system control in the following sections.

1.3 Literature on Modeling of PEM Fuel Cells

The previous section examined critical aspects of fuel cell development and emphasized the important role of modeling in the process. In particular, modeling transport phenomena

in the cell and the resulting performance is of special interest, since it allows for inspection of variables of interest inside a cell that might otherwise be unavailable. Such information can be crucial in understanding the behavior of a fuel cell stack, or characterizing its performance and lifetime. Accordingly, the interest in modeling transport phenomena in fuel cells has continuously increased since the seminal works of Springer et al. [11] and Bernardi et al. [12] in the early 1990s. These studies developed two of the main models for membrane water transport and remain among the most adopted approaches in more general models to this date. Throughout the last two decades, many models have been developed to investigate the different transport phenomena in PEM fuel cells. These models can be characterized based on the domain of application, the spatial dimension, and the temporal behavior.

As for the domain of application, many models are developed to study the transport phenomena in a single layer in the cell. Many models have focused on water transport inside the PEM [70–72], where contributions from various transport mechanisms, including electro-osmotic drag, diffusion, thermo-osmosis, and hydraulic permeation have been discussed. Models have also been developed for transport in the gas flow channels [73, 74] and DM [75, 76]. Modeling the effects of microstructure on DM transport properties has also become popular. The first comprehensive model in this regard was the bundle of capillaries model developed by Weber et al. [77] and later extended to include contact angle distribution in the DM [78]. Stochastic reconstruction methods have also been proposed in recent years [79]. More recently, driven by the requirement to reduce precious metal loading in the CLs, models tailored to inspecting transport and reaction kinetics in the CLs have become the center of attention [80–85] and significant efforts have been dedicated to understanding the root causes of performance drop at Pt loadings below 0.15 mg/cm^2 on the cathode. In addition to these component level models, there are also numerous models that include transport in the entire cell [86–92]. Moreover, system-level models have been developed that include the fuel cell stack and the auxiliary equipment

such as the compressor [93], but not the details of the transport phenomena in a single cell. While the individual layer models help elucidate different transport mechanisms in each layer of the cell, the cell-level models help in understanding the behavior of each component in an operational cell, and the system-level models determine the overall response of the fuel cell system by taking the auxiliary equipment into account.

The cell models cover a wide range of spatial dimensions including 0D, 1D, pseudo-2D, 2D, pseudo-3D, and 3D. In 0D models the spatial distribution of the variables are ignored [93]. The 1D models usually investigate the transport in one dimension through the membrane [94–97], albeit some 1D models focus specifically on transport along the flow channels [98]. The pseudo-2D models investigate the transport in 2D without solving a fully coupled problem in both spatial dimensions [87]. Such models incorporate transport in the through-the-membrane and along-the-channel directions in a decoupled manner with the only coupling stemming from the boundary conditions. This approach has gained popularity because of its simplicity and computational efficiency. Many 2D models have also been developed with variations based on the selected dimensions; while some 2D models include transport along the channels and through the membrane, others only solve for the through-the-membrane direction while incorporating the land effects and the channel to channel variations in the third (in-plane) direction [89–91, 99]. The latter models may be reduced to 1D models through conformal mapping of the domain [100–102]. Another simplification to such models, called the bi-domain modeling approach, was proposed by Zaglio et al., who solved the problem as two separate 1D problems; one under the channel and one under the land [103]. Pseudo-3D models have also been developed that balance model fidelity and computational efficiency [3, 104, 105]. In these models the transport through the membrane is solved as a 2D problem coupled to a 1D channel model through boundary conditions. Finally, 3D models include transport phenomena in all physical directions, offering the highest fidelity with highest computational cost [86, 106].

In terms of the temporal behavior, most of the early models developed were steady state [11, 64]. However, in recent years more dynamic models have been developed due to the interest in investigating the dynamic behavior of the fuel cell [94, 107, 108]. Nevertheless, researchers continue to develop steady state models that provide a deeper understanding of the performance limitations by incorporating details of thermal and mass transport in the complicated structure of PEM fuel cells [62, 91, 105].

Kinetic models used to describe the HOR and ORR half reaction should also be considered for fuel cell model development. HOR has facile kinetics and can be modeled with the usual Butler-Volmer (BV) equation or its simplifications such as the Tafel kinetics very well [1]. Nevertheless, other HOR kinetic models have been proposed and employed in the fuel cell literature. Of particular interest is the dual-pathway kinetic model initially proposed by Wang et al. [109] and implemented in some of the recent fuel cell models [89, 91]. In contrast to HOR, the ORR has sluggish kinetics and require further attention. Most of the early fuel cell models resorted to the BV kinetics model or some of its approximations for ORR. More recently, however, the effects of oxides covering the active Pt sites have been included in modified Tafel models for ORR [110]. Several other ORR kinetics models have been proposed, with the double-trap (DT) kinetics model being the most notable one that has been adopted by many researchers. The DT model was originally proposed by Wang et al. [111] and later modified by Moore et al. [112]. Further modifications of the DT model have also been proposed in the last few years [113, 114]. In addition to these models, there is a rather extensive debate as to how the environmental conditions in the CL affect ORR kinetics. For instance, the ORR kinetics are believed to be affected by the relative humidity [115–118]. Moreover, the ionomer thin film is believed to impact the activity [119–121], therefore, further convolving the in-situ experimental results. The key observation is that ORR kinetics are far from being fully understood. The situation is further exacerbated by the fact that the experimental results are often convoluted due to mass transport limitations at higher currents, the effects of the ionomer thin film on

the catalyst activity, and the environmental conditions. Therefore, further modeling and experimental works are required to clarify these kinetics.

Another area of interest is real-time modeling to obtain information about the states of the cell. This is motivated in part by the desire to reduce the number of sensors in the system and becomes critical in light of the difficulties associated with measuring mass and temperature distributions within the components of a cell. Recent advancements in technologies such as neutron imaging [122–124], magnetic resonance imaging (MRI) [125], X-ray computed tomography [61, 126], small angle X-ray scattering (SAXS) [127] and small angle neutron scattering (SANS) [128], as well as novel experimental methods for measuring gas transport resistance [102, 129, 130] have shed light on the transport mechanisms such as the intricate two-phase flow behavior in porous layers. Nevertheless, these measurements cannot be performed on-board a vehicle. As such, real-time modeling remains the main tool to provide information about the state of temperature and water throughout the cell. However, most of the high fidelity models developed to date are computationally expensive and do not lend themselves to real-time applications [89, 90, 131]. On the other hand, existing real-time models do not incorporate the important physical phenomena that affect the transport in the cell. Therefore, achieving a careful balance between fidelity and computational efficiency remains a challenge.

One of the popular real-time models that has been extensively used by the controls community is the work of Pukrushpan et al., who developed a system-level lumped-parameter (0D) model of the PEM fuel cell [93]. The model does not include any spatial variations. Furthermore, it relies extensively on empirical relations obtained through curve fittings and does not describe many of the physical phenomena, such as the two-phase flow in the cell. Other models for real-time control and estimation of the variables in the cell have been developed [132–134]. Efforts for modeling PEM fuel cells with equivalent circuits have also been reported [135]. Acknowledging the significance of distributions along the cathode channel, Headley and Chen have investigated lumped models with the

addition of several control volumes in the cathode channel for temperature and humidity distribution modeling [136]. In spite of such efforts, these models are very simplistic in nature and do not capture many of the physical aspects of the cell behavior. In addition to numerical models, analytical modeling has also attracted some interest. Kulikovsky has worked extensively in this area [137]. The analytical framework benefits from high computational efficiency, while its main drawback is in the use of limiting assumptions to arrive at the analytical formulation. Finally, data driven and black-box modeling techniques such as neural networks have been utilized for real-time simulations, as well [138]. Despite low computational expenses of such models, their adoption has been hindered by the fact that they require a lot of experimental data to achieve reasonable accuracy and they only provide an input-output map for the system without any insight into or knowledge about the internal states of the fuel cell.

Efforts have also been made to address the need for higher fidelity physics-based models that can be used in real time. Grotsch et al. [132], McCain et al. [94, 139], and Siegel et al. [88] developed 1D through-the-membrane models with two-phase flow in the GDLs to study the dynamic behavior of the cell. The main drawback of these works lies in the isothermal assumption and the neglecting of the reactant concentration distribution along the gas flow channels. Another work in this area is by Promislow et al., who incorporated thermal transport and the along-the-channel transport into their model [87]. Nevertheless, the fidelity of such models must be significantly improved by incorporating more intricate physical phenomena before they can be used to address the durability issues in a fuel cell. For example, these models typically treat the catalyst layers as interfaces and disregard the complex nature of transport in these active layers. It is thus evident that despite such efforts, there remains a gap in the fuel cell modeling literature for models that strike a balance between fidelity and computational cost.

1.4 Literature on Model Parameterization

The fuel cell models, similar to those of other electrochemical energy systems, such as batteries, usually have tens of parameters that may affect their predictions. This is especially the case for physics-based models that are derived from first principles, as such models often incorporate various physical attributes of a cell along with detailed kinetics of electrochemical reactions. Given that the prediction capabilities of these models depend not only on their structure (*i.e.*, the first principles and assumptions used in deriving the model), but also on the availability of accurate parameter values, the problem of parameter identification calls for critical investigation.

Despite its centrality to model accuracy and reliability, parameter identification has not received much attention in the fuel cell literature, where arbitrarily assigning parameter values [54, 92, 140], or doing so based on expert knowledge [90, 114, 141], and citing qualitative agreement with experimental data as evidence for model validity is common [89, 90, 142]. In other instances, parameter identification is treated as material characterization [143], wherein the model parameters are obtained through component characterization techniques. While these methods are crucial to enhance understanding of fuel cell behavior and improve model performance, they are often costly and require specialized equipment. Moreover, even extensive characterization efforts could only unveil a handful of parameters, typically with considerable uncertainty [144]. For instance, significant efforts have been aimed at determining thermal conductivity of various layers in a fuel cell assembly, often resulting in values that vary by orders of magnitude for the same material set [145, 146]. Lastly, even obtaining all model parameters through such ex-situ experiments would not guarantee accurate model predictions. This lack of prediction accuracy is mainly due to the inherent and inevitable simplifications of mathematical models. However, this does not indicate that the models do not have predictive

power. Rather, it motivates effective parameter identification as a necessary step towards unleashing the full predictive capability of physics-based models.

The fact that parameter identification remains an understudied subject in the fuel cell modeling literature can be mostly attributed to the computational cost of available physics-based models that do not lend themselves to systematic optimization-based model parameterization, which typically require a large number of model evaluations. However, some in the fuel cell community have already utilized these techniques. For example, nonlinear least squares have been used to fit models of oxygen reduction reaction (ORR) to kinetic data [112, 113]. Others have used polarization data to identify full cell model parameters with these methods [147, 148]. The utility of having multiple measurements to improve model predictions has also been pointed out [149]. While these works stand out in terms of their efforts for systematic parameter identification, they are still limited in their application. Specifically, they only identify a few of the model parameters using optimization techniques and rely on literature values for the other parameters. More importantly, the choice of parameters to be identified through optimization and the operating conditions used to collect experimental data are made arbitrarily or based on the researchers' physical intuition about the problems. This amounts to an important gap in the fuel cell modeling literature, which this dissertation aims to address.

Fortunately, the problem of parameter identification is common among many fields, some of which offer a vast body of literature on the topic. Most importantly, we note that the recent battery modeling literature has focused extensively on parameter identification and closely related problems. In particular, sensitivities of the well-known models have been studied [150–152], parameter identifiability of the models have been investigated [153–157], various methods for simultaneous identification of multiple model parameters have been employed [152, 158], bounds on parameter estimates have been developed [159], and Bayesian statistics have been used to infer parameter distributions [160]. More recently, there has been a move towards optimally designing experiments for param-

eter identification [161–164]. In addition to this recent battery literature, other studies in fields ranging from system biology [165, 166] to process industry [167] offer further basis for systematic parameter identification efforts that may be utilized to enhance the predictive capability of fuel cell models.

1.5 Literature on Fuel Cell Power Systems Control

Fuel cell power systems need to be controlled to ensure robust and optimal power delivery. Therefore, the control task is to maximize the fuel cell power output while minimizing parasitic losses due to auxiliary equipment such as the compressor. Additionally, the operating conditions of the fuel cell stack can be regulated in order to maximize its lifetime. These requirements, often in competition with each other, render the task of controlling the fuel cell power system a critical one. There have been numerous studies in the literature to address these issues from different perspectives. While most of the approaches to date are focused on the system-level performance to efficiently regulate power output [93, 98, 168, 169], some studies have also targeted the cell-level performance to avoid specific phenomena, such as flooding, membrane dehydration, and local reactant starvation [170, 171].

On the system level, the control objective is to enable power tracking capability by the fuel cell system. To this end, various control strategies have been utilized. Golbert et al. [98, 169] designed an adaptive controller as well as a model predictive control (MPC) architecture for this purpose. Similarly, multivariable linear feedback techniques have been used [172]. Other studies have aimed at regulating the net power output of the entire system incorporating the balance of plant while ensuring the safe operation of the fuel cell stack [93, 173]. Such studies typically incorporate the dynamics of the compressor, the humidifier, and the supply and return manifolds. These studies also seek to avoid oxygen starvation by regulating the oxygen stoichiometry (also known as the oxygen

excess ratio) in the cathode. This is motivated by the fact that oxygen starvation is known to contribute to the catalyst degradation [4, 25]. More broadly, avoiding reactant starvation is one of the most common control objectives in the literature that has been implemented in a variety of forms, including multivariate linear feedback [93, 173–175], reference governors [176–178], and MPC [168, 170, 179–184]. Another area of focus in the literature has been the energy management of hybrid power plants where fuel cell is one of the power sources. Here again, reference governors [185, 186], MPC [168], and optimal control have been heavily utilized [187].

Generally, the system-level model-based control architectures seek to deliver the maximum power while incorporating some system constraints, such as the ability to provide enough oxygen to the fuel cell stack. However, these architectures are based on simplified models of the fuel cell that usually neglect thermal and two-phase flow dynamics of the cell. Therefore, they are limited in their ability to predict the cell behavior under varying drive cycles encountered in automotive applications. To overcome these issues, researchers have studied the control problem using more detailed models of fuel cells. McCain et al. [171] studied the controllability and observability of liquid water in the GDL using a 1D two-phase model linearized at three critical conditions. They found that voltage measurements are critical to observability of different modes. McKay et al. [188, 189] studied humidity and temperature control of the cell using a controllable membrane humidifier. Additionally, fault diagnosis for fuel cells has been studied and fault tolerant control strategies have been utilized to protect against potential causes of performance degradation including flooding and membrane dehydration effects [190], as well as reactant starvation [191]. One of the interesting works in this area is that of Burkholder et al., who studied voltage instability due to two-phase flow regimes [192] and proposed the use of Lyapunov exponent of the voltage return map as an instability statistic to design active stability controllers that induce stabilizing pressure perturbations [193].

These studies are fundamental to developing control strategies for fuel cell systems. However, since they rely heavily on mathematical models to represent the system dynamics, their performance is determined by the accuracy of the underlying models. The models used in these studies are generally not descriptive of the intricate two-phase flow and temperature dynamics in the fuel cell. As such, concentrated efforts on controlling these fuel cell dynamics are not common in the literature. Nevertheless, experimental results point to great potential for improvement in this area. For instance, Cho et al. [122] reported that if proper purge conditions are used, then water removal from the membrane can, to some extent, be controlled separately from the flow field and the porous media. This holds great promise for avoiding porous media flooding and membrane dehydration. However, a systematic approach to synthesize effective controllers that utilize these potentials is not available in the literature.

Mitigating degradation can be an additional goal of the control design problem. Accordingly, some recent works have tried to address durability issues with control strategies, such as MPC [170, 194]. Specifically, Luna et al. utilized an observer-based nonlinear model predictive controller to avoid fuel and oxidant starvation along the flow channel [170]. Notably, they also accounted for the membrane hydration state in their MPC formulation. In a follow-up work, they used a similar architecture to optimize the electrochemical surface area (ECSA) during operation [194]. While providing valuable insight about the controller design, these studies still use rather simplified models of the fuel cell, only consider one mode of degradation, and are based on some empirical notion of the degradation process without proper validation. Furthermore, selection of suitable degradation criteria is still an open challenge that is difficult to address without a multidisciplinary perspective. For instance, Luna et al. have focused on maintaining an optimal value for the ECSA during operation, citing the loss of ECSA due to changes in the liquid water level as a degradation criterion [194]. However, while ECSA loss is indeed a major concern, it is commonly attributed to Pt dissolution and migration in the

fuel cell literature [54, 195–197] and controlling the liquid water is not expected to have a significant mitigating impact.

1.6 Research Objectives

The preceding literature review reflects the extensive research activities in various aspects of PEM fuel cell development. At the same time, it also identifies opportunities for further progress. In particular, there seems to be a gap between the electrochemical literature trying to improve the scientific understanding and design of PEM fuel cells, and the fuel cell control literature, that has focused on output power tracking for the most part with only minimal consideration of degradation effects. Accordingly, in this dissertation we take a step towards filling this gap by creating a model-based framework for degradation-conscious control of PEM fuel cells, where our main research objectives include:

- Developing and validating a computationally efficient physics-based model of PEM fuel cells that captures the distributions of critical variables throughout an operating fuel cell in all three physical direction. Such a model can be used as a software sensor to provide information about internal conditions of automotive PEM fuel cells.

- Developing a framework for effective model parameterization to enable quantitative predictions. Particularly, the framework should address the challenges of parameter selection for identification, experimental design, and systematic identification. Such a framework would allow PEM fuel cell models to be parameterized effectively with limited non-invasive measurements.

- Developing a model-based degradation-conscious control framework to simultaneously enable tacking of a power demand, maximize the overall system efficiency, and extend the system's lifetime by ensuring operation in a safe region. Realization of such a control framework can lead to enhanced performance and durability

of the existing PEM fuel cell stacks and enable their widespread adoption in the automotive industry.

1.7 Dissertation Contributions and Organization

The above-mentioned research objectives of this dissertation are met through several novel contributions to the fuel cell modeling and control literature as described below.

1.7.1 Model Development and Validation

- *A physics-based and computationally efficient pseudo-2D bi-domain model of PEM fuel is developed.*

  The model accounts for complex behavior in an operating fuel cell, while taking advantage of natural time and length scale separations to spatio-temporally decouple the problem and achieve simulation times that are more than an order of magnitude faster than real time. Importantly, the model captures the distributions of water and temperature along the flow channels and through the membrane, while distinguishing between the local conditions under the channel and land locations. Moreover, the catalyst layer is modeled explicitly, where the volume fraction of different phases are taken into account and detailed models for reaction kinetics are employed. The proton and mass transport trade-offs in the cathode catalyst layer are effectively captured with a new lumped model that allows for efficient and fast simulations. Lastly, an iterative scheme is developed for stable and efficient simulation of counter-flow configuration. These measures are detailed in Chapter 2. The model has also been presented at a number of conferences [198–200] and published in archival format [201, 202].

- *The developed model is extensively validated with experimental performance data.*

Experimental voltage and resistance data obtained with two different fuel cell material sets at a variety of operating conditions relevant to automotive applications are used to validate the model. The results of this experimental validation effort are also presented in Chapter 2 and have been archived in a journal publication [202].

1.7.2 Effective Model Parameterization

- *An extensive sensitivity analysis is conducted to examine the impact of the various model parameters on different outputs of interest.*

  An extended local sensitivity analysis is used to study the parameter sensitivities and inspect the potential parameter interactions. In particular, the analysis is carried out under a variety of operating conditions that are designed to cover the entire range of conditions that are of practical interest. The results of the analysis are used to highlight the various aspects of parameter identifiability. It is shown that physics-based models of PEM fuel cells, and more broadly those of electrochemical devices, are overparameterized with badly conditioned Hessian matrices that diminish the prospects of successful parameter identification. The methods and results are discussed in detail in Chapter 3 and have been documented in conference and journal publications [203, 204].

- *A framework is developed to robustly select the best parameters for identification, design robust optimal experiments for this purpose, and identify the selected parameters with a systematic approach.*

  Results from the extended local sensitivity analysis are utilized to develop a framework for effective parameter identification. In particular, the sensitivity data are used to select an optimal set of parameters that are best suited for model tuning to a given set of measurements. The selection is also robust to assumptions about nominal parameter values. The same procedures are used for model-based

experimental design to maximize parameter identifiability prospects with limited measurements. Lastly, a multi-step identification algorithm is developed to ensure a well-constrained inverse problem formulation. The framework and its verification are presented in Chapter 4. These results have also been published in a number of conference and journal publications [204–207].

1.7.3 Degradation-Conscious Control Framework

- *A control-oriented model is derived for use in an MPC setting.*

  Despite its computational efficiency, the model developed in Chapter 2 is not suitable for optimization-based control methods, such as MPC. Therefore, further simplification is employed to derive a control-oriented model. The result is a 1D through-the-membrane model that describes the most critical conditions with only 8 state variables. Three additional states are used to model the reactant supply dynamics so that the entire fuel cell system can be considered for control formulation. The rationale behind the fuel cell model simplifications and the modeling equations for the entire system are presented in Chapter 5. The results in this chapter have also been presented in conference and archival publications [208, 209].

- *A linear time-varying MPC (LTV-MPC) framework is developed for degradation-conscious control of the PEM fuel cell system.*

  The control-oriented nonlinear model is successively linearized about the current operating point to obtain a linear model. The linear model is used to formulate the control problem, where a rate-based MPC formulation is employed. The controller objective is to ensure offset-free tracking of the power demand, while maximizing the overall system efficiency and enhancing its durability. To this end, the fuel consumption and the power loss due to auxiliary equipment are minimized. Moreover, the internal states of the fuel cell stack are constrained to avoid harmful conditions

that are known stressors of the fuel cell components. Membrane dry-out, rapid changes in the membrane hydration, and reactant starvation are among the considered stressors. However, the framework has the flexibility to accommodate further lifetime indicators as required by the particular application. It is also shown that the control commands can be generated in real time, allowing practical hardware implementation. The control problem formulation is presented in Chapter 5 and documented in conference and archival publications [208–210].

Chapter 2

A Computationally Efficient Model for Automotive PEM Fuel Cells

2.1 Introduction

Similar to the state-of-the-art battery management systems that rely on reduced-order models to make critical decisions that affect the performance and lifetime of the battery pack [211], a fuel cell management system depends on a model of the fuel cell stack and the auxiliary components [93,208]. This motivates the need for real-time models that can run efficiently on-board the vehicle and act as soft sensors, providing information about the distribution of critical variables in the fuel cell stack.

As mentioned in Chapter 1, despite recent efforts, there remains a gap in the fuel cell modeling literature for models that strike a balance between fidelity and computational cost. To fill this gap, the objective of this chapter is to develop a PEM fuel cell model that is geared toward real-time simulation on-board the vehicle and provides critical information for fuel cell management and control systems. To this end, we utilize the disparate time scales of the involved transient phenomena as well as the large aspect ratio of the cell components to spatio-temporally decouple the problem and obtain a computationally

efficient solution. Development of a new reduced-order model for water balance across the cell and a simplified method to account for mass and charge transport trade-offs in the cathode catalyst layer further contribute to the computational efficiency of the model. Additionally, the bi-domain modeling approach employed here allows for distinguishing the transport phenomena under the channel and under the land locations. Lastly, a novel iterative scheme enables efficient counter-flow simulations. Overall, these considerations render the model suitable for real-time monitoring of unmeasured and critical states within the fuel cell stack. The model is also experimentally validated with performance data from a differential cell as well as an automotive short stack under a variety of operating conditions.

The rest of the chapter is organized as follows. The model formulation is presented in Section 2.2, which describes the steps for developing the computationally efficient model. The presented model is then extensively validated with experimental data from two stacks and shown to provide good agreements with the data with reasonable parameter values in Section 2.3. Finally, some simulation case studies are presented in Section 2.4 to further demonstrate the model's capabilities, followed by a brief summary in Section 2.5. The description of variables and parameters in this chapter can be found in the nomenclature.

2.2 Model Development

2.2.1 Modeling Domain

The modeling domain is shown in Fig. 2.1. This is a pseudo-2D bi-domain ($P2D^2$) model, which captures the distributions in all three physical directions in a decoupled manner. In particular, a 1D through-the-membrane transport model is developed for the MEA. This 1D model is solved twice, once under the channel and once under the land area. This bi-domain modeling approach was first proposed by Zaglio et al. [103] to efficiently

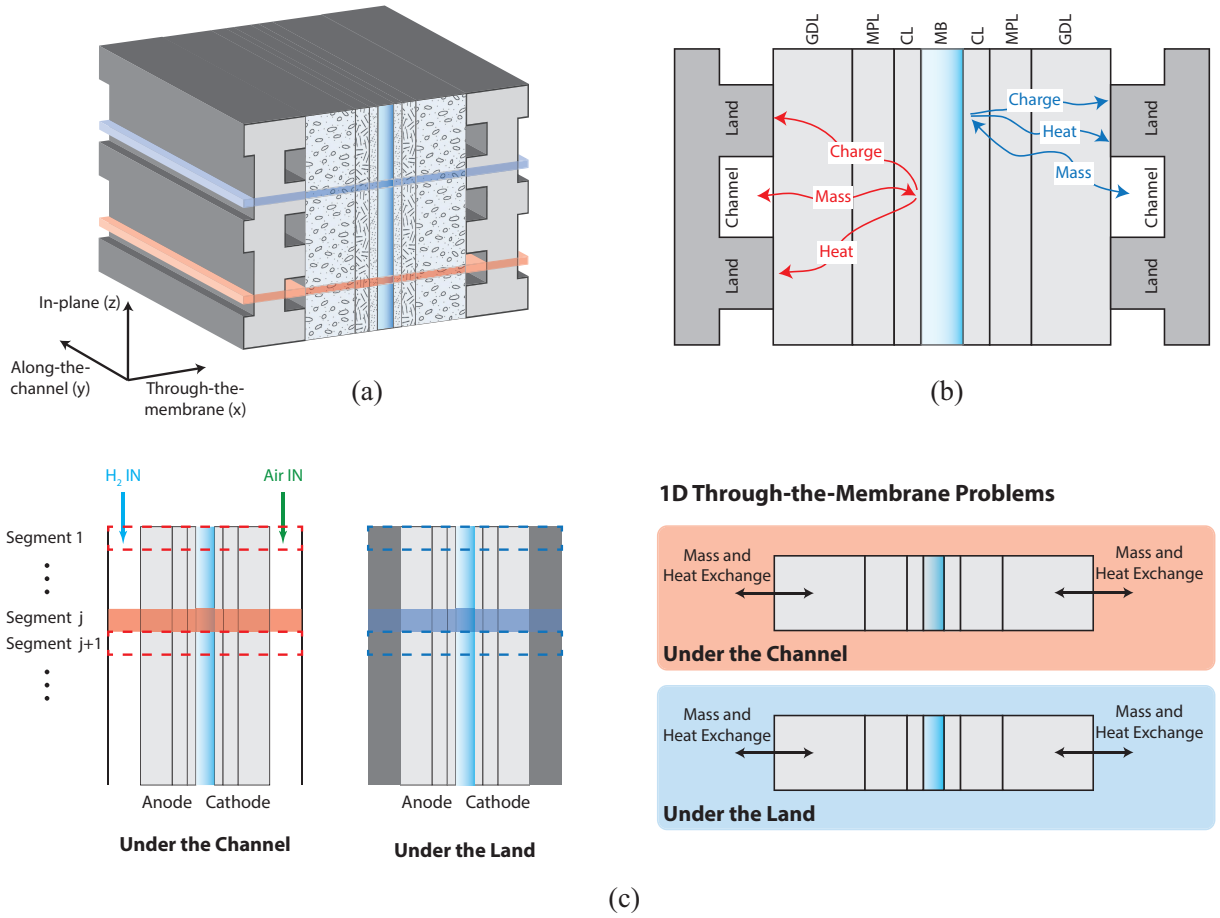

Figure 2.1: Schematic of the modeling approach: (a) the modeling domains under the channel and under the land, (b) example illustrations of different transport paths under the channel and under the land, and (c) the pseudo-2D bi-domain (P2D^2) modeling approach that decouples the along-the-channel and the through-the-membrane directions and solves two separate 1D problems at each location along the channels.

capture the in-plane distributions without the need for a 2D model. Simplifying the 2D modeling domain to a 1D domain through conformal mapping has also been proposed in the literature [100, 102]. While this method benefits from the highest computational efficiency, it would not allow one to distinguish between the local conditions in different parts of the cell, which can be critical, especially within the context of degradation studies. Therefore, we use the bi-domain approach here to balance the computational cost and model fidelity requirements.

The idea underlying the bi-domain modeling approach is that an effective transport

length for each of the transport equations can be defined on either domain, *i.e.*, under the channel or under the land area. This effective length can be used to solve the corresponding transport problems for heat, mass, and charge. This is illustrated in Fig. 2.1. In particular, the effective mass transport path is longer under the land area, whereas the regions under the channels have longer charge and heat transport paths. Here we account for the differences in mass and heat transport paths, while the charge transport problems are treated similarly in both regions, since the corresponding differences are negligible. In each case, the effective transport lengths between the channel and the CL are calculated by:

$$d_{\text{transport}} = \sqrt{\left(0.5\left(\frac{\text{TP}}{\text{IP}}\right)(w_{\text{CH}} + w_{\text{LN}})\right)^2 + (\delta_{\text{DM}})^2}, \tag{2.1}$$

where δ_{DM} is the sum of the thicknesses of the diffusive layers (CL, MPL, and GDL), w_{CH} is the channel width, and w_{LN} is the land width. The effective length defined above also accounts for the material anisotropy through the $\frac{\text{TP}}{\text{IP}}$ factor, which is the ratio of the relevant effective transport property in the through-plane (TP) direction to that in the in-plane (IP) direction. This factor is determined based on the anisotropic material properties for each transport problem, which include thermal conductivities, porosity correction factors, and effective permeabilities for the heat transport, diffusive gas transport, and convective liquid water transport problems, respectively. Finally, the transport length at any intermediate location within the diffusive layers can be found by scaling of the above equation accordingly.

The bi-domain MEA model is then extended along the flow channel using a pseudo-2D (P2D) modeling approach, where the only coupling between the channel and MEA models are obtained through the channel boundary conditions that account for mass and heat exchange between the GDLs and flow channels (see Fig. 2.1(c)) [104]. This approach is suitable for PEM fuel cell modeling due to the large aspect ratio of the cell components,

as they typically have thicknesses on the micrometer scale while being more than tens of centimeters in length.

2.2.2 Flow Channel Model

The flow channel model is a set of ordinary differential equations (ODEs) that determine the flow rates of reactant, nitrogen, and water in each channel. In particular, each ODE has the form of:

$$\frac{d\dot{M}_j}{dy} = f_j(y), \tag{2.2}$$

where $\dot{M}_j$ denotes the molar flow rate of species j in the channel and the right hand side term (f_j) for each species is given in Table 2.1. In short, the channel model accounts for reactant consumption, gas crossover through the membrane (see Section 2.2.3.5), and water exchange with the MEA model.

Table 2.1: Right hand side for the channel model ODEs (equation 2.2)

Species	$f_i(y)$
N_2 anode	$[wN_{N_2,\mathrm{mb}}]_{\mathrm{CH}} + [wN_{N_2,\mathrm{mb}}]_{\mathrm{LN}}$
N_2 cathode	$-[wN_{N_2,\mathrm{mb}}]_{\mathrm{CH}} - [wN_{N_2,\mathrm{mb}}]_{\mathrm{LN}}$
H_2 anode	$-\left[w(\frac{i_{\mathrm{dens}}}{2F} + 2N_{O_2,\mathrm{mb}} + N_{H_2,\mathrm{mb}})\right]_{\mathrm{CH}} - \left[w(\frac{i_{\mathrm{dens}}}{2F} + 2N_{O_2,\mathrm{mb}} + N_{H_2,\mathrm{mb}})\right]_{\mathrm{LN}}$
O_2 cathode	$-\left[w(\frac{i_{\mathrm{dens}}}{4F} + N_{O_2,\mathrm{mb}} + \frac{N_{H_2,\mathrm{mb}}}{2})\right]_{\mathrm{CH}} - \left[w(\frac{i_{\mathrm{dens}}}{4F} + N_{O_2,\mathrm{mb}} + \frac{N_{H_2,\mathrm{mb}}}{2})\right]_{\mathrm{LN}}$
water	$[w(N_{\mathrm{v,GDL}} + N_{\mathrm{l,GDL}})]_{\mathrm{CH}} + [w(N_{\mathrm{v,GDL}} + N_{\mathrm{l,GDL}})]_{\mathrm{LN}}$

It should be noted that a full model may also resolve the distribution of pressure and temperature along the flow channels [201]. However, we develop a simplified model here by assuming the channel temperatures to be identical to the coolant temperature at each location along the channel. The coolant temperature distribution is obtained from known inlet and outlet temperatures. Particularly, the temperature distribution is assumed to

be directly related to the current distribution. This is based on the fact that most of the heat generated in the cell is due to the reversible and irreversible heat of the ORR, whose dependence on current density can be approximated to be linear. Therefore, the variation in coolant temperature from inlet to outlet is assumed to scale linearly with the local current density. In addition, a linear pressure distribution is assumed from inlet to outlet in each channel, based on the knowledge of inlet and outlet pressures. This assumption is valid when slugs of liquid water do not exist in the channels, which is the case under most robust operating conditions used for automotive stacks. With these assumptions the model requires further information, *i.e.*, outlet channel pressures and coolant temperatures. Nevertheless, such information is typically available through inexpensive and reliable sensor measurements. On the other hand, these assumptions significantly simplify the model by enabling the use of a coarser grid along the flow channel. In particular, a priori knowledge of temperature distribution along the flow channel can be used to estimate the total amount of water vapor that can be accommodated at each location along the channel. Any amount of water in excess of this maximum allowable vapor content is assumed to condense immediately due to fast phase change kinetics and be carried to the next channel segment as liquid water. Therefore, there is no need to explicitly account for such phase change phenomena that render the channel model stiff and make the numerical solution difficult to obtain.

2.2.3 Full-Order Through-the-Membrane Mass and Heat Transport Model

In essence, the model solves several partial differential equations (PDEs) on a 1D domain through the MEA thickness to obtain the distribution of water and temperature. These

governing equations are as follows:

$$\varepsilon_{\mathrm{g}} \frac{\partial c_i}{\partial t} = \nabla \cdot (D_i^{\mathrm{eff}} \nabla c_i) + S_i, \tag{2.3}$$

$$\rho_{\mathrm{l}} \varepsilon \frac{\partial s}{\partial t} = \nabla \cdot (\frac{\rho_{\mathrm{l}} K_l^{\mathrm{eff}}}{\mu_{\mathrm{l}}} \nabla p_{\mathrm{l}}) + S_{\mathrm{l}}, \tag{2.4}$$

$$\sum_{\alpha} \varepsilon_\alpha \rho_\alpha c_{p,\alpha} \frac{\partial T}{\partial t} = \nabla \cdot (k_T^{\mathrm{eff}} \nabla T) + S_T, \tag{2.5}$$

$$\varepsilon_{\mathrm{ion}} \frac{\rho_{\mathrm{ion}}}{EW} \frac{\partial \lambda}{\partial t} = \nabla \cdot (N_{\mathrm{w,mb}}) + S_\lambda, \tag{2.6}$$

Note that the model neglects convective heat and gas transport, as their effects are shown to be negligible under most operating conditions [212, 213]. The source terms for mass and energy conservation are given in Table 2.2 and Table 2.3, respectively. We provide an overview of each equation below. The complete description for the model variables and parameters can also be found in the nomenclature.

Table 2.2: Mass conservation source terms for governing equations

Domain	S_{rct}	S_{v}	S_{l}	S_λ
Anode CL (ACL)	$\frac{i_{\mathrm{dens}}}{2F \cdot \delta_{\mathrm{CL}}^{\mathrm{an}}}$	$S_{\mathrm{pc}} - S_{\mathrm{ad}}$	$-M_{H_2O} S_{\mathrm{pc}}$	$S_{\mathrm{ad}} + \frac{2N_{O_2,\mathrm{mb}}}{\delta_{\mathrm{CL}}^{\mathrm{an}}}$
Cathode CL (CCL)	$\frac{i_{\mathrm{dens}}}{4F \cdot \delta_{\mathrm{CL}}^{\mathrm{ca}}}$	$S_{\mathrm{pc}} - S_{\mathrm{ad}}$	$-M_{H_2O} S_{\mathrm{pc}}$	$S_{\mathrm{ad}} + \frac{i_{\mathrm{dens}}}{2F \cdot \delta_{\mathrm{CL}}^{\mathrm{ca}}} + \frac{N_{H_2,\mathrm{mb}}}{\delta_{\mathrm{CL}}^{\mathrm{ca}}}$
MPL and GDL	0	S_{pc}	$-M_{H_2O} S_{\mathrm{pc}}$	–

Table 2.3: Heat source terms for equation 2.5

Domain	S_T
Anode CL (ACL)	$-M_{H_2O} S_{\mathrm{pc}} H_{\mathrm{pc}} + S_{\mathrm{ad}} H_{\mathrm{ad}} + H_{\mathrm{HOR}}$
Cathode CL (CCL)	$-M_{H_2O} S_{\mathrm{pc}} H_{\mathrm{pc}} + S_{\mathrm{ad}} H_{\mathrm{ad}} + H_{\mathrm{ORR}} + R_{\mathrm{CL}}^{\mathrm{ca,eff}} i_{\mathrm{dens}}^2$
Membrane	$R_{\mathrm{mb}} i_{\mathrm{dens}}^2$
MPL and GDL	$-M_{H_2O} S_{\mathrm{pc}} H_{\mathrm{pc}}$

Equation 2.3 describes the diffusive gas phase transport in the porous layers of the cell (CL, MPL, and GDL), where ε_g is the layer porosity available for gas transport ($\varepsilon_g = \varepsilon(1 - s)$, with s being the liquid saturation and ε the compressed layer porosity)

and D_i^{eff} denotes the effective diffusivity for species i (see Section 2.2.3.4). The last term (S_i) is the relevant source term for the specific gas species (see Table 2.2). This equation applies to vapor and reactant transport on both the anode and cathode sides of the cell.

Equation 2.4 describes the mass conservation for liquid water. Specifically, this equation models the pressure drop of liquid phase in the CLs, MPLs, and GDLs according to Darcy's law. Here, ρ_{l}, $K_{\text{l}}^{\text{eff}}$, μ_{l}, and p_{l} denote the density, effective permeability, viscosity, and pressure of the liquid phase, respectively, and ε denotes the porosity of the layer. The effective permeability is obtained by multiplying the absolute ($K_{\text{l,abs}}$) and relative ($K_{\text{l,rel}}$) permeability values (*i.e.*, $K_{\text{l}}^{\text{eff}} = K_{\text{l,abs}} K_{\text{l,rel}}$) and a 5-th order power law is used to estimate the relative permeability (*i.e.*, $K_{\text{l,rel}} = s^5$). Finally, S_{l} is the appropriate source term (see Table 2.2). The liquid saturation (s) that appears on the left hand side of this equation is a variable that depends on capillary pressure. Therefore, closure equations that relate the saturation level to the capillary pressure are required. While elaborate models have been developed for this purpose [78, 89], here we use a simplified approach, which is described in Section 2.2.3.1.

Equation 2.5 is the energy conservation equation, which governs the temperature distribution. In this equation, ρ_α, ε_α, and $c_{p,\alpha}$ are the density, volume fraction, and specific heat capacity of phase α, respectively, where α can be the gas, liquid, or solid phase. In addition, k_T^{eff} is the effective thermal conductivity and S_T denotes the heat source term (see Table 2.3).

Finally, equation 2.6 governs water transport in the ionomer phase throughout the CCM. Therefore, its domain of application is the anode and cathode catalyst layers and the membrane. In this equation, ε_{ion}, ρ_{ion}, and EW denote the ionomer volume fraction, density, and equivalent weight, respectively, while λ is the dimensionless number that quantifies the water content in the ionomer, *i.e.*, the number of water molecules per sulfonic acid group. The last term, S_λ, is the source term accounting for water generation,

absorption, and desorption (see Table 2.2).

Table 2.4: Ionomer water uptake and transport properties

Property [Units] [Reference]	Equation
n_d [−] [10]	$1.2\tanh(\frac{\lambda}{2.5})$
$D^{\text{eff}}_{\text{w,mb}}$ [$\frac{\text{cm}^2}{\text{s}}$] [214]	$0.0539\times(1+\frac{M_{H_2O}\rho_{\text{ion}}}{EW}\lambda)^{-2}(1+0.0027\lambda^2)\times$ $\left[1+\tanh(\frac{\lambda-2.6225}{0.8758})\right]\exp(\frac{-3343}{T})$
$D_{T,\text{mb}}$ [$\frac{\text{mol}}{\text{cm·K}}$] [13]	$\frac{1.04\times10^{-4}}{M_{H_2O}}\exp(-\frac{2362}{T})$
$K_{p,\text{mb}}$ [cm^2] [215]	$10^{-16}\times(-12.57+0.06T)$
k_{ad} [$\frac{\text{cm}}{\text{s}}$] [216]	$1.14\times10^{-5}f_v\exp\left[2416(\frac{1}{303}-\frac{1}{T})\right]$ for absorption
	$4.59\times10^{-5}f_v\exp\left[2416(\frac{1}{303}-\frac{1}{T})\right]$ for desorption
	$f_v(\lambda)=\frac{18\lambda}{\frac{EW}{\rho_{\text{ion}}}+18\lambda}$ (water volume fraction in ionomer)
κ_{ion} [$\frac{\text{S}}{\text{cm}}$] [77]	$\kappa_{\text{res}}+\kappa_0(f_v(\lambda)-f_v(\lambda_{\text{th}}))^{1.5}\exp\left[\frac{E_{\text{act,mb}}}{R}(\frac{1}{303.15}-\frac{1}{T})\right]$
	$\lambda_{\text{th}}=2$ is the threshold water content for conductivity
$k_{T,\text{mb}}$ [$\frac{\text{W}}{\text{m·K}}$] [217]	$0.177+3.7\times10^{-3}\lambda$

The water flux in the ionomer phase across the CCM, $N_{\text{w,mb}}$, includes the effects of EOD, diffusion, hydraulic permeation, and thermo-osmosis and is calculated as follows:

$$N_{\text{w,mb}}=n_d\frac{i_{\text{dens}}}{F}-\frac{\rho_{\text{ion}}}{EW}\xi_{\text{diff,mb}}D^{\text{eff}}_{\text{w,mb}}\nabla\lambda-\frac{K_{p,\text{mb}}}{\mu_{\text{l}}M_{H_2O}}\nabla p_{\text{l}}+D_{T,\text{mb}}\nabla T, \tag{2.7}$$

where n_d is the EOD coefficient, i_{dens} denotes the local current density, F is the Faraday's constant, $D^{\text{eff}}_{\text{w,mb}}$ and $K_{p,\text{mb}}$ are the effective membrane water diffusion and permeability coefficients, respectively, and $D_{T,\text{mb}}$ is the thermal water diffusivity in the membrane. Note that thermo-osmosis is shown to drive water from the cold to the hot side for a hydrophilic membrane [13] and as a convention, a positive flux denotes water flux towards the cathode. Moreover, a linear liquid water pressure is assumed across the membrane thickness. The membrane water transport properties are given in Table 2.4. There is considerable uncertainty surrounding such transport properties. These issues are very well reviewed by others [14, 218] and the particular choice of the properties used here is

based on an extensive literature review and can be modified depending on the application. Nevertheless, the uncertainty in the material properties warrants use of fitting parameters for membrane water flux, when agreement with experimental data is desired. For this reason, we have introduced a scaling factor for water diffusion, $\xi_{\mathrm{diff,mb}}$, which is identified during model parameterization. We also note that a similar model tuning strategy has been suggested in the literature [67].

We now provide further description for the source terms given in Tables 2.2 and 2.3. We start with the phase change source term, S_{pc}, which is given by:

$$S_{\mathrm{pc}} = \begin{cases} k_{\mathrm{evp}}(0.05+s)\left[c_{\mathrm{sat}}(T) - c_{\mathrm{v}}\right] & \text{if } c_{\mathrm{v}} < c_{\mathrm{sat}}(T)\,,\ s > 0 \\ k_{\mathrm{cnd}}(0.05+s)\left[c_{\mathrm{sat}}(T) - c_{\mathrm{v}}\right] & \text{if } c_{\mathrm{v}} \geq c_{\mathrm{sat}}(T) \end{cases}, \tag{2.8}$$

where $k_{\mathrm{evp/cnd}}$ denotes the phase change rate, $c_{\mathrm{sat}}(T)$ is the temperature dependent saturated vapor concentration, and c_{v} is the vapor concentration. As the pore size gets smaller, a larger interfacial area is available for phase change [78]. To model this effect, the phase change rate in the CLs is chosen to be the highest (50000 1/s), followed by that in the MPLs (1000 1/s) and GDLs (500 1/s). Moreover, we note that high rates are used to ensure the facile phase change kinetics as suggested in the literature [219]. The dependency on the liquid saturation is used to model the fact that the interfacial area available for phase change scales almost linearly with liquid saturation [219]. Finally, 0.05 is used to capture the effects of a hydrophilic pore network that allows for phase change to occur at very low liquid saturation levels [220]. The rate of phase change is expected to decline with temperature [221], which is not taken into account here. The saturated vapor concentration is defined as:

$$c_{\mathrm{sat}}(T) = \frac{p_{\mathrm{sat}}(T)}{RT}, \tag{2.9}$$

where R denotes the universal gas constant and p_{sat} is the temperature dependent satu-

ration pressure [222]:

$$p_{\text{sat}}(T) = 0.61121 \exp\left[\left(18.678 - \frac{T - 273.15}{234.5}\right)\frac{T - 273.15}{T - 16.01}\right] \quad [\text{kPa}]. \tag{2.10}$$

As for water exchange between the ionomer and the adjacent pore space, the water absorption/desorption source term, S_{ad}, is given by:

$$S_{\text{ad}} = \frac{k_{\text{ad}} \cdot \rho_{\text{ion}}}{\delta_{\text{CL}} \cdot EW}\left(\lambda^* - \lambda\right), \tag{2.11}$$

where k_{ad} is the interfacial water transfer coefficient (see Table 2.4), δ_{CL} denotes the CL thickness, and λ^* is the dynamic quasi-equilibrium water content for the ionomer, which is further described in Section 2.2.3.2. Note that both electrochemical (due to ORR) and chemical (due to direct hydrogen combustion) water productions contribute to S_λ. In other words, the produced water is assumed to be in absorbed (ionomer) phase. This is in agreement with the assumed structure for the CL in this dissertation and has also been used by others [140].

Regarding the heat source terms, H_{pc} is the enthalpy of phase change:

$$\begin{aligned} H_{\text{pc}} = &- 2.367 \times 10^{-5} T^4 + 1.882 \times 10^{-2} T^3 - 4.672 T^2 \\ &- 2.098 \times 10^3 T + 3.178 \times 10^6 \qquad [\text{kJ/g}]\ . \end{aligned} \tag{2.12}$$

Furthermore, H_{ad} denotes the heat of sorption/desorption [107]:

$$H_{\text{ad}} = \begin{cases} M_{H_2O} H_{\text{pc}} - 28.28 \times 10^3 \left[\text{erf}(\frac{18.68 \lambda M_{H_2O}}{EW} + 0.4016) - 1\right] & \text{sorption}, \\ -M_{H_2O} H_{\text{pc}} + 55.65 \times 10^3 \left[\text{erf}(\frac{10.39 \lambda M_{H_2O}}{EW} + 1.116) - 1\right] & \text{desorption}. \end{cases} \tag{2.13}$$

Lastly, denoting the Peltier coefficient for HOR/ORR [223] by $\Pi_{\text{HOR/ORR}}$ and the reaction

overpotential by $\eta_{\mathrm{HOR/ORR}}$, the heat of reaction, $H_{\mathrm{HOR/ORR}}$, is given by:

$$H_{\mathrm{HOR}} = \frac{i_{\mathrm{dens}}}{\delta_{\mathrm{CL}}^{\mathrm{an}}}(\eta_{\mathrm{HOR}} + \Pi_{\mathrm{HOR}}), \tag{2.14}$$

$$H_{\mathrm{ORR}} = \frac{i_{\mathrm{dens}}}{\chi\delta_{\mathrm{CL}}^{\mathrm{ca}}}(\eta_{\mathrm{ORR}} + \Pi_{\mathrm{ORR}}), \tag{2.15}$$

where χ is the cathode CL effective utilization factor (see Section 2.2.4.2).

2.2.3.1 Liquid Saturation-Capillary Pressure Relations in Porous Layers

With regards to liquid water transport, the model utilizes Darcy's law to capture pressure drop in the liquid phase, as shown in equation 2.4. It should be noted that the solution variable in this equation is the liquid pressure (p_{l}). Assuming constant gas phase pressure in the through-the-membrane direction, the variations in liquid pressure uniquely determine the variations in the capillary pressure (p_{c}), which is defined as the difference between the liquid and gas phase pressures, *i.e.*, $p_{\mathrm{c}} = p_{\mathrm{l}} - p_{\mathrm{g}}$ and $\nabla p_{\mathrm{c}} = \nabla p_{\mathrm{l}}$. With known p_{c}, the liquid saturation (s) that appears in these equations can be determined. For this purpose, the Leverett J-function is used as the closure equation [224]:

$$p_{\mathrm{c}} = p_{\mathrm{l}} - p_{\mathrm{g}} = -\frac{\sigma_{\mathrm{l}}\cos(\theta_{\mathrm{layer}})}{\sqrt{K_{\mathrm{abs}}/\varepsilon}}[1.417s - 2.12s^2 + 1.263s^3], \tag{2.16}$$

where σ_{l} is the liquid water surface tension, θ_{layer} is the contact angle of liquid water on the layer's surface, and K_{abs} denotes the layer's absolute permeability. It is worth mentioning that the Leverett J-function was originally developed for homogeneous sand and its applicability to fuel cell porous layers is questionable. In light of such observations, more detailed models for the liquid water transport have been developed in recent years, the most notable of which is the mixed wettability model [78, 223, 225, 226] that has become popular [91]. Nevertheless, recent literature also points to the fact that a representative elementary volume (REV) cannot be clearly defined in the through-plane direction for fuel cell porous layers [227]. Therefore, even the most advanced macrohomogeneous

models will not have sufficient fidelity to capture the details of liquid water distribution in these layers. Accordingly, the Leverett J-function approach is adopted here for simplicity. Indeed, this model can be parameterized to capture the aggregate behavior of liquid accumulation in the porous layers with acceptable accuracy for real-time modeling purposes.

2.2.3.2 Ionomer Water Uptake

It is imperative for any transient model of a PEM fuel cell to properly capture the dynamics of water sorption, desorption, and transport across the membrane. Historically, diffusive [11] and hydraulic [12] models have been used for this purpose. However, there is abundant evidence in the literature suggesting that interfacial transport phenomena as well as swelling of the polymer backbone may play a significant role in water uptake and transport dynamics [228, 229]. In particular, the gravimetric water uptake experiments conducted by Satterfield et al. have shown very long time constants for membrane water sorption, while the desorption time constants were found to be an order of magnitude smaller [229]. They suggested that the sorption behavior may be explained through the contributions of interfacial water transport and stress relaxation in the polymer, whereas the desorption dynamics are dominated by the interfacial phenomena. Their experiments included a step in the humidity from fully dry to fully saturated conditions that resulted in significant relaxation behavior. Other studies have found much less pronounced impact of the relaxation dynamics when the membrane was subjected to smaller changes in the humidity conditions [230]. Similar results have been reported for ionomer thin films [231]. Dynamic vapor sorption (DVS) experiments by Kusoglu et al. have also shown relatively long water uptake times with a time constant that increases with membrane hydration [232,233]. Their results also indicate that the asymmetry between sorption and desorption is not as pronounced as that observed in Satterfield et al.'s experiments. Such significant difference was also challenged by Silverman et al., who found the desorption

to be only about twice faster than sorption [234]. In-situ measurements of membrane swelling and hydration by GM researchers have also found the hydration and dehydration rates to be similar [235].

Based on the preceding discussion, it stands to reason to incorporate the slow ionomer water uptake process into the model. Silverman et al. have developed a coupled transport and mechanical model that captures such phenomena [107, 234]. However, adding the mechanical model will result in additional complexity that must be avoided for the purpose of performance modeling. Therefore, we simply use a dynamic variable to represent the quasi-equilibrium water content [198, 236, 237]:

$$\lambda^* = (1-\varphi)\lambda_{\text{eq}} + s_{\text{relax}}, \tag{2.17}$$

where φ determines the contribution of relaxation phenomena to the ionomer water uptake (a value of 0.35 is used for the simulations in this dissertation), and s_{relax} is a variable accounting for the dynamics of stress relaxation. In particular, its dynamics are assumed to be first order:

$$\dot{s}_{\text{relax}} = -\frac{1}{\tau_{\text{relax}}}(s_{\text{relax}} - \varphi\lambda_{\text{eq}}), \tag{2.18}$$

where λ_{eq} is the equilibrium water content given by [238]:

$$\begin{aligned}\lambda_{\text{eq}} =& (1-s)\left[(14.22a^3 - 18.92a^2 + 13.41a)\left(1 + 0.2325a^2\left(\frac{T-303}{30}\right)\right)\right] \\ &+ s\left[9.22 + 0.181(T - 273.15)\right].\end{aligned} \tag{2.19}$$

In the above equation, a denotes the water activity in the CL, which is equal to the the relative humidity, and s is the local liquid saturation. Finally, the relaxation time constant, τ_{relax}, is defined as:

$$\tau_{\text{relax}} = \exp(2 + 0.2\lambda), \tag{2.20}$$

where the time constant is chosen to vary with the ionomer water content in accordance with evidence in the literature for this dependence [232]. The stress relaxation is also supposedly a thermally activated process [229, 239]. Therefore, it would be reasonable to assume an Arrehnius type temperature dependence for the associated time constant, which is not included here. Additionally, the effects of compressive stresses on membrane water uptake [235, 240], and the much debated discrepancy between water uptake by ionomer thin film and bulk ionomer [231, 232] are not taken into account in the model. Future parametric studies can aim at investigating these effects along with the effects of changes to the relaxation model parameters to understand their impact on the overall dynamic response of the cell.

2.2.3.3 Local Transport Resistance in the Catalyst Layer

Early models of PEM fuel cells regarded CLs as interfaces with no consideration of their structural features. However, the significance of these structural features to the cell performance has been established. A particularly important issue that has resulted in significant efforts in CL modeling is the additional transport resistance observed at lowered Pt loading or with high loaded electrodes after degradation inducing cycles [241, 242]. The experimental approach has utilized limiting current measurements with varying gas composition and/or pressure to separate the pressure dependent and pressure independent transport resistances [102]. The transport resistance in the CL is almost entirely independent of pressure and can be estimated with such limiting current measurements. Using this approach, it has been found that the CL transport resistance increases at lower Pt loadings [130, 243–247] and this increase is strongly dependent on the available Pt area for reaction. Therefore, the resistance appears to be due to the increased flux near each active site at lower loadings [44]. Temperature sensitivities were used to determine the contributions of Knudsen diffusion and permeation through the ionomer thin film to the electrode transport resistance [248]. The ionomer thin film was found to be the dominant cause

of transport resistance in the CL. More recently, the impact of carbon support and its porous structure on the local reactant and bulk protonic transport resistances have been highlighted [45, 249]. Particularly, micro-pores with an opening smaller than 2 nm have been found to limit the reactant access to the Pt deposited inside the carbon pores. Despite such efforts, the root cause of the increased resistance remains largely unknown [46]. Several hypotheses have been made, but neither has been thoroughly validated.

Numerous models have been proposed to investigate the distribution of critical variables throughout the CLs and unveil the cause of increased transport resistance at lower loadings. The agglomerate model has been the most popular one for this purpose. In this model, the Pt particles are assumed to be dispersed on the primary carbon particles, many of which are assumed to aggregate during the fabrication process to form larger agglomerates covered by an ionomer thin film. The pore space in the CL is divided into two parts: the primary pores between carbon particles in each agglomerate, and the secondary pores formed between the agglomerates. Several variations of this model have been proposed where the intra-agglomerate space is either filled with water (*i.e.*, water-filled agglomerates) [250, 251] or ionomer (*i.e.*, ionomer-filled agglomerates) [84, 252].

Initially, a wide range of agglomerate sizes (100-1000 nm) had been used and significant variations in the ionomer film thickness (10-100 nm) had been reported to match the experimental data [82, 148]. Cetinbas et al. have developed a hybrid method for reconstruction of the CL microstructure [41, 42] and reported an agglomerate size distribution between 25 to 300 nm with most agglomerates having a radius in the range of 75 to 200 nm [42]. However, the upper limit of the modeling values for the agglomerate size and film thickness is not corroborated by microscopy studies [83]. Therefore, the validity of this structural picture has come under further scrutiny. In light of these experimental observations, some have argued that the agglomerates probably do not exist and have proposed homogeneous models for the electrode [82]. Others have continued to use the agglomerate models with agglomerate radii as small as 40 nm [85, 90], which

is close to the size of a carbon primary particle. Of particular interest is the work by Nissan researchers [85], who showed that the conventional flooded-agglomerate model is not capable of reproducing experimental results with small agglomerate size and partial ionomer coverage. They modified the model to incorporate transport resistance near the electrochemical surface and showed that the modified model successfully predicted the experimental trends. Generally, more recent models rely on interfacial resistance at either the ionomer-gas or the Pt-ionomer interface or both to reproduce experimental transport resistance values. Jinnouchi et al. used molecular dynamics simulations to associate such resistance with a dense ionomer layer near the Pt surface [37]. Overall, attributing the additional resistance to interfacial phenomena has become increasingly common in the literature.

Despite its commonality, the interfacial resistance has not been experimentally verified. In fact, Liu et al. measured transport resistance in ionomer thin films and found no evidence of interfacial resistance when 3D diffusion was taken into account [253]. The uncertainty surrounding ionomer thin film properties, such as water uptake [231, 254–256], ionic conduction [257], and gas permeation [83], which can be significantly affected by confinement and substrate interactions [258], has further contributed to the ambiguity of the source of this increased resistance. Some recent works have disputed the interfacial resistances or downplayed its significance. For instance, Darling has proposed an agglomerate model, in which the increased resistance is mostly attributed to the spherical diffusion through the agglomerate [259]. Others have investigated the inhomogeneity of mass fluxes near the Pt particles in agglomerates and the overlap between several agglomerates as possible culprits [260, 261]. Most recently, Muzaffar et al. [47] have investigated literature data with a previously developed agglomerate model [262] and found that the reduction in Pt loading probably leads to higher levels of flooding in both the CL and GDL due to reduced vaporization capability of the CL with decreased thickness. They also elevated the fact that both experimental [263] and numerical studies [264, 265] show

only partial coverage of catalyst particles with ionomer, leaving an alternative transport path for oxygen to reach the active sites without facing the interfacial resistance at the Pt-ionomer interface. Therefore, they concluded that the increased transport resistance may be attributable to reduced oxygen diffusivity due to pore blocking effects of liquid water and the interfacial resistance does not play a significant role. The importance of water management in successful use of low loaded electrodes was also pointed out by Srouji et al. [266].

The preceding literature review shows that the structural picture of the electrodes and the understanding of the factors that contribute to the transport resistance are still incomplete. Therefore, further model development and experimental investigations are required. Nevertheless, it should be noted that for the purpose of a full cell simulation, most of the proposed models can be parameterized to capture the local oxygen transport resistance, which is the most critical outcome of such models. Moreover, Kulikovsky has demonstrated that under certain conditions that are most relevant to typical fuel cell operation, the agglomerate model is not required [267]. Therefore, unless the goal of the model is to investigate different electrode designs at the nano-scale, a homogeneous model will be sufficient. Here, we use the model proposed by Hao et al. [82], which was shown to appropriately capture the increased resistance at lower loadings. The model achieves this by assuming full ionomer coverage and introducing rather significant interfacial resistances, which, in light of the above discussion, are disputable. Nevertheless, it is the general trend of the variations in the transport resistance that is required for our purposes. The model is briefly presented here and the reader is referred to the original publication for further details [82].

The model assumes Pt particles are deposited on primary carbon particles that are fully covered by an ionomer thin film. Liquid water in the pores of the electrode forms a thin film on top of the ionomer. This structural picture is used to derive the volume fraction of each phase (Pt, carbon, ionomer, and pore space) in both the anode and cathode

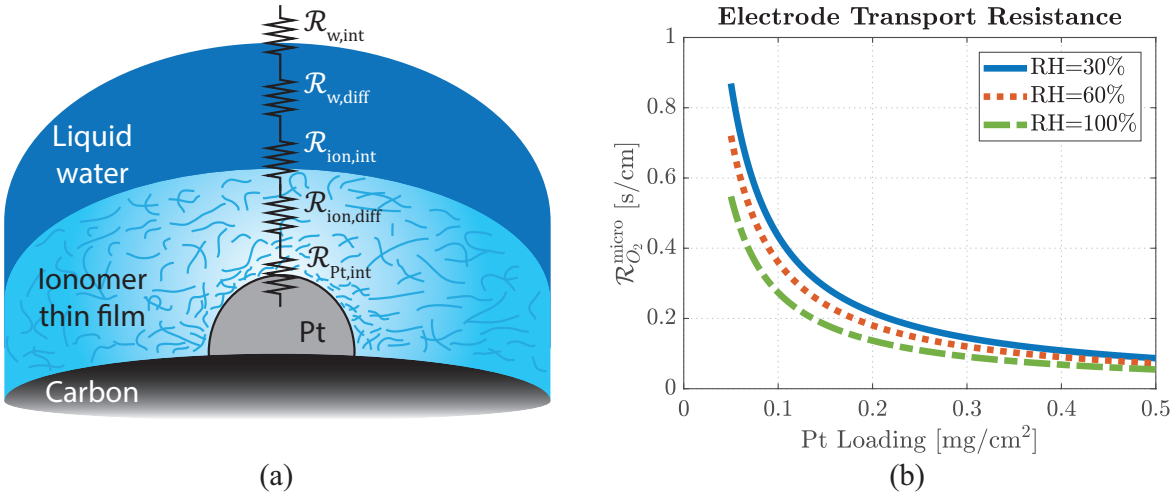

Figure 2.2: Local oxygen transport resistance in cathode CL: (a) schematic of various resistances between the CL pore space and the Pt surface and (b) example transport resistance variations with Pt loading for three humidity conditions.

CLs. However, the local transport resistance to hydrogen in the anode CL is assumed negligible and the resistance calculations are only carried out for oxygen transport in the cathode CL. In particular, the oxygen in the pore space has to (1) dissolve in water, (2) diffuse through the water film, (3) dissolve in ionomer, (4) diffuse through the ionomer film, and (5) be adsorbed on the Pt surface, as shown in Fig. 2.2(a). The model does not account for spherical diffusion, but uses instead a 1D diffusion equation to calculate the local flux of oxygen:

$$N_{O_2} = \frac{c_{O_2,\text{pore}} - c_{O_2,\text{Pt}}}{\mathcal{R}_{O_2}^{\text{micro}}}, \tag{2.21}$$

where N_{O_2}, $c_{O_2,\text{pore}}$, and $c_{O_2,\text{Pt}}$ are the oxygen flux near the Pt surface, oxygen concentration in the CL pore space, and its concentration at the Pt surface, respectively. $\mathcal{R}_{O_2}^{\text{micro}}$ is the total local transport resistance (see Fig. 2.2):

$$\mathcal{R}_{O_2}^{\text{micro}} = \mathcal{R}_{\text{w,int}} + \mathcal{R}_{\text{w,diff}} + \mathcal{R}_{\text{ion,int}} + \mathcal{R}_{\text{ion,diff}} + \mathcal{R}_{\text{Pt,int}}^{\text{eff}}, \tag{2.22}$$

where the first, third, and last terms describe the interfacial resistances at the liquid film,

ionomer film, and Pt surfaces, respectively. The second and fourth terms denote the diffusional resistances through the water and ionomer thin films:

$$\mathcal{R}_{\mathrm{w,diff}} = \frac{\delta_{\mathrm{w}}}{D_{O_2,\mathrm{w}}}, \tag{2.23}$$

$$\mathcal{R}_{\mathrm{ion,diff}} = \frac{\delta_{\mathrm{ion}}}{D_{O_2,\mathrm{ion}}}. \tag{2.24}$$

A key argument made in developing the model is a geometrical one, where an effective diffusion length through the ionomer is calculated based on the effective surface area of a single Pt particle and the effective ionomer surface area available for that particle:

$$A_{\mathrm{Pt}}^{\mathrm{eff}} = 4\pi r_{\mathrm{Pt}}^2 \theta_{\mathrm{Pt}}, \tag{2.25}$$

$$A_{\mathrm{ion}}^{\mathrm{eff}} = \frac{4\pi(r_{\mathrm{c}} + \delta_{\mathrm{ion}})}{n_{\mathrm{Pt}}}, \tag{2.26}$$

where r_{Pt} and r_{c} are the Pt and carbon primary particle radii, respectively, θ_{Pt} denotes the fraction of Pt surface not covered with oxide species (see Section 2.2.5), δ_{ion} is the ionomer film thickness, and n_{Pt} is the number of Pt particles deposited on a single carbon particle. The effective ionomer film thickness is then calculated by:

$$\delta_{\mathrm{ion}}^{\mathrm{eff}} = \frac{A_{\mathrm{ion}}^{\mathrm{eff}}}{A_{\mathrm{Pt}}^{\mathrm{eff}}} \delta_{\mathrm{ion}}. \tag{2.27}$$

The same scaling factor is used to scale the interfacial resistance at the Pt surface:

$$\mathcal{R}_{\mathrm{Pt,int}}^{\mathrm{eff}} = \frac{A_{\mathrm{ion}}^{\mathrm{eff}}}{A_{\mathrm{Pt}}^{\mathrm{eff}}} \mathcal{R}_{\mathrm{Pt,int}}. \tag{2.28}$$

This scaling is one of the most important features of the model, as it compensates for the fact that 3D spherical diffusion is neglected, and allows for the effects of high fluxes near sparsely deposited Pt particles to be captured by the model (see Fig. 2.2). It is imperative, however, to be cautious and not put too much emphasis on the source of the local transport resistance in this model. As mentioned earlier, the electrode structure assumed in this model is contentious. Nevertheless, on a macro-level, the predictions

match the experimental observations, which is the most important aspect for full cell simulations.

Finally, another important assumption made in the model is that the interfacial resistances are proportional to the diffusional resistances. This is done due the lack of measured data for the interfacial resistances at various interfaces. In particular, three fitting parameters k_1, k_2, and k_3 are introduced:

$$\mathcal{R}_{\text{ion,int}} = k_1 \frac{\delta_{\text{ion}}}{D_{O_2,\text{ion}}}\,,\ \mathcal{R}_{\text{Pt,int}} = k_2 \frac{\delta_{\text{ion}}}{D_{O_2,\text{ion}}}\,,\ \mathcal{R}_{\text{w,int}} = k_3 \frac{\delta_{\text{w}}}{D_{O_2,\text{w}}}. \tag{2.29}$$

Therefore, the various terms contributing to the transport resistance are identified.

It is also important to have a consistent set of structural parameters for the CLs. To this end, the volume fraction of different phases in the CL, including Pt, carbon, ionomer, and pore space are calculated as follows [41, 252]:

$$\varepsilon_{\text{c}} = \frac{1}{\rho_{\text{c}}} \frac{L_{\text{c}}}{\delta_{\text{CL}}}, \tag{2.30}$$

$$\varepsilon_{\text{Pt}} = \frac{1}{\rho_{\text{Pt}}} \frac{L_{\text{Pt}}}{\delta_{\text{CL}}}, \tag{2.31}$$

$$\varepsilon_{\text{ion}} = (IC)\varepsilon_{\text{c}} \frac{\rho_{\text{c}}}{\rho_{\text{ion}}} \left(1 + \frac{M_{H_2O}\rho_{\text{ion}}}{\rho_{\text{l}} EW}\lambda\right), \tag{2.32}$$

$$\varepsilon_{\text{CL}} = 1 - \varepsilon_{\text{c}} - \varepsilon_{\text{Pt}} - \varepsilon_{\text{ion}}. \tag{2.33}$$

where ε_i is the volume fraction of phase i (carbon, Pt, ionomer, pore space), $L_{\text{c/Pt}}$ is the carbon/Pt loading, ρ_i is the density of i, and IC denotes the ionomer to carbon ratio. The remaining volume not occupied by carbon, Pt, or ionomer constitutes the CL pore space (ε_{CL}). Lastly, the ionomer and liquid water film thicknesses are given by:

$$\delta_{\text{ion}} = r_{\text{c}} \left[\left(\frac{\varepsilon_{\text{ion}}}{\varepsilon_{\text{c}}} + 1\right)^{(1/3)} - 1 \right], \tag{2.34}$$

$$\delta_{\text{w}} = \left[s\varepsilon_{\text{CL}} \left(\frac{r_{\text{c}}^3}{\varepsilon_{\text{c}}}\right) + (r_{\text{c}} + \delta_{\text{ion}})^3 \right]^{(1/3)} - (r_{\text{c}} + \delta_{\text{ion}}). \tag{2.35}$$

This completes the CL model used in this dissertation. The reader is referred to [82] for

further details about this model.

2.2.3.4 Effective Diffusivity Calculations

To calculate the effective diffusivity for each gaseous species, we start with the binary molecular diffusivity values that are shown in Table 2.5. Accounting for the Knudsen diffusion regime, which is especially important for the MPL and CL due to their smaller pore size [248], the overall diffusivity is estimated with the Bosanquet relation [268]:

$$D_i = \left(\frac{1}{D_{\mathrm{Kn},i}} + \frac{1}{D_{i,j}} \right)^{-1}, \tag{2.36}$$

where $D_{i,j}$ is the binary diffusivity of species i in j and $D_{\mathrm{Kn},i}$ is the Knudsen diffusion coefficient for species i, which is given by [268]:

$$D_{\mathrm{Kn},i} = \frac{2 r_{\mathrm{Kn}}}{3} \sqrt{\frac{8RT}{\pi M_i}}. \tag{2.37}$$

In the above equation, r_{Kn} denotes the Knudsen radius for the porous layer of interest.

Table 2.5: Binary diffusion coefficients

Species [Reference]	Binary Diffusivity [cm^2/s]
O_2 [268]	$D_{O_2,N_2} = 0.181 \frac{101.325}{p} (\frac{T}{273.2})^{1.75}$
H_2 [269]	$D_{H_2,H_2O} = 0.915 \frac{101.325}{p} (\frac{T}{307.1})^{1.75}$
H_2O anode [269]	$D_{H_2O,H_2} = 0.915 \frac{101.325}{p} (\frac{T}{307.1})^{1.75}$
H_2O cathode [269]	$D_{H_2O,N_2} = 0.293 \frac{101.325}{p} (\frac{T}{298.2})^{1.75}$

To derive the effective diffusion coefficients, the tortuosity of transport pathways must be taken into account. Therefore, the effective diffusivity is given by:

$$D_i^{\mathrm{eff}} = \frac{\varepsilon}{\tau} D_i, \tag{2.38}$$

where τ is the tortuosity factor for the porous layer. The tortuosity factor is often esti-

mated with a Bruggeman type relation as follows [144]:

$$\tau = \varepsilon^{-n_{\text{Brugg}}} \tag{2.39}$$

Additional modifications to the above Bruggeman relation are required for flooded porous layers. Alternatively, an approximation of the following form may be employed [144]:

$$D_i^{\text{eff}} = f(\varepsilon)g(s)D_i \tag{2.40}$$

where $f(\varepsilon)$ and $g(s)$ are used to model the effects of porosity reduction and liquid accumulation on increased tortuosity. Here, we use the following relations for f and g [144]:

$$f(\varepsilon) = \varepsilon(\frac{\varepsilon - 0.11}{1 - 0.11})^{n_e}, \tag{2.41}$$

$$g(s) = (1 - s)^{n_v}, \tag{2.42}$$

where n_v and n_e are used as fitting parameters for the model.

2.2.3.5 Gas Crossover through the Membrane

Gas permeation through the membrane affects the cell performance. Most importantly, nitrogen buildup in the recirculating anode feed should be taken into account. However, reactant crossover can also be important, since it results in performance loss [15, 270]. Accordingly, the model accounts for crossover of all gaseous species. It is assumed that the hydrogen crossing over to the cathode reacts with the available oxygen immediately to produce water. The same assumption applies to the oxygen that crosses over to the anode side. Overall, the crossover fluxes are given by:

$$N_{i,\text{mb}} = \Psi_i \frac{p_{i,\text{CL}}^{\text{ca}} - p_{i,\text{CL}}^{\text{an}}}{\delta_{\text{mb}}}, \tag{2.43}$$

where $p_{i,\text{CL}}^{\text{an/ca}}$ denotes partial pressure of gas species i (H_2, O_2, or N_2) in the anode/cathode CL, Ψ_i denotes the corresponding membrane gas permeability, which is given in Table

2.6 for different species, and δ_{mb} is the membrane thickness. Lastly, the nitrogen partial pressures can be approximated by their respective values in the flow channels with small errors. However, partial pressures of oxygen and hydrogen must be evaluated in the CLs due to their non-negligible fluxes through the thickness of the porous layers.

Table 2.6: Membrane gas permeability

Species [Reference]	Permeability [mol/(cm · bar · s)]
H_2 [271]	$15.70 \times 10^{-9} \exp(\frac{-20280}{RT}) + f_v \times 45.00 \times 10^{-9} \exp(\frac{-18930}{RT})$
O_2 [271]	$6.74 \times 10^{-9} \exp(\frac{-21280}{RT}) + f_v \times 50.50 \times 10^{-9} \exp(\frac{-20470}{RT})$
N_2 [272]	$(0.0295 + 1.21 f_v - 1.93 {f_v}^2) \times 10^{-9} \exp[\frac{24000}{R}(\frac{1}{303} - \frac{1}{T})]$

2.2.4 Transport Model Simplifications

2.2.4.1 Reduced-Order Model for Mass Transport Across the MEA

The coupled system of PDEs presented in equations 2.3-2.6 requires considerable computational effort to solve. Therefore, it should be simplified for real-time modeling. As a first step in simplifying the solution, we note that the gas phase dynamics are fast. Therefore, the dynamics for reactant concentration can be safely ignored. Furthermore, only the reactant concentrations at the active sites are of interest and their distribution throughout the MPL and GDL thickness is of no critical importance. Assuming that the local current density is known, a molar flux can be calculated for each reactant. Specifically, $N_{O_2} = \frac{i_{\text{dens}}}{4F}$ and $N_{H_2} = \frac{i_{\text{dens}}}{2F}$. This molar flux combined with the known channel concentration can be utilized to estimate reactant concentration at the active sites and replace the diffusion PDE for reactants with the following algebraic equations:

$$c_{O_2,\text{Pt}} = c_{O_2,\text{CH}} - \mathcal{R}_{O_2} \frac{i_{\text{dens}}}{4F}, \tag{2.44}$$

$$c_{H_2,\text{Pt}} = \frac{RT}{H_{H_2}} \left(c_{H_2,\text{CH}} - \mathcal{R}_{H_2} \frac{i_{\text{dens}}}{2F} \right), \tag{2.45}$$

where $\mathcal{R}_i$ is the total transport resistance for reactant i between the channel and the Pt sites and $c_{i,\mathrm{CH}}$ and $c_{i,\mathrm{Pt}}$ denote the concentration of i in the flow channel and at the Pt sites, respectively. Note that the Henry's law constant, H, appears explicitly for H_2 [1], but is implicitly included in $\mathcal{R}_{\mathrm{O}_2}$ for O_2 [82] (see Section 2.2.3.3). The reactant transport resistance is calculated as the sum of convective resistance through the flow channel and diffusive resistances through the different porous layers:

$$\mathcal{R}_i = \mathcal{R}_{i,\mathrm{CH}} + \mathcal{R}_{i,\mathrm{GDL}} + \mathcal{R}_{i,\mathrm{MPL}} + \mathcal{R}_{i,\mathrm{CL}} + \mathcal{R}_{i,\mathrm{CL}}^{\mathrm{micro}}. \tag{2.46}$$

The first term on the right hand side denotes the convective transport resistance at the GDL-CH interface, while the second to fourth terms describe the diffusional gas transport resistance through different layers. The last term in equation 2.46 is the local transport resistance in the CL. In this dissertation, this last term is assumed zero for all gas species except O_2, whose local transport resistance is non-negligible (see Section 2.2.3.3). The convective resistance is determined by the Sherwood number [3]:

$$\mathcal{R}_{i,\mathrm{CH}} = \frac{D_{\mathrm{h}}}{Sh \cdot D_i}. \tag{2.47}$$

where D_{h} is the channel hydraulic diameter, Sh is the Sherwood number, and D_i is the diffusivity of species i in free space (*i.e.*, no porosity/tortuosity correction is applied). The diffusional resistance through each cell layer is given by:

$$\mathcal{R}_{i,\mathrm{layer}} = \frac{\delta_{\mathrm{layer}}}{D_i^{\mathrm{eff}}}, \tag{2.48}$$

where δ_{layer} is the particular layer thickness and D_i^{eff} is the effective diffusivity of species i in that layer (see Section 2.2.3.4).

The next step in simplifying the governing equations relates to the water transport problem through the MEA thickness. In particular, we are interested in a reduced-order model that captures the sorbed water (λ) distribution through the CCM as well as the

water vapor concentration in the MEA. To this end, we note that although the ionomer water transport equation (equation 2.6) represents a nonlinear diffusion equation, its solution usually tends to yield a linear distribution for λ. This is especially the case for thin membranes, which are typically used in state-of-the-art fuel cell stacks. This observation allows us to capture the distribution of λ with three states across the CCM thickness; one for the anode CL, one for the membrane, and one for the cathode CL. Therefore, equation 2.6 can be replaced by three ODEs:

$$\varepsilon_{\text{ion}}^{\text{an}} \frac{\rho_{\text{ion}}}{EW} \frac{d\lambda_{\text{CL}}^{\text{an}}}{dt} = \frac{1}{\delta_{\text{CL}}^{\text{an}}} \left(-N_{\text{w,mb}}^{\text{an}} + 2N_{O_2,\text{mb}} \right) + S_{\text{ad}}^{\text{an}}, \tag{2.49}$$

$$\varepsilon_{\text{ion}}^{\text{ca}} \frac{\rho_{\text{ion}}}{EW} \frac{d\lambda_{\text{CL}}^{\text{ca}}}{dt} = \frac{1}{\delta_{\text{CL}}^{\text{ca}}} \left(N_{\text{w,mb}}^{\text{ca}} + \frac{i_{\text{dens}}}{2F} + N_{H_2,\text{mb}} \right) + S_{\text{ad}}^{\text{ca}}, \tag{2.50}$$

$$\varepsilon_{\text{ion}}^{\text{mb}} \frac{\rho_{\text{ion}}}{EW} \frac{d\lambda_{\text{mb}}}{dt} = -\frac{1}{\delta_{\text{mb}}} \left(N_{\text{w,mb}}^{\text{ca}} - N_{\text{w,mb}}^{\text{an}} \right), \tag{2.51}$$

where $N_{\text{w,mb}}^{\text{an/ca}}$ denotes the water flux on either side of the membrane (equation 2.7) and λ_{mb} and λ_{CL} are the average membrane and CL ionomer water contents, respectively. This approach is equivalent to using a coarse spatial discretization for the original PDE with only 3 control volumes across the CCM thickness. The above equation set governs the dynamics for sorbed water through the CCM by accounting for water transport in the ionomer phase, electrochemical water production, and water exchange with the pore space. Additionally, recall that any reactant crossed over through the membrane is assumed to react immediately to produce water in the ionomer phase.

As for the average vapor concentration in the CLs, the associated dynamics are given by:

$$\varepsilon_{\text{g,CL}}^{\text{an}} \frac{dc_{\text{v,CL}}^{\text{an}}}{dt} = \frac{1}{\delta_{\text{CL}}^{\text{an}}} \left(-\frac{c_{\text{v,CL}}^{\text{an}} - c_{\text{v,CH}}^{\text{an}}}{\mathcal{R}_{\text{v}}^{\text{an}}} \right) + S_{\text{pc}}^{\text{an}} - S_{\text{ad}}^{\text{an}}, \tag{2.52}$$

$$\varepsilon_{\text{g,CL}}^{\text{ca}} \frac{dc_{\text{v,CL}}^{\text{ca}}}{dt} = \frac{1}{\delta_{\text{CL}}^{\text{ca}}} \left(-\frac{c_{\text{v,CL}}^{\text{ca}} - c_{\text{v,CH}}^{\text{ca}}}{\mathcal{R}_{\text{v}}^{\text{ca}}} \right) + S_{\text{pc}}^{\text{ca}} - S_{\text{ad}}^{\text{ca}}. \tag{2.53}$$

In the above equations, $\mathcal{R}_{\text{v}}^{\text{an/ca}}$ is the total resistance to vapor transport between the CL

and the channel, which can be calculated by equation 2.46. These equations account for vapor diffusion, water exchange with the ionomer, and the phase change process. Similar to reactant transport, the underlying dynamics are fast and may be ignored. Here, we have chosen to work with the dynamic equations rather than the steady state approximations mostly for numerical simplicity. In particular, note that equations 2.49-2.53 must be solved in a coupled manner to determine the water balance across the CCM. Assuming quasi-steady state conditions for vapor concentrations would result in replacement of the above ODEs (equations 2.52 and 2.53) with algebraic counterparts. However, solving the complete set of ODEs is simpler in terms of the numerical computations, since the dynamics result in some level of numerical damping and improve convergence speed [273]. Therefore, it is helpful not to disregard the associated dynamics. Nevertheless, the quasi-steady state assumption is still utilized for vapor concentrations throughout the rest of the MEA. More specifically, we initially disregard the phase change source term and obtain a linear distribution of vapor concentration through the thickness of all layers, namely, the CL, MPL, and GDL. This can be done by utilizing the diffusional resistances in each layer as well as the known boundary conditions at the CL and channel. In particular, we can formulate this as the following system of linear equations to be solved for vapor concentrations at the interfaces of various layers:

$$\begin{bmatrix} 1+\frac{\mathcal{R}_{\mathrm{v,CL}}}{\mathcal{R}_{\mathrm{v,MPL}}} & -\frac{\mathcal{R}_{\mathrm{v,CL}}}{\mathcal{R}_{\mathrm{v,MPL}}} & 0 \\ -1 & 1+\frac{\mathcal{R}_{\mathrm{v,MPL}}}{\mathcal{R}_{\mathrm{v,GDL}}} & -\frac{\mathcal{R}_{\mathrm{v,MPL}}}{\mathcal{R}_{\mathrm{v,GDL}}} \\ 0 & -1 & 1+\frac{\mathcal{R}_{\mathrm{v,GDL}}}{\mathcal{R}_{\mathrm{v,CH}}} \end{bmatrix} \begin{bmatrix} c_{\mathrm{v,CL-MPL}} \\ c_{\mathrm{v,MPL-GDL}} \\ c_{\mathrm{v,GDL-CH}} \end{bmatrix} = \begin{bmatrix} c_{\mathrm{v,CL}} \\ 0 \\ c_{\mathrm{v,CH}} \end{bmatrix} \tag{2.54}$$

The above system is obtained by applying vapor flux continuity conditions across different layers, *i.e.*, the vapor flux through the CL should be the same as that through the MPL and GDL. The two known quantities in the above system are the boundary conditions, *i.e.*, the vapor concentration at the flow channel and the CL (known from initial guess). The solution of the system will determine the vapor concentrations at the interface of

the layers. This system is solved for both the anode and cathode sides. Overall, this allows us to obtain an approximate distribution of vapor concentration through the MEA thickness. Once this distribution is available, any supersaturated vapor results in liquid accumulation through condensation and the vapor fluxes are updated accordingly.

A final simplification step is that of decoupling the transport equations for heat and liquid water from those of gas and sorbed water. Essentially, we assume the temperature and liquid saturation remain constant for the duration of a single time step. After the mass transport model is solved and a current and voltage distribution is obtained, the liquid saturation and cell temperature distributions are updated by calling their respective subroutines that solve the underlying PDEs. In the case of liquid saturation, this decoupling results in minimal loss of accuracy, as the dynamics of liquid accumulation and removal are much slower than other transient phenomena. Therefore, liquid saturation can be assumed to be constant for a short duration. This under-relaxation approach has also been used in the literature and shown to improve convergence [89, 106]. As for the temperature updates, the scheme employed here can result in loss of accuracy, since the temperature dynamics can be fast, on par with the other considered transient phenomena. Nonetheless, it should be noted that for the purpose of on-line estimation, we are seeking an approximate solution and the significant computational benefits offered by this approach make it a rational choice. Furthermore, some of the errors brought about by this decoupling can be compensated for through effective parameterization of the model, which is in itself a by-product of the computational efficiency offered by these simplifications.

2.2.4.2 Proton and Gas Transport Trade-off in the Cathode CL

With the structural assumptions and local oxygen transport resistance calculations described in Section 2.2.3.3, it remains to efficiently model the trade-off between proton and reactant mass transport in the cathode CL. It should be noted that a distributed model

of the CL that solves for the variations of oxygen concentration and ionomer conductivity through the CL thickness will automatically explore such trade-offs [89]. However, such an approach will be computationally intensive, as it requires keeping track of a relatively large number of states through the CL thickness. Therefore, the challenge is in obtaining an approximate solution to this problem with the minimal number of state variables. Specifically, the aim is to develop a lumped model that requires only average values of ionomer water content (according to equation 2.50), liquid saturation, and oxygen concentration in the cathode CL, rather than their respective distributions. To this end, we define a new parameter for cathode CL utilization (χ). This parameter is used to explore the proton and gas transport trade-offs in the cathode CL. Particularly, χ represents the fraction of the cathode CL that is accessible to both oxygen and protons without significant mass or proton transport limitations. To calculate χ, one has to minimize the sum of ohmic and ORR activation losses in the CL, as shown schematically in Fig. 2.3. This is done by first estimating the effective proton transport resistance in the cathode CL using the method proposed by Neyerlin et al. [274]. Shortly, the model calculates this effective protonic resistance as a function of the total resistance:

$$R_{\mathrm{CL}}^{\mathrm{ca}} = \frac{\delta_{\mathrm{CL}}^{\mathrm{ca}}}{(\varepsilon_{\mathrm{ion}}^{\mathrm{ca}})^{n_{\mathrm{Brugg}}} \kappa_{\mathrm{CL}}^{\mathrm{ca}}}, \tag{2.55}$$

$$R_{\mathrm{CL}}^{\mathrm{ca,eff}} = \frac{\chi R_{\mathrm{CL}}^{\mathrm{ca}}}{3+\zeta} + (1-\chi) R_{\mathrm{CL}}^{\mathrm{ca}}, \tag{2.56}$$

where $R_{\mathrm{CL}}^{\mathrm{ca}}$ and $R_{\mathrm{CL}}^{\mathrm{ca,eff}}$ denote the total and effective cathode CL protonic resistance, respectively, n_{Brugg} is the Bruggeman exponent that is used to model the connectivity of the ionomer network [14], and ζ is a polynomial fit to the solution obtained by Neyerlin et al. [274], given by:

$$\zeta = -8.287 \times 10^{-3} \vartheta^2 + 7.184 \times 10^{-1} \vartheta - 2.072 \times 10^{-3}. \tag{2.57}$$

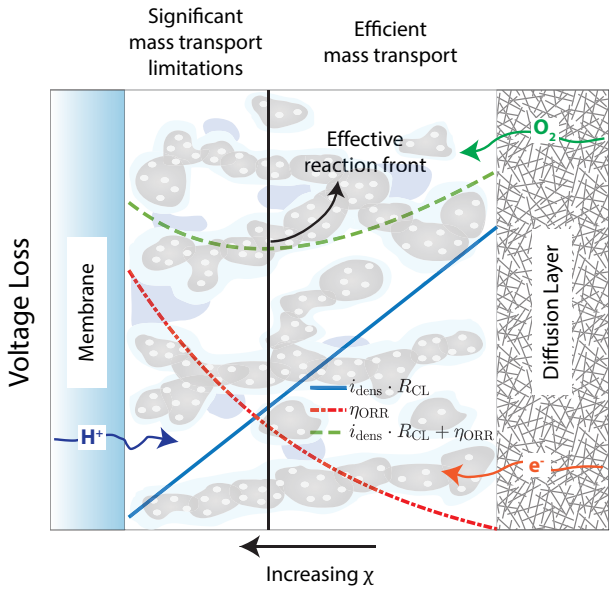

Figure 2.3: Schematic for calculation of cathode CL utilization factor: The effective reaction front, shown with the vertical black line, is defined to be at the location of minimum voltage loss due to a combination of mass and proton transport limitations. It is assumed that no ORR takes place to the left of the effective reaction front due to severe mass transport limitations.

In this equation, $\vartheta = \frac{i_{\text{dens}} R_{\text{CL}}^{\text{ca}}}{b}$, where $b = \frac{2.303RT}{\alpha_{\text{ca}} F}$ is the Tafel slope. It should be noted that Neyerlin et al. developed their results for effective CL protonic resistance using a simplified Tafel expression [274]. However, we use a coverage-dependent ORR kinetics model (see Section 2.2.5), which is expected to impact the estimated resistance to some extent. This difference is neglected here for simplicity.

If oxygen transport is efficient and imposes no limitations, *i.e.*, $\chi = 1$, then the above calculation yields the same estimate for the effective protonic resistance in the cathode CL as that obtained by Neyerlin et al. [274]. In case of oxygen transport limitations, *i.e.*, $\chi < 1$, it is assumed that a fraction $1-\chi$ of the CL close to the membrane is not accessible to oxygen. Therefore, no reaction takes place in this region of the CL and protons coming through the membrane have to be transferred through this portion of the CL without participating in the ORR, *i.e.*, $(1-\chi)\delta_{\text{CL}}$ is treated as an extension of the membrane. This results in an additional protonic resistance in the CL, which is taken into account

through the second term on the right hand side of equation 2.56. Since the portion of CL closest to membrane does not participate in the ORR, the effective resistance to oxygen transport through the CL thickness has to be modified accordingly. In particular, we modify equation 2.48 for oxygen transport resistance in the CL as follows:

$$\mathcal{R}_{O_2,\mathrm{CL}} = \frac{\chi \delta_{\mathrm{CL}}^{\mathrm{ca}}}{D_{O_2}^{\mathrm{eff}}}. \tag{2.58}$$

As mentioned earlier, χ can be determined by minimizing the sum of activation and CL proton transport losses. This minimization can be carried out analytically as follows:

$$\frac{d\left(\eta_{\mathrm{ORR}} + i_{\mathrm{dens}} R_{\mathrm{CL}}^{\mathrm{ca,eff}}\right)}{d\chi} = 0, \tag{2.59}$$

where η_{ORR} is the ORR activation overpotential, which is affected by mass transport limitations (see Section 2.2.5). The solution is obtained through symbolic calculation, which yields a rather involved expression that is not presented here due to space considerations. It should be noted that the solution has to satisfy $\chi \in [0, 1]$. In case the computed solution is out of this range for some conditions, it is simply projected onto this domain. For instance, $\chi > 1$ yields the intuitive result of $\chi = 1$. This completes the reduced model formulation for the cathode CL.

2.2.5 Terminal Voltage and Reaction Kinetics

The terminal cell voltage is given by:

$$E_{\mathrm{cell}} = E_{\mathrm{OCV}} - \eta_{\mathrm{HOR}} - \eta_{\mathrm{ORR}} - i_{\mathrm{dens}}\left(R_{\mathrm{mb}} + R_{\mathrm{CL}}^{\mathrm{ca,eff}} + R_{\mathrm{elec}}\right). \tag{2.60}$$

The various terms in the above equation are given in Table 2.7. The description of various parameters can be found in the nomenclature. For any given cell voltage, this equation is solved iteratively to find the corresponding current density at each location along the flow channel.

Table 2.7: Terminal cell voltage and reaction kinetics

Quantity	Equation
E_{OCV}	$1.229 - 8.5 \times 10^{-4}(T - 298.15) + \left(\frac{RT}{4F}\right) \ln\left(p_{\mathrm{H_2,Pt}}{}^2 p_{\mathrm{O_2,Pt}}\right)$
η_{ORR}	$\frac{RT}{\alpha_{\mathrm{ca}} F}\left[\ln\left(\frac{i_{\mathrm{dens}}+i_x}{i_{0,\mathrm{ca}}\chi\delta_{\mathrm{CL}}^{\mathrm{ca}} a_{\mathrm{Pt}}^{\mathrm{ca}}}\right) + \frac{\omega\theta_{\mathrm{PtO}}}{RT}\right]$
η_{HOR}	$\frac{RT}{\alpha_{\mathrm{an}} F}\left(\frac{i_{\mathrm{dens}}}{i_{0,\mathrm{an}}\delta_{\mathrm{CL}}^{\mathrm{an}} a_{\mathrm{Pt}}^{\mathrm{an}}}\right)$
R_{mb}	$\frac{\delta_{\mathrm{mb}}}{\kappa_{\mathrm{mb}}}$ (see Table 2.4 for membrane conductivity)
$R_{\mathrm{CL}}^{\mathrm{ca,eff}}$	equation 2.56
R_{elec}	model parameter (constant)
Auxiliary variables	
$i_{0,\mathrm{ca}}$	$f_{\mathrm{RH}}(1-\theta_{\mathrm{PtO}}) i_{0,\mathrm{ca}}^{\mathrm{ref}}\left(\frac{c_{\mathrm{O_2,Pt}}}{c_{\mathrm{O_2}}^{\mathrm{ref}}}\right)^{\gamma_{\mathrm{ca}}} \exp\left(\frac{-E_{\mathrm{act,ca}}}{R}\left(\frac{1}{T} - \frac{1}{303}\right)\right)$
$i_{0,\mathrm{an}}$	$i_{0,\mathrm{an}}^{\mathrm{ref}}\left(\frac{c_{\mathrm{H_2,Pt}}}{c_{H_2}^{\mathrm{ref}}}\right)^{\gamma_{\mathrm{an}}} \exp\left(\frac{-E_{\mathrm{act,an}}}{R}\left(\frac{1}{T} - \frac{1}{303}\right)\right)$
i_x	$2FN_{H_2,\mathrm{mb}}$

The ORR kinetics model used here is based on the modified Tafel expression proposed by Subramanian et al. [110] that accounts for coverage of Pt sites with oxide species. The oxide coverage profile with respect to electrode potential as well as its dynamic growth are of critical importance in accurately modeling the transient performance of the cell. Accordingly, we use the following model for oxide growth dynamics, which assumes that water oxidizes Pt sites [92, 241]:

$$\begin{aligned}\frac{d\theta_{\mathrm{PtO}}}{dt} =& k_{\mathrm{PtO}}\left[RH(1-\theta_{\mathrm{PtO}})\exp\left(\frac{\alpha_{\mathrm{PtO}} F\eta_{\mathrm{PtO}} - E_{\mathrm{PtO}}\theta_{\mathrm{PtO}}}{RT}\right)\right. \\ & \left. -\theta_{\mathrm{PtO}}\exp\left(-\frac{(1-\alpha_{\mathrm{PtO}})F\eta_{\mathrm{PtO}}}{RT}\right)\right]. \end{aligned} \tag{2.61}$$

In this equation k_{PtO} is the oxide formation rate constant and η_{PtO} is given by:

$$\eta_{\mathrm{PtO}} = E_{\mathrm{OCV}} - \eta_{\mathrm{ORR}} - E_{\mathrm{rev,PtO}}, \tag{2.62}$$

where $E_{\mathrm{rev,PtO}}$ is the reversible potential for PtO formation. Modeling the oxide film

growth is especially important in capturing the voltage/current transients at higher potentials.

Finally, it should be pointed out that the ORR kinetics are assumed to be RH dependent based on the experimental observations in the literature [116, 117]. Although the significance of this effect has been questioned [115, 118], the approach adopted herein is still beneficial in capturing the impact of lowered RH on accessibility of Pt particles deposited inside the inner catalyst pores of high surface area carbon support [275, 276]. This RH dependency is captured through the factor f_{RH} that scales the cathode exchange current density. This factor depends on the ionomer water content as follows:

$$f_{RH} = (1 - \sigma_f) f_{RH,c} + \sigma_f, \tag{2.63}$$

where σ_f is a sigmoid function defined as:

$$\sigma_f = \frac{1}{1 + \exp(\frac{f_{RH,a}\lambda_{\text{sat}}(T) - \lambda}{f_{RH,b}})}. \tag{2.64}$$

In the above equations, $f_{RH,a}$, $f_{RH,b}$, and $f_{RH,c}$ are fitting parameters and $\lambda_{\text{sat}}(T)$ denotes the ionomer water content under saturated condition at any given temperature (see Table 2.4).

2.2.6 Boundary Conditions

The heat equation (equation 2.5) is solved with convective boundary conditions at the coolant channel interfaces on both the anode and cathode sides. The convection coefficient (h_{conv}) is treated as a fitting parameter for the model. For liquid water transport (equation 2.4), a zero flux boundary condition is used at the membrane interface with the CL, while

the channel boundary condition is given by:

$$p_{\mathrm{l,CH}} = \begin{cases} 0 & \text{under the channel} \\ \min(p_{\mathrm{l}}^{\mathrm{N}},\ 0.1) & \text{under the land} \end{cases} \tag{2.65}$$

where $p_{\mathrm{l}}^{\mathrm{N}}$ denotes the liquid pressure in the control volume adjacent to the flow channel. Liquid water under the land faces extra resistance in flowing into the channel. The above boundary conditions are intended to model this additional resistance.

2.2.7 Numerical Implementation

The PDEs for heat and liquid water transport (equations 2.4 and 2.5) are spatially discretized using the control volume (CV) method. The through-plane direction is discretized using 20 CVs for each GDL, 4 CVs for each MPL, 4 CVs for each CL, and 1 CV for the membrane. The Backward Euler method is used for time stepping in both cases. For the liquid water transport problem, Jacobian linearization is utilized for the nonlinear terms [277]. The resulting linear system in each case (heat and liquid water transport problems) is tri-diagonal and is solved using the Thomas algorithm [278]. It should be pointed out that the relative permeability is zero when no liquid exists within a control volume. This eliminates the diffusive term and is known to cause stability issues. In recent PEM fuel cell modeling literature, this issue has been overcome by adding a small artificial value to the permeability to ensure it never vanishes [90, 279]. While this approach is certainly acceptable given that the added values are much smaller than the uncertainty in the actual permeability estimates, it is not a consistent stabilization method, since it increases the permeability artificially. In this work, we utilize permeability upstreaming as a consistent way of dealing with such instability issues [280]. Upstreaming essentially amounts to evaluating the relative permeability using the liquid saturation of the control volume in the upstream, which ensures that the permeability at the advancing front is

never zero.

As for the water balance problem across the CCM, the set of ODEs given by equations 2.49-2.53 are discretized in time using the Backward Euler method. This was deemed necessary, as the equation system is stiff and the numerical damping offered by backward Euler helps in this regard [273]. The discretized system is solved along with the algebraic equation for the cell voltage (equation 2.60) using the Newton iterations with analytical Jacobian. Finally, forward Euler is used for the channel model (Table 2.1). Regarding the spatial discretization along the flow channels, either 12 or 27 nodes are used for the presented results depending on the channel length, as we have found that a channel segment that is larger than 1 cm in length, can result in numerical inaccuracies in our implementation. Finally, a fixed time step size of 100 milliseconds is used for the model.

A version of the model has been implemented in C. The code is then used as an S-Function block in Simulink in order to simplify the user interface. The P2D^2 Simulink model with co-flow channel configuration and 12 nodes along the flow channel runs about 50 times faster than real time on a laptop computer with a 2.4 GHz processor. The worst case computation for a given time step typically takes less than 10 milliseconds. The counter-flow configuration is typically between 2 to 3 times slower than the co-flow case due to the iterative scheme employed (see Section 2.2.7.2). All of these computation times are cut in half when the land region is not considered, *i.e.*, a P2D model. This is the case for the model validation presented in Section 2.3.

2.2.7.1 Potentio-dynamic vs. Galvano-dynamic Simulations

The model is formulated assuming potentio-dynamic mode of operation, *i.e.*, cell voltage is the input to the model and current density is one of its predicted outputs. This approach allows us to obtain the current distribution along the flow channels without the need for an iterative scheme, as the cell voltage at each location can be used directly to estimate the local current density, while ensuring the electrode potential remains constant along

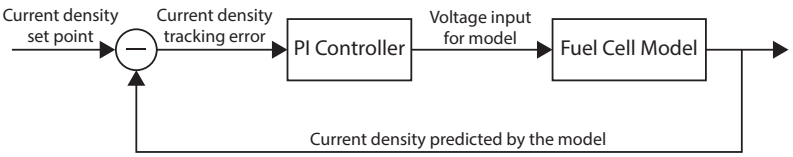

Figure 2.4: The numerical scheme used for galvano-dynamic simulations, where a PI controller is used to find the correct voltage input to the model.

the flow channel. On the other hand, modeling the galvano-dynamic mode of operation will require an iterative method to ensure that the electrodes are equipotential along the flow channel and will result in a loss of computational efficiency. To avoid this issue while simulating galvano-dynamic operation, we close the loop on the potentio-dynamic model using a simple proportional-integral (PI) controller to adaptively change the set point for cell voltage so that the predicted current density matches the galvano-dynamic input current density. This approach, shown in Fig. 2.4, ensures zero steady-state error due to the integral action. Nevertheless, some transient error exists, which can be minimized by properly tuning the controller gains. In our simulations we have found that zero tracking error is achieved within 2 seconds of load change for all of the tested conditions. This time is in fact less than 1 second for most of the cases. Therefore, the transient loss of accuracy is minimal and the computational benefits clearly outweigh such losses.

2.2.7.2 Iterative Scheme for Counter-Flow Configuration

The model also has the capability to simulate the counter-flow configuration. This is achieved by designing a new iterative scheme. In particular, the anode stream flows in the opposite direction of the cathode and coolant streams under the counter-flow configuration. Therefore, this case cannot be handled easily within the P2D modeling framework, as this framework relies heavily on the flow of information on both sides of the cell being in the same direction. This necessitates the need for an iterative scheme. The intuitive approach would be to guess the concentration values at the anode outlet and solve the model as if it were co-flow with these values as the anode inlet values. The initial guess can then

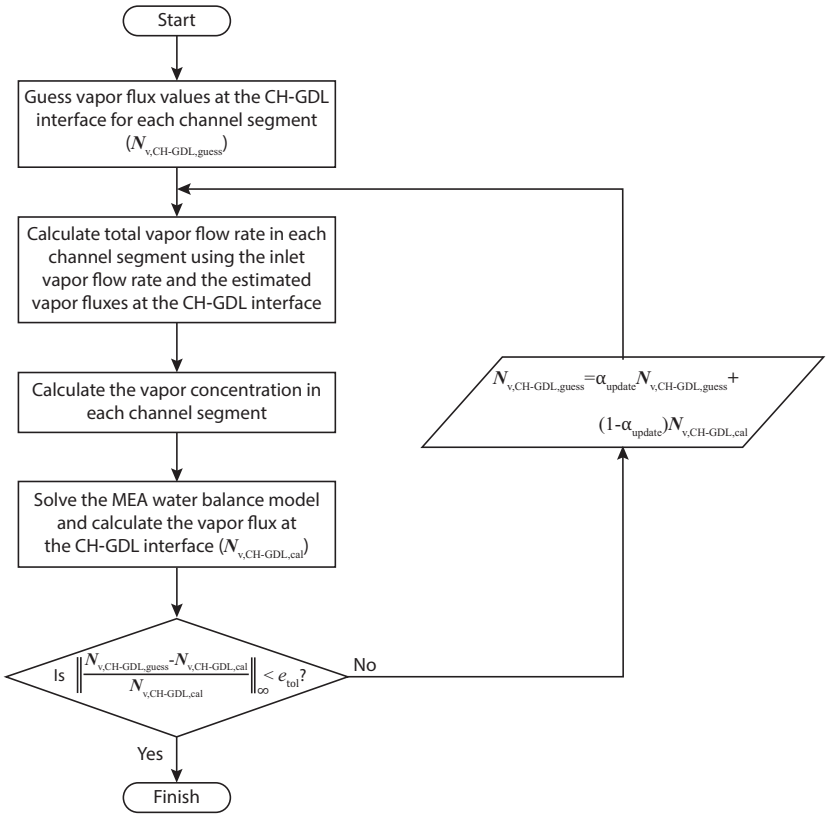

Figure 2.5: Flowchart for the iterative scheme used to simulate counter-flow mode of operation. e_{tol} is the tolerance used for convergence and $\alpha_{\text{update}} \in [0, 1]$ is an iteration parameter that affects the convergence rate. We use $e_{\text{tol}} = 0.005$ and $\alpha_{\text{update}} = 0.5$ in the simulations presented here and solutions from previous time steps are used to warm-start the iterations.

be refined until the calculated anode outlet values match the known inputs. However, this approach, which is known as the shooting method, creates a positive feedback loop for the estimation of water flow rates in the anode channel, leading to numerical instabilities. Instead, we have designed the iterations around the total water flow rate in each segment of the anode channel: we start with an estimate of the vapor flux at the channel-GDL interface at each location along the anode channel. These flux values are used to calculate the total water vapor flow rate and the corresponding vapor concentration in each channel segment. The vapor concentration values in the anode channel can be used to solve the model similar to the co-flow case and calculate the vapor fluxes at the anode channel-GDL interfaces. The calculated values are compared with the initial guessed values and the

process is repeated until convergence is achieved. This iterative scheme is shown in Fig. 2.5 and is numerically stable and converges (with a relative tolerance of 2%) in less than 10 iterations in most cases. With this number of iterations, the model can still achieve real-time performance even when the worst case computations are considered.

2.3 Model Validation

2.3.1 Experimental Data

The model is validated against data from two stacks with different material sets and designs. The detailed operating conditions and stack designs are proprietary. However, a high level description of each stack and the corresponding dataset is provided below.

The first dataset, denoted by "Stack A", contains polarization and high frequency resistance (HFR) data, measured at 1 kHz, obtained from a cell with a cathode Pt loading of 0.15 mg/cm^2 and a small active area (40 cm^2) operated under differential operating conditions (high stoichiometric ratio). This dataset, which is collected under co-flow configuration, includes 4 different operating conditions intended to replicate various real-world scenarios and constitutes a rather wide operating range, covering temperatures from 40 to 80 °C. Importantly, high current densities up to 3 A/cm^2 are achieved in each case, allowing for the model predictions under such high loads to be critically examined. Due to differential operation setting, no significant transients are observed in the data. Therefore, model validation is carried out using the steady state polarization and HFR values from Stack A.

The second dataset, denoted by "Stack B", contains only polarization data from an automotive size stack with a 0.4 mg/cm^2 cathode Pt loading and a large active area (about 300 cm^2). All of the tests are conducted at 70 °C, while the effects of humidity conditions have been extensively explored. Variations in the reactant stoichiometric ratios and low

stoichiometry operation allow us to better investigate mass transport limitations.

It should be noted that the plates used in both stacks have very small land/channel ratio on both the anode and cathode sides. As such, the in-plane distributions are disregarded in the model, *i.e.*, the transport equations are only solved under the channel (P2D model). The role of transport under the land is explored with the P2D^2 model in Section 2.4.

2.3.2 Model Parameterization

A set of 20 parameters is chosen to fit the model to the experimental data. This particular choice was made based on a preliminary sensitivity analysis that showed the model predictions to be sensitive to variations in these parameters at the experimental operating conditions. The uncertainty in the morphology of different cell components and the continuum modeling framework further motivated this choice. The set of fitting parameters are shown in Table 2.8 along with the identified values for each stack.

The parameters specified in Table 2.8 represent factors that control the kinetic, ohmic, and mass transport characteristics of the cell response. Therefore, they can be identified separately using data from different parts of the polarization curve (see Chapter 4). However, in this chapter we identify all of the parameters together using the entire dataset. In particular, we seek parameter values that minimize the following cost function:

$$\begin{aligned} J(\boldsymbol{\theta}) =& \frac{\|\boldsymbol{e_V}(\boldsymbol{\theta})\|_2}{\sqrt{n_V}} + \frac{\|\boldsymbol{e_R}(\boldsymbol{\theta})\|_2}{\sqrt{n_R}} + r_1 \|I(|\boldsymbol{e_V}(\boldsymbol{\theta})| - 10) \odot (|\boldsymbol{e_V}(\boldsymbol{\theta})| - 10)\|_2 \\ &+ r_2 \|I(|\boldsymbol{e_R}(\boldsymbol{\theta})| - 10) \odot (|\boldsymbol{e_R}(\boldsymbol{\theta})| - 10)\|_2, \end{aligned} \tag{2.66}$$

where $\odot$ denotes element-wise multiplication, $\boldsymbol{e_V}$ is the vector containing n_V voltage prediction errors in mV, $\boldsymbol{e_R}$ is the vector of n_R HFR prediction errors in $\mathrm{m\Omega \cdot cm^2}$ (for Stack A data), r_1 and r_2 are weight parameters (both set to 100 here), and $I(x)$ denotes

Table 2.8: Model parameters for identification and the identified values

Parameter [Units]	Range	Scaling	Stack A	Stack B
ω [kJ/mol]	$[10^{-1}, 10^{1}]$	Logarithmic	4.77	5.88
$i_{0,\mathrm{an}}^{\mathrm{ref}}$ [A/cm^2]	$[10^{-3}, 10^{-1}]$	Logarithmic	0.1	0.003
$i_{0,\mathrm{ca}}^{\mathrm{ref}}$ [A/cm^2]	$[10^{-9}, 10^{-6}]$	Logarithmic	1.29×10^{-7}	9.7×10^{-7}
α_{ca} [$-$]	[0.5, 1]	Linear	0.81	0.55
γ_{ca} [$-$]	[0.5, 1]	Linear	0.99	0.86
$E_{\mathrm{act,ca}}$ [kJ/mol]	[30, 80]	Linear	53.4	51.1
$E_{\mathrm{rev,PtO}}$ [V]	[0.75, 0.9]	Linear	0.76	0.79
k_{cross} [$-$]	[0.001, 2]	Linear	0.0102	0.52
$\xi_{\mathrm{diff,mb}}$ [$-$]	[0.1, 10]	Logarithmic	1.0	1.18
$f_{\mathrm{RH,a}}$ [$-$]	[0.4, 0.9]	Linear	0.60	0.53
$f_{\mathrm{RH,b}}$ [$-$]	[0.5, 4]	Linear	0.58	0.50
$f_{\mathrm{RH,c}}$ [$-$]	[0.3, 1]	Linear	0.37	0.56
R_{elec} [m$\Omega \cdot$ cm^2]	[30, 60]	Linear	54	30.4
κ_0 [S/cm]	[0.15, 0.55]	Linear	0.31	0.41
κ_{res} [S/cm]	[0.001, 0.006]	Linear	0.0026	0.0021
$E_{\mathrm{act,mb}}$ [kJ/mol]	[10, 30]	Linear	25.2	25.7
$k_{T,\mathrm{scale}}$ [$-$]	[0.1, 10]	Logarithmic	0.704	0.611
h_{conv} [W/(cm$^2 \cdot$ K)]	[0.05, 20]	Logarithmic	12.79	0.059
n_v [$-$]	[1, 3]	Linear	2.59	1.86
n_e [$-$]	[1, 3]	Linear	1.89	2.93

the indicator function of x, given by:

$$I(x) = \begin{cases} 1 & x > 0 \\ 0 & x \leq 0 \end{cases} . \tag{2.67}$$

With this, the last two terms in equation 2.66 put an additional penalty on voltage errors exceeding 10 mV or HFR errors exceeding 10 m$\Omega \cdot$ cm^2. This cost is minimized for each stack separately, identifying a different parameter set for each stack. Note that the

steady state data is used for parameterization. Since the model is transient in nature, it is allowed enough time to reach the steady state conditions before comparison is made with the experimental data. Moreover, since the parameters have largely different ranges, they are all scaled to a unit interval (between 0 and 1) using linear or logarithmic minmax scaling (see Table 2.8):

$$\bar{\theta}_i = \frac{\theta_i - \theta_{i,\min}}{\theta_{i,\max} - \theta_{i,\min}}, \tag{2.68}$$

$$\log \bar{\theta}_i = \frac{\log \theta_i - \log \theta_{i,\min}}{\log \theta_{i,\max} - \log \theta_{i,\min}}, \tag{2.69}$$

where $\bar{\theta}_i$ is the normalized parameter value and $\theta_{i,\min/\max}$ denotes the respective parameter bound. This scaling was determined to be essential in successfully identifying all of the parameters together. The identification is carried out using particle swarm optimization (PSO) [281] in MATLAB, which is a global optimization routine that efficiently explores the entire parameter space to find the optimal parameter set. A swarm size of 200 was used and the optimization was terminated after 200 iterations, at which point the cost was not decreasing any further. The algorithm was executed several times for each dataset and the results with lowest cost are reported here. It should be noted that due to the stochastic nature of the algorithm, each run can yield a new parameter set.

2.3.3 Results for Stack A

The polarization curves for the 4 conditions comparing the experimental data and the model predictions are shown in Fig. 2.6. The corresponding results for the HFR are provided in Fig. 2.7. It should be noted that each polarization curve consists of 15 points, starting from open-circuit voltage (OCV) and ending at 3 A/cm^2. This results in a total of 60 polarization data points across all 4 operating conditions. As for HFR data, only 7 measurements were made, shown as filled diamonds in Fig. 2.7. The experimental trend lines shown in the figure are estimations based on prior measurements using the

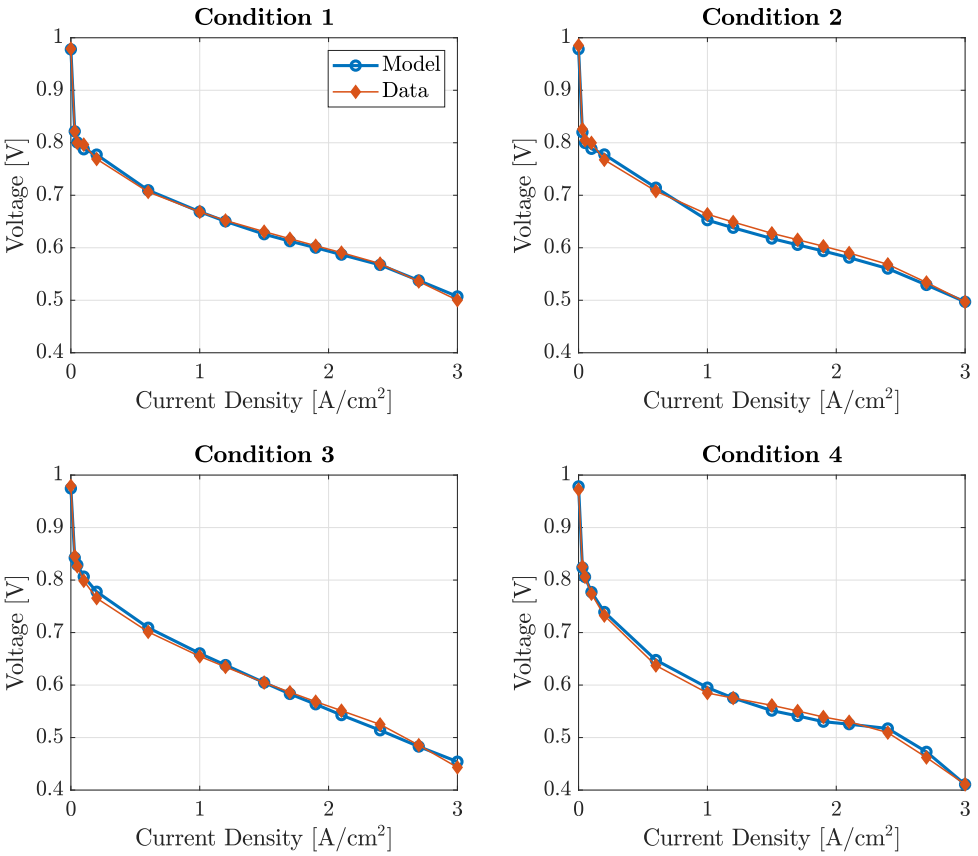

Figure 2.6: Model validation results using Stack A data. Polarization curves for 4 different operating conditions are considered.

same test stand.

Overall, we observe that the model captures the trends in the data very well. The maximum error in voltage across all 60 data points is 11.9 mV, while the maximum HFR error is 10 m$\Omega\cdot$cm^2. The fact that these fits are obtained with reasonable parameter values further highlights the model's capability to capture the most relevant physical phenomena critical to performance predictions.

A few comments about the parameterization process are in order. First, we found that the polarization data alone may be fitted with a variety of parameter combinations. In other words, the model is not structurally identifiable [282] using only voltage measurements at these 4 operating conditions. The fact that a polarization curve may be reproduced with different parameter combinations has also been pointed out by oth-

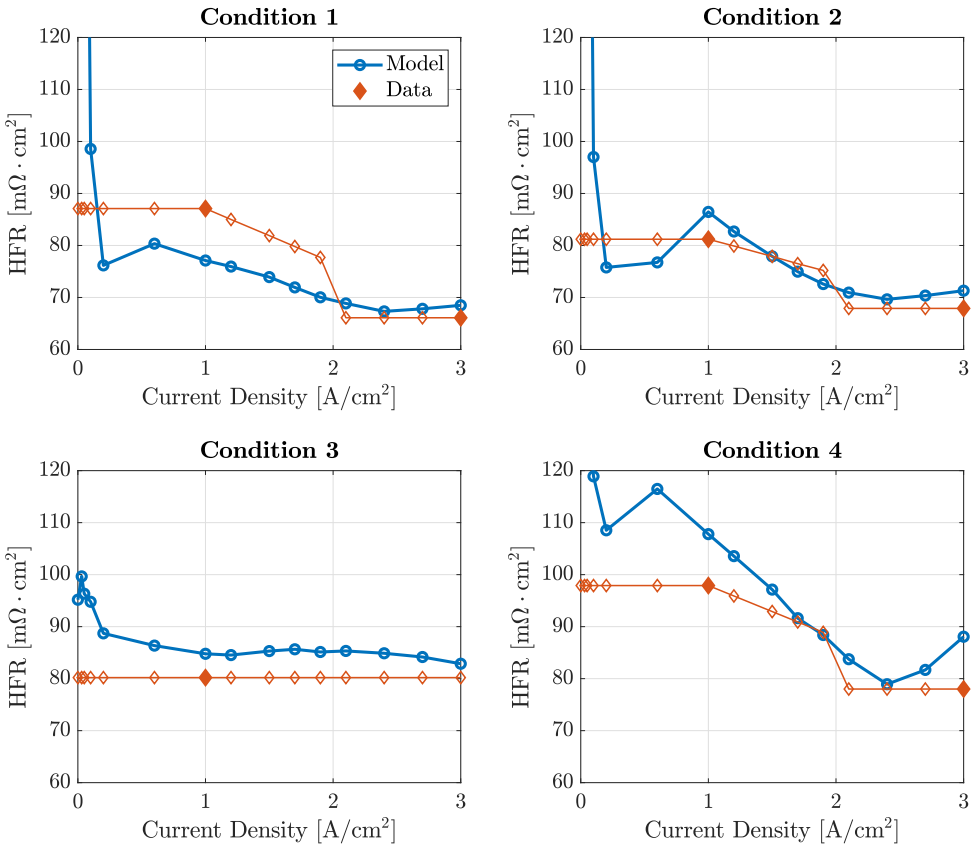

Figure 2.7: Model validation results using Stack A data. HFR data for 4 different operating conditions are considered. The measurement points are shown as filled diamonds. The empty diamonds are estimates based on prior testing data using the same test stand and do not represent actual measurements in this particular dataset.

ers [149,283]. Nonetheless, the operating conditions can be optimized to ensure maximum information is contained in the polarization data. In fact, even in this dataset, having the polarization data at 40 and 80°C helps reduce the uncertainty in the identified parameters considerably. Second, as pointed out recently by Vetter et al. [218, 284], most of the consequential parameters in these types of PEM fuel cell models are related to the membrane water uptake and transport. Therefore, adding the HFR data to the identification process can considerably increase the confidence in parameter estimates. These issues are discussed further in Chapters 3 and 4.

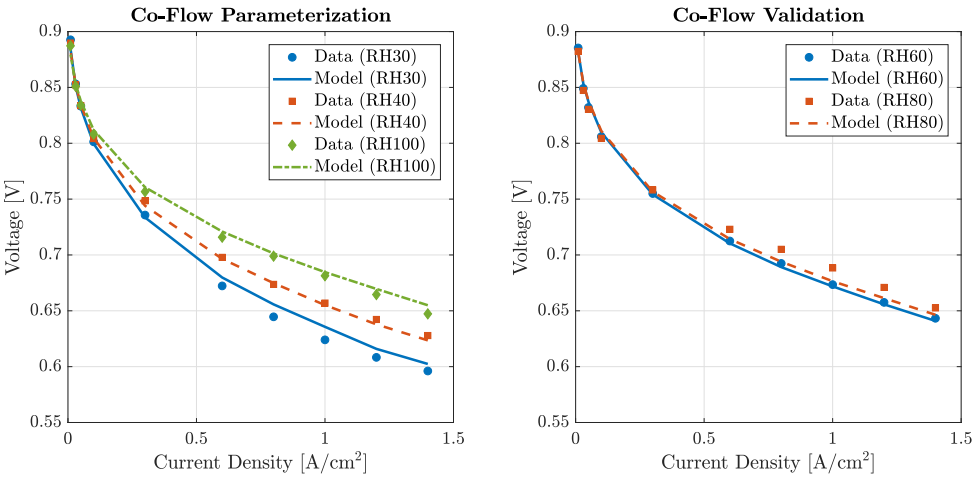

Figure 2.8: Model validation results using Stack B data. Polarization data were collected under five humidity conditions. Three polarization curves were used for model parameterization (left), while two curves were used for validation (right).

2.3.4 Results for Stack B

The validation results using data obtained from Stack B with co-flow configuration are shown in Fig. 2.8. Overall, 5 different humidity conditions were tested, ranging from 30% to 100% RH. The RH value indicates humidity conditions in both the anode and cathode channels. The data at three RH conditions were used in the optimization routine to parameterize the model. The same parameter values were then used to validate the model predictions against experimental values for the other two humidity conditions. As seen in Fig. 2.8, the model predictions match the experimental results closely. The largest error in voltage prediction is 12.8 mV. This indicates the model's capability in accurately predicting the stack performance when parameterized properly. Nevertheless, we note that during model parameterization, we were able to find several parameter combinations that yield reasonable model predictions as compared to available voltage measurements. This further signifies the structural identifiability issues that are common for fuel cell models and warrants more investigation of the topic that is pursued in Chapters 3 and 4.

The transient behavior for the dry conditions (RH=30%) is shown in Fig. 2.9. The figure depicts voltage dynamics from experimental data with co-flow configuration along

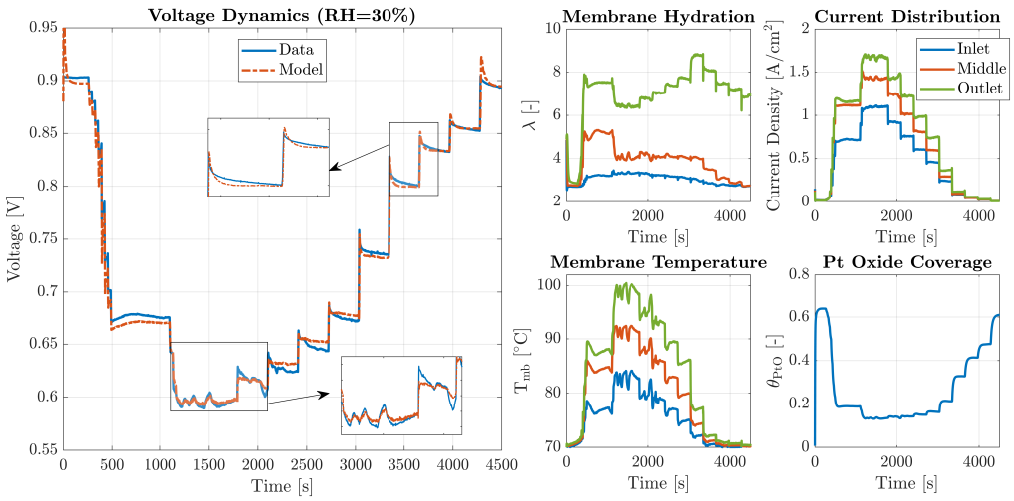

Figure 2.9: Voltage dynamics comparing modeling results and measurements obtained on Stack B at RH=30% (left) and the corresponding model predictions for membrane hydration distribution, current distribution, membrane temperature distribution, and PtO coverage dynamics (right).

with the corresponding model predictions. It is observed that the model captures most of the features seen in the transient measurements. In particular, the nonmonotonic voltage response (seen as overshoot and undershoot) to step changes in the current density is mostly captured. This response is due to membrane hydration/dehydration at higher current densities, while Pt oxide coverage dynamics is the main contributing factor at lower current densities. Note that the model predictions for the immediate response to current density variations are also affected by the PI controller performance. Therefore, some discrepancies between the model and measured transients immediately following a step change in current density are to be expected.

In Fig. 2.9, two sections of the voltage transient response are magnified and provided in the insets for further discussion. The first part corresponds to the highest load used in the experiments (1.4 A/cm^2). During this time, some voltage swings are observed, which correspond to variations in the inlet coolant temperature. A decrease in the inlet coolant temperature is observed to result in an increase in the cell voltage, which is attributable to better membrane hydration. The voltage sensitivity to these temperature variations

is accurately captured by the model. The second inset shows the voltage dynamics at lower loads above 0.8 V. For this case we observe a voltage overshoot followed by a relatively slow decay in the measured cell voltage after the current density is lowered. This behavior is mainly due to the formation of oxide species on Pt sites and is partially captured by the model (see the Pt oxide coverage plot in Fig. 2.9). In particular, the measurements show signs of a second-order system with two separate time constants; a fast decay on the order of tens of seconds, followed by slower response that settles on the order of hundreds of seconds. This behavior may be attributable to formation of different oxide species [285]. Since the present model only incorporates PtO coverage, the slow dynamics are not captured accurately. Nonetheless, such behavior rarely has relevance to performance optimization for it to prompt further model development.

In addition to voltage dynamics, Fig. 2.9 also shows the membrane hydration, average membrane temperature, and current density distribution along the flow channel, as well as the oxide coverage dynamics. Membrane hydration, temperature, and current density are all seen to increase along the flow channels. However, membrane hydration shows an interesting behavior, where it dramatically increases near the outlet region. This is especially the case for drier conditions with the co-flow configuration. Under such conditions, the low inlet humidity results in a dry membrane. But the water produced near the inlet of the cell humidifies the channel gas streams, which in turn helps improve hydration near the outlet region.

To finalize our discussion on the modeling results for the experimental conditions, Fig. 2.10 provides the along-the-channel distributions of current density, membrane hydration, normalized water crossover, and channel and CL RH at a current density of 1.4 A/cm^2 (corresponding to Time = 1700 s in Fig. 2.9). The plots also provide a comparison between distributions for the co-flow and counter-flow configurations. A few observations are in order. First, we note the close correspondence between the current density and membrane hydration distributions along the flow channels. Particularly, the membrane

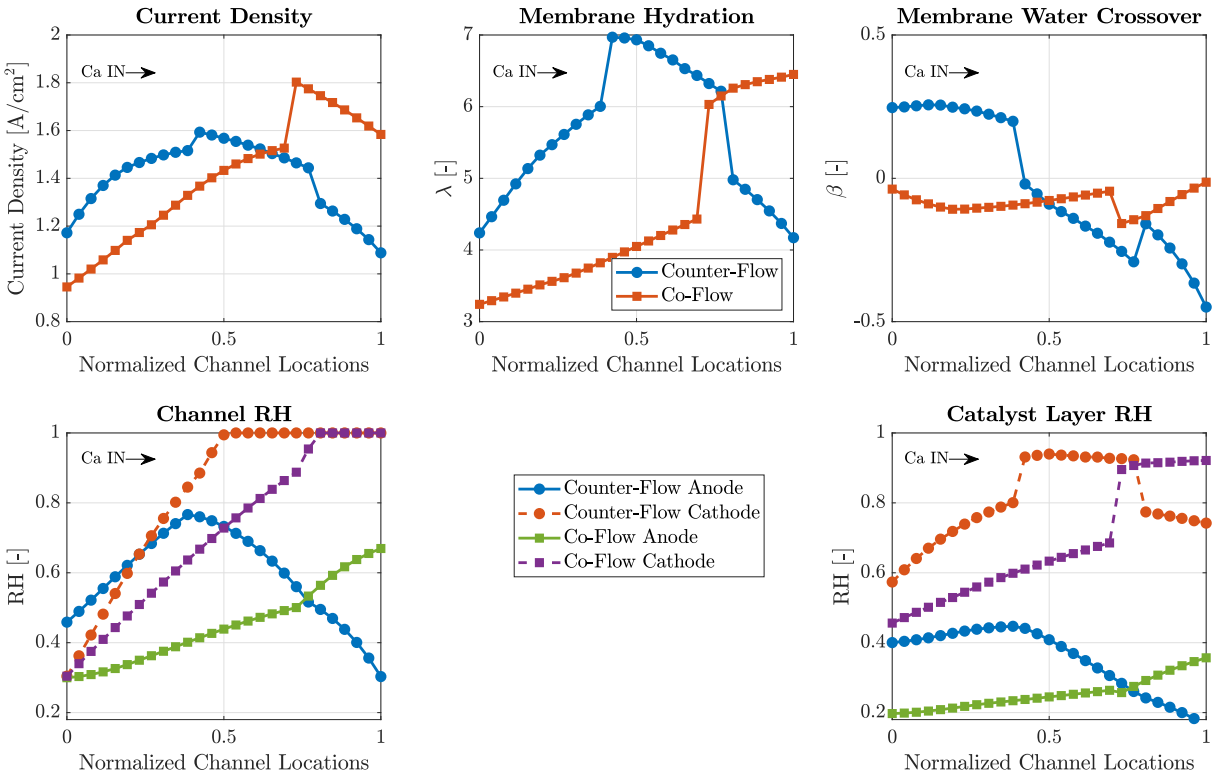

Figure 2.10: Effects of flow configuration on along-the-channel distributions at 1700 s as predicted by the model. Current density, membrane hydration, and normalized membrane water crossover distribution (top), and relative humidity distributions in the anode and cathode channels and catalyst layers (bottom).

hydration is seen to increase monotonically from inlet to outlet for the co-flow case, whereas a peak in membrane hydration is observed near the middle of the cell for the counter-flow configuration. As for the current densities, the distribution for the counter-flow case aligns with its corresponding membrane hydration. For the co-flow case, the current density is seen to initially increase from the inlet towards the outlet with improved membrane hydration. However, near the outlet, the current density drops slightly due to mass transport limitations. In fact, this current distribution is typical for co-flow operations and the location of the peak current density is closely related to the inlet humidity conditions, with higher humidities resulting in a peak current density closer to the inlet. The figure also shows the normalized membrane water crossover defined as the

rate of water crossover to the anode side normalized by the local water generation:

$$\beta = \frac{N_{\mathrm{w,mb}}}{i_{\mathrm{dens}}/2F}. \tag{2.70}$$

As is typically the convention, a positive value denotes flow from anode to cathode. This plot clearly shows the water recirculation mechanism for the counter-flow configuration, wherein near the cathode inlet the humidified anode outlet stream results in a net water crossover towards the cathode. However, as we move along the cathode channel and the cathode stream becomes humidified, the net water crossover changes towards the anode, humidifying the incoming dry anode stream. This mechanism, which can also be seen from the channel RH distributions, is the main feature of counter-flow operation reported in both experimental and modeling literature [86, 104, 286, 287]. The same plot also shows that the net water crossover is consistently towards the anode side for the co-flow case, which is in agreement with experimental observations for state-of-the-art and thin membranes [288]. Finally, the CL RH values are also shown in Fig. 2.10. This plot highlights the fact that even when the channel streams are saturated, the CL can experience sub-saturated conditions due to the heat released through the electrochemical reactions. This has also been observed experimentally in the literature [289].

While measurements for such distributions were not available in our experimental set-up, their qualitative agreement with experimental results in the literature showcase the present model's capabilities in capturing these trends. Overall, the very good quantitative agreement with available measurements, the aforementioned qualitative agreement with literature data, the robustness of the numerical algorithms in solving the model for real operating conditions without convergence issues, and the fact that these results are obtained more than an order of magnitude faster than real time all point to the utility of the present model and the underlying numerical approach to act as a software sensor for PEM fuel cell systems.

2.4 Simulation Case Studies

With the model validated with various experimental data in the previous section, we now turn our attention to some of its prediction capabilities using some load cycling scenarios. While a P2D version of the model was used for validation, the P2D^2 model is used in this section to demonstrate the ability of the bi-domain modeling approach in capturing the in-plane distributions. Here, the current density is cycled between low and high loads under two distinct conditions. Simulations for each condition are conducted with both co-flow and counter-flow configurations. The operating conditions are shown in Table 2.9. When the anode and cathode conditions are not separately identified (*e.g.*, RH), they are taken to be the same. Each loading condition is maintained for 300 seconds before a step change in the load. This time allows for the cell dynamics to settle to a quasi steady state. Moreover, note that the step change in the load is chosen to be large enough to excite the system dynamics. Similarly, the two sets of operating variables (cold wet and hot dry) are chosen to show the model's prediction capabilities under extreme conditions. A complete list of parameter values used for these simulations is provided in the Appendix Table A1.

Table 2.9: Operating conditions used for simulation case studies

Condition	Cold Wet (CW) Low Load	Cold Wet (CW) High Load	Hot Dry (HD) Low Load	Hot Dry (HD) High Load
i_{dens} [A/cm^2]	0.6	2	0.6	2
St_{H_2}/St_{O_2} [-]	1.5	1.5	1.5	1.5
RH [-]	90	90	30	30
$T_{\text{cool,in}}$ [°C]	50	50	80	80
ΔT_{cool} [°C]	6	12	6	12
p_{in} [bar]	2	2	2	2
Δp_{an} [mbar]	35	70	35	70
Δp_{ca} [mbar]	80	160	80	160

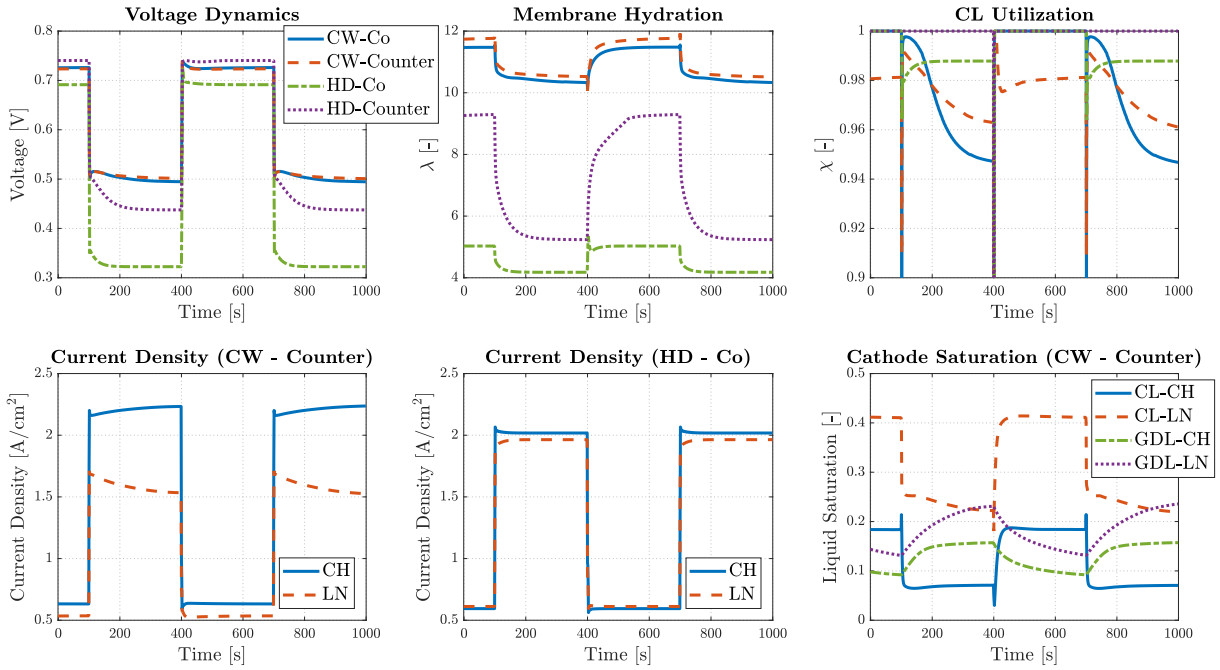

Figure 2.11: Average dynamic response of the cell to load cycling. The top row shows average dynamics for all four simulation case studies, while the bottom row illustrates current density dynamics under the land and channel regions as well as the cathode liquid saturation for selected simulations.

The average dynamic responses of the cell under the various simulation scenarios are shown in Fig. 2.11. As seen in the figure, the step increase in the load results in a very small undershoot in voltage, which is then followed by a slow decay. The initial undershoot can be attributed to a combination of EOD that dries out the anode side of the membrane as well as the existence of the PtO layer that has accumulated at higher voltage. The slow decay in voltage that follows is seen to be a direct consequence of membrane dry-out. This can in turn be attributed to the significant heat that is generated at this higher load, as well as the high EOD. The figure also shows that the flow configuration does not have a significant impact under cold and wet conditions, whereas counter-flow configuration considerably improves performance under hot and dry conditions. This is to be expected, since counter-flow operation yields better membrane hydration conditions as can also be seen in the figure.

Fig. 2.11 further shows the average cathode CL utilization (χ) for the different scenarios. It is observed that the cold and wet conditions result in lowered CL utilization. This is due to mass transport losses incurred by the accumulated liquid water under these conditions. The CL is also not fully utilized under the high load for the hot and dry conditions with co-flow configuration. Although the average utilization is very close to unity, this amounts to a very interesting observation, namely, dry ionomer in the cathode CL can also cause local mass transport losses and reduce the catalyst available for ORR. Of course, this behavior can already be captured by comprehensive fully coupled models [89]. Nevertheless, computationally efficient solutions with this level of fidelity are not commonly pursued in the literature.

Fig. 2.11 also provides the distinct current density profiles under the channel and land regions for two of the simulated cases. As seen in the figure, the current density is lower under the land region for the cold and wet condition, which is due to the mass transport limitations. However, for the hot and dry conditions the current production under the land is on par with that under the channel, since better hydration under the land compensates for increased mass transport resistance. Lastly, the figure shows liquid saturation in the cathode CL and GDL under the land and channel regions for the cold and wet conditions. Clearly, the land region is more susceptible to flooding due to lower temperatures and higher mass transport resistance. More interesting, however, is the dynamics of liquid accumulation in the CL and GDL. The CL shows a tendency to flood rapidly, within 20 seconds of the load change, whereas liquid accumulation in the GDL is seen to be much slower not reaching steady state under the land even after 300 seconds. These disparate time scales are due to differences in porosities of the layers, as well as the environmental conditions experienced by each layer.

To further demonstrate the model's prediction capabilities, example distributions obtained from the model for two of the simulated scenarios are shown in Fig. 2.12. The

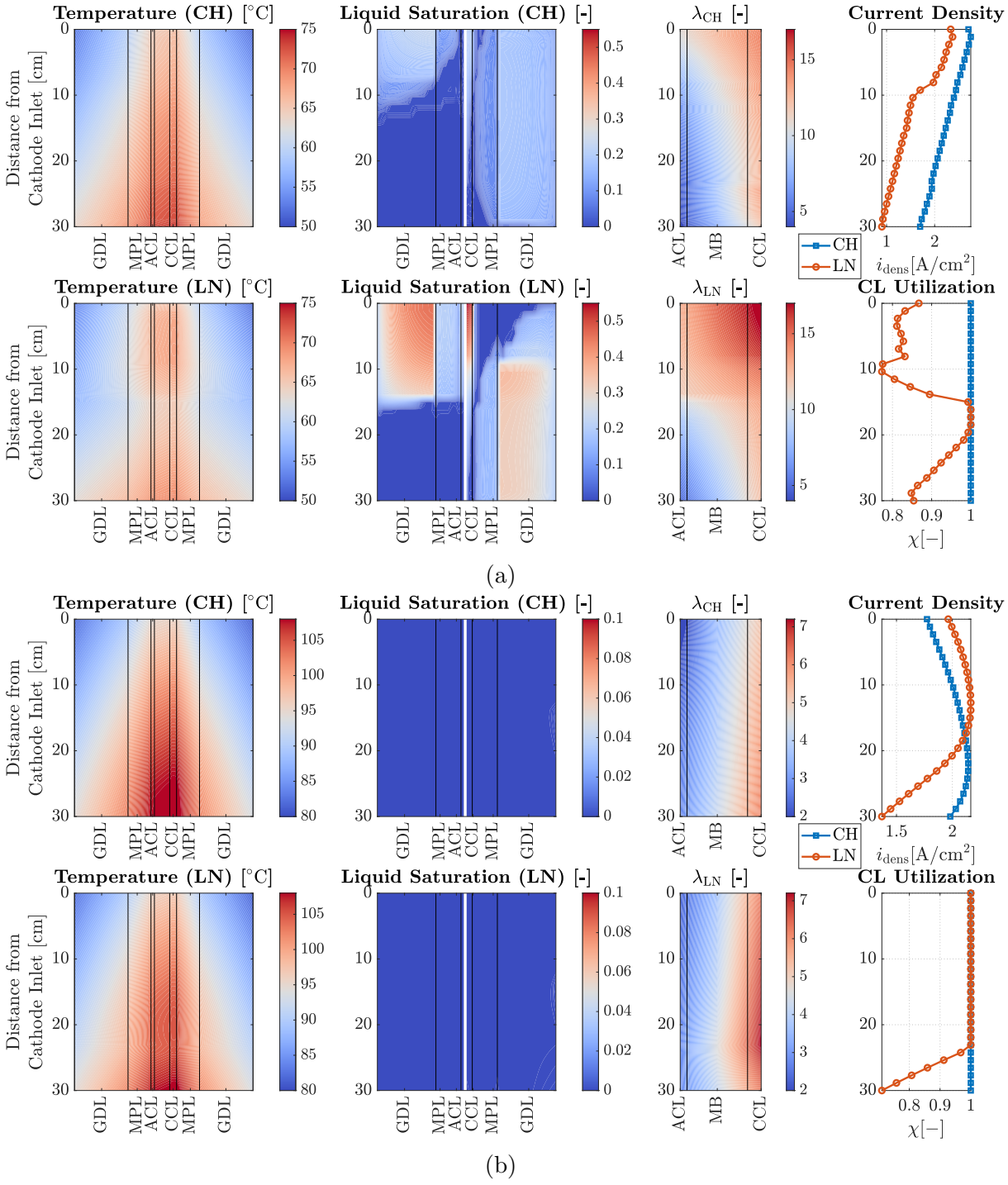

Figure 2.12: Distributions of temperature, liquid saturation, ionomer water content, current density, and cathode CL utilization for: (a) cold wet conditions (T = 50 °C and RH = 90%) with counter-flow configuration and (b) hot dry conditions (T = 80 °C and RH = 30%) with co-flow configuration at 990 s.

model is seen to capture the main features of the in-plane distributions, namely, higher mass transport resistance under the lands, which leads to increased flooding and improved membrane hydration, and the higher temperature under the channels. More specifically, the distributions for cold and wet conditions with counter-flow configuration (Fig. 2.12(a)) show that liquid accumulates mostly under the land region. In this region, each GDL is more prone to flooding near the outlet of its respective gas stream. However, the cathode CL is mostly flooded near the cathode inlet, which is due to the significant water crossover from the anode side in this region. The good hydration on the anode side also results in improved membrane hydration near the cathode inlet. The figure also shows the along-the-channel current distributions for both the channel and land regions, where it is observed that current generation under the land is suppressed due to mass transport limitations. Another interesting observation relates to cathode CL utilization under the land and the fact that it is reduced near the cathode inlet due to cathode CL flooding in this region. Moreover, we observe that this reduced utilization has also resulted in higher temperatures in this region due to higher volumetric heat generation.

Lastly, Fig. 2.12(b) shows the same distributions for the hot and dry conditions under co-flow configuration. We observe that no liquid has accumulated anywhere in the cell. As for the current distributions under the channel and land regions, they go through a peak as we move along the flow channel. Near the channel inlet, the land region produces more current due to better hydration. Once the peak current is achieved, the current under the land region drops more sharply due to more severe mass transport limitations. These transport limitations also result in reduced cathode CL utilization under the land near the channel outlet.

These results demonstrate the prediction capabilities of the model presented here. As mentioned earlier, it is the balance between the fidelity and the low computational cost of the present modeling framework rather than the specific simulation results that is of significance. The fact that the model is able to reproduce the behavior that is captured

by much more computationally intensive models verifies the approach adopted herein. Finally, the high fidelity and efficiency of the model offers significant advantages for real-time estimation as well as the tasks that require repetitive model evaluations such as optimization of operating conditions.

2.5 Summary and Conclusions

A high fidelity and computationally efficient model of PEM fuel cells is presented. The model takes advantage of the disparate time and length scales to spatio-temporally decouple the problem and achieve a performance that is more than an order of magnitude faster than real time. Particularly, the model efficiently captures the in-plane and through-plane distributions utilizing a pseudo-2D bi-domain modeling approach. Additionally, a novel reduced-order model for water balance across the MEA is presented and a simple analytical method is used to model the proton and mass transport trade-offs in the cathode CL and capture its effective utilization. These novelties further contribute to the efficiency of the presented model.

An optimization-based approach is used to parameterize the model for two different fuel cell stacks. The model is validated against a variety of operating conditions for the two stacks and shown to capture the experimental performance measurements. Finally, simulation case studies are presented to showcase the model's prediction capabilities under different operating scenarios. Based on these results, it is concluded that the fidelity and computational efficiency of the model make it a suitable tool towards real-time monitoring of automotive PEM fuel cell systems. The issues faced during model parameterization efforts presented in this chapter warrant further investigation of the parameter identification problem. Accordingly, the next two chapters extensively focus on this problem and develop a framework for effective model parameterization.

Chapter 3

Sensitivity Analysis and Parameter Identifiability

3.1 Introduction

As highlighted in Chapter 1, the fuel cell literature is yet to capitalize on considerable opportunities for effective model parameterization. Accordingly, our objective in this and the next chapter is to fill this gap by developing a systematic approach for parameter identification tailored specifically to fuel cell applications. In particular, we aim to answer the following questions: How are different model outputs affected by model parameters? What are the major difficulties associated with large-scale parameter identification problems? How many and which of the model parameters can be accurately identified given a particular set of measurements? How can we optimally design the experiments for the purpose of parameter identification? And finally, how do we ensure that our results are robust to initial assumptions about the values of model parameters?

To answer these questions, in this and the next chapter we develop a systematic procedure using as an example the model presented in Chapter 2. Importantly, the low computational cost of the model enables a large number of model evaluations. Using this

model as an example, we analyze identifiability of its parameters employing a sensitivity-based approach. Particularly, we start with an extensive sensitivity analysis that considers a large number of model parameters. This analysis is conducted considering a variety of operating conditions that can be used to collect experimental data. Moreover, in order to make our approach robust to initial assumptions about the parameter values, we carry out the sensitivity analysis at several points in the parameter space to obtain a more global picture of the sensitivity results. Using these sensitivity results, we study the identifiability of the model parameters and examine parameter subset selection for identification.

The rest of the chapter is organized as follows. First, the problem of parameter identification is explained in Section 3.2. This is followed by the methods for sensitivity analysis in Section 3.3 and a discussion of the main results in Section 3.4, where sensitivities of various model outputs to the considered parameters are investigated. Identifiability analysis and relevant issues are discussed in Section 3.5, before concluding with a brief summary of the chapter.

3.2 Parameter Identification Problem

The parameter identification problem consists of finding the model parameters given some measured data, whose behavior is to be captured by the model. To make this more concrete, first we note that the model can be described using a set of differential-algebraic equations (DEAs):

$$\dot{\boldsymbol{x}} = \boldsymbol{f}(\boldsymbol{x}, \boldsymbol{z}, \boldsymbol{u}, \boldsymbol{\theta}), \;\; \boldsymbol{x}(0) = \boldsymbol{x_0} \tag{3.1}$$

$$\boldsymbol{0} = \boldsymbol{g}(\boldsymbol{x}, \boldsymbol{z}, \boldsymbol{u}, \boldsymbol{\theta}), \;\; \boldsymbol{z}(0) = \boldsymbol{z_0} \tag{3.2}$$

$$\tilde{\boldsymbol{y}} = \boldsymbol{h}(\boldsymbol{x}, \boldsymbol{z}, \boldsymbol{u}, \boldsymbol{\theta}), \tag{3.3}$$

where $\boldsymbol{x}$ is the vector containing dynamic states of the model (*e.g.*, membrane temperature and hydration), $\tilde{\boldsymbol{y}}$ is the vector of predicted outputs (*e.g.*, cell voltage), $\boldsymbol{z}$ is the vector of algebraic variables (*e.g.*, solid phase potential when double layer capacitance is ignored), $\boldsymbol{u}$ is the vector of inputs (*e.g.*, channel pressure and coolant temperature), and $\boldsymbol{\theta}$ denotes the vector of model parameters (*e.g.*, exchange current density for oxygen reduction reaction). The vector valued functions $\boldsymbol{f}$, $\boldsymbol{g}$, $\boldsymbol{h}$ represent the system dynamics, algebraic constrains, and output equations, respectively. Note that while fuel cell models are typically described with PDEs, all such models may be written in DAE format after proper spatial discretization. Furthermore, while a model can make predictions about internal states of the cell (*i.e.*, $\tilde{\boldsymbol{y}}$ can contain elements of $\boldsymbol{x}$), we use $\tilde{\boldsymbol{y}}$ to denote only the model predictions for which experimental data can be measured. Henceforth, we refer to $\tilde{\boldsymbol{y}}$ as predicted outputs, with the understanding that the corresponding measurements can be taken in an actual experimental setting. Given the above generic model description, parameter identification (also known as parameter tuning) is to find a suitable vector $\boldsymbol{\theta}$ such that the model predictions given by $\tilde{\boldsymbol{y}} = \boldsymbol{h}(\boldsymbol{x}, \boldsymbol{z}, \boldsymbol{u}, \boldsymbol{\theta})$ match the available measurements, $\boldsymbol{y}$, as closely as possible.

The parameter identification problem can be solved using a variety of methods, among which least squares is the most common approach. However, an identifiability analysis must precede parameter identification. Identifiability can be analyzed in both a local and a global sense. A parameter is locally identifiable if it can be determined uniquely in a neighborhood around a nominal parameter value, given a set of measurements [290]; no two parameter values that are close enough would result in the same model predictions. On the other hand, global identifiability indicates that no two parameter values, no matter how far apart, can give the same predictions [290]. This means that among all possible parameter values, there is only one that can best represent the given measurements.

Given these definitions, an identifiability analysis of model parameters prior to param-

eter identification is warranted. To carry out such analysis, one must understand what the root causes of unidentifiability are. Particularly, what can render a model parameter unidentifiable? An obvious answer is the case where a model parameter has no impact on the predicted outputs. A more subtle case is when a combination of model parameters impacts the predicted outputs together. For instance, if a model has two parameters, a and b, but they always appear as a product (ab) throughout the model, then neither of these parameters will be identifiable. In fuel cell models, this happens, for example, with exchange current density and volumetric surface area of Pt in the catalyst, as they always appear as a product in the BV model of reaction kinetics. These examples amount to what is known as structural unidentifiability [291]; *i.e.*, the model structure does not allow for unique identification of these parameters even if every variable of interest could be measured with perfect precision.

This notion of identifiability, while useful, falls short in practical settings. In particular, a model parameter might be structurally identifiable but require a lot of measurements with high precision to be identified. In such cases, the notion of practical identifiability yields better insight, as it accounts for the limited quantity and precision of the measurements [291]. Readers interested in a more formal treatment of the subject are encouraged to consult the review paper by Miao et al. and references therein [291].

A variety of methods have been reported in the literature to investigate both practical and structural identifiability issues. Structural identifiability analysis requires the structure of the model to be known and, having its roots in control theory [282], usually utilizes tools such as differential algebra [292] and implicit function theorem [293], to name a few. One of the more recent developments in this area is the use of extended observability analysis for this purpose [294, 295]. Despite such rich history, these methods are usually limited to small problems and do not lend themselves to large-scale models. Fortunately, practical identifiability analysis does not suffer from such a shortcoming and may be readily applied to large-scale problems. In this respect, Monte Carlo methods [291], correlation

analysis [296], and sensitivity-based methods [165] have been developed in the literature. Among these, the methods based on sensitivity analysis are most commonly utilized, as they scale easily and also provide information about the structure of the model without the need for a full-blown structural identifiability analysis [291, 296]. Accordingly, we use a sensitivity-based identifiability analysis method to closely investigate the structure of our model and study the identifiability of its parameters.

Sensitivity analysis is a rich topic in itself with a vast body of literature. A good sensitivity analysis requires consideration of different aspects of the problem. Therefore, in the next sections we discuss this in detail and present our sensitivity analysis results before moving on to identifiability analysis.

3.3 Sensitivity Analysis: Methods

Sensitivity analysis is commonly used as a tool to investigate the impact of different input factors (e.g., operating conditions or model parameters) on outputs of interest. Examples of sensitivity analysis in the fuel cell literature usually include perturbing input factors of interest individually to quantify each factor's significance [90, 297–299]. More recent studies have conducted rigorous sensitivity analyses on fuel cell models [284, 300, 301]. In this regard, the recent work by Vetter et al. [284] stands out, as they consider a relatively large set of parameters and also conduct a global sensitivity analysis, where they find that the parameters impacting membrane water uptake and transport to be of profound importance. It is based on this important conclusion that they suggest efforts should be aimed at accurate estimation of such parameters. This statement offers a different viewpoint for sensitivity analysis: while sensitivity results have been typically used to guide research efforts in optimizing the design and material properties from a performance standpoint, they can be interpreted in a different light to enhance the predictive power of fuel cell models. In other words, in most of the previous cases sensitivity analysis can

be considered as a use case for the model to improve fuel cell designs, whereas Vetter et al.'s suggestion amounts to using sensitivity analysis in order to refine the model itself by proper parameter identification. In this sense, the analysis presented in this chapter is similar to that of Vetter et al. [284]. However, we extend their results in several important ways: (1) the model used in this study is more comprehensive than Vetter et al.'s and it incorporates transport effects along the flow channels, (2) we consider a larger set of model parameters, and (3) we extensively analyze the sensitivity results in terms of the dependencies between the parameters as suggested by sensitivity directions and not only sensitivity magnitudes that were used in Vetter et al.'s study. For completeness, a detailed account of our methods is presented after a brief overview of the model and the parameters considered for this study.

3.3.1 Model Configuration and Parameters

We use the model explained in Chapter 2. Specifically, the P2D version of the model is used with co-flow configuration. This is to keep the computational cost for the sensitivity analysis manageable. The model parameters include those that describe geometrical features of the cell design, reaction kinetics, physical properties of the material set, as well as several fitting coefficients used to match the model predictions with experimental data. To conduct the sensitivity analysis, we have chosen 50 of the model parameters from all the parameter classes mentioned above. Notably, geometrical parameters are also included, which are usually known for a given fuel cell stack. Nonetheless, the design geometry can impact the sensitivity of other model parameters. Therefore, to ensure that our results are not constrained by a specific stack design, we include these parameters in our sensitivity analysis. The chosen parameters are shown in Table 3.1 along with their units, and corresponding ranges. We note that a number of parameters are factors used to scale nominal model parameters. These include k_{cross}, $k_{T,\text{scale}}$, and $K_{\text{per,scale}}$, which

scale the membrane gas permeability, and porous layer thermal conductivity and liquid permeability, respectively.

Table 3.1: Model parameters used for sensitivity analysis.

Parameter	Units	Range	Scaling
ω	[kJ/mol]	[1, 20]	Linear
α_{an}	[-]	[1.2, 2.0]	Linear
α_{ca}	[-]	[0.4, 1.0]	Linear
$i_{0,\text{an}}$	[A/cm^2]	[10^{-3}, 10^{-1}]	Logarithmic
$i_{0,\text{ca}}$	[A/cm^2]	[10^{-9}, 10^{-6}]	Logarithmic
γ_{an}	[-]	[0.5, 1]	Linear
γ_{ca}	[-]	[0.5, 1]	Linear
$E_{\text{act,an}}$	[kJ/mol]	[5, 20]	Linear
$E_{\text{act,ca}}$	[kJ/mol]	[30, 80]	Linear
$E_{\text{rev,PtO}}$	[V]	[0.75, 0.85]	Linear
$E_{\text{act,PtO}}$	[kJ/mol]	[5, 20]	Linear
k_{cross}	[-]	[0.01, 10]	Logarithmic
$\xi_{\text{diff,mb}}$	[-]	[0.1, 10]	Logarithmic
$f_{\text{RH,a}}$	[-]	[0.4, 0.9]	Linear
$f_{\text{RH,b}}$	[-]	[0.2, 4]	Linear
$f_{\text{RH,c}}$	[-]	[0.3, 1]	Linear
R_{elec}	[m$\Omega \cdot$ cm^2]	[30, 80]	Linear
κ_0	[S/cm]	[0.2, 0.6]	Linear
κ_{res}	[S/cm]	[10^{-4}, 0.006]	Linear
$E_{\text{act,mb}}$	[kJ/mol]	[5, 30]	Linear

EW_{mb}	[g/mol]	[600, 1200]	Linear
EW_{CL}	[g/mol]	[600, 1200]	Linear
$k_{T,\mathrm{scale}}$	[-]	[0.1, 10]	Logarithmic
h_{conv}	[W/(cm$^2 \cdot$ K)]	[0.05, 10]	Logarithmic
n_v	[-]	[1, 3]	Linear
n_e	[-]	[1, 3]	Linear
$\varepsilon_{\mathrm{MPL}}$	[-]	[0.4, 0.65]	Linear
$\varepsilon_{\mathrm{GDL}}$	[-]	[0.5, 0.85]	Linear
θ_{CL}	[°]	[90.5, 100]	Linear
θ_{MPL}	[°]	[110, 150]	Linear
θ_{GDL}	[°]	[100, 130]	Linear
$K_{\mathrm{per,scale}}$	[-]	[0.02, 50]	Logarithmic
w_{ch}	[cm]	[0.1, 0.4]	Linear
w_{rib}	[cm]	[0.02, 0.3]	Linear
h_{ch}	[cm]	[0.01, 0.1]	Linear
L_{ch}	[cm]	[15, 40]	Linear
δ_{mb}	[μm]	[8, 30]	Linear
δ_{MPL}	[μm]	[20, 70]	Linear
δ_{GDL}	[μm]	[100, 240]	Linear
$ECSA_{\mathrm{an}}$	[m^2/g]	[40, 90]	Linear
$ECSA_{\mathrm{ca}}$	[m^2/g]	[40, 90]	Linear
$\varepsilon_{\mathrm{CL,an}}$	[-]	[0.3, 0.7]	Linear
$\varepsilon_{\mathrm{CL,ca}}$	[-]	[0.3, 0.7]	Linear

$L_{\text{Pt,an}}$	[mg/cm^2]	[0.05, 0.3]	Linear
$L_{\text{Pt,ca}}$	[mg/cm^2]	[0.05, 0.4]	Linear
IC_{an}	[-]	[0.6, 1.3]	Linear
IC_{ca}	[-]	[0.6, 1.3]	Linear
$wt\%_{\text{Pt,an}}$	[-]	[0.2, 0.7]	Linear
$wt\%_{\text{Pt,ca}}$	[-]	[0.2, 0.7]	Linear
n_{Brugg}	[-]	[1, 3]	Linear

3.3.2 Sensitivity Calculations

A variety of methods have been suggested in the literature to calculate model sensitivities. Among them, the derivative-based approach is the most commonly used due to its easy and possibly efficient implementation. This approach estimates the sensitivities as follows:

$$\mathbf{S} = \frac{\partial \tilde{\boldsymbol{y}}}{\partial \boldsymbol{\theta}}, \tag{3.4}$$

where $\mathbf{S}$ is the sensitivity matrix, whose (i,j)-th entry denotes the sensitivity of the i-th predicted output to the j-th parameter. When multiple outputs and parameters are considered, a scaled version is typically used to ensure the results are not affected by the choice of units. Naturally, the sensitivity results obtained with this method are only valid in the immediate neighborhood of the nominal parameter values that are used to evaluate the model.

To better explore the entire range of individual parameters and obtain sensitivities that are more representative of the sensitivity values throughout this range, here we adopt a sample-based approach. In particular, to calculate the sensitivity of parameter i at any point in the parameter space, we start by mapping the parameter range onto a

unit interval using linear or logarithmic min-max scaling as done in Chapter 2:

$$\bar{\theta}_i = \frac{\theta_i - \theta_{i,\min}}{\theta_{i,\max} - \theta_{i,\min}}, \tag{3.5}$$

$$\log \bar{\theta}_i = \frac{\log \theta_i - \log \theta_{i,\min}}{\log \theta_{i,\max} - \log \theta_{i,\min}}, \tag{3.6}$$

where $\bar{\theta}_i$ is the scaled parameter value that lies between 0 and 1, and $\theta_{i,\min} \leq \theta_i \leq \theta_{i,\max}$. Logarithmic scaling is used when the parameter range spans more than two orders of magnitude, while linear scaling is used otherwise. We then take n_s equidistant samples from the unit interval and evaluate the model outputs using the corresponding parameter values. The (j, i)-th element of the sensitivity matrix is then given by:

$$\boldsymbol{s}_{j,i} = \left(\frac{n_s}{\sum_{k=1}^{n_s} \tilde{y}_{j,k}} \right) \frac{1}{n_s - 1} \sum_{k=1}^{n_s - 1} \frac{\tilde{y}_{j,k+1} - \tilde{y}_{j,k}}{\bar{\theta}_{i,k+1} - \bar{\theta}_{i,k}}, \tag{3.7}$$

where $\tilde{y}_{j,k}$ denotes the j-th output evaluated using the k-th sample and $\bar{\theta}_{i,k}$ is the k-th sample of parameter i. Note that the sensitivity is normalized by the mean of the output and is therefore dimensionless. We use $n_s = 7$ samples in this chapter.

The above approach to calculating parameter sensitivities is motivated by the fact that the parameter perturbations during the analysis should be on par with those applied during parameter identification [302]. However, the successful application of such a method depends on the particular problem structure. Specifically, if perturbing a parameter can result in non-monotonic variations in the model output, then this analysis may break down. Nonetheless, the outputs of our model vary monotonically in most cases. Non-monotonic behavior is typically restricted to certain regions in a parameter interval, which can be effectively captured by increasing the number of samples. This method of sensitivity calculation allows us to better investigate the entire range of any given parameter rather than restricting the analysis to the immediate neighborhood of the nominal value.

While exploring the entire range of the parameter under consideration, the above

method keeps the other parameters fixed at their nominal values. Therefore, it still results in a local analysis. A global analysis is needed to inspect the parameter interaction, wherein all parameters are varied simultaneously to calculate the sensitivity results [303]. However, global analysis typically utilizes Monte-Carlo methods, which require evaluating the model at a large number of sampled points in the parameter space for convergence of the multi-dimensional integrals. Therefore, such analysis becomes computationally infeasible for large-scale models.

Given the shortcomings of local and global analyses, we seek an approach that strikes a balance between its validity region and the computational burden associated with it. Accordingly, we conduct an extended local analysis, wherein sensitivities are analyzed locally about several sampled points in the parameter space. This extended analysis yields a more global picture of the model sensitivities. Analogous methods have been used as efficient screening tools to narrow down the number of parameters [303]. Based on the result of this extended analysis, the following statistics can be calculated:

$$\bar{s}_i = \underset{k}{\text{med}} \ \|\boldsymbol{s}_i^k\|_2 \tag{3.8}$$

$$s_i^* = \sqrt{\underset{k}{\text{var}} \ \|\boldsymbol{s}_i^k\|_2}, \tag{3.9}$$

where $\boldsymbol{s}_i^k$ denotes the sensitivity vector for the i-th parameter evaluated at the k-th sample point in the parameter space, $\bar{s}_i$ is the median of sensitivity magnitudes for parameter i, and s_i^* denotes the corresponding standard deviation. We use the median, which is chosen due to its robustness to outliers, as an indicator of the overall parameter sensitivity. On the other hand, the standard deviation indicates how significantly a given parameter's sensitivity depends on other model parameters.

So far, we have focused on the magnitude of the sensitivity vectors. While this is an informative measure to quantify the impact of each parameter, it does not offer any insight into parameter interactions. For instance, if two parameters have large sensitivity

magnitudes but have similar effects on the outputs, they cannot be uniquely identified and the resulting parameter identification problem is ill-conditioned. Therefore, to quantify the similarity between two sensitivity vectors, $\boldsymbol{s}_i^k$ and $\boldsymbol{s}_j^k$ evaluated at sample point k in the parameter space, we use the following collinearity index [304, 305]:

$$\psi_{i,j}^k = \cos(\phi_{i,j}^k) = \frac{\left|\boldsymbol{s}_i^{k^\mathsf{T}} \boldsymbol{s}_j^k\right|}{\left\|\boldsymbol{s}_i^k\right\|_2 \left\|\boldsymbol{s}_j^k\right\|_2}, \tag{3.10}$$

where $\phi_{i,j}^k$ denotes the angle between the sensitivity vectors and the collinearity index, $\psi_{i,j}^k$, lies between 0 and 1, indicating orthogonal and collinear sensitivity directions, respectively.

It should be noted that if the pair of sensitivity vectors have small magnitudes, this collinearity index is of limited utility. In such a case, the parameters are non-influential and even if they are completely independent of one another, they cannot be effectively identified. Therefore, in our analysis in the next section, we only highlight the collinearity indices for the influential parameters as characterized by their high sensitivity magnitudes. Further note that the above definition of collinearity only allows for analyzing pairs of parameters. Therefore, we only use this definition to inspect parameter pairs and visualize the similarity between the effects of different parameter pairs without the need for coordinate transformations. However, when selecting parameter subsets for optimal identification results, we utilize more elaborate methods that allow for analyzing the linear dependence between a set of selected parameters (see Section 3.5).

3.3.3 Sampling of the Parameter Space for Extended Local Analysis

As mentioned previously, we conduct local sensitivity analysis about several points in the parameter space to obtain a more globally valid picture of the model sensitivities. Choosing the appropriate method to sample the parameter space is thus critical. Particularly,

our emphasis is on efficiently exploring the entire parameter space with the fewest number of points. This is especially important due the fact that the space under consideration is a 50-dimensional space. To this end, we map this high dimensional parameter space onto a unit hypercube using min-max scaling as described before. We then use the quasi-random Sobol sequence to efficiently sample the entire space [303]. The main advantage of this sequence is that it has low discrepancy, meaning that the gaps between the generated points are relatively uniform. Using MATLAB built-in function for the Sobol sequence, we generate 350 samples in the 50-dimensional unit hypercube.

One caveat of generating the points in the parameter space using the Sobol sequence is that it is physics-agnostic. Therefore, many of the parameter combinations might yield unreasonable results even if the ranges for each of the parameters were reasonably constrained. To remedy this, we use an initial screening step. This step entails simulating the model for the parameter values generated by the Sobol sequence using the 4 automotive operating conditions that were used for Stack A in Section 2.3.3. The experimental data obtained under these conditions with state-of-the-art MEA materials are then used to evaluate the Sobol sample. Particularly, for each sampled point in the parameter space, the model's voltage predictions are compared with the corresponding experimental measurements and the sample is accepted if:

$$\|\boldsymbol{e}_V\|_\infty = \|\boldsymbol{E}_{\text{model}} - \boldsymbol{E}_{\text{data}}\|_\infty \leq e_{\max},$$

where $\boldsymbol{E}_{\text{model}}$ and $\boldsymbol{E}_{\text{data}}$ are the model predictions and the available measurements, respectively, and $e_{\max}$ denotes the error threshold that is chosen to be 300mV. With this choice of threshold, 55 samples are accepted. Given the high dimensionality of the parameter space under consideration, this is a very small number of samples, which is constrained by our computational capabilities. Nonetheless, as is shown in Section 3.4, the particular structure of the model leads to reasonable convergence of the sensitivity results even with

this small number of samples.

3.3.4 Library of Operating Conditions

For a complete sensitivity and identifiability analysis, a variety of operating conditions must be considered. This is especially important, since some operating conditions may be more informative for parameter identification. Accordingly, we consider the entire space of potential operating conditions and use a full-factorial design with 3 levels to explore this space. In particular, we consider variations in the channel pressure (p_{ch}), the coolant inlet temperature ($T_{\text{cool,in}}$), the anode and cathode relative humidity (RH_{an}, RH_{ca}), and the hydrogen and oxygen stoichiometric ratio (St_{H_2}, St_{O_2}) as follows:

$$p_{\text{ch}} \in \{1.5,\ 2.5,\ 3.5\}\ [\text{bar}],$$

$$T_{\text{cool,in}} \in \{40,\ 60,\ 80\}\ [^{\circ}\text{C}],$$

$$RH_{\text{an}} \in \{30,\ 60,\ 90\}\ [-],$$

$$RH_{\text{ca}} \in \{30,\ 60,\ 90\}\ [-],$$

$$St_{H_2} \in \{1.5,\ 2.0,\ 2.5\}\ [-],$$

$$St_{O_2,\text{lcd}} \in \{1.5,\ 3.0,\ 4.5\}\ [-],$$

$$St_{O_2,\text{hcd}} \in \{1.5,\ 2.0,\ 2.5\}\ [-],$$

where the oxygen stoichiometry changes based on the load; $St_{O_2,\text{lcd}}$ values are used at current densities below 1 A/cm^2 and $St_{O_2,\text{hcd}}$ values are used at higher current densities. Moreover, a cross-pressure of 0.1 bar is maintained between the anode and cathode, *i.e.*, the anode pressure is 0.1 bar higher than the cathode. The current density values (i_{dens}) and the variations in the corresponding coolant temperature (ΔT_{cool}) are the same for all

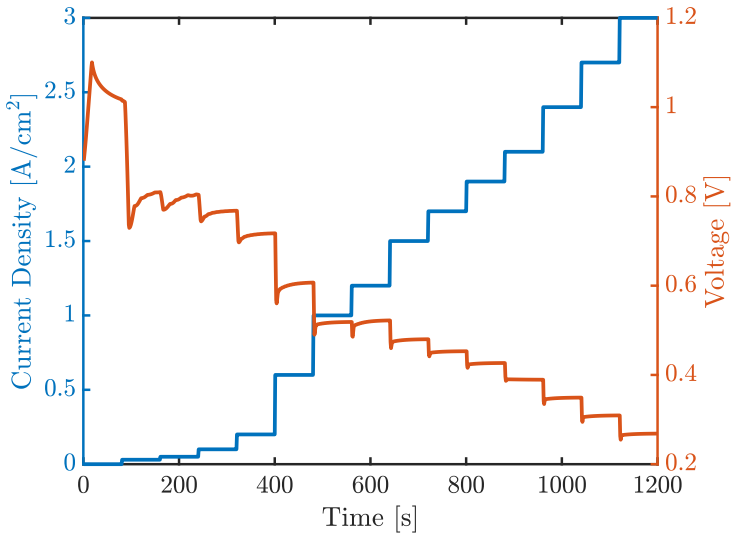

Figure 3.1: Current density profile used to collect data for sensitivity analysis and an example nominal voltage response.

operating conditions:

$$i_{\text{dens}} = [0.0,\ 0.03,\ 0.05,\ 0.1,\ 0.2,\ 0.6,\ 1.0,\ 1.2,\ 1.5,\ 1.7,\ 1.9\ 2.1,\ 2.4,\ 2.7,\ 3.0]\ [\text{A/cm}^2]$$

$$\Delta T_{\text{cool}} = [0.5,\ 0.5,\ 0.5,\ 1.0,\ 2.0,\ 5.0,\ 10,\ 10,\ 10,\ 10,\ 10,\ 12,\ 12,\ 12,\ 12]\ [^\circ\text{C}]$$

The 15 points chosen on the polarization curve can roughly be divided into the three regions typically known, namely, the kinetic, ohmic, and mass transport regions. Given the 6 variable factors that determine the operating conditions and the 3 levels chosen for each one, a full factorial design yields a total of 729 operating conditions. For each parameter value, the model is evaluated using all of these operating conditions to generate the required sensitivity data.

3.3.5 Data Collection Method

For any given set of parameter values and choice of operating conditions, the model is simulated starting from open-circuit voltage and the load is increased in a step manner to reach the highest current density at 3 A/cm^2 (see Fig. 3.1). Each load is maintained for 80 seconds and the data for the last 10 seconds are averaged for the quasi-steady state

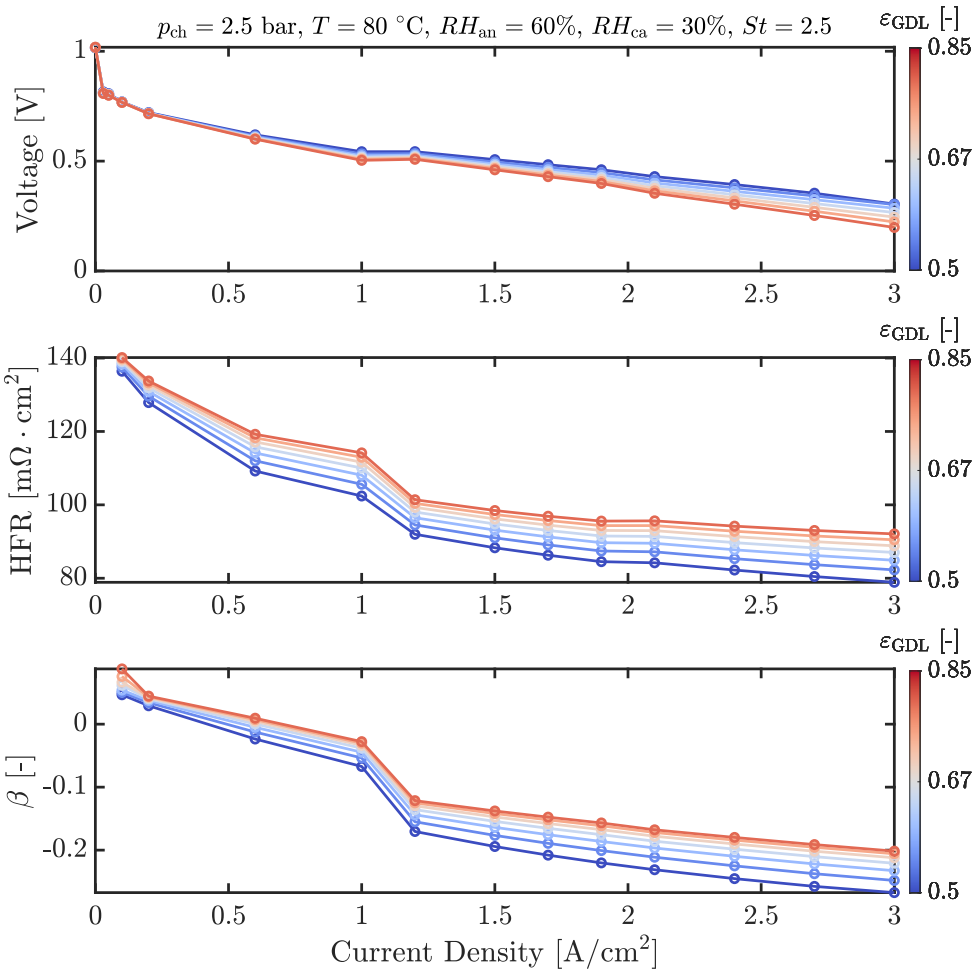

Figure 3.2: Example output variations to parameter perturbations. Three output predictions are considered in this chapter, namely, the cell voltage, high frequency resistance, and membrane water crossover. The outputs are shown for different GDL porosity values under one operating condition in the library.

values that are used for the sensitivity calculations. Here, we analyze sensitivity of 3 model outputs to the different parameters. These outputs include cell voltage, HFR, and membrane water crossover defined by equation 2.70 (see Fig. 3.2). The cell voltage data is collected for all 15 points on the polarization curve. However, only the last 10 data points for the HFR and water crossover are used corresponding to the ohmic and mass transport regions. The data at lower current densities are left out of the analysis due to considerable uncertainty in the corresponding measurements during actual experiments.

3.4 Sensitivity Analysis: Results and Discussion

3.4.1 Convergence of Sensitivity Results

An important consideration is the convergence of the sensitivity results given the small number of points chosen to sample a high-dimensional parameter space. In particular, the question is whether 55 samples are enough to claim the results are representative of the sensitivities throughout the parameter space. Since median and standard deviation are the statistics of choice for our analysis, Fig. 3.3 shows the corresponding results for increasing number of samples in the parameter space. As seen in the figure, while the statistics change as we increase the number of samples from 5 to 45, they remain relatively unchanged when the samples are increased to 55. We therefore conclude that given the particular structure of the problem, the small number of samples used here appears to be enough to obtain a valid representation of model sensitivities. Nonetheless, we acknowledge that further rigorous analysis is required to concretely determine the number of samples needed for convergence.

3.4.2 Single Measurement

We begin our analysis of the sensitivity results with individual model predictions, *i.e.*, we consider the voltage, HFR, and water crossover sensitivities separately. The results are shown in Fig. 3.4. The figure shows the results for all points in the parameter space and highlights the median values. Starting with the voltage sensitivity results in Fig. 3.4(a), we observe that the ORR kinetic parameters have highest sensitivities. Particularly, the ORR charge transfer coefficient (α_{ca}) has the highest sensitivity among all parameters followed by the ORR reference exchange current density ($i_{0,\mathrm{ca}}$). Other important parameters, as characterized by their high sensitivity magnitudes, are those that

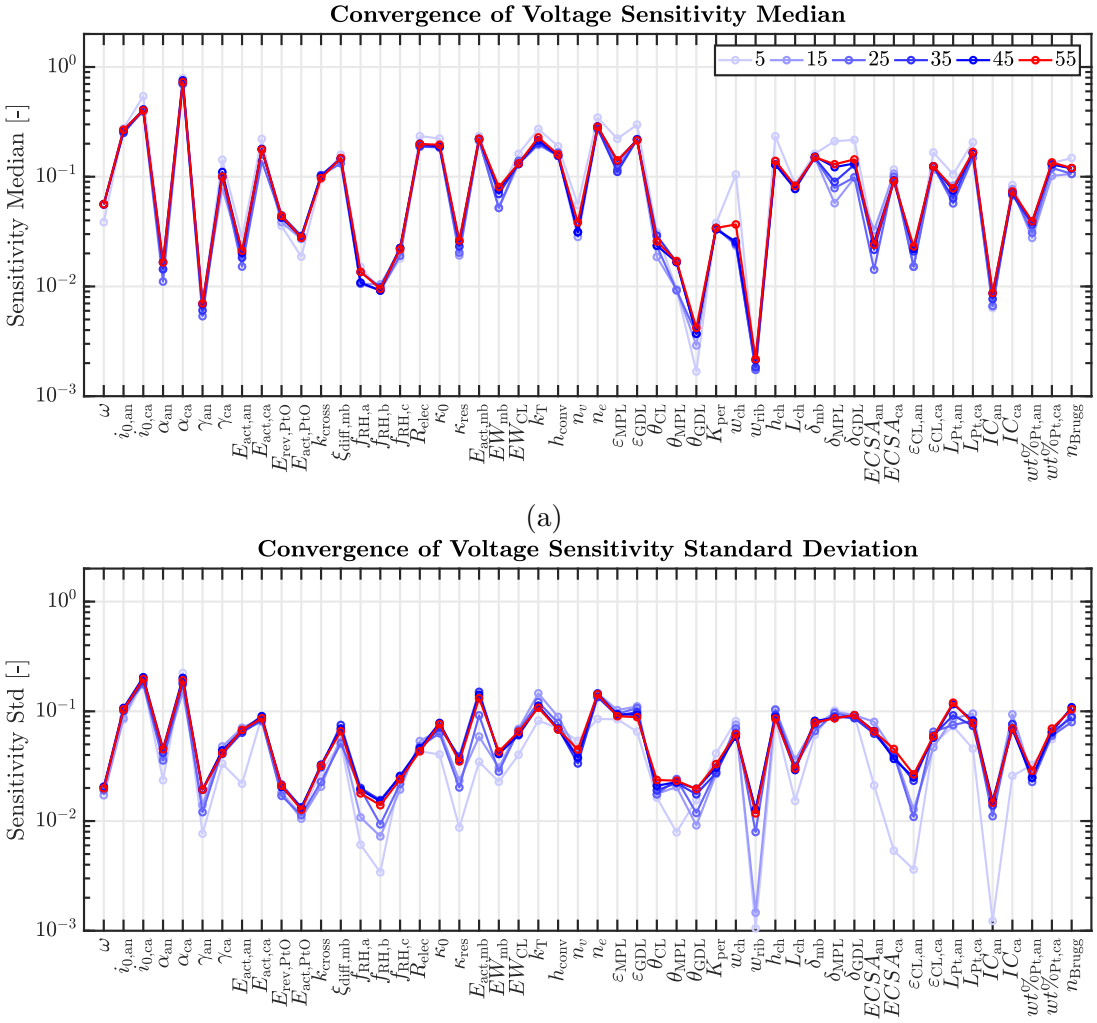

Figure 3.3: Convergence of sensitivity results with increasing number of samples in the parameter space. The (a) median, and (b) standard deviation of voltage sensitivities are calculated over multiple sampled points in the parameter space.

control the membrane transport properties. These include parameters impacting water transport through the membrane ($\xi_{\text{diff,mb}}$), as well as those affecting proton transport efficiency (R_{elec}, κ_0, $E_{\text{act,mb}}$), which influence the resistance of the cell. Finally, the parameters controlling the thermal (k_T, h_{conv}) and mass transport behavior of the cell (n_e, ε_{MPL}, ε_{GDL}) also demonstrate relatively high voltage sensitivities. On the other hand, some of the parameters related to hydrophobicity of the porous layers (θ_{MPL}, θ_{GDL}) and some geometrical features (w_{rib}) show negligible sensitivities.

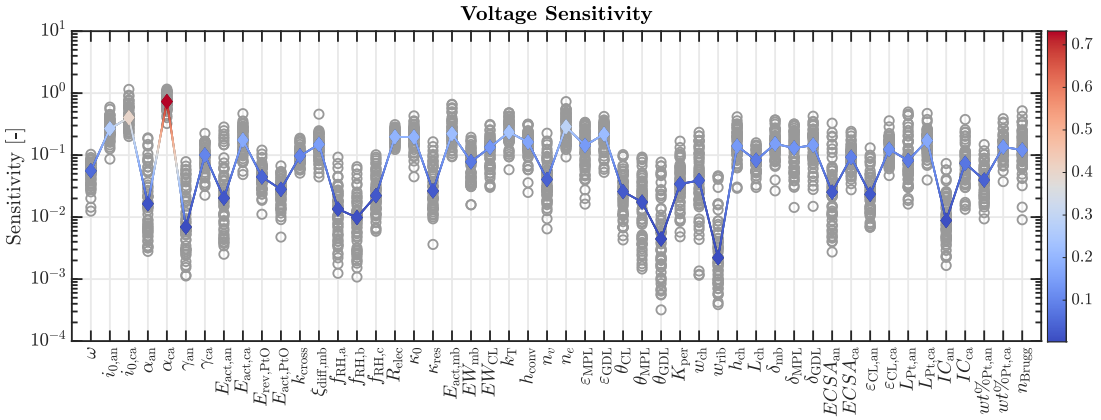

(a)

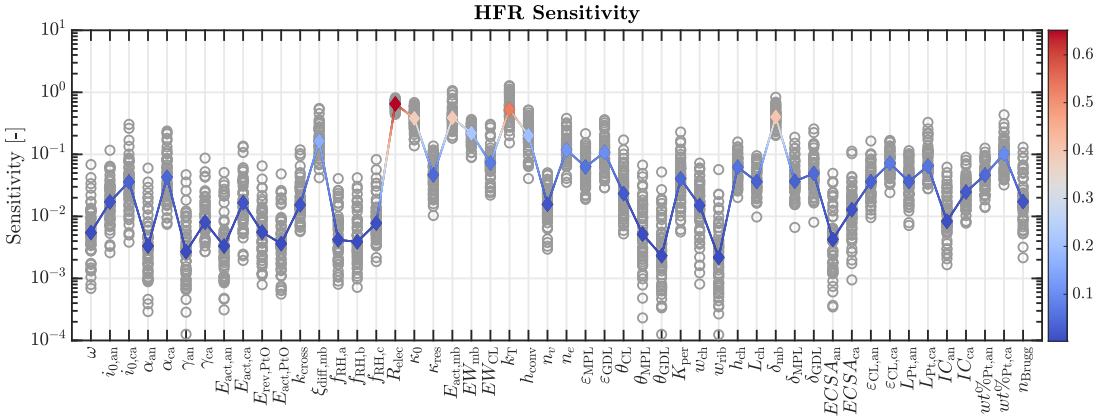

(b)

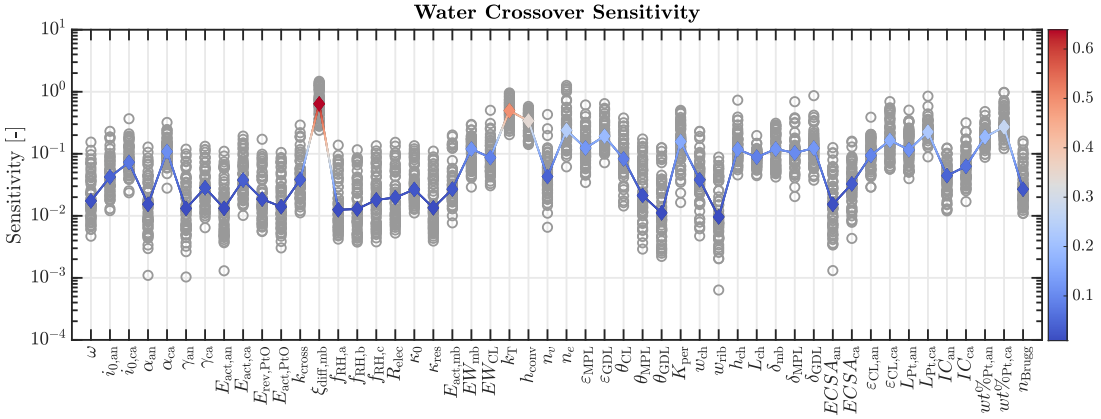

(c)

Figure 3.4: Parameter sensitivities for individual output predictions: (a) voltage, (b) high frequency resistance, and (c) membrane water crossover. Results for all points in the parameter space are shown with gray circles. The sensitivity medians are also shown, where the line color changes with the sensitivity value.

At this point, it is critical to emphasize that all these sensitivity results depend on the underlying model and are only useful when interpreted with the model structure in mind. This makes interpretation of the results a crucial step in the overall analysis. For example, a high sensitivity value for a given parameter does not necessarily mean that the parameter is also physically important. It only indicates that the particular structure of the model with all the underlying assumptions and the ranges considered for the parameter values renders that particular parameter sensitive. The same can be said of insensitive parameters, where their insensitivity is not always indicative of their lack of importance in a physical setting. This point cannot be overemphasized, as sensitivity results are commonly misinterpreted in the literature. For instance, Vetter et al. [284] used their sensitivity results as a corroborating evidence that contact resistances are important in fuel cell modeling. While we do not contest this particular claim, we note that these sensitivity results were generated with a model that promotes the importance of contact resistances. Therefore, making broad conclusions about the physical importance of a parameter founded on model-based sensitivities is not always warranted. Accordingly, we believe that these results are best used to inspect and enhance the model in conjunction with experiments and expert knowledge. For instance, if the results indicate that the measurements should be insensitive to a particular parameter, but the actual experimental data or expert opinion indicate otherwise, this can be used as a basis to revisit the model assumptions and make the necessary changes to ensure the model sensitivities match those of the physical system.

Following the above arguments, we note that some of the insensitivities captured in our results are artifacts of the modeling assumptions. Examples of these include the contact angle of the porous layers and the landing width. The literature has established the importance of porous layer water retention capabilities, which are affected by the layer's hydrophobicity [306–309]. The lack of voltage sensitivity in our results mostly stems from the fact that these properties directly affect liquid water distribution in the

porous layers, which does not have an appreciable impact on the voltage predictions under dry conditions. However, our results do not show significant voltage sensitivity to the contact angles even under wetter conditions. This insensitivity indicates that the continuum Leverett approach used is not sufficient to capture the experimental variations with only one contact angle as the variable [310]. Therefore, if the application at hand requires more accurate description of the two-phase flow phenomena, model enhancement is required. Such improvements may also take the form of reparameterizing the sub-models. The same can be said of the land width, where experimental evidence and more detailed models clearly show the importance of this factor [89,311,312]. The insensitivity observed in our results is due to the fact that the version of the model (P2D) used for sensitivity analysis does not capture the in-plane transport phenomena, thereby leaving the landing width as a non-influential parameter.

The HFR sensitivities are shown in Fig. 3.4(b), where fewer parameters have high sensitivity compared to the voltage. In particular, mostly those parameters that directly affect the cell resistance are deemed to be sensitive (R_{elec}, κ_0, $E_{\text{act,mb}}$, δ_{mb}). Other notably sensitive parameters are those that control membrane water crossover ($\xi_{\text{diff,mb}}$) and heat transport across the cell (k_T, h_{conv}). Particularly, the thermal conductivity of the cell layers appears to be one of the most sensitive parameters (k_T). This can be attributed to the fact that heat transport can profoundly impact the membrane water content, thereby affecting the cell resistance.

Lastly, the membrane water crossover sensitivities are shown in Fig. 3.4(c), where the scaling factor for membrane water diffusivity ($\xi_{\text{diff,mb}}$) and the thermal conductivity of the cell layers (k_T) are found to be the most influential parameters. The high sensitivity of water crossover to $\xi_{\text{diff,mb}}$ is expected, as this parameter directly controls water diffusivity in the membrane. On the other hand, the high sensitivity of k_T may seem counter-intuitive. However, the thermal balance of the cell is known to contribute significantly to the overall water balance across the MEA [89,313–315] and this result indicates that the

model indeed captures such behavior.

Considering all of the 3 output sensitivities at the same time, the voltage seems to be the richest signal that is affected by many of the model parameters. This represents an opportunity for parameter identification, as variations in the model parameters can be observed in the measured voltage. On the other hand, this also amounts to an important challenge, as many parameters impact voltage simultaneously and their effects are typically difficult to deconvolute. Fortunately, the other output predictions demonstrate a rather selective sensitivity to parameter variations, where only a few parameters affect the HFR and water crossover predictions. Therefore, these additional output predictions can be used in conjunction with voltage to better deconvolute the impact of different parameters for successful identification. This can be viewed as common knowledge, as additional measurements are typically known to help with parameter identification. Nonetheless, the methods presented in this dissertation can be used to quantify how much utility there is in adding any particular measurement and determine which of the model parameters can be identified with acceptable precision given the available measurements.

The relative independence of sensitivity vectors is another important measure that must be taken into account. Accordingly, the collinearity indices based on the 3 output predictions and defined by equation 3.10 are shown in Figs. 3.5-3.7. The figures are generated based on local sensitivity data and only highlight the pairs, where the magnitude of the sensitivity vector for either parameter is non-negligible and the angle between the corresponding sensitivity vectors is less than 45°.

Starting with the collinearity between voltage sensitivity vectors in Fig. 3.5, we observe that many kinetic parameters have similar impacts on the voltage predictions. Specifically, the ORR reference exchange current density ($i_{0,\mathrm{ca}}$) and charge transfer coefficient (α_{ca}) are seen to have a large collinearity index. This is an expected result, as these two parameters have very similar effects on the voltage predictions determined by the BV model. Other highly collinear pairs include (κ_0, $E_{\mathrm{act,mb}}$) and (δ_{mb}, $E_{\mathrm{act,mb}}$). Again, these

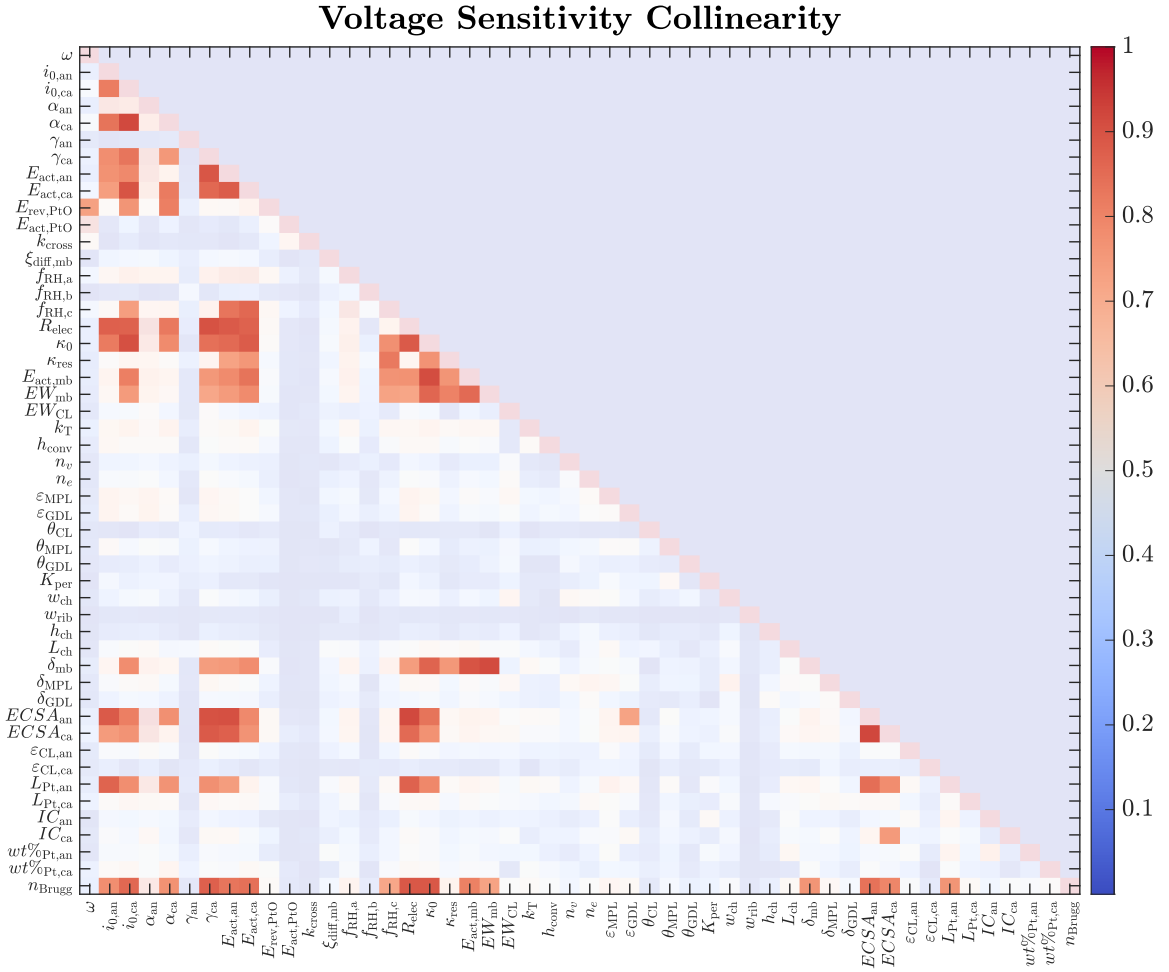

Figure 3.5: Collinearity indices for the voltage sensitivity vectors. The off-diagonal values that are larger than 0.707 are highlighted, as they indicate an acute angle of less than 45° between the corresponding sensitivity vectors, which leads to considerable similarity between the corresponding parameter effects.

results may be expected, as all these three parameters impact the membrane resistance, thereby influencing the ohmic voltage loss.

In addition to these expected results, we also observe some counter-intuitive behavior, where, for example, some of the ohmic parameters are found to be highly correlated with kinetic parameters as measured by their impact on voltage predictions. Particularly, the collinearity index for the (κ_0, $i_{0,\mathrm{ca}}$) pair is greater than 0.9, while it is about 0.77 for the (κ_0, $ECSA_{\mathrm{ca}}$) pair. This does not indicate that these parameter pairs are physically related to each other; rather, this means that the particular model structure may not

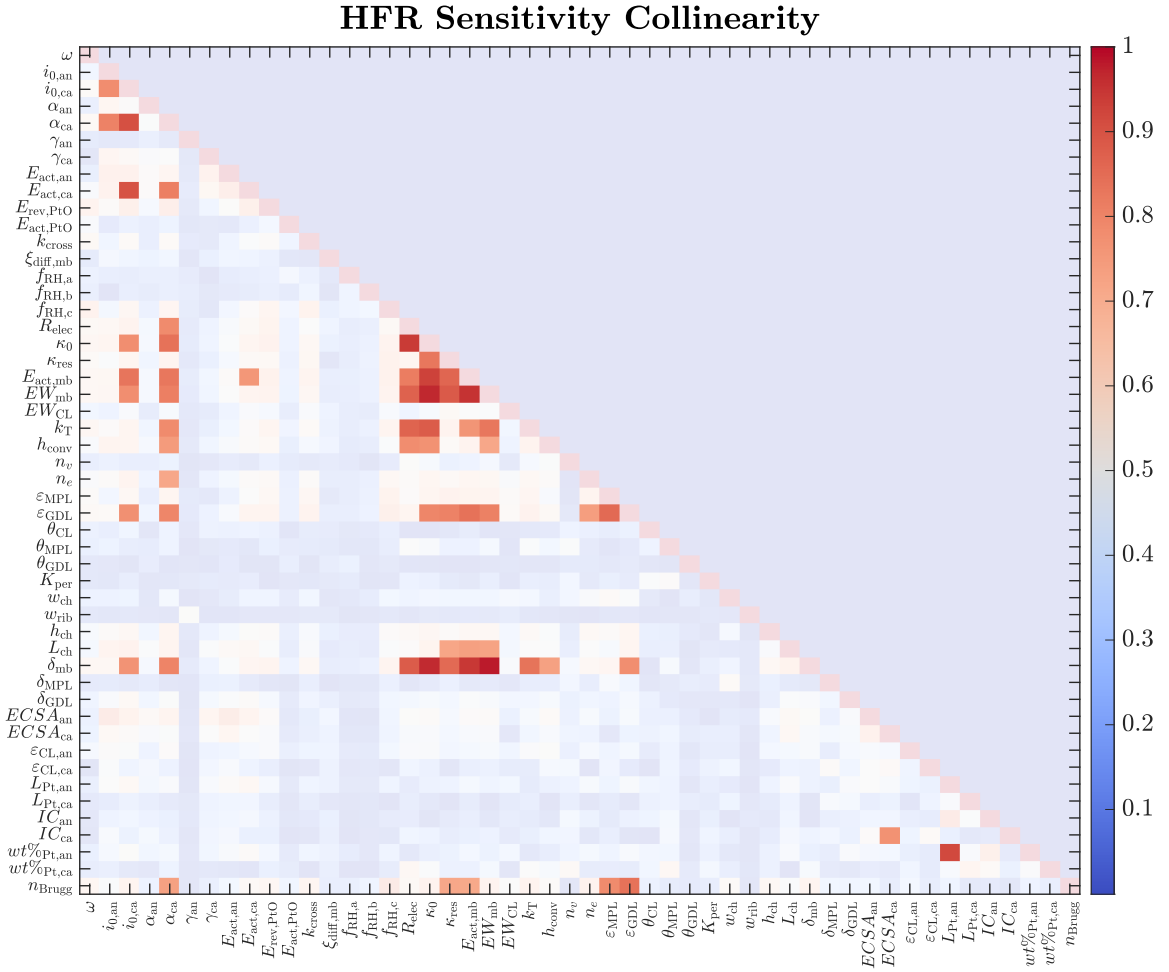

Figure 3.6: Collinearity of the resistance sensitivity vectors. The off-diagonal values that are larger than 0.707 are highlighted, as they indicate an acute angle of less than 45° between the corresponding sensitivity vectors, which leads to considerable similarity between the corresponding parameter effects.

allow for distinguishing their impact from one another using only voltage data. In other words, the same polarization curve may be obtained by tweaking either of the parameters in such correlated pairs. If the experimental results show a clearly distinguishable impact of such parameter pairs on the voltage measurements, then this result would point to the deficiency of the model in capturing this behavior and calls for model refinement.

Moving on to the collinearity indices based on HFR sensitivities as shown in Fig. 3.6, we observe that almost all of the parameters that were determined to impact HFR in Fig. 3.4(b) appear to be largely collinear when considered in pairs. Therefore, HFR

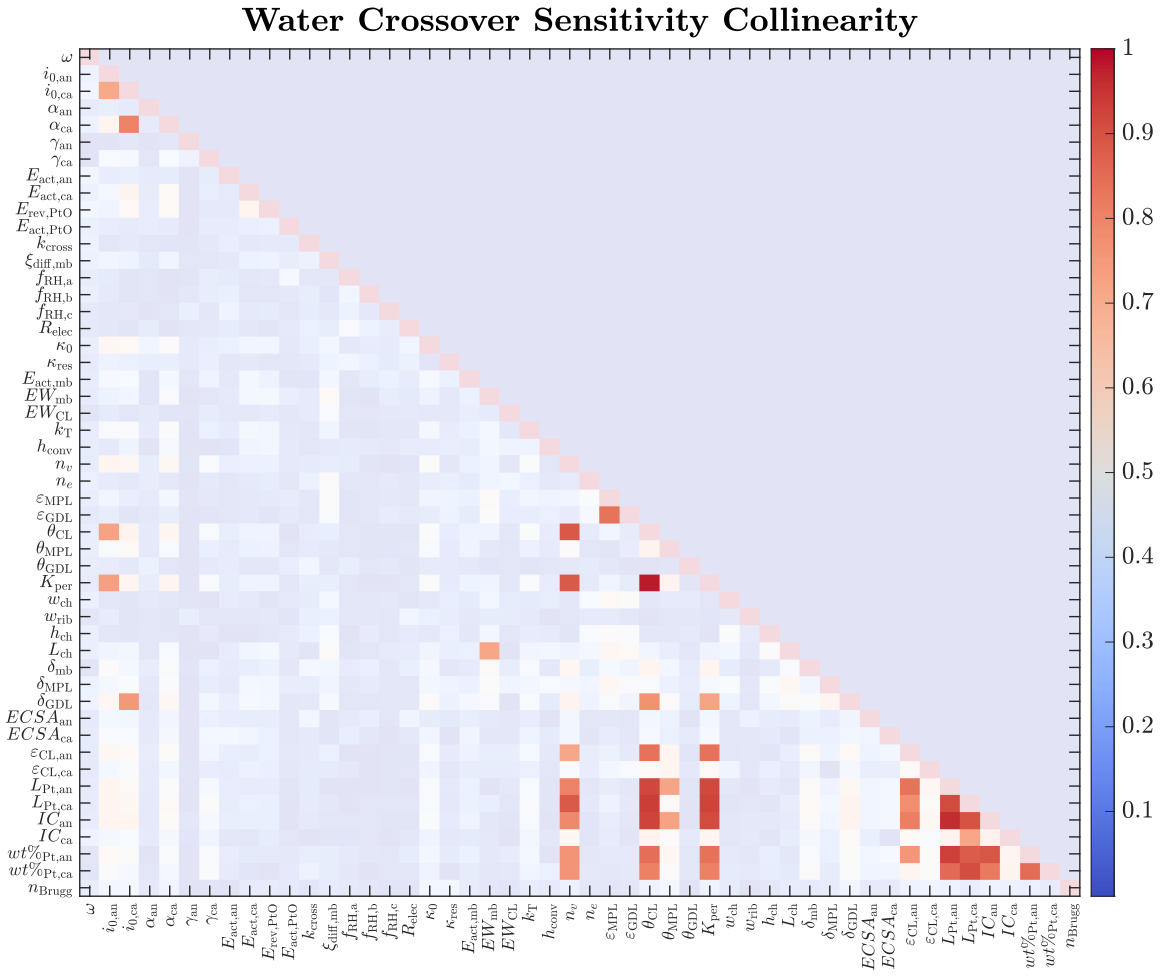

Figure 3.7: Collinearity of the water crossover sensitivity vectors. The off-diagonal values that are larger than 0.707 are highlighted, as they indicate an acute angle of less than 45° between the corresponding sensitivity vectors, which leads to considerable similarity between the corresponding parameter effects.

measurements alone may not be sufficient to identify all of these parameters. As for membrane water crossover sensitivities, Fig. 3.7 illustrates that many of the catalyst layer structural properties impact water crossover predictions in the same manner. For example, the anode catalyst layer Pt loading ($L_{\mathrm{Pt,an}}$) and its ionomer to carbon ratio (IC_{an}) have a collinearity index of 0.96. This is due to the fact that in our model construction, they both affect the porosity of the catalyst layer; increasing either the Pt loading or the ionomer to carbon ratio reduces the porosity. Since porosity affects the water retention capabilities of the catalyst layer, which is adjacent to the membrane, variation in either parameter

lead to similar impacts on the membrane water crossover predictions.

Finally, we point out that the results presented in Figs. 3.5-3.7 are generated using all operating conditions from the library discussed earlier. Therefore, even if the results indicate high similarity between two parameters, there might still be an opportunity of decorrelating their sensitivities by judiciously selecting the operating conditions. This is an important motivation for the optimal experimental design that is presented in the Chapter 4.

3.4.3 Multiple Measurements

Having presented sensitivity results for different outputs individually, we now turn our attention to the case where multiple output predictions are considered at the same time. Here we consider three cases. In the first two cases, voltage prediction is considered along with either the HFR or membrane water crossover. For the last case, all three outputs are examined simultaneously. For these combined prediction cases, the sensitivity vectors are obtained by simply concatenating the corresponding sensitivity vectors for each individual output prediction. Therefore, the sensitivities to different parameters inherit the main characteristics of the individual output predictions as seen in Fig. 3.8. Particularly, we observe that adding HFR prediction to voltage results in increased sensitivity of the resistance parameters, such as κ_0 and R_{elec}, while the sensitivity of the important kinetic parameters, such as α_{ca}, remain high. Similarly, including membrane water crossover prediction alongside voltage promotes the parameters that determine water balance across the MEA, such as $\xi_{\text{diff,mb}}$. Lastly, considering all three output predictions together promotes the sensitivity of parameters that impact each output individually.

The above discussion shows that adding measurements can make more parameters sensitive enough for the purpose of identification. However, in addition to having an observable impact on the output predictions, the effect of parameters should be uniquely

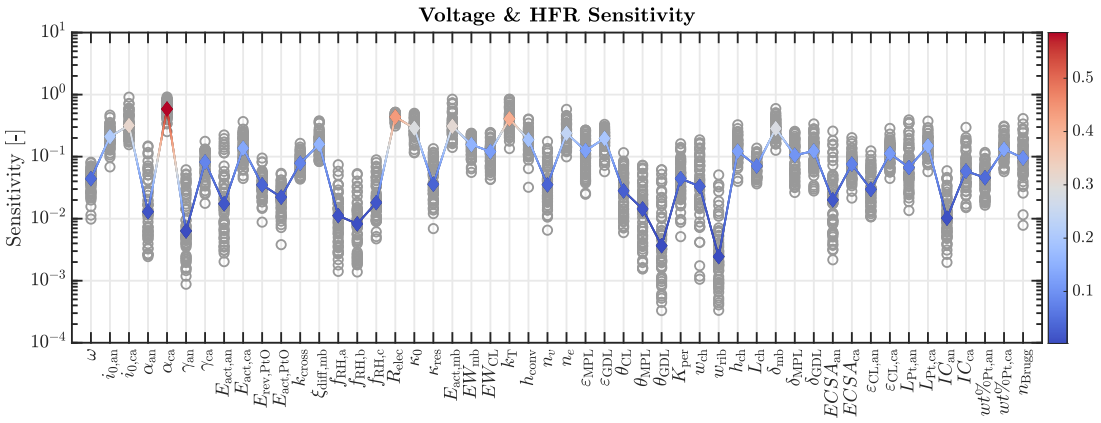

(a)

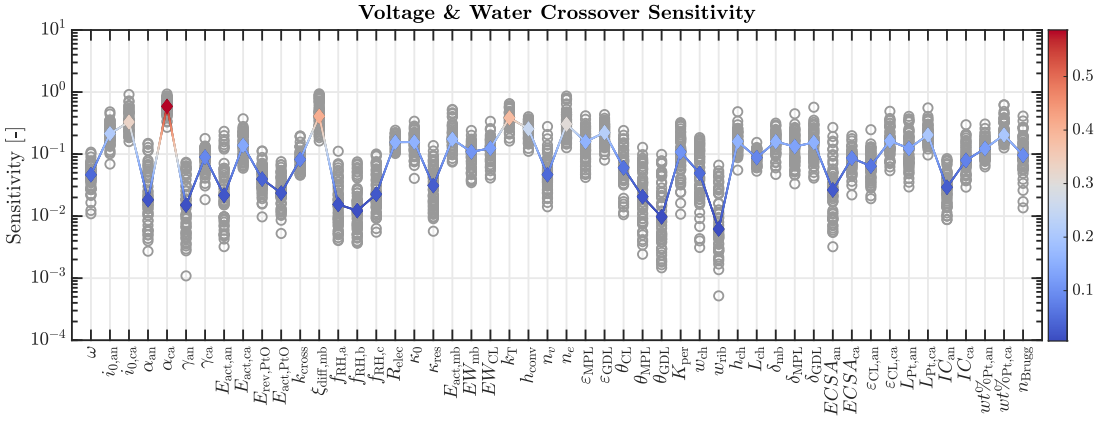

(b)

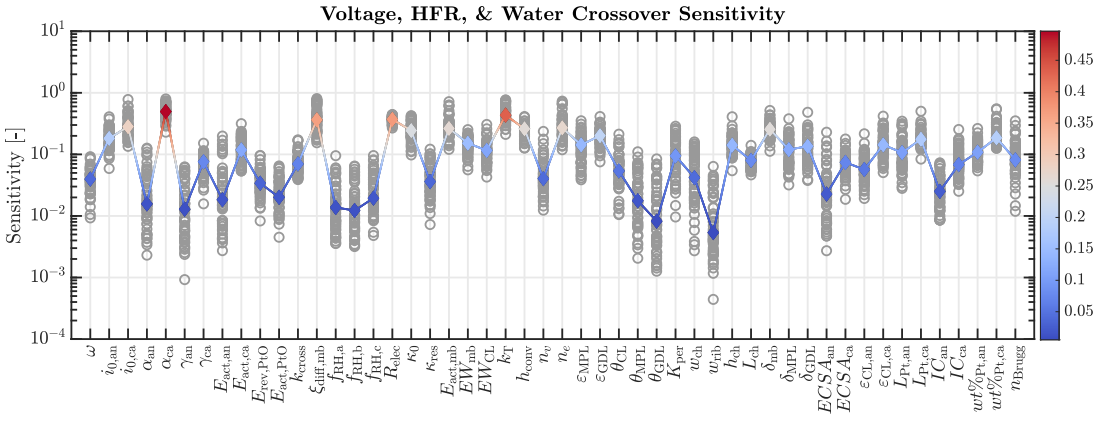

(c)

Figure 3.8: Parameter sensitivities for multiple output predictions: (a) voltage and HFR, (b) voltage and membrane water crossover, and (c) voltage, HFR, and membrane water crossover. Results for all points in the parameter space are shown with gray circles. The sensitivity medians are also shown, where the line color changes with the sensitivity value.

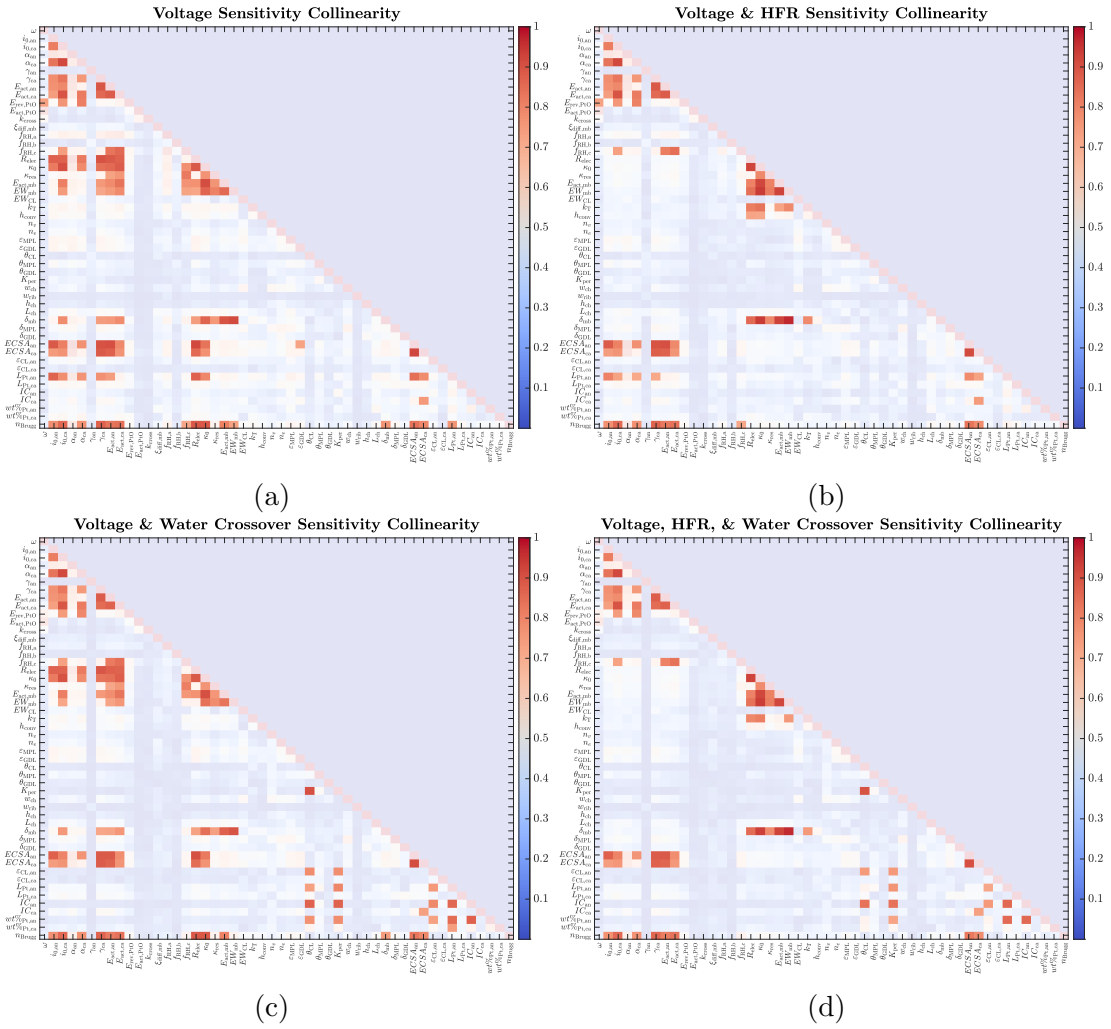

Figure 3.9: Collinearity of sensitivity vectors based on single and multiple predicted outputs: using (a) voltage, (b) voltage and HFR, (c) voltage and water crossover, and (d) voltage, HFR, and water crossover as the predicted outputs.

distinguishable from one another for practical identifiability. Therefore, the role of additional measurements in deconvoluting parameter effects should be investigated. Accordingly, Fig. 3.9 shows how the collinearity indices between pairs of sensitivity vectors change as additional output predictions are considered. We observe that adding measurements generally tends to decorrelate parameter effects. For instance, using only voltage data (Fig. 3.9 (a)) can lead to correlations between some of the ohmic and kinetic parameters (*e.g.*, κ_0 and $i_{0,\text{ca}}$ have a collinearity index of $\psi = 0.9$). When HFR is used along with voltage (Fig. 3.9 (b)), these correlations are significantly reduced (*e.g.*, $\psi = 0.55$ for

κ_0 and $i_{0,\mathrm{ca}}$). Adding the membrane water crossover to the measurements further decorrelates the effects of certain parameters. For example, the collinearity index is $\psi = 0.71$ for $L_{\mathrm{Pt,an}}$ and α_{ca} with voltage and HFR measurements (Fig. 3.9 (b)), but reduces to $\psi = 0.41$ when membrane water crossover is considered (Fig. 3.9 (d)).

The above analysis shows the magnitude of each parameter's impact on the model predictions and its degree of independence from other parameters as additional measurements are considered. Notably, we've seen how adding measurements can promote identifiability by increasing the sensitivity while decorrelating the effect of different parameters. While this seems rather intuitive, the significance of these results lies in their quantification of the parameter sensitivities and their interactions. The methods presented herein can thus be used to focus the resources on identification of most crucial parameters and help with effective model parameterization. This is further demonstrated in Chapter 4.

3.4.4 Impact of Operating Conditions

So far, our analysis has been based on data generated using all of the operating conditions in the library. However, it is conceivable that certain operating conditions can better reveal the impact of a particular parameter and improve its identifiability. To further demonstrate this, Fig. 3.10 shows how the sensitivity of model parameters can change with the operating condition. Particularly, voltage sensitivity to the porous layer thickness is shown in Fig. 3.10(a) for different operating conditions in the library, where considerable variations in voltage sensitivity are observed as the operating conditions are varied. One main trend that is highlighted in the figure is the decreasing sensitivity with increased cathode flow rate. This is an expected result as the layer's thickness mostly impacts mass transport losses, which are heightened at lower stoichiometric ratios.

To further demonstrate the impact of operating conditions, Fig. 3.10(b) shows the ordered voltage sensitivities for 5 different parameters. Particularly, the sensitivity at

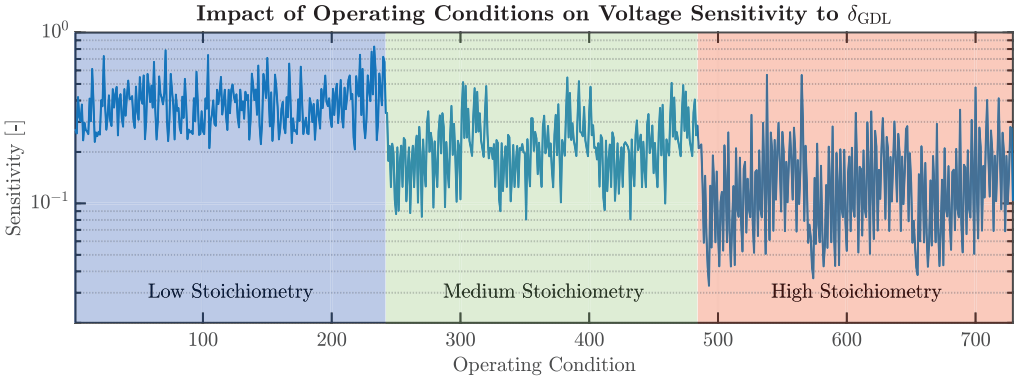

(a)

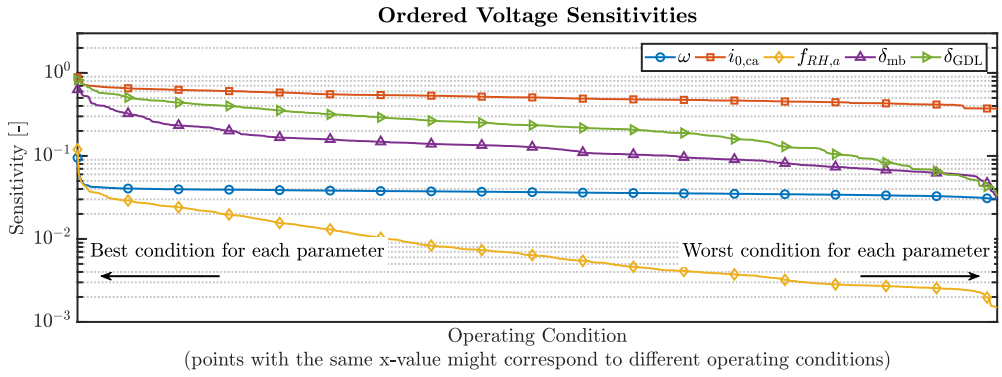

(b)

Figure 3.10: Impact of operating conditions on voltage sensitivities: (a) variations in voltage sensitivity to δ_{GDL} with changes in operating conditions, and (b) voltage sensitivities for multiple parameters shown in a descending order from the best to worst operating condition as measured by the corresponding parameter sensitivity.

each operating condition is calculated. The results are then ordered in a decreasing fashion such that the first point on each line indicates the best operating condition at which the highest sensitivity is obtained for the parameter of interest. This ordering is done to better illustrate the effect of operating conditions on parameter sensitivities. The figure clearly shows how operating conditions can increase or diminish the sensitivity of a parameter. We can also observe that the degree to which the operating conditions affect the sensitivity varies with the parameter. For instance, the sensitivities of $f_{\mathrm{RH,a}}$, δ_{mb}, and δ_{GDL} show considerable dependence on the operating conditions as they can vary by almost two orders of magnitude based on the condition. The sensitivity of other parameters on the other hand, may demonstrate moderate to negligible dependence on

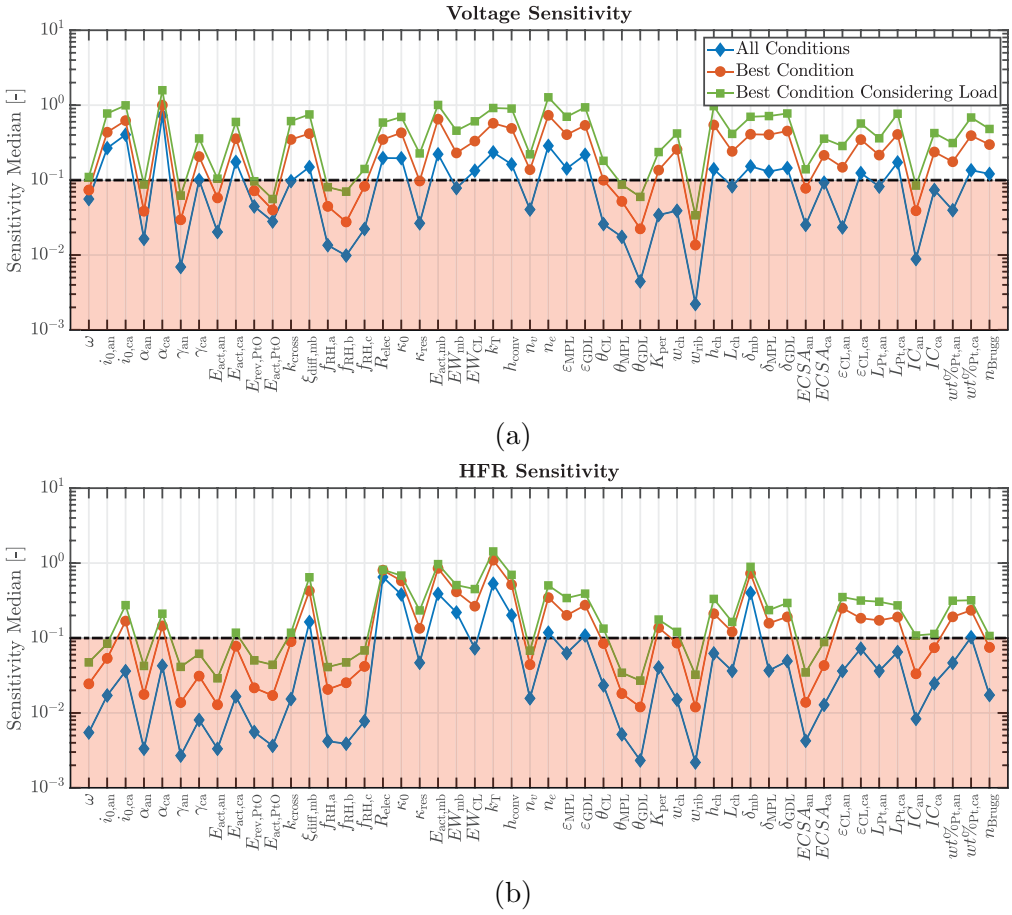

Figure 3.11: Variations in (a) voltage and (b) HFR sensitivities as the best operating conditions are used.

the operating conditions, as is the case for ω and $i_{0,\mathrm{ca}}$.

The observable impact of operating conditions on parameter sensitivities motivates a closer look at the sensitivity results. Specifically, the question is how much would a parameter sensitivity increase if only the best operating condition is used to calculate it rather than using all of the operating conditions. An interesting aspect of this is whether a parameter that is deemed insignificant as measured by its average sensitivity at all operating conditions, can have a discernible impact under particular conditions. This is illustrated in Fig. 3.11, where the voltage and HFR sensitivities based on three calculations are shown: (1) using all operating conditions, (2) using only the operating condition that results in highest parameter sensitivity, and (3) using the most sensitive loading

condition of the best operating condition. For the third case, the voltage and HFR data at each condition are characterized based on the load region (kinetic, ohmic, and mass transport regions). Only data from the most sensitive region are then used to calculate the sensitivity. The figure shows that for most parameters, considering only one particular operating condition rather than all conditions in the library significantly enhances the sensitivity. Most notably, if we set a sensitivity threshold of 0.1 for identifiability, as shown in the figure, we observe that a number of parameters that are unidentifiable considering all operating conditions, are indeed identifiable at specifically chosen conditions. The channel width (w_{ch}) and the residual ionomer conductivity (κ_{res}) are examples of such parameters (see Fig. 3.11(a)). Such discernible impact of operating conditions on parameter identifiability motivates the need for optimal experimental design that is addressed in Chapter 4.

3.5 Identifiability Analysis and Parameter Subset Selection

Using the sensitivity results obtained in the previous section, we now turn our attention to identifiability analysis. Recall that a parameter is identifiable if (1) it has an observable impact on the model predictions for which measurements are available, and (2) its impact is unique in the sense that the same behavior cannot be reproduced by variations in other parameters. To further analyze identifiability, we consider a least-squares setting. Particularly, assume that $\boldsymbol{y}$ is the vector of available measurements. We further assume, for the purpose of discussion, that there exists at least one set of parameter values for which our model predictions, $\tilde{\boldsymbol{y}}$, exactly match the measurements. We denote such a

parameter set by $\boldsymbol{\theta}^*$. Therefore, we have:

$$\boldsymbol{y} = \tilde{\boldsymbol{y}}_{\boldsymbol{\theta}^*} = \boldsymbol{h}(\boldsymbol{x}, \boldsymbol{z}, \boldsymbol{u}, \boldsymbol{\theta}^*), \tag{3.11}$$

where the dependence of $\tilde{\boldsymbol{y}}$ on the parameter set is made explicit. The question is whether $\boldsymbol{\theta}^*$ is unique and how it can be found. To answer this, we formulate a nonlinear least-squares problem, which minimizes the following cost:

$$\chi_{\text{LS}}(\boldsymbol{\theta}) = \sum_{i=1}^{N} \left(y_i - \tilde{y}_{\boldsymbol{\theta},i}\right)^2, \tag{3.12}$$

where N is the number of available data points. By restricting our analysis to the immediate neighborhood of $\boldsymbol{\theta}^*$, we can use Taylor expansion to evaluate $\tilde{\boldsymbol{y}}_{\boldsymbol{\theta}}$:

$$\tilde{\boldsymbol{y}}_{\boldsymbol{\theta}} \approx \tilde{\boldsymbol{y}}_{\boldsymbol{\theta}^*} + \frac{\partial \tilde{\boldsymbol{y}}}{\partial \boldsymbol{\theta}}(\boldsymbol{\theta} - \boldsymbol{\theta}^*), \tag{3.13}$$

where the higher order terms are neglected. Plugging equation 3.13 into 3.12 and using 3.11, we have:

$$\chi_{\text{LS}}(\boldsymbol{\theta}) \approx \sum_{i=1}^{N} \left[\frac{\partial \tilde{y}_i}{\partial \boldsymbol{\theta}}(\boldsymbol{\theta} - \boldsymbol{\theta}^*)\right]^2 = (\mathbf{S}\boldsymbol{\Delta\theta})^{\mathsf{T}}(\mathbf{S}\boldsymbol{\Delta\theta}), \tag{3.14}$$

where $\Delta\boldsymbol{\theta} = \boldsymbol{\theta} - \boldsymbol{\theta}^*$ and the definition of the sensitivity matrix (equation 3.4) is used to write the last equality. This last equation indicates that the optimal solution is obtained when $(\mathbf{S}^{\mathsf{T}}\mathbf{S})\boldsymbol{\Delta\theta} = \mathbf{0}$. If the Hessian ($\mathbf{H} = \mathbf{S}^{\mathsf{T}}\mathbf{S}$) has full rank, then $\Delta\boldsymbol{\theta} = 0$ is the unique solution, which indicates that $\boldsymbol{\theta} = \boldsymbol{\theta}^*$, meaning that the parameters are locally identifiable at $\boldsymbol{\theta}^*$. In case the Hessian is rank deficient, there is an infinite number of solutions that yield a zero least-squares cost (belonging to the null space of $\mathbf{S}^{\mathsf{T}}\mathbf{S}$). This means that the parameter identification problem does not have a unique solution. Note that rank-deficiency of the Hessian captures both requirements of identifiability; in theory, a zero sensitivity vector or one that is linearly dependent on other sensitivity vectors yields a rank deficient Hessian. In practice, this derivation indicates that a poorly conditioned

Hessain matrix, which can be caused by small sensitivity magnitudes or highly dependent sensitivity vectors, can hinder parameter identifiability. Specifically, the condition number of the sensitivity matrix is defined as:

$$\kappa_{\mathbf{H}} = \frac{\lambda_{\max}(\mathbf{H})}{\lambda_{\min}(\mathbf{H})}, \tag{3.15}$$

where $\lambda_{\max}$ and $\lambda_{\min}$ denote the largest and smallest eigenvalues of the Hessian, respectively. The significance of the condition number and, more generally, the eigenvalues of the Hessian, lies in the fact that they control the rate of reduction in the least-squares cost in the direction of each eigenvector: a large (small) eigenvalue means a rapidly (slowly) decaying cost along the direction of the corresponding eigenvector.

Since the identifiability of the model parameters depend on the eigenvalues of the Hessian, the spectra of these eigenvalues are shown in Fig. 3.12 for sensitivity matrices obtained at several points in the parameter space. The figure shows an interesting spectra, wherein, the eigenvalues are evenly spread over many orders of magnitude. The literature refers to this phenomenon as "sloppiness" of the model [316–318]. It has been suggested that accurate parameter identification is impossible under such circumstances and the focus should instead be on predictive behavior of the model [317]. This assertion has since been challenged in the literature and it has become clear that sloppiness and identifiability are two very distinct concepts and neither implies the other [319–321]. Most recently, Chis et al. have even argued that sloppiness is not a useful concept and the focus should be on parameter identifiability [319]. Nonetheless, sloppiness can have implications for identifiability: it is more difficult to distinguish the identifiable parameters from the unidentifiable ones in a sloppy model. Particularly, note that the eigenvalue spectra in Fig. 3.12 show no discernible gap between the large and small eigenvalues. Therefore, the influential eigenvectors cannot be easily selected.

How can one address this difficulty due to model sloppiness? We believe that tools

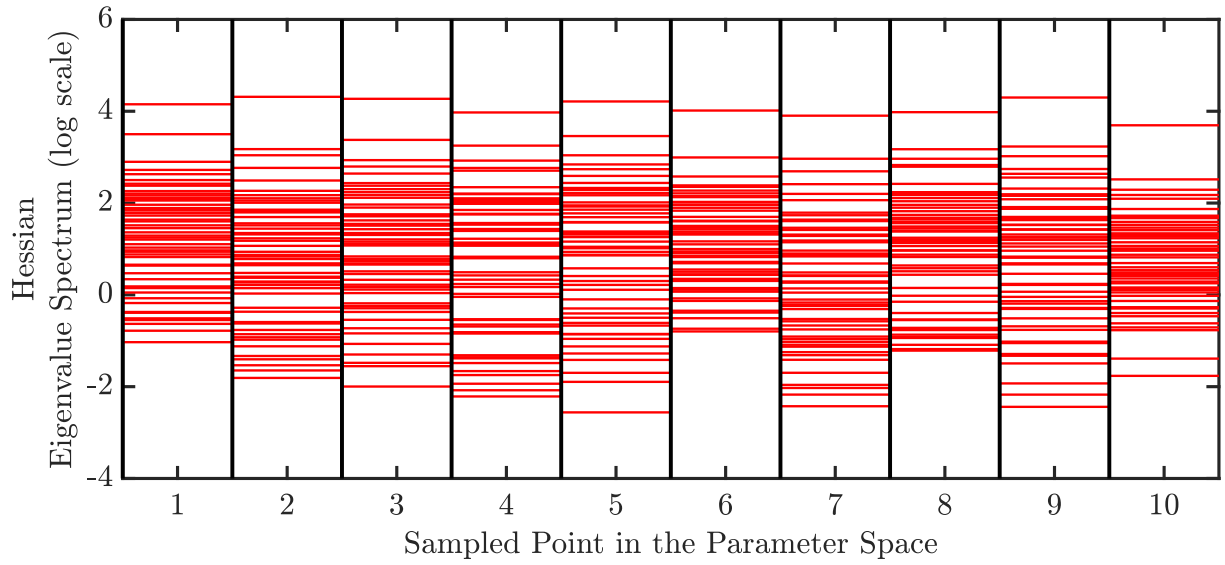

Figure 3.12: Sloppiness of the eigenvalue spectra of the least squares cost Hessian.

from the literature on identifiability analysis remain relevant. In particular, we focus on selecting subsets of parameters that can be identified using the available measurements. To determine whether the selected subset is identifiable, we use the metric proposed by Brun et al. [322], which amounts to a threshold on the smallest eigenvalue of the resulting Hessian:

$$\lambda_{\min}(\mathbf{H_I}) \geq \bar{\lambda}_{\text{th}},$$

where $\mathbf{H_I}$ is the Hessian matrix obtained from the sensitivities of the selected parameters and $\bar{\lambda}_{\text{th}}$ is the chosen threshold. Recall that the smallest eigenvalue controls the slowest rate of decay of the least-squares cost. By ensuring that the minimum eigenvalue is greater than some threshold, we are controlling the decay rate of the cost.

Taking the eigenvalue threshold into account, we rank parameters with two approaches: (1) based on the sensitivity magnitude and (2) using the orthogonal method [323]. The orthogonal method uses the Gram-Schmidt orthogonalization procedure and selects the parameter with the largest sensitivity first. At each following step of the algorithm, the component of each parameter sensitivity that is orthogonal to the sensitivity vectors of the

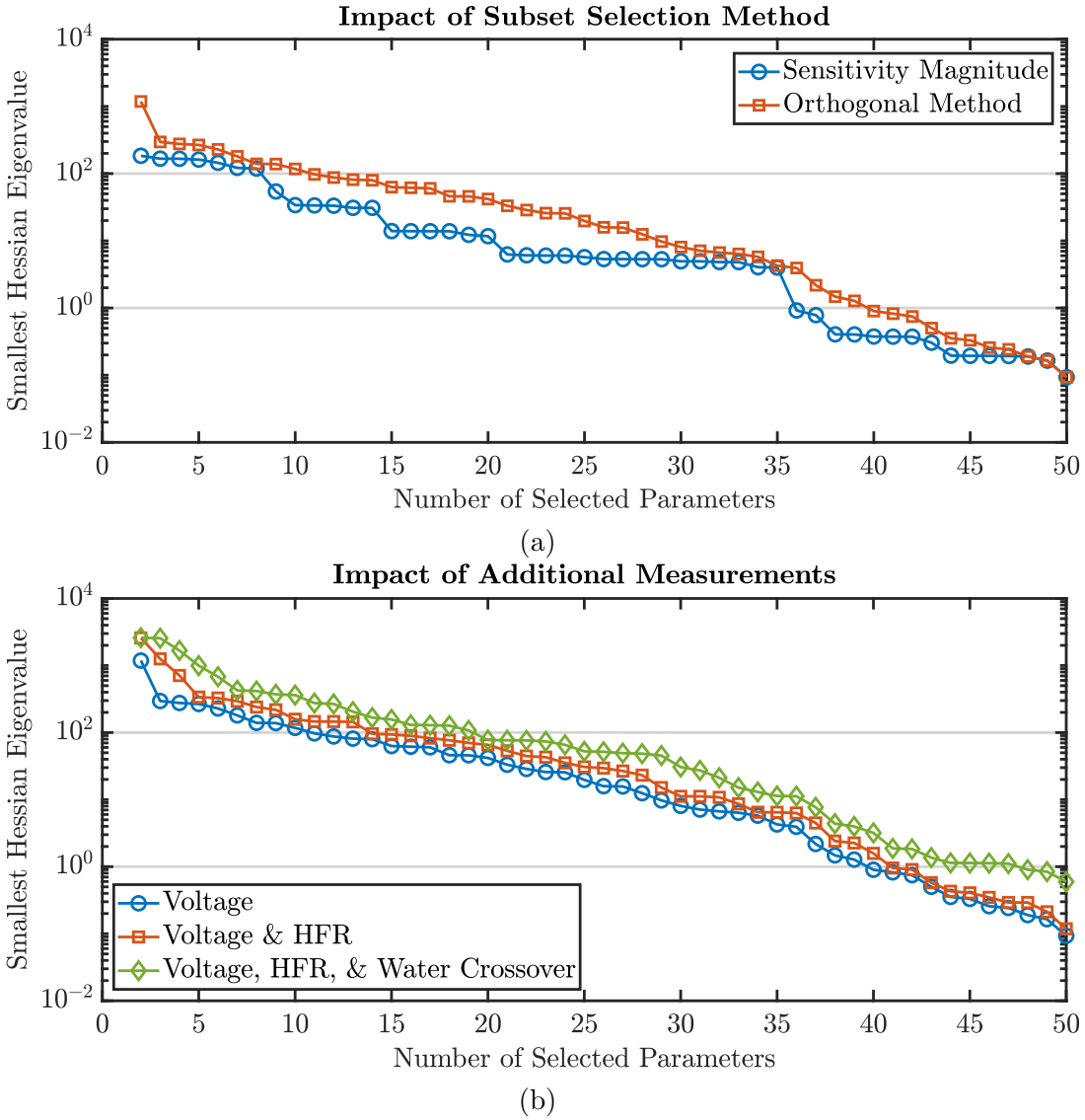

Figure 3.13: The minimum eigenvalue of the Hessian for different number of selected parameters: (a) effect of parameter subset selection method (based on voltage sensitivities) and (b) effect of additional measurements (based on orthogonal method).

previously selected parameters is calculated. The parameter with the largest orthogonal component is then selected as the next most influential parameter. This is implemented using the MATLAB QR factorization.

The advantage of orthogonal method over the magnitude based approach is in the fact that it accounts for linear dependencies between parameter sensitivities. Therefore, between two parameter subsets of equal size selected with these methods, the one based on

orthogonal method has less linear dependency and is therefore expected to have a larger minimum eigenvalue. This is shown in Fig. 3.13(a), which, using sensitivity data at one of the points in the parameter space, shows the minimum Hessian eigenvalue for different sizes of selected parameter subsets. The figure clearly shows that parameter selection based on the orthogonal method yields a better conditioned Hessian. For instance, if we choose an eigenvalue threshold of $\bar{\lambda}_{\text{th}} = 1$, and choose a subset of 36 parameters using the magnitude-based approach, the selected subset would be deemed unidentifiable as the minimum eigenvalue is 0.92. On the other hand, a subset of the same size obtained with the orthogonal method yields a minimum eigenvalue of 3.93 and is therefore identifiable according to the chosen threshold.

To analyze the effect of additional measurements on improvements in parameter identifiability, Fig. 3.13(b) shows the minimum Hessian eigenvalue using different measurements. It is observed that adding measurements can indeed improve the condition of the Hessian, thereby enhancing parameter identifiability. We emphasize again, that while the main results may seem intuitive, it is the quantitative and rigorous treatment of such behavior that constitutes the main contribution of this work.

To make these results more tangible, Table 3.2 shows the top 10 parameters ranked based on the voltage sensitivities using both the sensitivity magnitude and the orthogonal method. When using the voltage sensitivity magnitude, the reference ORR exchange current density ($i_{0,\text{ca}}$) is the second most important parameter. However, the orthogonal method yields a much lower rank for this parameter, since its sensitivity is highly collinear with that of the transfer coefficient (α_{ca}). The orthogonal method promotes ranking of parameters that have the largest unique impact, which is independent of previously ranked parameters. The table also shows parameter rankings based on multiple measurements using the orthogonal method. We observe that, for instance, using HFR alongside voltage as the outputs of interest, improves the ranking of parameters that impact the cell resistance (R_{elec} is ranked second when HFR is used as an additional output). Analogously,

considering membrane water crossover as an additional output of interest promotes the ranking of parameters that have a profound impact on this output, such as $\xi_{\text{diff,mb}}$.

Table 3.2: Parameter rankings with different methods and multiple measurements

Ranking	Voltage (Magnitude)	Voltage (Orthogonal)	Voltage, HFR (Orthogonal)	Voltage, HFR, Water Crossover (Orthogonal)
1	α_{ca}	α_{ca}	α_{ca}	α_{ca}
2	$i_{0,\text{ca}}$	h_{ch}	R_{elec}	R_{elec}
3	n_e	n_e	n_e	$\xi_{\text{diff,mb}}$
4	h_{ch}	δ_{GDL}	$k_{T,\text{scale}}$	n_e
5	ε_{GDL}	$k_{T,\text{scale}}$	h_{ch}	$k_{T,\text{scale}}$
6	δ_{GDL}	ε_{GDL}	h_{conv}	K_{per}
7	$i_{0,\text{an}}$	h_{conv}	δ_{GDL}	h_{ch}
8	δ_{MPL}	δ_{MPL}	$E_{\text{act,mb}}$	h_{conv}
9	$E_{\text{act,ca}}$	$i_{0,\text{ca}}$	ε_{GDL}	ε_{GDL}
10	$E_{\text{act,mb}}$	$i_{0,\text{an}}$	δ_{mb}	δ_{GDL}

Finally, we emphasize that the analysis in this section was conducted using sensitivity data obtained locally about one of the sample points in the parameter space. Moreover, all of the operating conditions in the library are used in the analysis. Therefore, even though these results might indicate that a large number of model parameters may be identifiable, such an identification would require a prohibitively large set of experiments. We discuss these points in more detail in the next chapter, where we refine our analysis to select a subset of parameters that is expected to be optimal in the entire parameter space and use experimental design as a tool to improve parameter identification.

Overall, these results underline the importance of rigorous identifiability analysis as an important tool to complement expert intuition when selecting parameters for identification. While many of our results might appear intuitive, their significance lies in the quantitative procedure used to obtain them and such conformation with expert knowledge further verifies the proposed methodology. The rigorous and systematic nature of

the presented procedure makes it applicable even in the absence of expert knowledge and could lead to new insights. Due to the very same characteristics of the procedure, even though the example results are specific to the particular fuel call model considered, the procedure itself can be applied to other models, as well.

3.6 Summary and Conclusions

A systematic procedure is presented on a pseudo-2D, non-isothermal, and two-phase model of a PEM fuel cell to study the output sensitivities to a variety of the model parameters. In particular, three common measurements are considered for the sensitivity analysis, namely, the cell voltage, HFR, and membrane water crossover. A large set of model parameters are investigated using an extended local sensitivity analysis, which is carried out by performing local analyses about several points in the parameter space. The parameters that have the highest impact on individual output predictions are determined. Moreover, the collinearity between pairs of parameters is investigated, where some physically unrelated pairs are found to have similar impacts on model predictions. The effect of operating conditions on parameter sensitivities is shown, where sensitivity of some parameters is found to vary considerably with the conditions. It is also shown that a number of parameters that generally have low sensitivity, can become more sensitive under certain operating conditions. Finally, the sensitivity results are used to analyze identifiability of model parameters, where it is found that the parameter selection method and additional measurements can clearly influence identifiability of the selected subset of parameters. These results are further expanded in the next chapter, wherein we focus on robust optimal parameter subset selection and experimental design for the purpose of identification.

Chapter 4

Parameter Subset Selection, Optimal Experimental Design, and Multi-Step Identification Algorithm

4.1 Introduction

One of the main challenges associated with parameter identification in a large-scale model is that such models usually have a large number of parameters, many of which may not be practically identifiable given the available measurements. Under such circumstances, it is imperative to select a subset of parameters for identification [324]. Particularly, the selected subset must only include parameters that can be identified using the available data. Moreover, the parameters must be selected in a way that ensures the predictive capability of the model is maintained [325].

These are conflicting requirements that necessitate close inspection of output sensitivities to different parameters to ensure that the selected subset has the required characteristics. Accordingly, several methods have been proposed in the literature to ensure the selected subset is optimal [165, 291, 322, 323, 326]. Among these, methods that optimize a

scalar metric of the Fisher information matrix (FIM) to maximize the precision of parameter estimates are commonly utilized [304,326,327]. Other approaches that directly focus on minimizing the model's prediction error have also been proposed [325, 328]. However, to date, these methods have not been applied to fuel cell models, which leaves significant room to improve model parameterization.

Another important aspect of parameter identification is the data used for this purpose. In particular, the data must contain enough information that allows the effects of different model parameters to be distinguished. The degree to which a dataset is informative is controlled by the experimental conditions used to collect the data and the corresponding model sensitivities. Therefore, model-based experimental design approaches have attracted considerable attention in the literature [329–334]. These techniques seek to find optimal experiments that are maximally informative for parameter identification. This is done, for example, by using the model to find conditions that maximize the sensitivity of the predicted output to model parameters [152]. Other proposed schemes maximize a scalar measure of the FIM [333, 334], similar to parameter subset selection algorithms.

The idea of optimally designing experiments to reveal a parameter of interest is certainly not new to the fuel cell community. Using differential conditions to achieve uniform distributions in a cell that allows characterization of MEAs [243] and using low reactant concentrations to characterize the transport resistances [102, 130] are examples of this idea. However, these approaches are based on expert knowledge and are typically limited to specialized studies that focus on a particular behavior of the cell. Moreover, they are not guaranteed to be optimal for parameter identification. Therefore, there is a need to adopt the above-mentioned methods to fuel cell applications and rigorously optimize the experiments for effective model parameterization. We also note that recent battery literature has extensively utilized model-based optimal experimental design with considerable success [152, 153, 161–164]. This further highlights the potential benefits of using these

methods for enhanced modeling of fuel cells, as many of the underlying equations are similar to battery models.

Once the subset of parameters to be identified is selected and the optimal conditions are used to collect the experimental data, the parameters can be identified. This last step is formulated as an optimization problem, whose solution typically minimizes the output prediction error of the model. Importantly, the structure of the available data can be utilized to improve identification results. Therefore, formulation of this step also requires consideration of model sensitivities to ensure the optimal solution is achieved. Here again, the fuel cell modeling literature is yet to capitalize on such potentials, leaving an important gap that should be addressed.

The above discussion points to several possibilities to improve parameter identification in fuel cell models. Accordingly, in this chapter we develop a systematic framework for effective model parameterization that addresses some of the current shortcomings of the fuel cell literature. Having investigated the sensitivities of various model predictions to different parameters in Chapter 3, here we focus on the problems of parameter subset selection and optimal experimental design. Particularly, we use our extended local sensitivity analysis results to select a subset of parameters for identification that is robust to initial assumptions about the nominal parameter values. We use similar procedures for robust optimal experimental design to obtain a set of experiments that are maximally informative for identification of the selected parameters. Finally, a multi-step parameter identification approach is proposed and tested with synthetic experimental data generated by the model.

The rest of the chapter is organized as follows. First, the problem of parameter subset selection is addressed in Section 4.2. The robust optimal experimental design procedure is then discussed in Section 4.3 followed by a description of the proposed multi-step identification algorithm in Section 4.4. The results for an identification case study are presented in Section 4.5 before closing with a brief summary in Section 4.6.

4.2 Robust Parameter Subset Selection

Our exclusive focus in this chapter is on parameter identifiability. Accordingly, we note that while we had considered 50 parameters for sensitivity analysis, many of these parameters, such as those describing the channel geometry, are known for a given stack. Although these parameters were included in our sensitivity analysis to ensure that our results are not constrained to a particular cell design, they are not suitable candidates for identification. Therefore, we narrow down the list of considered parameters in this chapter to focus on those that may be considered for model parameterization. Specifically, we limit our analysis here to a set of 31 parameters that are given in Table 4.1 below. Regarding the outputs of interest, here we assume that voltage and HFR are measured in the experiments as they often are in real-world testings. Therefore, our discussion here is based on the combined sensitivity of the voltage and HFR predictions. A summary of the sensitivity results is shown in Fig. 4.1 for the 31 parameters that are considered in this chapter.

Attempting to identify all of the model parameters results in an ill-conditioned inverse problem [335]. This necessitates the need for parameter subset selection so that the identification algorithm can focus exclusively on the parameters that are practically identifiable with the available measurements. We recall that a parameter is practically identifiable when it has an observable impact on the output predictions that is uniquely distinguishable from the impact of other parameters [291]. Therefore, a large sensitivity magnitude alone does not guarantee identifiability of a parameter; the corresponding sensitivity vector must also be independent from that of other parameters. Accordingly, this section provides an algorithm that selects an identifiable subset of parameters. This subset selection procedure may also be viewed as a regularization technique to alleviate the ill-conditioning of the inverse problem [166, 336]. Briefly, the proposed method is as

Table 4.1: Model parameters considered in this chapter

Parameter [Units]	Parameter [Units]
ω [kJ/mol]	$E_{\text{act,PtO}}$ [kJ/mol]
α_{an} [-]	α_{ca} [-]
$i_{0,\text{an}}$ [A/cm^2]	$i_{0,\text{ca}}$ [A/cm^2]
γ_{an} [-]	γ_{ca} [-]
$E_{\text{act,an}}$ [kJ/mol]	$E_{\text{act,ca}}$ [kJ/mol]
$E_{\text{rev,PtO}}$ [V]	$E_{\text{act,mb}}$ [kJ/mol]
$\xi_{\text{diff,mb}}$ [-]	$f_{\text{RH,a}}$ [-]
$f_{\text{RH,b}}$ [-]	$f_{\text{RH,c}}$ [-]
κ_0 [S/cm]	κ_{res} [S/cm]
$k_{T,\text{scale}}$ [-]	h_{conv} [W/(cm$^2 \cdot$ K)]
n_v [-]	n_e [-]
K_{per} [-]	θ_{GDL} [°]
θ_{CL} [°]	θ_{MPL} [°]
ε_{MPL} [-]	ε_{GDL} [-]
δ_{MPL} [μm]	δ_{GDL} [μm]
n_{Brugg} [-]	

follows:

1. Inspect the parameter set for highly collinear pairs and remove the parameter with smaller sensitivity magnitude from such pairs.

2. Choose the number of parameters, n_I, to be included in the subset. This is done using singular value decomposition.

3. Find the locally optimal subset of parameters at each point in the parameter space, for which sensitivity information has been calculated.

4. Find the globally optimal subset of parameters for the entire parameter space. The local solutions from the previous step are used to guide the optimization.

Below, each step is described in detail.

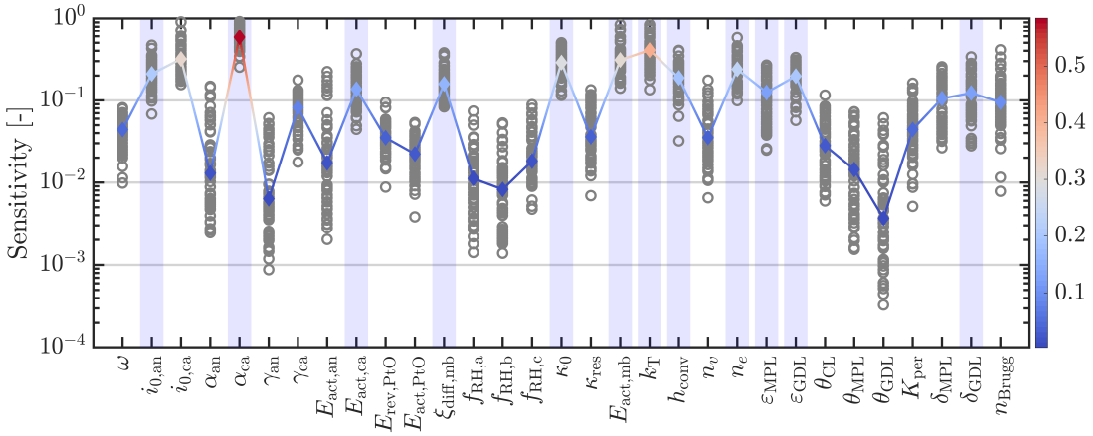

Figure 4.1: Summary of the sensitivity results based on voltage and HFR predictions and the results of the subset selection method presented in Section 4.2. The sensitivities at all sample points in the parameter space are shown as gray circles and the corresponding median is shown with the colored line, where the color changes based on the median sensitivity. The parameters selected by the method of Section 4.2 are highlighted with a light blue shade.

We start by inspecting the parameter sensitivities for highly collinear pairs. Particularly, we calculate the collinearity index (according to equation 3.10) for all parameter pairs at sampled points in the parameter space (see Section 3.3.3 for sampling details). The median of the calculated indices is then used as the representative collinearity index for each parameter pair over the entire parameter space:

$$\overline{\psi}_{i,j} = \underset{k}{\mathrm{med}}\ \psi^{k}_{i,j}, \tag{4.1}$$

where k is the index for the sample point in the parameter space and $\overline{\psi}_{i,j}$ is the median of the collinearity indices. Only one parameter from a pair whose median collinearity index is high can be practically identified [304]. Therefore, for pairs with $\overline{\psi}_{i,j}$ exceeding a threshold value of ψ_{th}, the parameter with lower sensitivity magnitude is discarded. Here we use $\psi_{\mathrm{th}} = 0.9$, which results in removal of $i_{0,\mathrm{ca}}$ and $E_{\mathrm{rev,PtO}}$ from the list of parameters due to their significant collinearity with α_{ca} and ω, respectively. Note that a large threshold is chosen to ensure a certain degree of flexibility is maintained in the

resulting set of parameters. More specifically, smaller thresholds can lead to removal of parameters that can have noticeably different impact than their collinear counterparts only at a few selective operating conditions.

In the second step we determine the number of parameters, n_I, that are needed to capture the variations in the data due to perturbations to the remaining parameters. Singular value decomposition [337] is a powerful tool for this purpose. In particular, at each sample point in the parameter space we calculate the singular values of the sensitivity matrix. Let these singular values be ordered as follows:

$$\sigma_1^k > \sigma_2^k > ... > \sigma_{n_\theta}^k \tag{4.2}$$

where σ_i^k denotes the i-th largest singular value of the sensitivity matrix obtained at the k-th sample point in the parameter space and n_θ is the number of parameters under consideration after the lower sensitivity parameters in collinear pairs have been removed ($n_\theta = 29$). We then seek to find the smallest r such that:

$$\overline{\sigma}_r^k = \frac{\sum_{j=1}^{r} \sigma_j^k}{\sum_{i=1}^{n_\theta} \sigma_i^k} \geq \overline{\sigma}_{\text{th}} \tag{4.3}$$

where $\overline{\sigma}_r^k$ monotonically increases with r and provides a measure as to how much of the total variations in the sensitivity directions are captured by the first r singular values. Moreover, $\overline{\sigma}_{\text{th}}$ is a threshold value that determines the number of selected singular values. Choosing a threshold of $\overline{\sigma}_{\text{th}} = 0.9$, we have found that, on average, 12 singular values are required to satisfy the above inequality at the sample points in the parameter space. Accordingly, we focus on selecting a subset of size $n_I = 12$ for identification.

The third step of the algorithm is finding the locally optimal subset of parameters for identification. To this end, we must determine which of the model parameters have the largest unique impact on the predicted outcomes. This is done using the sensitivity matrix defined by equation 3.7. Particularly, to select a parameter subset, we want to

choose columns of the sensitivity matrix that ensure the corresponding parameters can be identified with the required precision. The parameter estimation precision is determined by the corresponding covariance ($\boldsymbol{\Sigma_\theta}$), which is constrained by the inverse of the FIM through the Cramer-Rao bound [159]:

$$\boldsymbol{\Sigma_\theta} \geq \left(\mathbf{F}^k\right)^{-1}, \tag{4.4}$$

where $\mathbf{F}^k$ is the FIM at the k-th sample point in the parameter space, which is given by:

$$\mathbf{F}^k = \mathbf{S}^{k^\mathsf{T}} \mathbf{S}^k. \tag{4.5}$$

Note that the definition of the FIM also includes the covariance of the measurement noise, which, for the subset selection procedure, can be assumed to be identity without loss of generality [304]. With the Cramer-Rao bound and the FIM defined, we recall that the objective of this step is to select a subset of parameters, whose corresponding covariance is minimal. This can be achieved by minimizing the lower bound given by the inverse of the FIM. To this end, a scalar metric of the FIM is optimized. A number of scalar metrics have been suggested based on different criteria [338]. Among them, the D-optimality criterion is most commonly used [304], which maximizes the determinant of the FIM obtained from selected columns of the sensitivity matrix. Specifically, such an FIM is given by:

$$\mathbf{F}_I^k = \mathbf{S}_I^{k^\mathsf{T}} \mathbf{S}_I^k = \left(\mathbf{S}^k \mathbf{L}\right)^\mathsf{T} \left(\mathbf{S}^k \mathbf{L}\right), \tag{4.6}$$

where $\mathbf{L}$ is the selection matrix defined as:

$$\mathbf{L} = \left[\boldsymbol{e}_{i_1}, \boldsymbol{e}_{i_2}, \ldots, \boldsymbol{e}_{i_{n_I}}\right]. \tag{4.7}$$

In the above equation, $\boldsymbol{e}_j$ denotes the j-th standard unit vector and $\{i_1, i_2, ..., i_{n_I}\}$ is the set of selected parameter indices. We can now define the D-optimal selection criterion

explicitly:

$$\varphi_D^{k\,*} = \max \varphi_D(\mathbf{F}_I^k) = \max \log \det(\mathbf{F}_I^k), \tag{4.8}$$

where φ_D is the D-optimality criterion. To find the optimal solution, $\varphi_D^{k\,*}$, an integer program must be solved [304]:

$$\begin{aligned} \underset{i_1,i_2,\ldots,i_{n_I}}{\text{maximize}} \quad & \varphi_D(\mathbf{F}_I^k) \\ \text{subject to} \quad & \mathbf{F}_I^k = \left(\mathbf{S}^k\mathbf{L}\right)^{\mathsf{T}} \left(\mathbf{S}^k\mathbf{L}\right) \\ & \mathbf{L} = \left[\boldsymbol{e}_{i_1},\, \boldsymbol{e}_{i_2},\, \ldots,\, \boldsymbol{e}_{i_{n_I}}\right] \\ & i_j \in \{1,\ldots,n_\theta\},\ j = 1,\ldots,n_I. \end{aligned} \tag{4.9}$$

This is a combinatorial problem, whose solution may be obtained by exhaustive search for small problems [339]. However, the search space grows combinatorially and this approach becomes infeasible even for moderately-sized problems. Therefore, clustering methods have been utilized to reduce the size of the problem [304, 340]. Optimization routines such as genetic algorithm (GA) may also be used, albeit, with no guarantee of convergence to the true optimal solution [327]. Alternatively, the popular orthogonal method [323, 341, 342], which was discussed in Chapter 3, can be used to obtain a sub-optimal solution. Particularly, Chu et al. [326] showed that the orthogonal method is a forward selection algorithm that yields a sub-optimal solution for φ_D. Forward selection in this context refers to the fact that at each iteration, the algorithm only picks the best parameter to be added to the already selected list of parameters. In that sense, the orthogonal method leads to a greedy algorithm [343]. Variations of this algorithm have been suggested to consider multiple parameters at each stage, achieving more optimal results [326]. The advantage of the original orthogonal method lies in its simple implementation. For example, the QR algorithm in MATLAB can be readily used for this purpose [323]. Accordingly, we use the orthogonal method to find an initial sub-optimal

solution that is then refined through GA.

Since only local sensitivity data are used in the above process, the resulting subset of parameters is only locally optimal and not applicable throughout the entire parameter space. A more robust approach is therefore needed. Two such approaches have been commonly used in the literature based on the R-optimality and ED-optimality criteria [333]. In particular, the R-optimal selection criterion is based on a worst-case scenario and yields a selection that maximizes the minimum of the D-optimality criterion over the parameter space [332, 333]:

$$\varphi_R^* = \max \min_k \varphi_D(\mathbf{F}_I^k) = \max \min_k (\log \det(\mathbf{F}_I^k)), \tag{4.10}$$

On the other hand, the ED-optimality criterion maximizes the expected value of the D-optimality criterion over the parameter space [331, 333]:

$$\varphi_{ED}^* = \max \mathbb{E}\left[\varphi_D(\mathbf{F}_I)\right] = \max \mathbb{E}\left[\log \det(\mathbf{F}_I)\right], \tag{4.11}$$

Either criterion may be used to select a robust subset of parameters that is less dependent on the nominal parameter values. We have found the R-optimality criterion to be sensitive to outlier points in the parameter space. Therefore, we use the ED-optimality criterion in this chapter. The corresponding optimization problem is an integer program similar to that presented in equation 4.9, which is solved using GA. In this case, the local solutions obtained during the previous step are used in the initial GA population to guide the optimization. The GA algorithm is run multiple times and the best solution is selected.

Using the procedure outlined in this section, we have selected a subset of 12 parameters for identification, which are shown in Table 4.2 and highlighted in Fig. 4.1. We emphasize that this selection is optimal in an average sense, meaning that a better solution might exist in some regions of the parameter space. However, using the ED-optimality criterion helps ensure some degree of robustness to initial assumptions about the parameter values.

Table 4.2: Model parameters selected for identification

Parameter [Units]	Parameter [Units]
$i_{0,\text{an}}$ [A/cm^2]	α_{ca} [-]
$E_{\text{act,ca}}$ [kJ/mol]	$E_{\text{act,mb}}$ [kJ/mol]
$\xi_{\text{diff,mb}}$ [-]	κ_0 [S/cm] [-]
$k_{T,\text{scale}}$ [-]	h_{conv} [W/(cm$^2 \cdot$ K)]
δ_{GDL} [μm]	n_e [-]
ε_{MPL} [-]	ε_{GDL} [-]

4.3 Robust Optimal Experimental Design for Parameter Identification

Having selected an identifiable subset of parameters, we now consider the experimental data used for identification. Importantly, we note that the data used for this purpose must be informative to ensure successful identification. This requirement motivates model-based optimal experimental design (OED), wherein the model is used to find the operating conditions that render the predictions most sensitive to the parameters of interest. This idea is schematically shown in Fig. 4.2, where a numerical example is also illustrated.

The OED procedure requires solving an optimal control problem to obtain the most informative inputs. However, this approach is not computationally tractable for a large-scale model. Accordingly, methods such as input vector parameterization have been suggested [333], which searches over a discrete number of inputs to find the optimal solution. Alternatively, selecting an optimal set of conditions from a predefined library has been proposed as a computationally efficient method to solve the OED problem [161]. Since we have generated sensitivity data for a library of conditions, we use the latter approach to design maximally informative experiments for parameter identification.

When working with a library of operating conditions, the OED problem is very similar to the parameter subset selection discussed earlier and the same procedures apply.

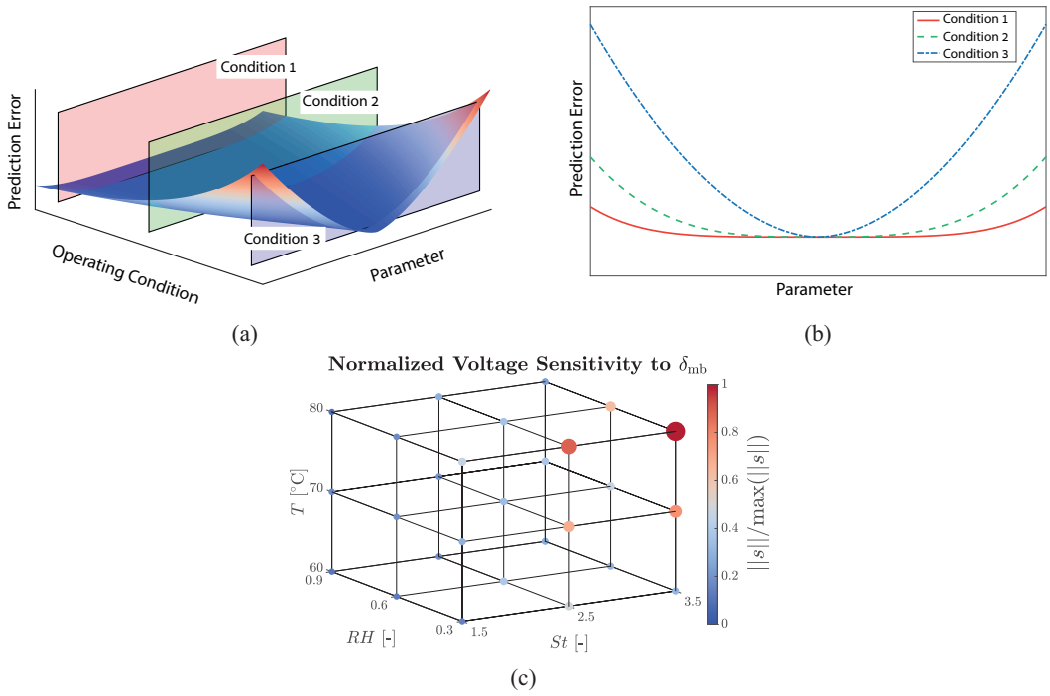

Figure 4.2: Optimal experimental design concept: (a) Schematic of model prediction errors as a function of parameter and operating condition, (b) schematic error variations with parameter for three example conditions, where the prediction error curve has a flat region for condition 1 rendering the parameter unidentifiable, while it is bowl-shaped for condition 3, which is ideal for parameter identifiability, and (c) example voltage sensitivities to membrane thickness, where hot and dry conditions are found to lead to increased sensitivity and improved identifiability of the membrane thickness.

Specifically, the sensitivity matrix obtained using the entire library of operating conditions consists of blocks that correspond to the individual experiments:

$$\mathbf{S}_I^k = \begin{bmatrix} (\mathbf{S}_I^k)_1 \\ (\mathbf{S}_I^k)_2 \\ \vdots \\ (\mathbf{S}_I^k)_{n_l} \end{bmatrix} \tag{4.12}$$

Here $(\mathbf{S}_I^k)_i$ denotes the sensitivity of the output predictions to the selected subset of parameters under the i-th set of operating conditions from the library of n_l conditions. We recall that we have $n_l = 729$ conditions in our library.

With the above block structure in mind, we note that while parameter subset selection is concerned with optimally choosing the columns of the sensitivity matrix to contain the most information, the OED focuses on choosing the best $(\mathbf{S}_I^k)_i$ blocks of the matrix for that same purpose. Therefore, D-optimality criterion is also commonly used for experimental design [161, 163, 164, 329]. The ED-optimality criterion may likewise be used for robust design [331, 333]. We note, however, that the orthogonal method is no longer applicable, since we are operating on sub-blocks of the sensitivity matrix rather than its columns. Instead, the local D-optimal solution can be obtained through convex relaxation of the underlying integer program [161]:

$$\begin{aligned} \underset{\eta_1,\eta_2,\ldots,\eta_{n_l}}{\text{maximize}} \quad & \log\det(\tilde{\mathbf{F}}_I^k) \\ \text{subject to} \quad & \tilde{\mathbf{F}}_I^k = \sum_{j=1}^{n_l} \eta_j \left(\mathbf{S}_I^k\right)_j^{\mathsf{T}} \left(\mathbf{S}_I^k\right)_j \\ & 0 \leq \eta_j \leq \frac{1}{n_u},\ j = 1, \ldots, n_l \\ & \sum_{j=1}^{n_l} \eta_j = 1, \end{aligned} \tag{4.13}$$

where n_u is the experimental budget, *i.e.*, the number of experiments to be selected from the library. Determining the experimental budget requires consideration of the actual experimental cost, as well as the computational cost required to evaluate the model for the selected experiments. Additionally, the number of selected experiments must provide enough information for parameter identification. Taking these into consideration, here we select $n_u = 6$ from the library.

The solution to the above convex program is a set of n_u experiments that are D-optimal at sample point k in the parameter space. In other words, this solution is only locally optimal. Therefore, to find an experimental design that is less dependent on the initial parameter values, the ED-optimality criterion of equation 4.11 is used.

Briefly, the robust OED procedure is as follows:

1. Choose the number of experiments, n_u, to be selected from the library.

2. Solve the convex program 4.13 to obtain the D-optimal design at the sampled points in the parameter space.

3. Use GA to obtain the ED-optimal design considering all of the sampled points. The D-optimal designs from the previous step are used in the initial population to guide the GA.

The experimental design resulting from this procedure is shown in Table 4.3. The identification results based on this robust OED procedure are compared with another experimental design using Latin Hypercube Sampling (LHS) with the same number of experiments ($n_u = 6$). The resulting LHS design is given in Table 4.4 and the identified parameters using both experimental design procedures are compared in Section 4.5.

Table 4.3: Robust optimal experimental design

Exp #	p_{ch} [bar]	$T_{\text{cool,in}}$ [°C]	RH_{an} [-]	RH_{ca} [-]	St_{H_2} [-]	St_{O_2} [-]
1	2.5	80	30	30	2.5	2.0
2	1.5	80	30	90	1.5	2.0
3	1.5	40	90	90	2.0	2.5
4	1.5	80	90	30	2.0	2.5
5	1.5	80	30	30	2.5	2.0
6	1.5	80	90	30	1.5	2.5

Table 4.4: Experimental design using LHS

Exp #	p_{ch} [bar]	$T_{\text{cool,in}}$ [°C]	RH_{an} [-]	RH_{ca} [-]	St_{H_2} [-]	St_{O_2} [-]
1	2.68	59	80	72	2.3	2.1
2	2.05	48	54	51	2.3	1.5
3	1.79	62	65	43	1.8	2.2
4	2.85	70	85	83	1.7	1.9
5	3.33	75	48	32	2.1	2.5
6	2.45	43	33	62	1.5	1.7

4.4 Multi-Step Parameter Identification Algorithm

So far, we have selected a subset of parameters for identification and designed informative experiments for that purpose. The last critical piece of the model parameterization framework is the identification algorithm. A good identification algorithm should be sufficiently constrained. An algorithm with too many degrees of freedom can lead to overfitting and poor parameter identification [335]. Regularization methods such as ridge regression [166, 336] and LASSO [344] are commonly used to constrain the identification process and formulate a well-conditioned problem. However, in the context of parameter identification, application of these methods typically requires prior information about the parameter values. Since we assume such information is not available, here we focus on using the structure of the data to constrain the identification procedure. We also recall that the parameter subset selection approach of Section 4.2 indeed regularizes the problem to a certain extent and the identification algorithm of this section is developed for further regularization.

The underlying principle of the algorithm proposed here is that the cell response shows varying sensitivity to parameter perturbations depending on the load as seen in Fig. 4.3. For instance, a parameter that affects reactant transport resistance might only become identifiable at higher loads. Therefore, we use this particular sensitivity structure to identify the selected parameters in multiple steps. Particularly, we divide the polarization curve and the corresponding HFR data into 3 sections based on the load (see Fig. 4.3): (1) low current density or kinetic region, (2) medium current density or ohmic region, and (3) high current density or mass transport region. The selected parameters are then grouped based on the corresponding sensitivities of the predicted outputs in each region. Specifically, the first parameter group consists of those parameters that are identifiable in the low current density region of the polarization curve, while the second and third groups

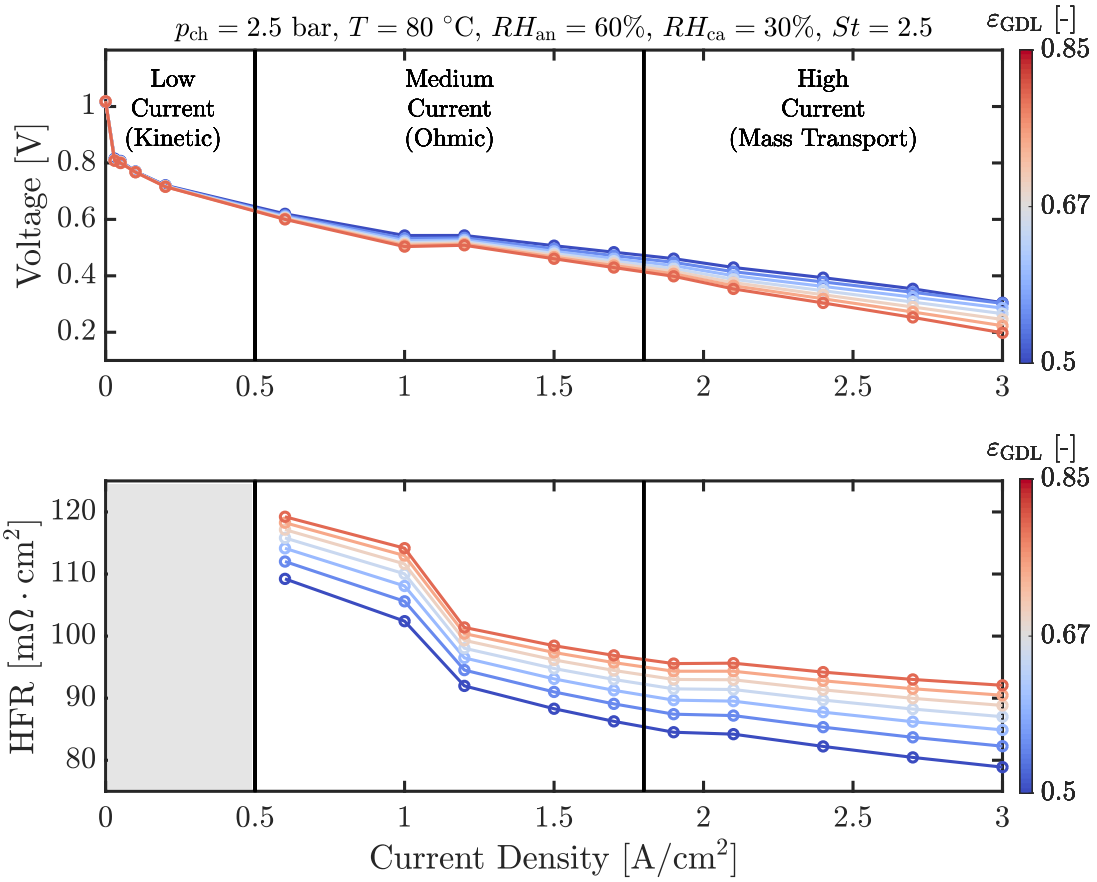

Figure 4.3: Sample output variations to changes in the GDL porosity, where different load regions are identified. The sensitivity of the predicted outputs varies with the load.

include the parameters that become identifiable at medium and high current densities, respectively. Identifiability in this context is measured by the average output sensitivity to the parameter of interest; a parameter is deemed identifiable in a particular region if the corresponding sensitivity is greater than a threshold value S_{th}, which is chosen to be 0.1 in this work. This grouping procedure based on output sensitivities is shown in Fig. 4.4.

Following the above grouping of parameters, the proposed multi-step identification algorithm is as follows:

1. Identify the parameters in the first group using data obtained at low current densities. The parameters in the other two groups are fixed at their nominal values.

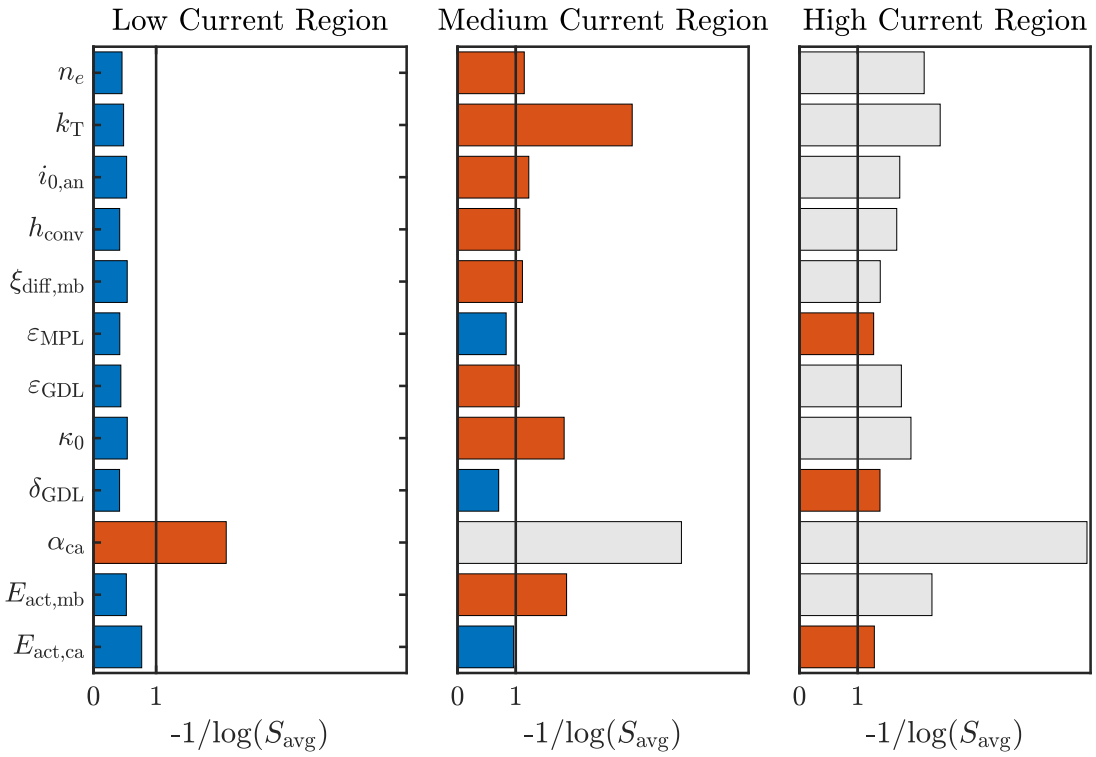

Figure 4.4: Combined voltage and HFR sensitivity for the entire library of operating conditions averaged among the samples in the parameter space. The blue, red, and gray bars denote, respectively, the parameters that are yet to be identified, those that are being identified in the current step, and those that were identified in a previous step and are being refined in the current step. The identifiability criterion is based on a sensitivity threshold that is chosen to be 0.1.

2. Identify the parameters in the second group using data obtained at medium current densities. Parameters in the third group are kept at their nominal values, while those that were identified in the first step are further refined by allowing them to vary within a contracted search space.

3. Identify the parameters in the third group using data obtained at high current densities. Previously identified parameters are allowed to vary, but their respective search spaces are contracted. Particularly, the search spaces for the parameters in the first group are shrunken further compared to their ranges in the second step of the algorithm.

4. Refine all identified parameters using the entire dataset. The search space for all

parameters are further contracted in this step to constrain the problem. This step is only used to refine the identified values.

The general idea is that the output sensitivities to parameter perturbations typically increase as the load is increased. Therefore, it is helpful to start the identification process by only using the data at low current densities and as our confidence in the parameter estimates increases, move to higher loads and identify the remaining parameters. The increased sensitivity at higher loads also means that it is critical to allow previously identified parameters to be refined as the load is increased. Such cumulative fitting enables more accurate parameter estimation [152, 161].

4.4.1 Alternative Implementations

Modified implementations of the general idea behind the presented multi-step identification algorithm are possible. A few potentially useful modifications are highlighted below:

- As we move to higher loads, our implementation disregards lower current density data points. Alternatively, one may use low current data at later stages of the identification algorithm along with larger weights for the higher current measurements (*i.e.*, weighted least squares).

- In our implementation the problem is regularized by contracting the search space for previously identified parameters. Alternatively, the same effect may be achieved by penalizing deviations from previously identified parameters. For example, ridge regression or LASSO formulations can be utilized in later stages of the algorithm.

- We only group the parameters based on their sensitivity variations with the current density. Alternatively, this grouping can be carried out by considering all of the operating conditions, such as the humidity and temperature. However, even though

this approach can lead to better regularized formulation, it is expected to require more experimental conditions to be effective.

While we do not pursue any of the above modifications in this dissertation, they offer some directions for further improvement of the proposed identification framework.

4.5 Verification of the Proposed Framework

As described above, the proposed model parameterization framework has three main components, namely, parameter subset selection (Section 4.2), optimal experimental design (Section 4.3), and the multi-step identification procedure (Section 4.4). In this section, we demonstrate the utility of each of these components. To this end, we use the model to generate synthetic experimental data with a set of nominal parameter values ($\boldsymbol{\theta}_{\text{nom}}$). The synthetic data are then used to identify the model parameters starting from perturbed values. Particularly, the optimization cost function is the weighted norm of the error:

$$J(\boldsymbol{\theta}) = w_V \frac{\|\boldsymbol{e}_V(\boldsymbol{\theta})\|_2}{\sqrt{n_V}} + w_R \frac{\|\boldsymbol{e}_R(\boldsymbol{\theta})\|_2}{\sqrt{n_R}}, \tag{4.14}$$

where $\boldsymbol{e}_V$ and $\boldsymbol{e}_R$ denote the prediction error vectors for voltage (measured in mV) and HFR (measured in $\text{m}\Omega \cdot \text{cm}^2$), respectively, n_V and n_R are the number of elements in $\boldsymbol{e}_V$ and $\boldsymbol{e}_R$, and w_V and w_R are the corresponding weights. Since the HFR varies in a smaller range compared to voltage, here we use $w_V = 1$ and $w_R = 10$. Given that we apply large perturbations to the nominal values and the above cost has many local minima, a gradient-based optimizer would fail to find the optimal solution. Use of a global optimizer is thus warranted. We have experimented with both GA and PSO algorithms and found that with the same level of effort to tune the optimizer hyper-parameters, the latter can find a more optimal solution. Therefore, we use PSO to identify the selected parameters.

To highlight the importance of each part of the framework, we consider 4 different cases for identification:

1. Only the selected parameters (Table 4.2) are perturbed from their nominal values. The OED conditions (Table 4.3) are used along with the multi-step identification procedure to identify the parameters.

2. Only the selected parameters (Table 4.2) are perturbed from their nominal values. The LHS conditions (Table 4.4) are used along with the multi-step identification procedure to identify the parameters.

3. Only the selected parameters (Table 4.2) are perturbed from their nominal values. The OED conditions (Table 4.3) are used along with a single-step identification procedure, where all of the selected parameters are identified using the entire dataset.

4. All parameters (Table 4.1), except those that were removed during the collinearity analysis ($i_{0,\text{ca}}$ and $E_{\text{rev,PtO}}$), are perturbed from their nominal values. The OED conditions (Table 4.3) are used along with the systematic identification procedure to identify the parameters.

In all of the above cases, the applied parameter perturbations are random. In particular, the perturbations to the selected parameters are drawn from $\mathcal{U}(-0.3, 0.3)$ (*i.e.*, uniform distribution between -0.3 and 0.3), while the perturbations to the parameters that are not included in the identification (case 4) are drawn from $\mathcal{U}(-0.15, 0.15)$. We also note that these perturbations are applied to the scaled parameter values and would amount to significant deviations from the nominal values on the original parameter axes. Additionally, it should be pointed out that the nominal values do not coincide with any of the sample points in the parameter space that are used to generate the sensitivity data, select the parameter subsets, and design the optimal experiments. These measures are taken to properly examine the robustness of the proposed framework.

The identified parameter values for the first two cases are provided in Table 4.5 along with the nominal and perturbed values. Moreover, the identification results for all of the

above scenarios are shown in Fig. 4.5 in terms of the relative absolute error (RAE) of the identified parameters, which is given by:

$$\text{RAE} = \frac{|\theta^* - \theta_{\text{nom}}|}{\theta_{\text{nom}}} \times 100, \tag{4.15}$$

where θ^* and θ_{nom} denote the identified and nominal parameter values, respectively. Fig. 4.5(a) compares the results from the first two scenarios and highlights the utility of OED. As seen in the figure, the maximum RAE in the parameter estimates is only 8.4% with the OED (for n_e), whereas the LHS design results in a maximum RAE of about 170% (for $\xi_{\text{diff,mb}}$). Moreover, the means of RAEs are 3.9% and 28.7% for the optimal and LHS experimental designs, respectively.

Table 4.5: Parameter identification results

Parameter [Units]	True	Perturbed	LHS	Robust OED
α_{ca} [-]	0.7	0.731	0.713	0.730
$i_{0,\text{an}}$ [A/cm^2]	0.01	0.0029	0.0109	0.0093
$E_{\text{act,ca}}$ [kJ/mol]	67.0	58.09	64.91	64.53
$\xi_{\text{diff,mb}}$ [-]	1.0	0.317	2.698	0.997
κ_0 [S/cm]	0.4	0.286	0.356	0.408
$E_{\text{act,mb}}$ [kJ/mol]	15	13.54	14.97	14.54
$k_{T,\text{scale}}$ [-]	1.0	0.715	0.542	1.021
h_{conv} [W/(cm$^2 \cdot$ K)]	1.0	0.2413	0.635	1.002
n_e [-]	1.8	2.166	1.387	1.649
ε_{MPL} [-]	0.60	0.5819	0.520	0.642
ε_{GDL} [-]	0.78	0.754	0.674	0.722
δ_{GDL} [μm]	135	156	112	137

In addition to the RAEs, the model's voltage and HFR predictions are shown in Figs. 4.6 and 4.7. Particularly, in Fig. 4.6 comparisons between the model outputs with nominal and identified parameters are shown for both OED and LHS cases with the data used in parameter identification. Fig. 4.7 compares the voltage and HFR dynamic trajectories under two different operating conditions that are not used during parameter identification, where model predictions with identified parameters are compared to those obtained

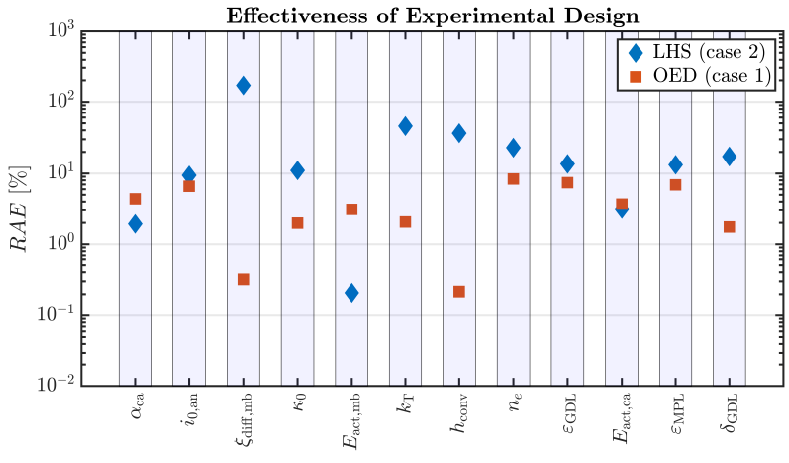

(a)

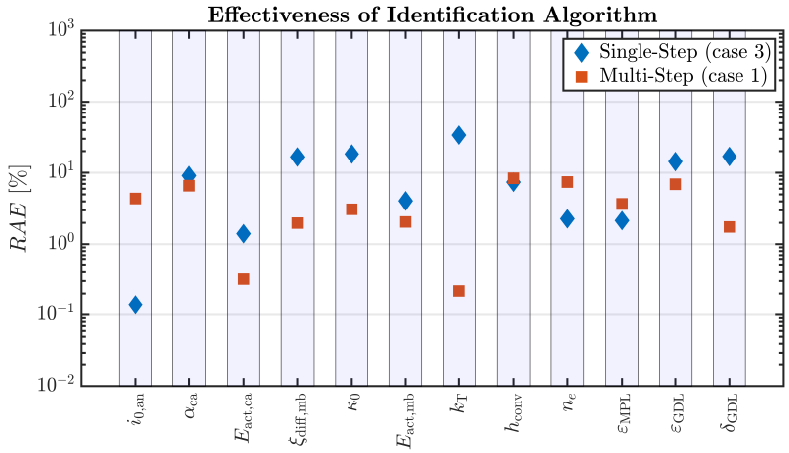

(b)

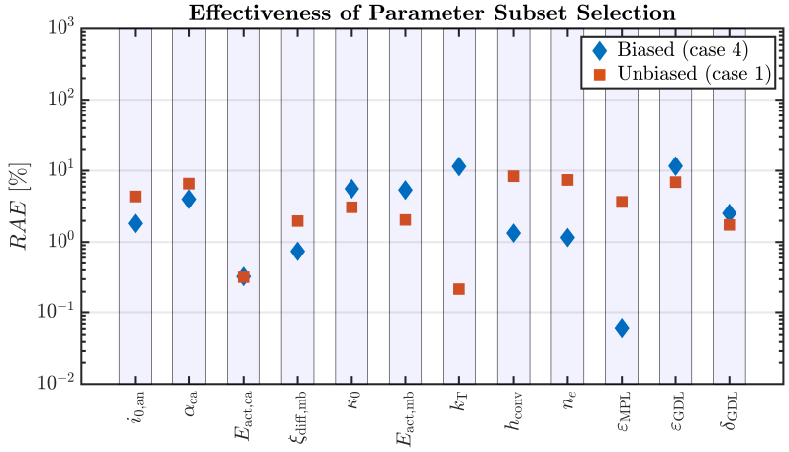

(c)

Figure 4.5: Relative error in parameter estimates obtained using synthetic data. Case 1 is compared to case: (a) 2, (b) 3, and (c) 4 to demonstrate the effectiveness of optimal experimental design (Section 4.3), the multi-step parameter identification algorithm (Section 4.4), and the subset selection method (Section 4.2), respectively.

with the nominal parameter values. A few observations follow: first we note that the OED conditions lead to more pronounced variations in the predictions; therefore, they better explore the space of output predictions and are more informative. Second, we observe that for both sets of conditions, the identified parameter values reproduce the synthetic experimental data used for parameter identification very well (see Fig. 4.6). This result emphasizes that a good fit to experimental data does not readily imply an accurate parameter identification. Lastly, as observed in Fig. 4.7, the identified parameter values using OED lead to more accurate model predictions on data that are not used during parameter identification. These observations, combined with the relative parameter estimation errors mentioned above, demonstrate the importance of having maximally informative experimental data for parameter identification, which can be obtained through model-based OED.

To show the effectiveness of the proposed multi-step identification algorithm, Fig. 4.5(b) compares the RAEs obtained using the proposed algorithm with those obtained from a single-step algorithm. The single-step algorithm uses the entire dataset to identify all of the selected parameters. Note that in both cases we use the data based on OED conditions of Table 4.3. The figure shows that the multi-step identification algorithm leads to smaller RAEs. The maximum and mean RAEs for the single-step case are 33.8% and 10.5%, respectively, which are higher than those obtained with the multi-step algorithm. This showcases the improved identification capability that is achieved by constraining the problem using the data structure.

Lastly, the subset selection approach is verified by comparing the identification results of case 1 with those of case 4, wherein the parameters that are not included in the selected subset are also perturbed from their nominal values. These results are shown in Fig. 4.5(c). We note that if the subset selection algorithm is successful, then the parameters that are not included in the selected subset are not expected to have a significant impact on the output predictions. Therefore, perturbations to these parameters should not lead

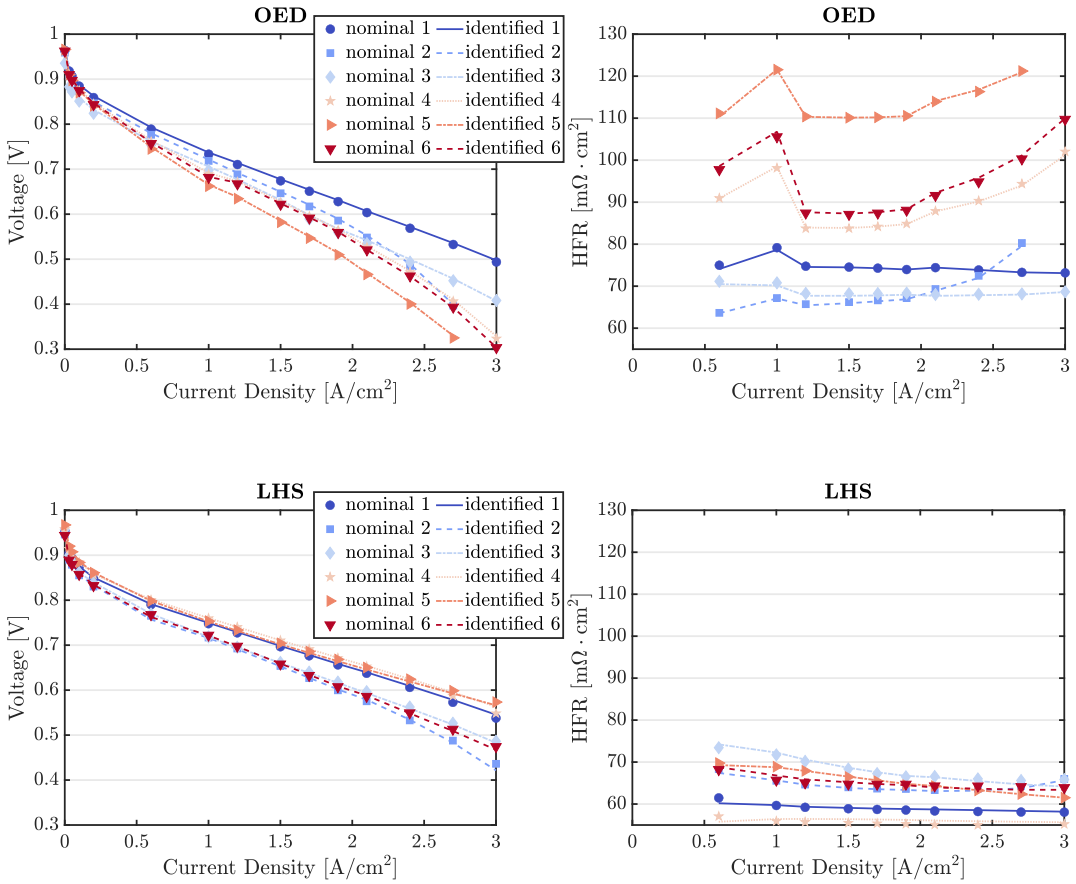

Figure 4.6: Polarization and HFR data obtained using OED and LHS conditions shown in Tables 4.3 and 4.4, respectively. Results for both the nominal parameter values (markers) and the identified values (lines) are shown. The identified values are based on case 1 (for OED) and case 2 (for LHS) and are shown in Table 4.5. Same axes limits are used to allow for direct comparison of the two experimental design results.

to considerable bias in the identified parameters. We further note that the parameters that were left out of the selected subset due to their collinearity with another parameter are not perturbed in case 4, as their perturbations can result in bias in the estimates of their collinear counterparts. As can be seen in the figure, perturbing the parameters outside of the selected subset does not have a significant impact on the relative errors in the parameter estimates. In particular, the maximum and mean RAEs are 11.6% and 3.8%, respectively, which are on par with those of case 1. Therefore, the subset selection algorithm has been successful.

These results show that regularization techniques such as parameter subset selection

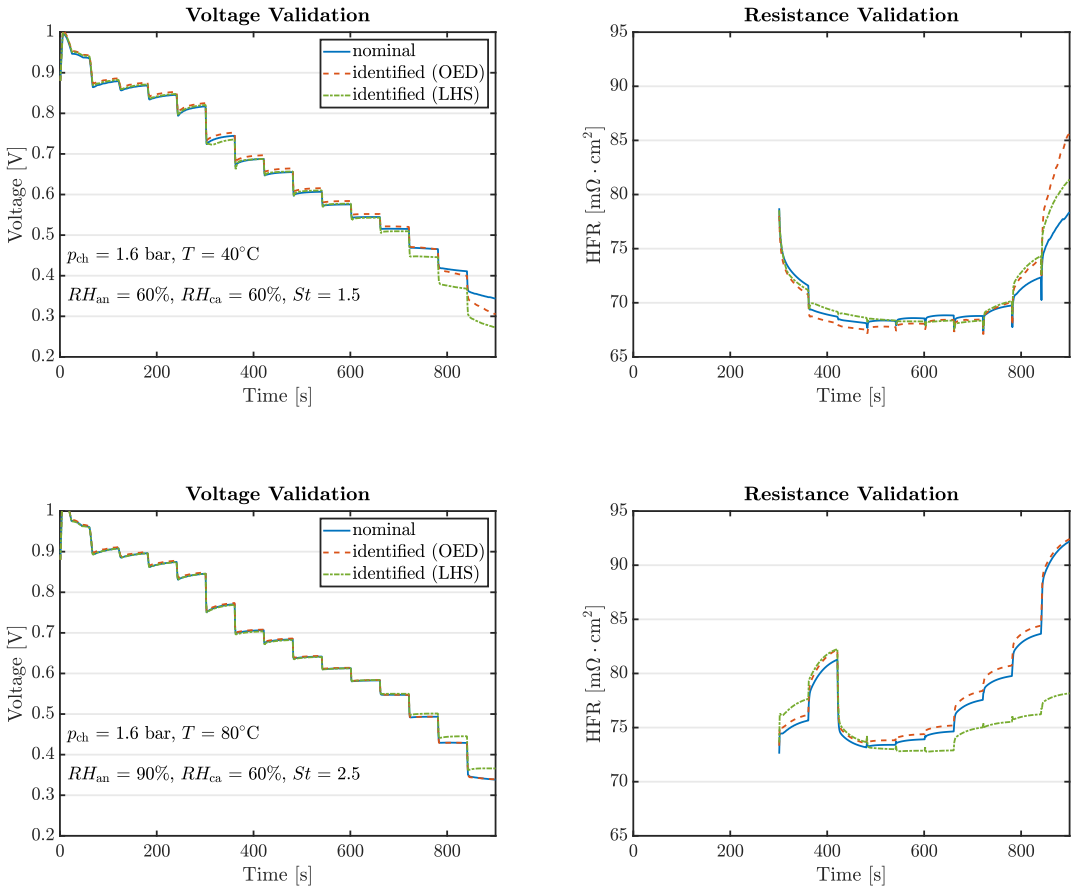

Figure 4.7: Validation results for identified parameter values using dynamic trajectories of voltage and resistance. Both OED and LHS results are shown in the figures for comparison. Two operating conditions are shown as examples, where the corresponding data at these conditions are not used during parameter identification.

and multi-step identification procedure along with optimal experimental design can significantly improve parameter identification. Moreover, by extending the analysis beyond the vicinity of a point in the parameter space, these procedures can be made robust to initial assumptions about the nominal parameter values. Since effective model parameterization is crucial to successful predictive modeling, these results can have profound implications for model-based design and control strategies.

4.6 Summary and Conclusions

A framework for systematic parameter identification for PEM fuel cell models is developed. The framework consists of three main components: (1) selecting a robust subset of parameters for identification, (2) using model-based design of experiments to obtain a robust set of maximally informative data for identification of the selected parameters, and (3) using the structure of the data to formulate a regularized identification problem. This framework is based on the extended local sensitivity analysis that is explained in Chapter 3. Particularly, sensitivities of model predictions to parameter perturbations are used to determine the parameters that have the largest unique impact on the predicted outputs. This is formalized through the D-optimality criterion. Importantly, rather than maximizing the local D-optimality criterion, we maximize its expected value over a number of sample points in the parameter space to ensure the resulting subset is less dependent on the nominal parameter values. The same procedure is applied to select the most informative operating conditions from a predefined library of conditions. Lastly, a multi-step identification procedure is proposed to regularize the optimization problem. The effectiveness of each of the components in the framework is verified through a case study, wherein synthetic experimental data generated with nominal parameter values are used to identify the selected parameters. The results demonstrate the efficacy of the proposed subset selection, optimal experimental design, and the multi-step identification procedures in improving parameter identification results. While the methods of this work are applied to a full cell model, they can also be utilized for sub-models that focus on a specific phenomenon. Therefore, it is suggested that fuel cell modelers adopt such methods to ensure that the models are properly parameterized and their full predictive capabilities are utilized.

Chapter 5

Degradation-Conscious Control

5.1 Introduction

The fuel cell durability challenges have prompted researchers to seek material solutions to ensure robust operation of the fuel cell stacks under a variety of dynamic operating conditions [25]. Reversal tolerant anode catalysts [55, 56] and various membrane additives and reinforcements [29–33] are examples of such developments. While these efforts have led to significant lifetime improvements, in most cases the cost and durability targets have proven too difficult to meet with material solutions alone [44]. Moreover, material-based solutions for durability enhancement, such as membrane additives, typically result in a higher fuel cell stack cost. On the other hand, some material-based cost saving measures, such as reducing Pt loading, have been found to lead to diminished durability [345, 346]. The shortcomings of the material-based approaches thus suggest that these efforts should be complemented with active control strategies to ensure that the full potential of the materials are utilized.

To develop a control strategy that can successfully address durability concerns, the stack materials have to be thoroughly characterized [347]. This characterization should determine safe bounds for the local environmental conditions for each component that lead

to prolonged lifetime. For instance, the membrane can be tested to determine the ranges of hydration, temperature, and hydration rate of change that ensure the membrane's longevity [34, 348]. When such information is available, one can develop effective control strategies that ensure operation within the safe bounds, thereby extending the stack's useful lifetime. Here we assume that quantitative bounds for safe operation of each component are available and develop a control strategy that ensures these bounds are respected during operation. We also note that determining the safety bounds is an active area of research, and that the vast body of literature on accelerated stress tests can be utilized to infer such bounds [349].

The challenge in designing an effective degradation-conscious controller is that the degradation constraints have to be imposed on the conditions internal to the fuel cell stack. However, only the channel conditions can be directly manipulated. For example, one may control the relative humidity of the gas streams in each channel, but cannot directly control the relative humidity in the catalyst layers. In other words, this is a PDE boundary value control problem [350]. Nonetheless, the PDEs can be transformed into ODEs with proper spatial discretization, which allows typical ODE control formulations to be used. Additionally, given the constrained nature of the problem, MPC is especially suitable for control design, since it provides a flexible and rigorous way of handling several types of constraints. Particularly, MPC solves a constrained finite horizon optimal control problem in a receding horizon manner (see Fig. 5.1) to obtain control inputs that satisfy various system constraints.

Following the above discussion and to address the existing gaps in the fuel cell control literature, here we propose a degradation-conscious control framework that can be used to improve the durability of the fuel cell stack. Specifically, starting with a 1D version of the fuel cell model presented in Chapter 2, we derive a reduced-order model for control design purposes. This reduced model is then linearized online about the current operating point and utilized in an LTV-MPC framework [351–353] that attempts to meet the

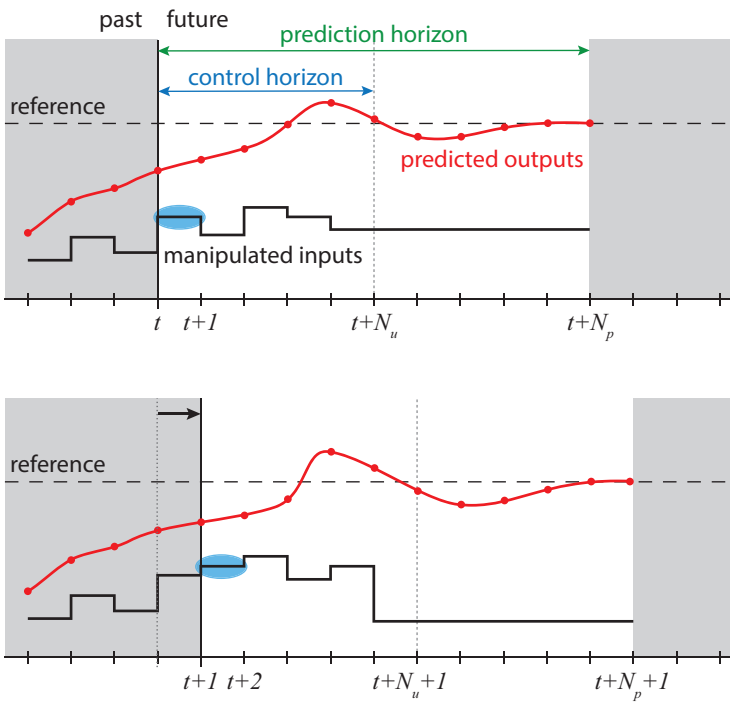

Figure 5.1: Schematic of the receding horizon concept implemented by MPC: At each time step, a finite horizon optimal control problem is solved. Only the first set of computed inputs in the sequence, highlighted by the blue oval, is applied to the system. At the next time step, new measurements or estimates of system states are used to define a new optimal control problem that is solved over a shifted horizon.

requested power demand, while minimizing the fuel consumption and maximizing the system efficiency, to the extent that these objectives do not compromise the system's safety or durability. While the particular control formulation is a novel addition to the fuel cell control literature, the most notable contribution of this chapter is the use of a high-fidelity physics-based model in our control design process, which allows us to directly account for local degradation phenomena. Importantly, the LTV-MPC formulation enables such a high-fidelity model to be used without incurring an excessive computational cost. Moreover, the framework is flexible and readily allows for additional degradation pathways to be included.

The rest of the chapter is organized as follows. First, the mathematical models used in this study are described in Section 5.2. The control problem formulation is then presented in Section 5.3, which discusses the underlying optimization problem for MPC. Next, the

results from a number of simulation studies are presented in Section 5.4, before closing with a chapter summary and brief concluding remarks in Section 5.5.

5.2 Mathematical Models

To formulate the control problem, we consider the fuel cell system, consisting of the fuel cell stack and the reactant and coolant supply subsystems, as shown in Fig. 5.2(a). We use a physics-based model of the PEM fuel cell to represent the actual fuel cell stack. The reactant and coolant supply subsystems are represented with a simplified model. Together, these models represent the entire fuel cell system and their combination is called the plant model. The plant model is then reduced for the purpose of control design. The reduced model is linearized online about the current operating point. This linearized reduced model is called the controller model and used in an LTV-MPC framework to generate the control commands. In this section, we describe both the plant and controller models. The parameter values used for simulations in this chapter can be found in Appendix Table A2.

5.2.1 Plant Model

5.2.1.1 Fuel Cell Model

A 1D version of the model that was presented in Chapter 2 is used here to represent the fuel cell stack. The state and output equations are briefly presented here for ease of access. Further modeling details, the functional form of material and transport properties, closure equations, and validation can be found in Chapter 2.

The fuel cell model has 37 dynamic states. Specifically, the model solves 4 transport PDEs to obtain the distribution of critical variables through the thickness of a cell. These critical variables include water vapor concentration, liquid saturation, temperature, and

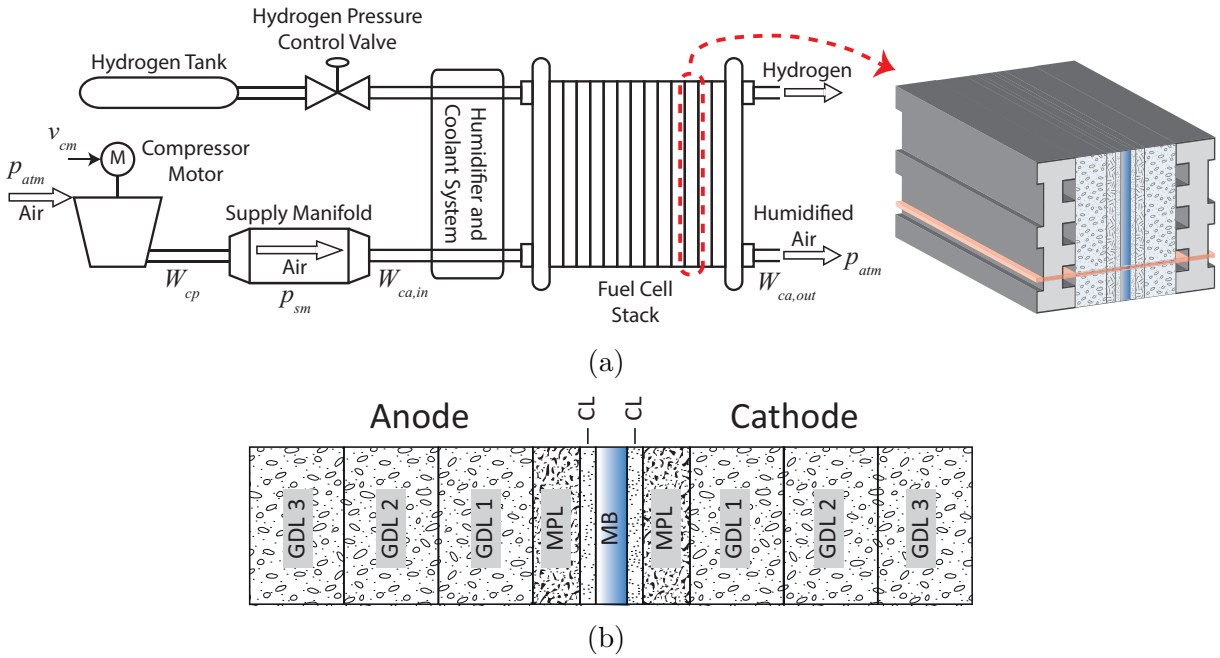

Figure 5.2: System schematics: (a) overall fuel cell system architecture and a single cell assembly, where the modeling domain is highlighted with the red plane and (b) control volumes used to discretize the model's PDEs.

ionomer water content and are respectively governed by:

$$\varepsilon_{\mathrm{g}} \frac{\partial c_{\mathrm{v}}}{\partial t} = \nabla \cdot (D_{H_2O}^{\mathrm{eff}} \nabla c_{\mathrm{v}}) + S_{\mathrm{v}}, \tag{5.1}$$

$$\rho_{\mathrm{l}} \varepsilon \frac{\partial s}{\partial t} = \nabla \cdot (\frac{\rho_{\mathrm{l}} K_l^{\mathrm{eff}}}{\mu_{\mathrm{l}}} \nabla p_{\mathrm{l}}) + S_{\mathrm{l}}, \tag{5.2}$$

$$\sum_{\alpha} \varepsilon_{\alpha} \rho_{\alpha} c_{p,\alpha} \frac{\partial T}{\partial t} = \nabla \cdot (k_T^{\mathrm{eff}} \nabla T) + S_T, \tag{5.3}$$

$$\varepsilon_{\mathrm{ion}} \frac{\rho_{\mathrm{ion}}}{EW} \frac{\partial \lambda}{\partial t} = \nabla \cdot (N_{\mathrm{w,mb}}) + S_{\lambda}, \tag{5.4}$$

Description of various source terms and effective transport properties for each layer of the cell can be found in chapter 2. The only difference here is that no spatio-temporal decoupling is employed in this chapter, and the above equations are solved in a coupled manner. Particularly, the PDEs are discretized using the control volume approach. The through-the-membrane discretization scheme is shown in Fig. 5.2(b), where the membrane, CLs, and MPLs are each represented with one control volume, whereas three control volumes

are used for each GDL. This spatial discretization leads to a total of 34 state variables from the above PDEs: 10 states for water vapor concentration (c_{v}), 10 states for liquid pressure (p_{l}), 11 states for temperature (T), and 3 states for ionomer water content (λ). Three additional state variables are used to account for ionomer stress relaxation and Pt oxide coverage:

$$\frac{ds_{\mathrm{relax}}}{dt} = \frac{1}{\tau_{\mathrm{relax}}}(s_{\mathrm{relax}} - \varphi\lambda_{\mathrm{eq}}), \tag{5.5}$$

$$\frac{d\theta_{\mathrm{PtO}}}{dt} = k_{\mathrm{PtO}}\left[RH(1-\theta_{\mathrm{PtO}})\exp\left(\frac{\alpha_{\mathrm{PtO}}F\eta_{\mathrm{PtO}} - E_{\mathrm{PtO}}\theta_{\mathrm{PtO}}}{RT}\right) - \theta_{\mathrm{PtO}}\exp\left(-\frac{(1-\alpha_{\mathrm{PtO}})F\eta_{\mathrm{PtO}}}{RT}\right)\right], \tag{5.6}$$

Further description for the above equations can be found in Chapter 2. Equation 5.6 along with equations 5.1-5.5 describe the dynamic state equations for the PEM fuel cell model with 37 states.

Regarding the output predictions, the cell voltage is given by equation 2.60 and the power output of the stack is determined by:

$$P_{\mathrm{fc}} = i_{\mathrm{dens}} \cdot E_{\mathrm{cell}} \cdot A_{\mathrm{fc}} \cdot n_{\mathrm{cell}}, \tag{5.7}$$

where A_{fc} is the active area of each cell and n_{cell} denotes the number of cells in the stack.

5.2.1.2 Reactant and Coolant Supply Subsystems Model

To model the reactant supply subsystem, we note that hydrogen is supplied from a high pressure tank, where the flow rate is controlled with a valve. The high pressure storage leads to negligible dynamics for the anode volume, where the pressure can be rapidly adjusted. Therefore, we neglect the fast dynamics for hydrogen supply and focus exclusively on the air supply dynamics, where the rotational dynamics of the compressor and the filling dynamics of cathode volume need to be captured by the model. Proper modeling of these dynamics allows control design that ensures safe (*i.e.*, no compressor surge or choke)

and sufficient (*i.e.*, no starvation) delivery of the oxygen required for the electrochemical reactions.

The model of the air supply subsystem is adopted from the literature. Particularly, Pukrushpan et al. developed a control-oriented model for the compressor and manifold filling dynamics with 9 states [93, 174]. The dynamic states of the model include oxygen, nitrogen, and vapor mass in the cathode, hydrogen and vapor mass in the anode, air mass in the cathode supply manifold, the pressure in the cathode supply and return manifolds, and the compressor speed. Later, Suh [354] showed that a reduced-order model with only 4 states can accurately capture the behavior of the model developed by Pukrushpan et al. [174]. The dynamic states of the reduced-order model developed by Suh [354] are the oxygen and nitrogen partial pressures in the cathode, the cathode supply manifold pressure, and the compressor speed. In this work, we use this reduced-order model with the modification that the states for oxygen and nitrogen partial pressures are lumped into a single state for the cathode pressure. Therefore, the dynamic states in our model include the compressor speed (ω_{cp}), the supply manifold pressure (p_{sm}), and the cathode pressure (p_{ca}). The corresponding dynamics are given by:

$$\frac{d\omega_{\text{cp}}}{dt} = \frac{1}{J_{\text{cp}}}(\tau_{\text{cm}} - \tau_{\text{cp}}), \tag{5.8}$$

$$\frac{dp_{\text{sm}}}{dt} = \frac{RT_{\text{cp}}}{M_{\text{a,atm}}V_{\text{sm}}}(W_{\text{cp}} - W_{\text{ca,in}}), \tag{5.9}$$

$$\begin{aligned}\frac{dp_{\text{ca}}}{dt} = &\frac{RT_{\text{CH,avg}}}{V_{\text{ca}}}\left(\frac{W_{O_2,\text{in}} - W_{O_2,\text{out}} - W_{O_2,\text{rct}}}{M_{O_2}} + \right. \\ &\left. \frac{W_{N_2,\text{in}} - W_{N_2,\text{out}}}{M_{N_2}} + \frac{W_{\text{v,in}} - W_{\text{v,out}} - W_{\text{v,rct}}}{M_{H_2O}}\right),\end{aligned} \tag{5.10}$$

where τ_{cm} and τ_{cp} are the motor and load torque of the compressor, respectively, J_{cp} is the compressor inertia, R is the universal gas constant, T_{cp} is the compressor flow temperature, $M_{\text{a,atm}}$ is the molar weight of atmospheric air, V_{sm} is the supply manifold volume, $T_{\text{CH,avg}}$ is the average temperature in the flow channel, V_{ca} is the cathode volume,

W_{cp} is the mass flow rate of air out of the compressor, $W_{\text{ca,in}}$ is the air mass flow rate into the cathode volume, $W_{i,\text{in}}$ and $W_{i,\text{out}}$ denote the mass flow rate of species i into and out of the cathode, respectively, and $W_{i,\text{rct}}$ is the mass flow rate of species i into the GDL. Note that $W_{O_2,\text{rct}}$ is always positive as oxygen is consumed during ORR. However, $W_{\text{v,rct}}$ can be negative, which indicates that vapor flows from the GDL into the cathode channel. The static relations for the terms in the above equations are provided in Table 5.1. Further details can be found in the works of Pukrushpan et al. [174] and Suh [354]. We also note that the compressor specifications used here, including the compressor efficiency map, are identical to the ones reported by these earlier works [174, 354].

Following the above calculations, the oxygen stoichiometry is given by:

$$St_{O_2} = \frac{W_{\text{O}_2,\text{in}}}{W_{\text{O}_2,\text{rct}}}. \tag{5.11}$$

Moreover, the power consumed by the compressor motor is determined as follows:

$$P_{\text{cm}} = \frac{v_{\text{cm}}}{R_{\text{cm}}} \left(v_{\text{cm}} - k_v \omega_{\text{cp}} \right), \tag{5.12}$$

where v_{cm} is the compressor motor voltage, which is an input to the model, and R_{cm} and k_v are compressor motor parameters.

With regards to the coolant circulation, the relation between the coolant flow rate and the corresponding change in its temperature is given by:

$$\begin{aligned} Q_{\text{cool}} &= \dot{m}_{\text{cool}} C_{p,\text{cool}} \Delta T_{\text{cool}} \\ &= h_{\text{conv}} A_{\text{cool}} \left[T_{\text{GDL}} - T_{\text{CH,avg}} \right] \\ &= h_{\text{conv}} A_{\text{cool}} \left[T_{\text{GDL}} - \left(T_{\text{cool,in}} + \frac{1}{2} \Delta T_{\text{cool}} \right) \right], \end{aligned} \tag{5.13}$$

where $\dot{m}_{\text{cool}}$, $C_{p,\text{cool}}$, $T_{\text{cool,in}}$, and ΔT_{cool} denote the coolant flow rate, its specific heat capacity, its inlet temperature, and its temperature change, respectively, h_{conv} is the convective heat transfer coefficient, A_{cool} is the area available for cooling, and T_{GDL} is the

Table 5.1: Static relations for air supply subsystem

Variable	Equation
τ_{cm}	$\eta_{\text{cm}} \frac{k_t}{R_{\text{cm}}} \left(v_{\text{cm}} - k_v \omega_{\text{cp}}\right)$
τ_{cp}	$\frac{C_p T_{\text{atm}}}{\eta_{\text{cp}} \omega_{\text{cp}}} \left[\left(\frac{p_{\text{sm}}}{p_{\text{atm}}} \right)^{\frac{\gamma-1}{\gamma}} - 1 \right] W_{\text{cp}}$
T_{cp}	$T_{\text{atm}} + \frac{T_{\text{atm}}}{\eta_{\text{cp}}} \left[\left(\frac{p_{\text{sm}}}{p_{\text{atm}}} \right)^{\frac{\gamma-1}{\gamma}} - 1 \right]$
W_{cp}	$\Phi \rho_{\text{a}} \frac{\pi}{4} d_{\text{c}}^2 U_{\text{c}} p_{\text{cp,in}} \sqrt{\frac{288}{T_{\text{cp,in}}}}$
$W_{\text{ca,in}}$	$k_{\text{ca,in}} \left(p_{\text{sm}} - p_{\text{ca}}\right)$
$W_{O_2,\text{in}}$	$\frac{x_{O_2}}{1+\omega_{\text{ca,in}}} W_{\text{ca,in}}$
$W_{N_2,\text{in}}$	$\frac{1-x_{O_2}}{1+\omega_{\text{ca,in}}} W_{\text{ca,in}}$
$W_{\text{v,in}}$	$\frac{\omega_{\text{ca,in}}}{1+\omega_{\text{ca,in}}} W_{\text{ca,in}}$
$W_{\text{ca,out}}$	$\frac{C_{\text{D}} A_{\text{T}} p_{\text{ca}}}{\sqrt{R T_{\text{CH,out}}}} C_{\text{W}}$
	$C_{\text{W}} = \left(\frac{p_{\text{atm}}}{p_{\text{ca}}} \right)^{\frac{1}{\gamma}} \sqrt{\frac{2\gamma}{1-\gamma} \left(1 - \left(\frac{p_{\text{atm}}}{p_{\text{ca}}} \right)^{\frac{\gamma-1}{\gamma}} \right)}$ for $\frac{p_{\text{atm}}}{p_{\text{ca}}} > \left(\frac{2}{\gamma+1} \right)^{\frac{\gamma}{\gamma-1}}$
	$C_{\text{W}} = \sqrt{\gamma} \left(\frac{2}{\gamma+1} \right)^{\frac{\gamma+1}{2(\gamma-1)}}$ for $\frac{p_{\text{atm}}}{p_{\text{ca}}} \leq \left(\frac{2}{\gamma+1} \right)^{\frac{\gamma}{\gamma-1}}$
$W_{O_2,\text{out}}$	$\frac{M_{O_2} p_{O_2}}{M_{O_2} p_{O_2} + M_{N_2} p_{N_2} + M_{H_2O} p_{\text{v}}} W_{\text{ca,out}}$
$W_{N_2,\text{out}}$	$\frac{M_{N_2} p_{N_2}}{M_{O_2} p_{O_2} + M_{N_2} p_{N_2} + M_{H_2O} p_{\text{v}}} W_{\text{ca,out}}$
$W_{\text{v,out}}$	$\frac{M_{H_2O} p_{\text{v}}}{M_{O_2} p_{O_2} + M_{N_2} p_{N_2} + M_{H_2O} p_{\text{v}}} W_{\text{ca,out}}$
$W_{O_2,\text{rct}}$	$M_{O_2} n_{\text{cell}} A_{\text{fc}} \frac{i_{\text{dens}}}{4F}$
$W_{\text{v,rct}}$	$M_{H_2O} n_{\text{cell}} A_{\text{fc}} \frac{c_{\text{v,CH}} - c_{\text{v,GDL3}}}{\mathcal{R}_{\text{v}}}$

temperature in the GDL3 control volume (see Fig. 5.2(b)). The model inputs for the coolant circulations subsystem include the coolant inlet temperature ($T_{\text{cool,in}}$) and its flow rate ($\dot{m}_{\text{cool}}$). Note that we do not explicitly model the heater and radiator for simplicity. Nonetheless, the dynamics of heating the coolant to a specific temperature is accounted for in the control formulation (see Section 5.3).

Lastly, here we assume that the compressor motor and all auxiliary equipment are

powered by the fuel cell system. Therefore, the net power output of the system is given by:

$$P_{\text{net}} = P_{\text{fc}} - P_{\text{cm}} - P_{\text{aux}}, \tag{5.14}$$

where P_{aux} is the total power consumed by all other auxiliary equipment, such as the cooling system and the humidifier. We further assume that this auxiliary power consumption scales linearly with the current density and the coolant flow rate:

$$P_{\text{aux}} = 0.5 + \frac{i_{\text{dens}}}{i_{\text{dens,max}}} + \frac{\dot{m}_{\text{cool}}}{\dot{m}_{\text{cool,max}}} \quad [\text{kW}], \tag{5.15}$$

where the maximum power consumption by all auxiliary equipment is assumed to be 2.5 kW. In our control formulation, we also maximize the overall system efficiency. To this end, we minimize the fraction of net power consumed by the auxiliary components, which is given by:

$$P_{\text{frac}} = \frac{P_{\text{cm}} + P_{\text{aux}}}{P_{\text{net}}}. \tag{5.16}$$

This completes our plant model formulation.

5.2.1.3 Plant Model Summary

The plant model has a total of 40 dynamic states:

$$\boldsymbol{x} = \left[\boldsymbol{c}_{\text{v}}^{\mathsf{T}},\, \boldsymbol{p}_{\text{l}}^{\mathsf{T}},\, \boldsymbol{T}^{\mathsf{T}},\, \boldsymbol{\lambda}^{\mathsf{T}},\, \theta_{\text{PtO}},\, \omega_{\text{cp}},\, p_{\text{sm}},\, p_{\text{ca}}\right]^{\mathsf{T}}, \tag{5.17}$$

where bold symbols denote vector-valued variables. The model inputs include relative humidity in the flow channels, coolant inlet temperature and its flow rate, compressor motor voltage, and the stack current density. Therefore, the input vector is given by:

$$\boldsymbol{u} = \left[RH_{\text{an}},\, RH_{\text{ca}},\, T_{\text{cool,in}},\, v_{\text{cm}},\, i_{\text{dens}},\, \dot{m}_{\text{cool}}\right]^{\mathsf{T}}, \tag{5.18}$$

where RH_{an} and RH_{ca} denote the channel RH values, which provide the required boundary conditions for equation 5.1 and also impact the membrane hydration state. Finally, the two main outputs of the plant model are:

$$\boldsymbol{y} = \left[P_{\text{net}},\ P_{\text{frac}}\right]^{\intercal}. \tag{5.19}$$

5.2.2 Controller Model

The model described in the previous subsection is not amenable to online computations required for optimization-based control. Therefore, a reduced-order model is developed for control design purposes. The plant model for the reactant and coolant supply subsystems is a lumped parameter model with 3 dynamic states and requires no further simplification. Accordingly, our focus for model reduction is on the fuel cell model, where we note that the states critical to both performance and durability are those that describe the conditions in the membrane and catalyst layers. For instance, the membrane hydration and its temperature are consequential to its durability [34, 355, 356] while also affecting the stack performance. Therefore, the reduced-order model must capture such critical states. On the other hand, the GDL and MPL conditions lead to intermediate states between the controlled channel environment and the membrane and catalyst layer states. Many of these intermediate states may be lumped into effective transport properties that do not vary considerably over a short time horizon. For example, while the amount of liquid in the GDL impacts the cell performance, GDL liquid accumulation is typically slow and significant variations are not expected over the span of a few seconds [89]. Therefore, the dynamics of corresponding states can be safely neglected in the reduced-order model and their effects can instead be represented with static transport properties.

Following the above discussion, we develop a reduced-order model for the cell with only 8 states (reduced from the 37 states of the full-order fuel cell model). Our particular focus is on the membrane hydration and temperature. Since accurate estimation of membrane

hydration requires the vapor concentrations in the CLs, these concentrations are modeled with two states. Similarly, the dynamics of liquid accumulation in the CLs are represented with two additional states. These were determined to be critical, since the low porosity and small thickness of the CLs can lead to their rapid flooding in a few seconds [89]. The controller model has to capture this behavior. Otherwise, the controller may generate inputs that lead to significant flooding of the CLs, from which it may not be able to recover the required performance.

With these considerations, the resulting control-oriented model of the cell has 8 states that focus on the membrane and catalyst layer conditions. Since the GDL and MPL states have been eliminated, the reduced-order model relies on transport parameters that are obtained from the full-order model. We present the state equations for the reduced-order model starting with the ionomer hydration dynamics that are similar to those of the full-order model and are repeated here for accessibility:

$$\varepsilon_{\text{ion}}^{\text{an}} \frac{\rho_{\text{ion}}}{EW} \frac{d\lambda_{\text{CL}}^{\text{an}}}{dt} = \frac{1}{\delta_{\text{CL}}^{\text{an}}} \left(-N_{\text{w,mb}}^{\text{an}} + 2N_{\text{O}_2,\text{mb}} \right) + S_{\text{ad}}^{\text{an}}, \tag{5.20}$$

$$\varepsilon_{\text{ion}}^{\text{ca}} \frac{\rho_{\text{ion}}}{EW} \frac{d\lambda_{\text{CL}}^{\text{ca}}}{dt} = \frac{1}{\delta_{\text{CL}}^{\text{ca}}} \left(N_{\text{w,mb}}^{\text{ca}} + \frac{i}{2F} + N_{\text{H}_2,\text{mb}} \right) + S_{\text{ad}}^{\text{ca}}, \tag{5.21}$$

$$\varepsilon_{\text{ion}}^{\text{mb}} \frac{\rho_{\text{ion}}}{EW} \frac{d\lambda_{\text{mb}}}{dt} = -\frac{1}{\delta_{\text{mb}}} \left(N_{\text{w,mb}}^{\text{ca}} - N_{\text{w,mb}}^{\text{an}} \right), \tag{5.22}$$

The above equations are identical to equations 2.49-2.51 and the descriptions can be found in Chapter 2. The membrane temperature dynamics are approximated by:

$$\begin{aligned} \frac{dT_{\text{mb}}}{dt} = & \frac{1}{(\rho c_p)_{\text{mb}}} \left(\frac{T_{\text{mb}} - T_{\text{CH,avg}}}{\delta^{\text{ca}} \mathcal{R}_T^{\text{ca}}} + \frac{T_{\text{mb}} - T_{\text{CH,avg}}}{\delta^{\text{an}} \mathcal{R}_T^{\text{an}}} \right) \\ & + \frac{S_{T,\text{mb}}}{(\rho c_p)_{\text{mb}}} + \frac{S_{T,\text{CL}}^{\text{ca}}}{(\rho c_p)_{\text{CL}}} + \frac{S_{T,\text{CL}}^{\text{an}}}{(\rho c_p)_{\text{CL}}}, \end{aligned} \tag{5.23}$$

where the membrane temperature is affected by heat transport to the gas and coolant channels and various heat source/sink terms. Specifically, $T_{\text{CH,avg}}$ is the average channel temperature, which is assumed to be equal to the average coolant temperature, *i.e.*,

$T_{\mathrm{CH,avg}} = T_{\mathrm{cool,avg}} = T_{\mathrm{cool,in}} + \frac{1}{2}\Delta T_{\mathrm{cool}}$. Moreover, S_T's denote the corresponding heat source terms (see Chapter 2 for details and note that the reaction source terms are also taken into account), $\delta^{\mathrm{an/ca}}$ is the total thickness of the cell layers (CL+MPL+GDL) on either side, and $\mathcal{R}_T^{\mathrm{an/ca}}$ denotes the total heat transport resistance between the membrane and the channels, which is a summation of conductive and convective heat transport resistances and is determined as follows:

$$\mathcal{R}_T = \frac{\delta_{\mathrm{CL}}}{k_{T,\mathrm{CL}}^{\mathrm{eff}}} + \frac{\delta_{\mathrm{MPL}}}{k_{T,\mathrm{MPL}}^{\mathrm{eff}}} + \frac{\delta_{\mathrm{GDL}}}{k_{T,\mathrm{GDL}}^{\mathrm{eff}}} + \frac{1}{h_{\mathrm{conv}}}, \tag{5.24}$$

where k_T^{eff} is the effective thermal conductivity of the layer.

Lastly, the dynamics of vapor concentration and liquid saturation in the CLs are given by:

$$\varepsilon_{\mathrm{g,CL}}^{\mathrm{an}} \frac{dc_{\mathrm{v,CL}}^{\mathrm{an}}}{dt} = \frac{1}{\delta_{\mathrm{CL}}^{\mathrm{an}}} \left(-\frac{c_{\mathrm{v,CL}}^{\mathrm{an}} - c_{\mathrm{v,CH}}^{\mathrm{an}}}{\mathcal{R}_{\mathrm{v}}^{\mathrm{an}}} \right) + S_{\mathrm{pc}}^{\mathrm{an}} - S_{\mathrm{ad}}^{\mathrm{an}}, \tag{5.25}$$

$$\varepsilon_{\mathrm{g,CL}}^{\mathrm{ca}} \frac{dc_{\mathrm{v,CL}}^{\mathrm{ca}}}{dt} = \frac{1}{\delta_{\mathrm{CL}}^{\mathrm{ca}}} \left(-\frac{c_{\mathrm{v,CL}}^{\mathrm{ca}} - c_{\mathrm{v,CH}}^{\mathrm{ca}}}{\mathcal{R}_{\mathrm{v}}^{\mathrm{ca}}} \right) + S_{\mathrm{pc}}^{\mathrm{ca}} - S_{\mathrm{ad}}^{\mathrm{ca}}, \tag{5.26}$$

$$\rho_{\mathrm{l}} \varepsilon_{\mathrm{CL}}^{\mathrm{an}} \frac{ds_{\mathrm{CL}}^{\mathrm{an}}}{dt} = \frac{\rho_{\mathrm{l}} K_{\mathrm{l}}^{\mathrm{eff}} (p_{\mathrm{l,MPL}}^{\mathrm{an}} - p_{\mathrm{l,CL}}^{\mathrm{an}})}{0.5\mu_l (\delta_{\mathrm{CL}}^{\mathrm{an}} + \delta_{\mathrm{MPL}}^{\mathrm{an}}) \delta_{\mathrm{CL}}^{\mathrm{an}}} - M_{H_2O} S_{\mathrm{pc}}^{\mathrm{an}}, \tag{5.27}$$

$$\rho_{\mathrm{l}} \varepsilon_{\mathrm{CL}}^{\mathrm{ca}} \frac{ds_{\mathrm{CL}}^{\mathrm{ca}}}{dt} = \frac{\rho_{\mathrm{l}} K_{\mathrm{l}}^{\mathrm{eff}} (p_{\mathrm{l,MPL}}^{\mathrm{ca}} - p_{\mathrm{l,CL}}^{\mathrm{ca}})}{0.5\mu_l (\delta_{\mathrm{CL}}^{\mathrm{ca}} + \delta_{\mathrm{MPL}}^{\mathrm{ca}}) \delta_{\mathrm{CL}}^{\mathrm{ca}}} - M_{H_2O} S_{\mathrm{pc}}^{\mathrm{ca}}, \tag{5.28}$$

where the CL vapor concentration is determined by the vapor flux into or out of the CL, and the source terms due to ionomer water absorption or desorption (S_{ad}) and the phase change process (S_{pc}). Similarly, the CL liquid accumulation is affected by the capillary transport of water and its evaporation or condensation. In the above equations, $\mathcal{R}_{\mathrm{v}}$ denotes the total diffusive and convective transport resistance for water vapor:

$$\mathcal{R}_{\mathrm{v}} = \frac{\delta_{\mathrm{CL}}}{D_{H_2O,\mathrm{CL}}^{\mathrm{eff}}} + \frac{\delta_{\mathrm{MPL}}}{D_{H_2O,\mathrm{MPL}}^{\mathrm{eff}}} + \frac{\delta_{\mathrm{GDL}}}{D_{H_2O,\mathrm{GDL}}^{\mathrm{eff}}} + \frac{D_{\mathrm{h}}}{Sh \cdot D_{H_2O}}, \tag{5.29}$$

where the first three terms are diffusive resistances to vapor transport across the cell layers and the last term is the convective resistance to vapor transport between the channel and

the GDL. Further calculation details can be found in Chapter 2.

The above state equations describe the reduced-order model of the fuel cell. In addition to these states, the state vector for the control-oriented model of the entire system includes the compressor and manifold filling dynamic states and is given by:

$$\boldsymbol{x} = \left[\lambda_{\mathrm{CL}}^{\mathrm{an}},\, \lambda_{\mathrm{CL}}^{\mathrm{ca}},\, \lambda_{\mathrm{mb}},\, T_{\mathrm{mb}},\, c_{\mathrm{v,CL}}^{\mathrm{an}},\, c_{\mathrm{v,CL}}^{\mathrm{ca}},\, s_{\mathrm{CL}}^{\mathrm{an}},\, s_{\mathrm{CL}}^{\mathrm{ca}},\, \omega_{\mathrm{cp}},\, p_{\mathrm{sm}},\, p_{\mathrm{ca}}\right]^{\intercal}. \tag{5.30}$$

The model inputs and outputs are identical to the full-order plant model shown in equations 5.18 and 5.19, respectively. In addition to the outputs, the following vector of constrained variables is predicted by the model:

$$\boldsymbol{z} = \left[E_{\mathrm{cell}},\, z_{\mathrm{surge}},\, z_{\mathrm{choke}},\, St_{O_2},\, \Delta T_{\mathrm{cool}}\right]^{\intercal}, \tag{5.31}$$

where E_{cell} and St_{O_2} are given by equations 2.60 and 5.11, respectively, ΔT_{cool} denotes the change in the coolant temperature (determined by equation 5.13), and z_{surge} and z_{choke} are the linear approximations for compressor surge and choke constraints, respectively, given by:

$$z_{\mathrm{surge}} = \frac{p_{\mathrm{sm}}}{p_{\mathrm{atm}}} - 50\, W_{\mathrm{cp}}, \tag{5.32}$$

$$z_{\mathrm{surge}} = \frac{p_{\mathrm{sm}}}{p_{\mathrm{atm}}} - 15.27\, W_{\mathrm{cp}}. \tag{5.33}$$

The variables contained in $\boldsymbol{z}$ are used to ensure safety constraints for the system operation (see Section 5.3).

The reduced-order model can be summarized as follows:

$$\begin{aligned} \dot{\boldsymbol{x}} &= \boldsymbol{f}(\boldsymbol{x}, \boldsymbol{u}, \boldsymbol{\Lambda}) \\ \boldsymbol{y} &= \boldsymbol{g}(\boldsymbol{x}, \boldsymbol{u}, \boldsymbol{\Lambda}) \\ \boldsymbol{z} &= \boldsymbol{h}(\boldsymbol{x}, \boldsymbol{u}, \boldsymbol{\Lambda}) \end{aligned} \tag{5.34}$$

where $\boldsymbol{x} \in \mathbb{R}^{11\times 1}$, $\boldsymbol{u} \in \mathbb{R}^{6\times 1}$, and $\boldsymbol{y} \in \mathbb{R}^{2\times 1}$ denote the state, input, and output vectors,

respectively, and $\boldsymbol{z} \in \mathbb{R}^{5\times 1}$ is the vector of constrained variables. Moreover, $\boldsymbol{\Lambda}$ is the vector containing the varying parameters of the reduced model that are obtained from the full-order model. In particular, it contains ionomer relaxation parameters (s_{relax}), PtO coverage (θ_{PtO}), diffusion resistances to vapor ($\mathcal{R}_{\text{v}}$) and reactant transport ($\mathcal{R}_{\text{rct}}$), thermal resistance on both sides of the cell ($\mathcal{R}_T$), and liquid pressure in the MPLs ($p_{\text{l,MPL}}$).

5.3 Control Problem Formulation

As mentioned earlier, our control objective is to track a power demand while maximizing the overall system efficiency and satisfying constraints that stem from safety or degradation considerations. Moreover, we aim to keep the computational cost low for feasibility of online implementation. Accordingly, we use an LTV-MPC framework [351–353], which allows for handling of various constraints on states and inputs with significantly lower computational burden compared to nonlinear MPC. The different steps of our formulation are described in detail below.

5.3.1 Linearized Dynamics and Augmented System Formation

We start our control design by linearizing the reduced-order dynamics about the current operating point to allow for linear quadratic MPC formulation. To this end, we note that the dynamics are linearized about a *non-equilibrium* point, $(\boldsymbol{x}_0, \boldsymbol{u}_0, \boldsymbol{\Lambda}_0)$, which leads to an additional term as follows:

$$\dot{\boldsymbol{x}} = \boldsymbol{f}(\boldsymbol{x}, \boldsymbol{u}, \boldsymbol{\Lambda}) \Rightarrow \dot{\boldsymbol{\xi}} = \mathbf{A}\boldsymbol{\xi} + \mathbf{B}\boldsymbol{\eta} + \boldsymbol{f}(\boldsymbol{x}_0, \boldsymbol{u}_0, \boldsymbol{\Lambda}_0) \tag{5.35}$$

$$\boldsymbol{y} = \boldsymbol{g}(\boldsymbol{x}, \boldsymbol{u}, \boldsymbol{\Lambda}) \Rightarrow \Delta\boldsymbol{y} = \mathbf{C}\boldsymbol{\xi} + \mathbf{D}\boldsymbol{\eta} \tag{5.36}$$

$$\boldsymbol{z} = \boldsymbol{h}(\boldsymbol{x}, \boldsymbol{u}, \boldsymbol{\Lambda}) \Rightarrow \Delta\boldsymbol{z} = \mathbf{C}_z\boldsymbol{\xi} + \mathbf{D}_z\boldsymbol{\eta} \tag{5.37}$$

where $\boldsymbol{\xi}$ and $\boldsymbol{\eta}$ are the state and input *deviations* from the linearization point, respectively. We note that the linearization is done analytically offline and the parameterized matrices are evaluated online to obtain an updated linear model. To time-discretize the continuous linear model, we use zero-order hold, which yields [357]:

$$\boldsymbol{\xi}_{k+1} = \mathbf{A}_d \boldsymbol{\xi}_k + \mathbf{B}_d \boldsymbol{\eta}_k + \mathbf{A}^{-1}(\exp(\mathbf{A}T_s) - \mathbf{I})\boldsymbol{f}(\boldsymbol{x}_0, \boldsymbol{u}_0, \Lambda_0) \tag{5.38}$$

where T_s denotes the sampling time for the system, $\mathbf{I}$ is the identity matrix of appropriate size, and the d subscript is used to represent matrices that are obtained after time discretization.

Following the above linearization, we use the rate-based formulation [358,359] for our MPC design. This approach enables zero-offset tracking, while allowing for constraints to be imposed on the rates of change of the inputs and states. Constraining input rate of change allows us to account for actuator dynamics without the need to explicitly model them, while the constraints on the rate of change of the states can help reduce degradation. Accordingly, we form the following augmented system for the rate-based formulation:

$$\boldsymbol{x}^{\text{aug}} = \left[\boldsymbol{\Delta\xi}^{\mathsf{T}},\, e,\, P_{\text{frac}},\, \boldsymbol{\xi}^{\mathsf{T}},\, \boldsymbol{\eta}^{\mathsf{T}}\right]^{\mathsf{T}}, \tag{5.39}$$

where the first element is the *change in deviation* from the linearization state, the second element is the power tracking error $e = P_{\text{command}} - P_{\text{net}}$, the third element denotes the fraction of generated power consumed by auxiliary components (equation 5.16), the fourth element is the deviation from the linearization state, and the last element represents the deviation from the inputs about which the system is linearized. It should be noted that $\boldsymbol{\xi}$ and $\boldsymbol{\eta}$ are only included in the augmented system to allow for constraints to be imposed on the states and inputs. The discretized state and constrained output equations of the

augmented system are given by:

$$\boldsymbol{x}_{k+1}^{\text{aug}} = \mathbf{A}^{\text{aug}}\boldsymbol{x}_k^{\text{aug}} + \mathbf{B}^{\text{aug}}\Delta\boldsymbol{\eta}_k, \tag{5.40}$$

$$\boldsymbol{\Delta z}_k = \mathbf{C}_z^{\text{aug}}\boldsymbol{x}_k^{\text{aug}}. \tag{5.41}$$

The system matrices are as follows:

$$\mathbf{A}^{\text{aug}} = \begin{bmatrix} \mathbf{A}_d & \mathbf{0} & \mathbf{0} & \mathbf{0} \\ \mathbf{C}_d & \mathbf{I} & \mathbf{0} & \mathbf{0} \\ \mathbf{I} & \mathbf{0} & \mathbf{I} & \mathbf{0} \\ \mathbf{0} & \mathbf{0} & \mathbf{0} & \mathbf{I} \end{bmatrix}, \quad \mathbf{B}^{\text{aug}} = \begin{bmatrix} \mathbf{B}_d \\ \mathbf{D}_d \\ \mathbf{0} \\ \mathbf{I} \end{bmatrix},$$

$$\mathbf{C}_z^{\text{aug}} = \left[\mathbf{0},\, \mathbf{0},\, \mathbf{C}_{z_d},\, \mathbf{D}_{z_d}\right],$$

where $\mathbf{0}$ and $\mathbf{I}$ denote zero and identity matrices of appropriate sizes, respectively.

5.3.1.1 Command Preview

In the above formulation, we assume that the command, *i.e.*, the requested power, remains constant (at its current value) throughout the prediction horizon of MPC. However, this is rarely the case in applications, as the command typically varies with time even within the prediction horizon. While the above approach can successfully track slowly varying commands, it may fail when the command changes rapidly. To allow for improved tracking under such circumstances, a command preview can be used [360, 361], where we assume that the time-varying command is known over a certain time horizon. The augmented system dynamics can be further modified to enable this command preview. Particularly, we modify the error dynamics based on the changing command:

$$e_{k+1} = \mathbf{C}_{d,1}\boldsymbol{\Delta\xi}_k + \mathbf{D}_{d,1}\boldsymbol{\Delta\eta}_k + e_k - \Delta r_k, \tag{5.42}$$

where $\mathbf{C}_{d,1}$ and $\mathbf{D}_{d,1}$ represent the first rows of the $\mathbf{C}_d$ and $\mathbf{D}_d$ matrices, respectively. Furthermore, $\Delta r_k = r_{k+1} - r_k$ and r_k denote the change in command and the command at time k, respectively. The command dynamics are then given by:

$$\widetilde{\boldsymbol{\Delta r}}_{k+1} = \mathbf{A}_r \widetilde{\boldsymbol{\Delta r}}_k, \tag{5.43}$$

where $\mathbf{A}_r$ and $\widetilde{\boldsymbol{\Delta r}}_k$ are as follows:

$$\mathbf{A}_r = \begin{bmatrix} \mathbf{0} & \mathbf{I} & \mathbf{0} & \dots & \mathbf{0} \\ \mathbf{0} & \mathbf{0} & \mathbf{I} & \dots & \mathbf{0} \\ \vdots & \vdots & \ddots & \ddots & \mathbf{0} \\ \mathbf{0} & \dots & \dots & \mathbf{0} & \mathbf{I} \\ \mathbf{0} & \dots & \dots & \mathbf{0} & \mathbf{I} \end{bmatrix},$$

$$\widetilde{\boldsymbol{\Delta r}}_k = \left[\Delta r_k,\, \Delta r_{k+1},\, \dots,\, \Delta r_{k+N_r}\right]^\mathsf{T}.$$

In the above relation, N_r denotes the preview horizon, beyond which the command is assumed to remain constant.

5.3.2 MPC Cost Function

The MPC cost for the rate-based formulation consists of quadratic stage and terminal costs:

$$J_N = (\boldsymbol{x}_{N_p}^{\text{aug}})^\mathsf{T} \mathbf{P}_N \boldsymbol{x}_{N_p}^{\text{aug}} + \sum_{k=0}^{N_p-1} \left[(\boldsymbol{x}_k^{\text{aug}})^\mathsf{T} \mathbf{Q}^{\text{aug}} \boldsymbol{x}_k^{\text{aug}} \right] + \sum_{k=0}^{N_u-1} \left[\Delta \boldsymbol{\eta}_k^\mathsf{T} \mathbf{R} \Delta \boldsymbol{\eta}_k \right] + \boldsymbol{\epsilon}^\mathsf{T} \boldsymbol{\mu} \boldsymbol{\epsilon}, \tag{5.44}$$

where the terminal cost is formulated based on the solution to the discrete algebraic Riccati equation (DARE) for the $[\boldsymbol{\Delta\xi}^\mathsf{T},\, e]^\mathsf{T}$ subsystem and is used to ensure closed-loop stability. Specifically, letting $\mathbf{P}_\infty$ denote the solution to the corresponding DARE, the

terminal penalty is given by:

$$\mathbf{P}_N = \begin{bmatrix} \mathbf{P}_\infty & \mathbf{0} \\ \mathbf{0} & \mathbf{0} \end{bmatrix}. \tag{5.45}$$

In the cost shown in equation 5.44, $\mathbf{Q}^{\text{aug}}$ and $\mathbf{R}$ are weighting matrices of appropriate size. Particularly, $\mathbf{Q}^{\text{aug}}$ is given by:

$$\mathbf{Q}^{\text{aug}} = \text{diag}\left(\mathbf{0},\, Q_e,\, Q_P,\, \mathbf{0},\, \mathbf{Q}_u\right), \tag{5.46}$$

where $\text{diag}(\cdot, \ldots, \cdot)$ denotes a block-diagonal matrix structure composed of the arguments. Finally, the last term in the cost is used to penalize violation of soft constraints, where $\boldsymbol{\epsilon}$ is the vector of slack variables (see Section 5.3.3). Additionally, we note that the formulation allows for different prediction (N_p) and control (N_u) horizons to be used (see Fig. 5.1). This is done to maintain a low computational cost by using a short control horizon while ensuring stability with a long prediction horizon. Particularly, when the control horizon is shorter than the prediction horizon, the control inputs remain unchanged beyond the control horizon and the model is simulated with a constant control input until the end of the prediction horizon. Therefore, the MPC has to solve for fewer control actions, which simplifies the optimization.

5.3.3 MPC Constraints

The actuator limits are taken into account by imposing the following input constraints:

$$30\% \leq RH_{\text{an}} \leq 100\%, \quad 30\% \leq RH_{\text{ca}} \leq 100\%,$$

$$65\,^\circ\text{C} \leq T_{\text{cool,in}} \leq 80\,^\circ\text{C}, \quad 60\,\text{V} \leq v_{\text{cm}} \leq 240\,\text{V},$$

$$0.05\,\text{A/cm}^2 \leq i_{\text{dens}} \leq 1.75\text{A/cm}^2, \quad 0.1\,\text{kg/s} \leq \dot{m}_{\text{cool}} \leq 4\,\text{kg/s}.$$

The above constraints are motivated by the fuel cell system capabilities. In case of the current density, we note that the lower bound is used to ensure operation away from the OCV, which is a known catalyst and membrane stressor [4]. The current density upper bound is chosen based on the compressor's capability to maintain a safe oxygen stoichiometry.

In addition to limits on the inputs, the rates of change of the inputs are also constrained. This is done to account for the actuator dynamics that are not explicitly modeled. For instance, the coolant temperature cannot change instantaneously due to the dynamics associated with the heater and radiator. Therefore, such dynamic limits are taken into account as follows:

$$|\Delta \mathrm{RH}_{\mathrm{an}}| \leq 10\%\, 1/\mathrm{s} \times T_{\mathrm{s}}, \quad |\Delta \mathrm{RH}_{\mathrm{ca}}| \leq 10\%\, 1/\mathrm{s} \times T_{\mathrm{s}},$$

$$|\Delta T_{\mathrm{cool,in}}| \leq 0.1\,^{\circ}\mathrm{C/s} \times T_{\mathrm{s}}, \quad |\Delta v_{\mathrm{cm}}| \leq 10\,\mathrm{V/s} \times T_{\mathrm{s}},$$

$$|\Delta i_{\mathrm{dens}}| \leq 0.5\ \mathrm{A/(cm^2 \cdot s)} \times T_{\mathrm{s}}, \quad |\Delta \dot{m}_{\mathrm{cool}}| \leq 0.2\ \mathrm{kg/s^2} \times T_{\mathrm{s}},$$

Note that the above constraints on the actuators are all enforced as hard constraints, *i.e.*, no constraint violation is allowed.

We also consider safety and degradation constraints that are imposed on the dynamic states or their rates of change, as well as the auxiliary $\boldsymbol{z}$ variables in equation 5.31. In particular, to ensure membrane durability we enforce:

$$5 \leq \lambda_{\mathrm{CL}} \leq 14, \quad 7 \leq \lambda_{\mathrm{mb}} \leq 14,$$

$$|\Delta \lambda_{\mathrm{mb}}| \leq 1\ 1/\mathrm{s} \times T_{\mathrm{s}}, \quad T_{\mathrm{mb}} \leq 87\,^{\circ}\mathrm{C}.$$

These constraints are imposed to avoid subjecting the membrane to significant hydration and dehydration cycles and inhibit its excessive heating. Furthermore, the rate of change of the membrane hydration is constrained, since it controls the mechanical stresses in the membrane that can lead to crack initiation or propagation.

The safe operation of the compressor is guaranteed through the following constraints:

$$40\,\text{kRPM} \leq \omega_{\text{cp}} \leq 100\,\text{kRPM},$$

$$z_{\text{surge}} \leq -0.1, \quad 0.6 \leq z_{\text{choke}},$$

$$1.5\,\text{bar} \leq p_{\text{sm}} \leq 3.5\,\text{bar}.$$

Moreover, to ensure robust and sufficient supply of reactants to the active sites in the CLs we impose the following limits:

$$1.5 \leq St_{O_2}, \quad 1.2\,\text{bar} \leq p_{\text{ca}} \leq 3.0\,\text{bar},$$

$$s_{\text{CL}} \leq 0.3, \quad 0.2\,\text{V} \leq E_{\text{cell}} \leq 0.9\,\text{V},$$

where the constraints on St_{O_2} and p_{ca} are used to ensure sufficient delivery of oxygen to the cathode channels at a high enough pressure and the constraint on s_{CL} and the lower bound for E_{cell} guarantee sufficient reactant concentration at the Pt surfaces. The upper bound for E_{cell} is essentially clipping the cell voltage for improved catalyst durability [57]. We also note that the hydrogen stoichiometry is assumed to be constant at 1.5.

Lastly, to avoid excessive heating of the cell, the change in the coolant temperature is limited:

$$\Delta T_{\text{cool}} \leq 10\,^{\circ}\text{C}.$$

We note that the safety and degradation constraints are all imposed as soft constraints with slack variables ($\boldsymbol{\epsilon}$) to ensure feasibility of the problem (see equation 5.44).

Overall, these constraints ensure safe and reliable operation of the entire fuel cell system and are used to extend the useful lifetime of the fuel cell stack. We note that it is the type of constraints that is of interest in this work rather than the specific numerical bounds used here, as such numerical values can be updated when the fuel cell system is extensively characterized based on safety and durability considerations.

5.3.4 MPC Optimization

To formulate the optimization problem we use the so-called *batch approach* [362], wherein the linearized dynamics are utilized to describe all future states in terms of the current states and future inputs. Following this approach and considering the constraints described above, we obtain the optimization problem below, which is a quadratic program (QP):

$$\begin{aligned} \underset{\boldsymbol{U}}{\text{minimize}} \quad & J_N = (\boldsymbol{U})^{\mathsf{T}} \mathbf{H} \boldsymbol{U} + \mathbf{2} \boldsymbol{q}^{\mathsf{T}} \boldsymbol{U} \\ \text{subject to} \quad & \mathbf{G} \boldsymbol{U} \leq \boldsymbol{W} + \mathbf{T} \boldsymbol{x}_0^{\text{aug}} \end{aligned} \tag{5.47}$$

where $\boldsymbol{U}$ is the input vector over the control horizon augmented with the slack variables:

$$\boldsymbol{U} = \left[\boldsymbol{\Delta\eta}_1^{\mathsf{T}}, \ldots \boldsymbol{\Delta\eta}_{N_u}^{\mathsf{T}}, \boldsymbol{\epsilon}^{\mathsf{T}} \right]^{\mathsf{T}}. \tag{5.48}$$

Derivation of the cost and constraint matrices in the above QP is straightforward and can also be found in the literature [362, 363].

5.3.5 MPC Tuning (Weights and Horizons)

The weighting matrices are chosen as follows:

$$Q_e = 50, \quad Q_P = 10, \quad \mathbf{Q}_u = \text{diag}\left(0,\, 2,\, 0,\, 0,\, 5,\, 0\right),$$
$$\mathbf{R} = \text{diag}\left(5,\, 5,\, 5,\, 0.05,\, 1,\, 2.5\right).$$

These weights are chosen to penalize the tracking error ($Q_e = 50$) and ensure offset-free tracking of the power demand when possible, while minimizing the power consumption by auxiliary equipment ($Q_P = 10$). Moreover, two of the system inputs are penalized (nonzero elements in $\mathbf{Q}_u$). Specifically, since hydrogen consumption is directly related to the stack current (assuming constant hydrogen stoichiometry), the current density is

penalized with a weight of 5 to minimize the fuel consumption. In addition, a small penalty (weight of 2) is imposed on the cathode channel RH to minimize the humidification requirements and explore opportunities for downsizing the humidifier. We also note that only the cathode RH is penalized, since humidifying the cathode requires a larger humidifier due to higher air mass flow rates compared to the hydrogen flow rates in the anode. The rates of change of the inputs are also penalized ($\mathbf{R}$), wherein the weights are chosen based on the scales of the inputs. Lastly, to obtain the terminal penalty, the DARE is solved with $\mathbf{R}_\infty = \mathbf{R}$ and:

$$\mathbf{Q}_\infty = \mathrm{diag}\left(\mathbf{0},\, Q_e,\, Q_P\right).$$

Regarding the MPC prediction and control horizons, we note that longer horizons typically improve the controller performance while increasing its computational cost [362]. However, the optimal choice of the prediction horizon depends on the particular problem. Here, a relatively long prediction horizon is needed to effectively control the membrane hydration state, since it has slow dynamics compared to other system states. However, longer prediction horizons may in fact lead to deteriorated performance with the current formulation. This is due to the fact that the reduced-order model is much simpler than the plant model and requires frequent updates based on the full-state feedback from the full-order model. Additionally, the MPC uses a linearized version of this simplified model, whose deviations from the original nonlinear model become more significant over time. The fact that linearization is done about a non-equilibrium point further contributes to this discrepancy.

To determine a good prediction horizon, a number of numerical experiments were conducted with the step profile shown in Section 5.4. Particularly, values of $N_p = 10$ to $N_p = 35$ were tested. It was found that a prediction horizon of $N_p = 20$ strikes a good balance between performance and computational cost. The same procedure was

used to determine the control horizon, where horizons between $N_u = 4$ and $N_u = 10$ were studied and a control horizon of $N_u = 5$ was found to yield good performance with minimal computational costs. Therefore, we set $N_p = 20$ and $N_u = 5$ for the simulations in Section 5.4.

5.3.6 Numerical Implementation

The entire degradation-conscious control framework is implemented in MATLAB. Particularly, the plant model is integrated with the stiff solver `ode23t`. The reduced-order dynamics are analytically linearized using CasADi [364]. The QP matrices are formulated using in-house MATLAB code and the optimization is solved with the Operator Splitting Quadratic Program (OSQP) solver [365] that uses the alternating direction method of multipliers (ADMM) [366]. A tolerance of 10^{-5} and a maximum number of iterations of 1000 are used. When a number of constraints become active, this iteration limit is reached. Nevertheless, our numerical experiments show negligible improvements in performance or constraint satisfaction when the algorithm is allowed to iterate longer to ensure convergence. Therefore, this maximum iteration limit was chosen to balance the algorithm convergence with its computational requirements. The framework is implemented using custom-written MATLAB code and run on a computer with a 2.5 GHz processor and 16 GB of RAM.

5.4 Simulation Case Studies

In this section we study the utility of the proposed framework with a variety of power demand profiles and discuss the robustness to parametric uncertainty and the impact of command preview.

5.4.1 Power Profile with Step Changes in the Demand

In the first case study, we consider a power demand profile that consists of several increasing and decreasing step changes in the load as shown in Fig. 5.3. Moreover, the profile also includes a high power demand that is not feasible for the fuel cell system considered in this work. This infeasible demand is used to illustrate the controller's ability in satisfying the various safety and degradation constraints while pushing the system to its limits. As can be observed in Fig. 5.3, the controller enables offset-free tracking of the power demand, where the net power generated by the system rapidly converges to the demand level after a step change. However, in some cases the controller response is slower to ensure the constraints are satisfied.

With regards to the fuel cell conditions, Fig. 5.3 illustrates that the controller successfully maintains the membrane hydration within the desired range. Similarly, the membrane temperature is maintained below the critical value, the liquid accumulation in the cathode catalyst layer is kept below 0.3, and sufficient oxygen delivery is ensured by sustaining the oxygen stoichiometry above 1.5. The figure also shows the compressor efficiency map with the trajectory of compressor model states overlaid. The controller successfully avoids compressor surge and choke and ensures sufficient pressure in the supply manifold. Moreover, the compressor efficiency is maximized (the efficiency is always greater than 72%). Lastly, the change in the coolant temperature is controlled to be below 10 °C to ensure the system is not overheated. Slight violations of some of the constraints are observed, which are due to the fact that these constraints are imposed as soft constraints to ensure feasibility. In practice, the constraints can be made tighter, if needed, to ensure safety and longevity are not compromised with such slight violations.

The inputs to the fuel cell system generated by the degradation-conscious controller are shown in Fig. 5.4. We note that all of the actuation limits are respected. The coolant flow rate is minimized to reduce the auxiliary power loss. Furthermore, the cathode

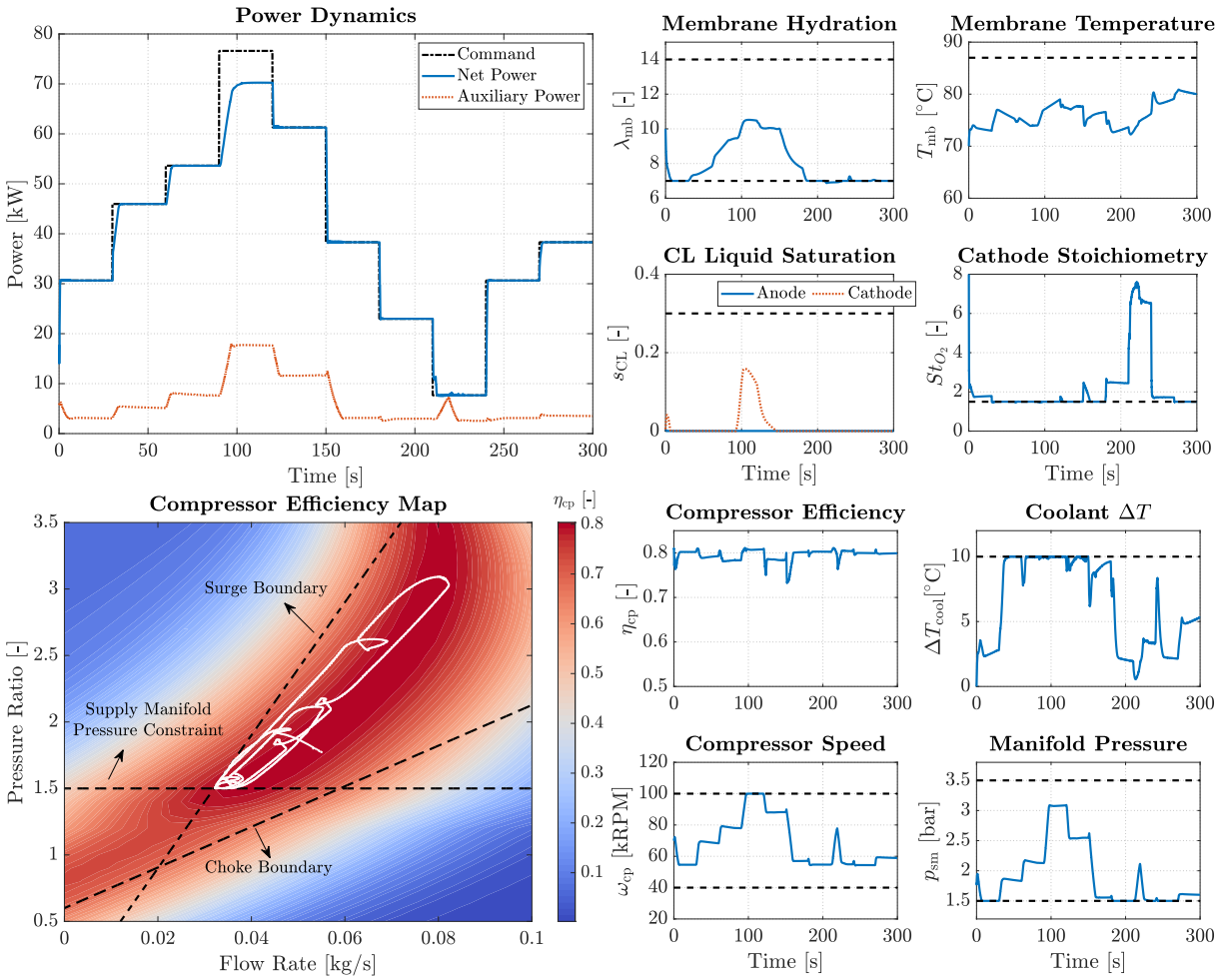

Figure 5.3: Power and system state trajectories for step changes in power demand. The dashed black lines indicate system constraints. The compressor state trajectories are overlaid on the compressor efficiency map, where the surge and choke constraints are also shown.

channel RH is minimized to reduce humidification requirements. Particularly, at higher loads, the membrane is hydrated with ORR product water. It is only at lower current densities that inlet humidification is deemed necessary to ensure sufficient hydration of the membrane. Another interesting observation is that after the load is reduced at 210 s, the controller builds up pressure in the cathode channel by running the compressor faster. This helps to initially compensate for lack of humidification. Once the cathode feed is sufficiently humidified, the compressor speed is reduced to minimize compressor power consumption.

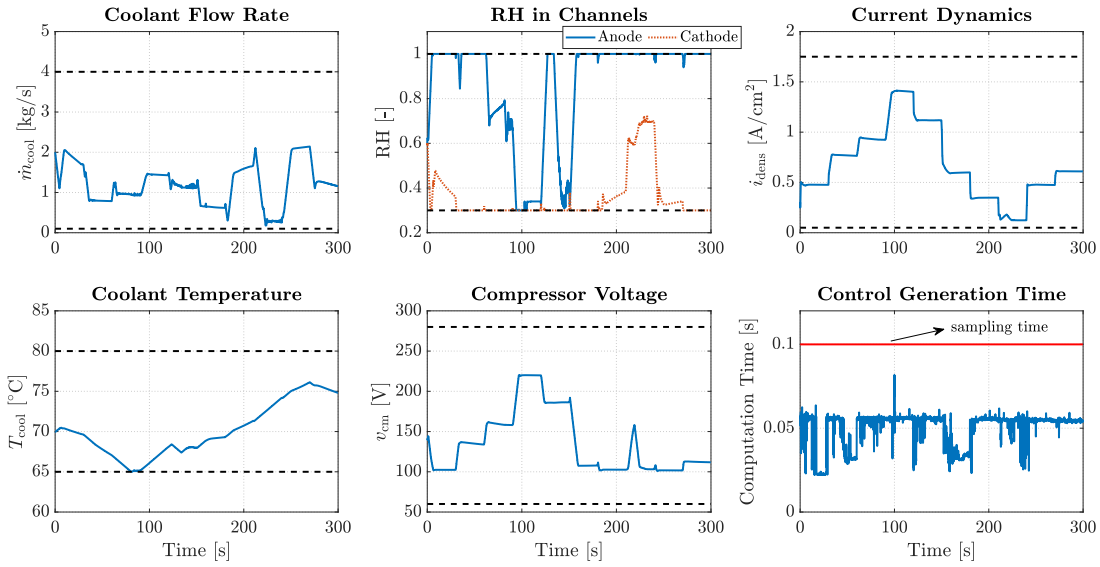

Figure 5.4: System input trajectories and their computation time for arbitrary power profile of Fig. 5.3. The input limits are shown as dashed black lines.

Fig. 5.4 also shows the time required to formulate and solve the QP of equation 5.48, where the computational time is seen to be consistently less than the sampling time. Note that the computation times shown in the figure also include the time to evaluate the analytically linearized dynamics and form the QP matrices. Therefore, the problem can be efficiently formulated and solved in real time on the hardware platform used in this chapter. Nonetheless, since embedded hardware is typically far less powerful than a desktop computer, further computational simplifications may be needed in practice.

One approach to reduce the computational burden in practice is to use a longer execution horizon (N_e), *i.e.*, instead of just using the first move, we can use the first few entries in the control sequence generated by the optimizer. The results from such an approach are shown in Fig 5.5, where the execution horizon is increased from 1 to 4 steps. We observe a slight deterioration in controller performance with increasing execution horizon. Particularly, as shown in the inset for the power dynamics plot, the power tracking capability is slowed down when longer execution horizons are used. Moreover, the ability to recover from constraint violation is slightly reduced as shown in the inset of the

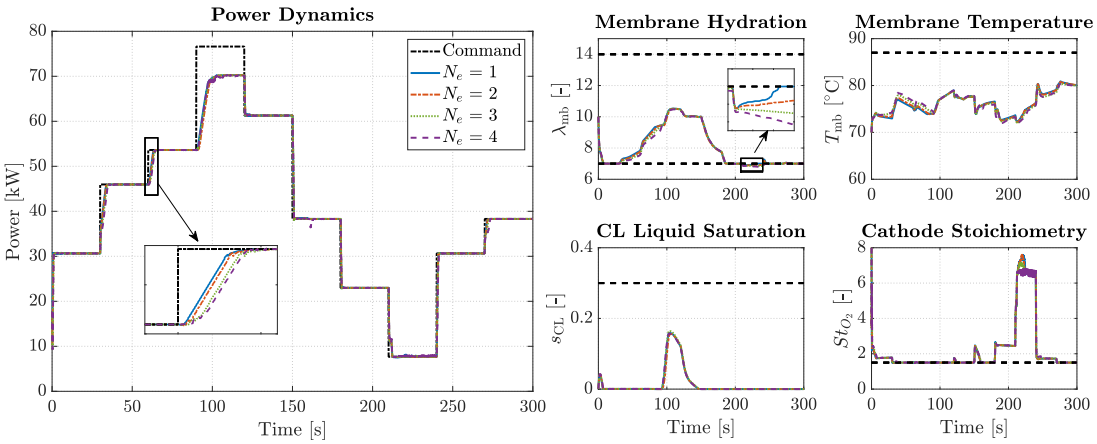

Figure 5.5: Effect of increasing execution horizon. The dashed black lines indicate system constraints.

membrane hydration plot. Nonetheless, such slight deterioration is not expected to have significant implications in terms of either the system performance or its durability. Therefore, longer execution horizons may be utilized in practice to alleviate the computational burden further, if needed.

Alternatively, a larger sampling time may be used for time-discretization. However, we have found that the controller performance is diminished more significantly with such an approach, because the resulting time-discretized linear dynamics are not able to capture the behavior of the continuous-time system.

5.4.1.1 Robustness to Parametric Uncertainty

Parametric uncertainty can deteriorate the performance of model-based controllers. To study the robustness of the proposed control framework to such uncertainties, perturbations are applied to the controller model parameters. Three example sets of perturbations are shown in Table 5.2. Note that all these perturbations are significant and lead to considerable quantitative change in the predictions of the controller model. However, we assume that the full-state feedback is not affected by these parameter perturbations. In other words, the parametric uncertainties only affect the predictions by the controller

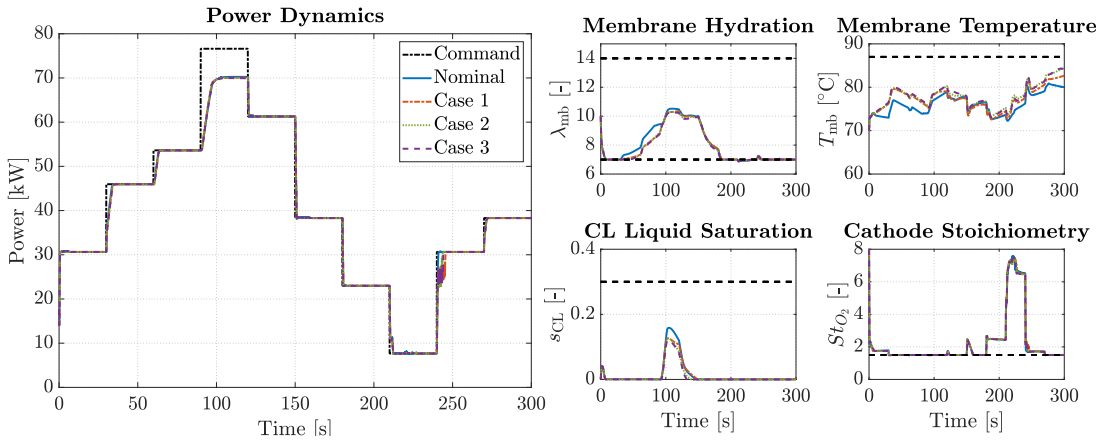

Figure 5.6: Robustness to parametric uncertainty under nominal full-state feedback. The dashed black lines indicate system constraints.

model.

Table 5.2: Considered parametric uncertainties

Case	Parameter Perturbations
1	$\delta_{\text{GDL}} \times 1.5$, $\delta_{\text{MPL}} \times 1.5$, $\alpha_{\text{ca}} + 0.2$
2	$\delta_{\text{GDL}} \times 1.5$, $\delta_{\text{MPL}} \times 1.5$, $\alpha_{\text{ca}} + 0.2$, $\varepsilon_{\text{GDL}} - 0.05$, $\varepsilon_{\text{MPL}} - 0.05$
3	$\delta_{\text{GDL}} \times 1.5$, $\delta_{\text{MPL}} \times 1.5$, $\alpha_{\text{ca}} + 0.2$, $\varepsilon_{\text{GDL}} - 0.05$, $\varepsilon_{\text{MPL}} - 0.05$, $k_T \times 0.5$

The results for all three cases of perturbations are shown in Fig. 5.6, where the results with the nominal parameter values are also shown for comparison. The controller displays good robustness to such parametric uncertainties. Particularly, the controller performance is not significantly affected by parameter perturbations as long as such perturbations do not change the *qualitative* nature of the predictions. While this is encouraging, we acknowledge that such robustness is mostly due to the perfect full-state feedback conditions assumed here. If the full-state information is affected by parametric uncertainties, the controller robustness is indeed compromised. This is illustrated in Fig. 5.7, where the

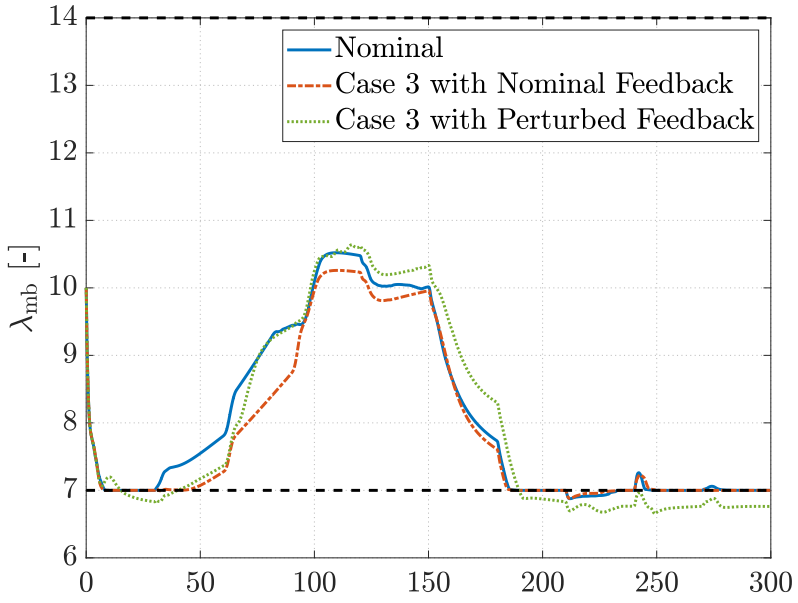

Figure 5.7: Robustness to parametric uncertainty under nominal and perturbed full-state feedback. The dashed black lines indicate hydration constraints.

membrane hydration under Case 3 perturbations with nominal and compromised feedback are compared with the case with no parameter perturbations. The figure clearly shows that constraint violation is more significant when the state feedback information is compromised due to parameter uncertainties. Under such circumstances, robust MPC approaches [367] may be sought to ensure constraint satisfaction and power tracking capabilities are maintained. Similarly, robust observer design techniques [368] can be helpful in this regard by enabling accurate state estimation despite parametric uncertainties. These topics are beyond the scope of this dissertation and can be investigated in future research.

5.4.2 Time-Varying Power Profiles

As a final step in evaluating the capabilities of the proposed degradation-conscious control framework, here we inspect its utility in following time-varying power demands, which is a more realistic scenario for automotive applications. In particular, we study several drive cycles in this subsection. To this end, the speed profile in each cycle is transformed into a

power demand profile using a simple vehicle model. The decelerating portions of a speed profile would lead to negative power. However, we limit the minimum power demand to 10 kW here, since we neither consider a hybridization scheme nor a fuel cell start-up shut-down capability in this work.

We start our analysis with the highway section of the US06 drive cycle (US06-HW). The power demand profile is shown in Fig. 5.8 along with the net power generated by the fuel cell system. We note that when no load preview is used, the controller displays a lag in following the power demand (Fig. 5.8(b)). With a preview horizon of only 5 steps (equivalent to 0.5 seconds), the power tracking capability is enhanced significantly at lower loads. Considering recent advances in human driver modeling [369] and the envisioned connected infrastructure of the future [370], it is indeed reasonable to assume a good-quality short command preview is available in real-world scenarios. Nonetheless, the system is not able to follow rapid and significant increases in the load even with the command preview, as seen at around 10 and 165 seconds in Fig. 5.8(a). This is due to the slow response of the fuel cell system and highlights the fact that hybridization is required for automotive applications.

Regarding the constraint satisfaction, Fig. 5.8 shows two of the most critical conditions, namely, membrane hydration and the oxygen stoichiometry, where it is observed that the respective constraints are successfully satisfied both with and without the command preview. However, the membrane hydration state is better maintained above the critical value with the command preview, which highlights the utility of the preview when the load is time-varying. Overall, these results indicate that the proposed framework can successfully follow time-varying power demands, while ensuring safe and enduring system operation, as determined by the constraints.

The input profiles for the US06-HW drive cycle calculated by the controller using the command preview information are shown in Fig. 5.9, where, similar to our earlier discussion, the cathode relative humidity and the coolant flow rate are minimized. Additionally,

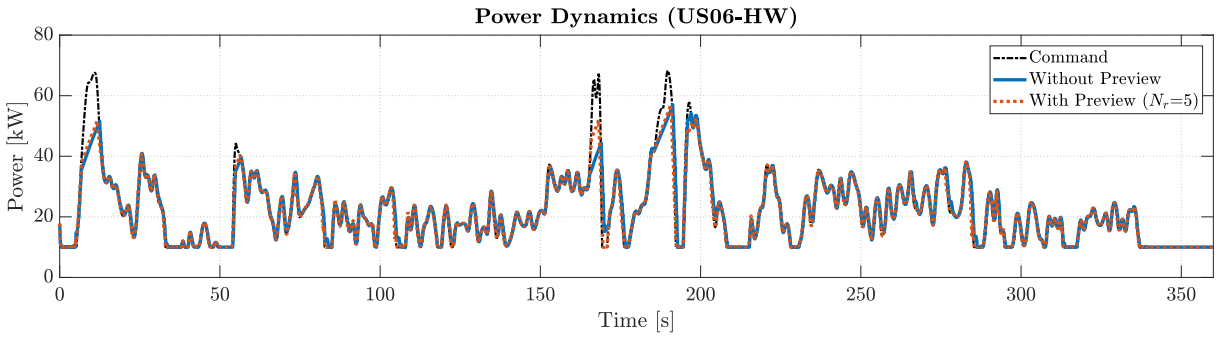

(a)

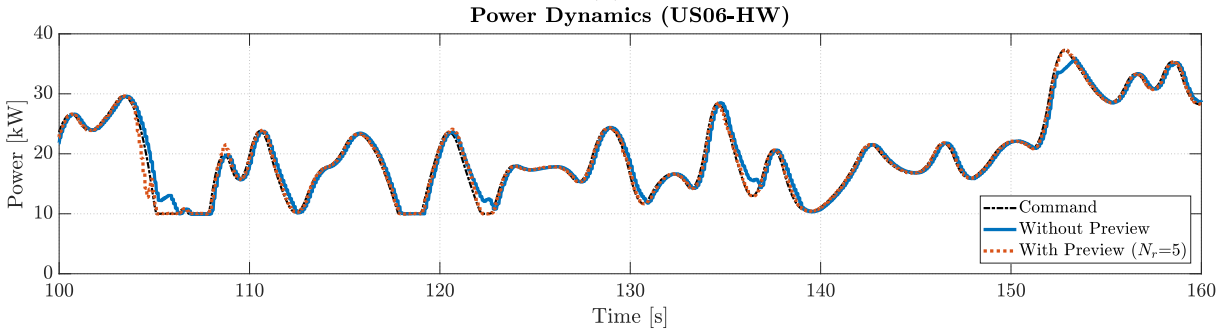

(b)

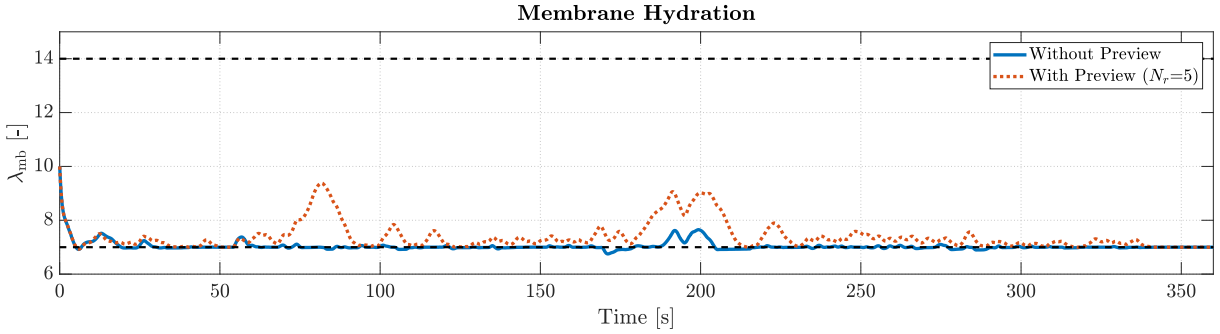

(c)

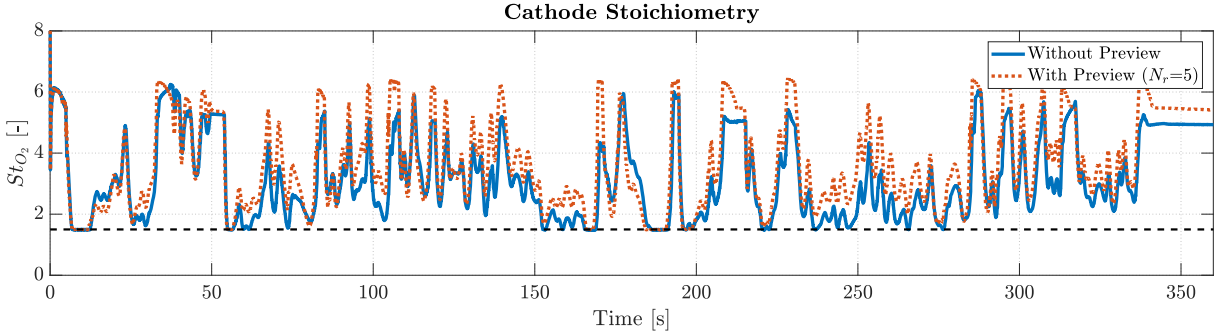

(d)

Figure 5.8: Dynamics for power and example constrained variables for US06 highway drive cycle: (a) power dynamics, (b) blown-up version of the power dynamics plot, where the effectiveness of command preview is observed, (c) membrane hydration, and (d) oxygen stoichiometry. The dashed black lines indicate system constraints.

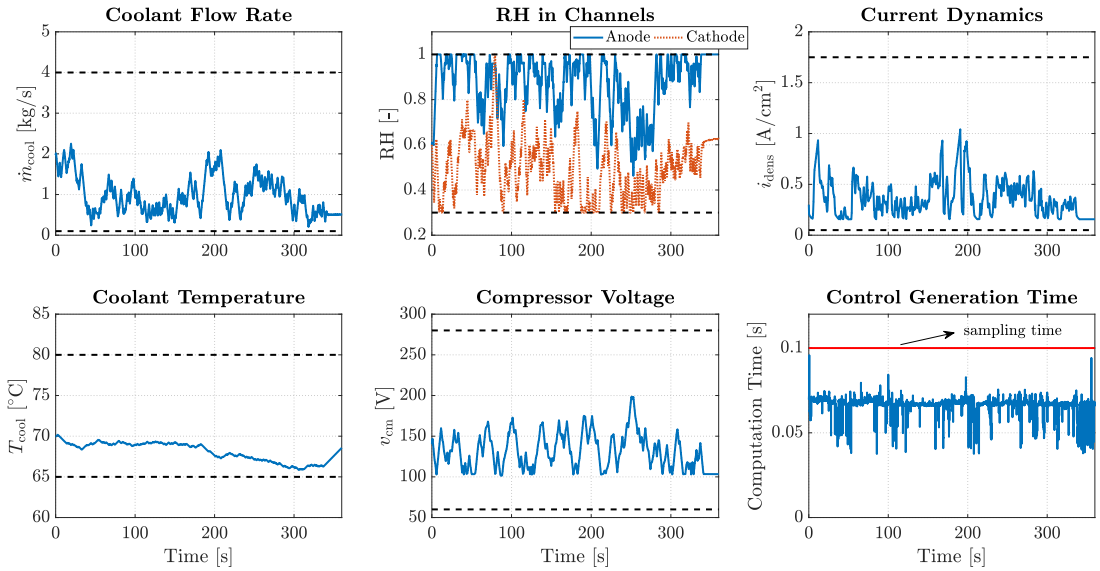

Figure 5.9: System input trajectories and their computation time for US06-HW drive cycle. The input limits are shown as dashed black lines.

the computation times for the control commands are still consistently below the sampling time.

Finally, the power profiles for four other drive cycles and the corresponding net power generation of the considered fuel cell system are shown in Fig. 5.10. The figure illustrates that the controller is indeed capable of following a variety of power demands, while satisfying the input and state constraints explained in Section 5.3.3.

Overall, these results highlight several opportunities in enhancing performance and durability of automotive PEM fuel cell systems through model-based control techniques and underline the importance of complementing material-based solutions with active control strategies to meet the cost and durability targets for these systems. Successful implementation of this framework in real-world applications requires the knowledge of proper lifetime indicators. The membrane hydration and its rate of change are among the key lifetime indicators used in this dissertation. Nonetheless, the framework allows for further such indicators to be included as they are discovered through extensive ongoing degradation studies. Therefore, the proposed framework offers a flexible strategy to meeting the

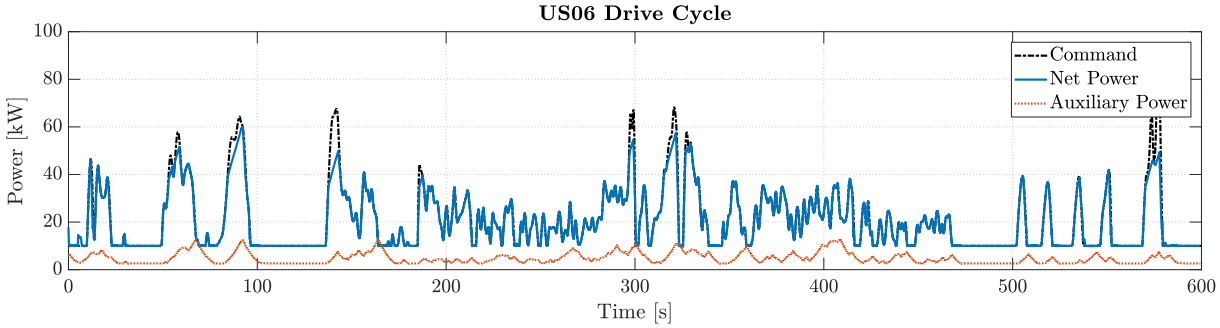

(a)

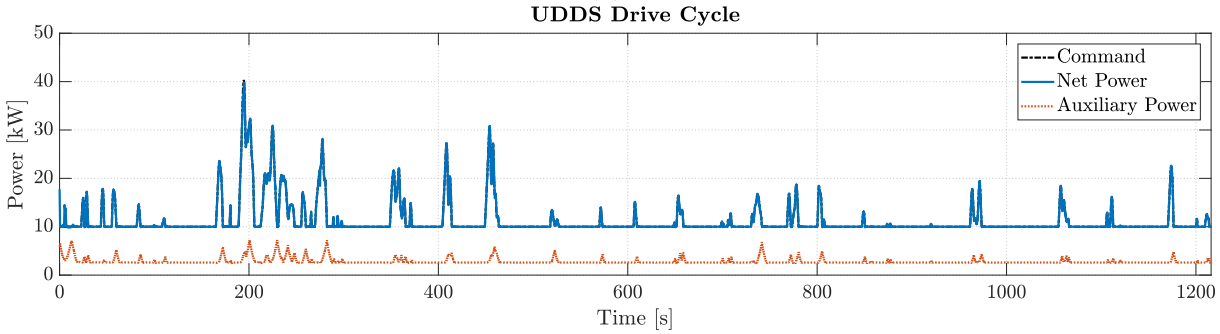

(b)

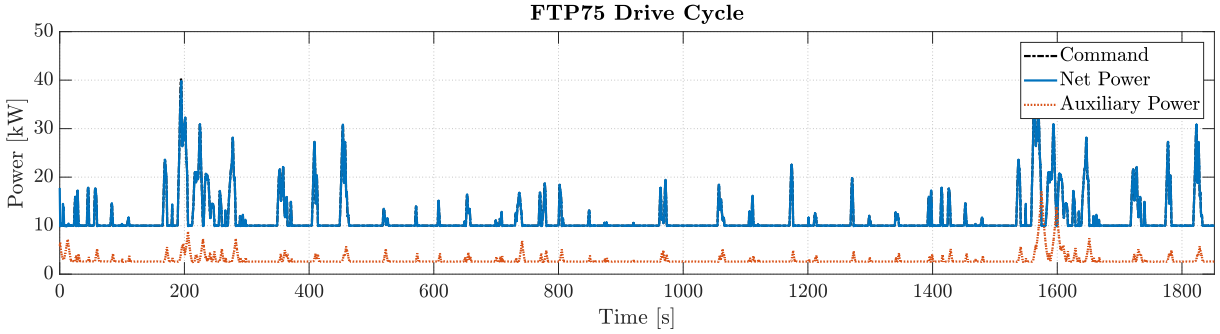

(c)

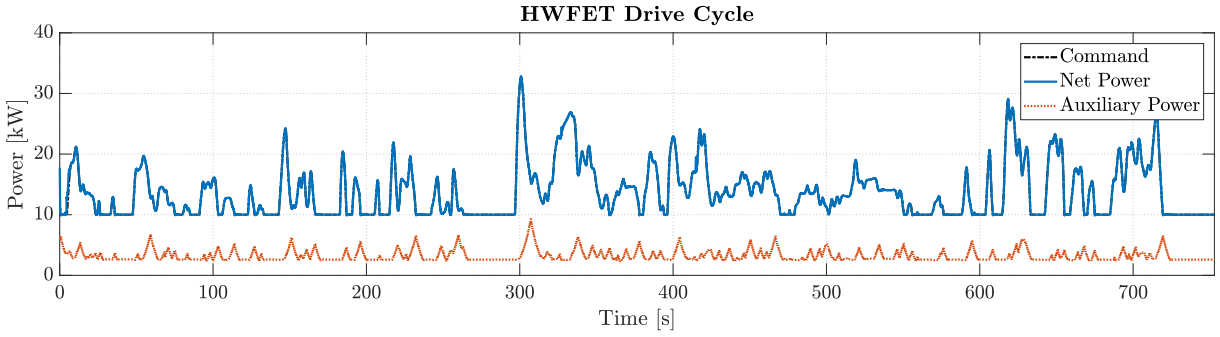

(d)

Figure 5.10: Power trajectories for different drive cycles: (a) US06, (b) UDDS, (c) FTP75, and (d) HWFET drive cycles.

increasing demands for these fuel cell systems and enabling their widespread commercialization.

5.5 Summary and Conclusions

A framework for degradation-conscious control of PEM fuel cell systems is developed. The framework employs LTV-MPC to meet a power demand, while maximizing the overall system efficiency, ensuring safe operation of the fuel cell system, and extending its lifetime. The latter two objectives are achieved by enforcing constraints on the compressor and fuel cell conditions. Particularly, these constraints are based on considerations that stem from compressor safety, membrane mechanical durability and the durability of the electrocatalyst. Moreover, the system efficiency is maximized by minimizing the fuel and auxiliary power consumption.

The framework is implemented by first developing a model of the fuel cell system that serves as the plant for our simulation-based studies. The plant model is then simplified to derive a reduced-order controller model for MPC optimization. The controller model is further simplified by linearizing it about the current operating point. This successive linearization enables the use of linear MPC formulations that lead to significant computational gains. The particular rate-based MPC formulation employed here allows us to account for actuator dynamics without the need to explicitly model the actuators. Furthermore, it enables constraint enforcement on the rate of change of the system states, which can have serious implications for fuel cell durability.

The results indicate that the proposed control framework is able to meet the requested power demand, even for time-varying profiles. Moreover, it ensures satisfaction of durability constraints and is thus expected to contribute to extending the system's lifetime. Lastly, we show that the results are calculated faster than real time in the computational hardware used in this chapter and highlight opportunities to further reduce computa-

tional cost and ensure successful implementation with embedded hardware. Therefore, the proposed framework offers a promising approach to complement the ongoing research in developing material-based solutions to address durability concerns in fuel cell systems.

Chapter 6

Summary and Outlook

6.1 Dissertation Summary

This dissertation develops a model-based degradation-conscious control framework for enhanced performance and durability of automotive PEM fuel cells. To this end, the dissertation first proposes a novel computationally efficient model of the fuel cell that can be used as a software sensor and provide critical information about the internal conditions of an operating fuel cell stack. To enable quantitatively predictive modeling, the problem of identifying the model parameters is considered extensively. Lastly, a version of the proposed model is used to develop a control framework that can be used to extend the lifetime of the fuel cell stack. Each of the specific contributions is further highlighted below.

6.1.1 Fuel Cell Modeling

Water and heat management are critical to efficient and durable operation of PEM fuel cell stacks. Information about the internal distribution of water and temperature throughout the stack is invaluable in enabling effective management strategies. However, sensor measurements for such vital information are rarely available, especially in automotive

applications. This fact motivates the need for a model that can act as software sensor and provide the much needed information about the internal conditions. Such a model has to capture the intricate physical phenomena in the fuel cell while maintaining real-time simulation capabilities that ensure the utility of the model as a software sensor. This poses a significant challenge as the underlying physical phenomena are typically modeled with a coupled system of nonlinear PDEs that require extensive computational resources to solve.

This dissertation addresses the above challenge by developing a physics-based and computationally efficient model of a PEM fuel cell in Chapter 2. Computational efficiency is achieved by taking advantage of the natural separation of length and time scales involved in the problem to spatio-temporally decouple it, developing a new reduced-order model for water balance across the MEA, and defining a new variable for cathode catalyst utilization that captures the trade-off between proton and mass transport limitations with minimal additional computational cost. Together, these considerations result in the model calculations to be carried out more than an order of magnitude faster than real time. Moreover, a new iterative scheme allows for simulation of counter-flow operation and makes the model flexible for different flow configurations. The proposed model is validated with a wide range of experimental performance measurements from two different fuel cells, where good quantitative agreement with available measurements is achieved. Finally, simulation case studies are presented to demonstrate the prediction capabilities of the model, where the results indicate the efficacy of the model in capturing complex two-phase and non-isothermal transport phenomena in all three physical direction in agreement with both experimental and high-fidelity modeling results from the literature.

The combination of the model's computational efficiency and numerical robustness, as well as the physical phenomena it captures, render the model a potentially effective tool for monitoring automotive PEM fuel cell stacks.

6.1.2 Model Parameterization

Effective model parameterization is critical to enabling quantitatively accurate predictions by physics-based models. Accordingly, this dissertation examines the problem of identifying model parameters in detail. Particularly, Chapter 3 extensively studies the sensitivities of the model predictions to different parameters. This is done by conducting an extended local sensitivity analysis for a variety of model parameters under numerous operating conditions that can be potentially used in automotive settings. The results from this extended sensitivity analysis are utilized to examine the parameter identifiability problem. It is shown that many of the parameters in such physics-based models of fuel cells are closely correlated as measured by their impact on the model outputs. The considered model predictions are consistent with outputs that are commonly measured in experimental settings, namely, the cell voltage, high frequency resistance, and membrane water crossover. Furthermore, the positive impact of additional measurements in decorrelating parameter effects is rigorously shown.

The correlation between parameter effects poses a significant challenge to successful parameter identification. To address this challenge, the dissertation develops a systematic framework for parameter identification in PEM fuel cell models in Chapter 4. The framework utilizes the extended local sensitivity results to find an optimal subset of parameters for identification. This is achieved through an optimization algorithm that maximizes the well-known D-optimality criterion. The sensitivity data are then used for optimal experimental design to ensure that the resulting experiments are maximally informative for the purpose of parameter identification. To make the experimental design problem computationally tractable, the optimal experiments are chosen from a predefined library of operating conditions. Finally, a multi-step identification algorithm is proposed to formulate a regularized and well-conditioned optimization problem. The identification algorithm benefits from the unique structure of output predictions, wherein sensitivities

to parameter perturbations typically vary with the load. To verify each component of the framework, synthetic experimental data generated with the model using nominal parameter values are used in an identification case study. The results confirm that each of these components plays a critical role in successful parameter identification.

Through the above efforts, this dissertation establishes the considerable challenges associated with successful parameter identification in the context of physics-based models of PEM fuel cells. The proposed parameter identification framework is a major contribution of this dissertation that can be used to parameterize complex fuel cell models more effectively.

6.1.3 Degradation-Conscious Control

The ultimate aim of this dissertation is to enable model-based control of PEM fuel cell systems to improve their performance and durability. Accordingly, Chapter 5 utilizes the modeling work presented in earlier chapters to develop such a control framework. Particularly, a linear time varying model predictive control framework is developed for degradation-conscious control of automotive PEM fuel cell systems. This is done by deriving a reduced-order nonlinear model of the entire system, including the reactant and coolant supply subsystems and the fuel cell stack. This nonlinear model is then successively linearized about the current operating point to obtain a linear model. The linear model is used to formulate the control problem, where a rate-based MPC formulation is employed. The particular MPC formulation enables the use of a high-fidelity model in control design without compromising computational feasibility. Using such a high-fidelity model to formulate the control problem constitutes one of the major contributions of this dissertation.

The controller objective is to ensure offset-free tracking of the power demand, while maximizing the overall system efficiency and enhancing its durability. To this end, the

fuel consumption and the power loss due to auxiliary equipment are minimized. Moreover, the internal states of the fuel cell stack are constrained to avoid harmful conditions that are known stressors of the fuel cell components. Membrane dry-out, rapid changes in the membrane hydration, and reactant starvation are among the stressors considered in this work. However, the framework has the flexibility to accommodate further lifetime indicators as required by the particular application. Simulation-based studies are carried out that showcase the utility of the proposed control framework in meeting the outlined objectives. It is also demonstrated that the control commands can potentially be generated in real time, allowing practical hardware implementation.

Given the flexibility and efficiency of the proposed degradation-conscious control framework, it is expected to complement the ongoing materials research efforts and contribute to extending the lifetime and enhancing the performance of automotive PEM fuel cell stacks.

6.2 List of Conference Presentations and Archival Publications

The above contributions have resulted in several conference presentations and publications, as well as a number of journal publications, as noted below.

6.2.1 Conference Presentations and Publications

1. A. Goshtasbi, J. Chen, J.R. Waldecker, S. Hirano, and T. Ersal. "*Robust Parameter Subset Selection and Optimal Experimental Design for Effective Parameterization of PEM Fuel Cell Models.*" 2020 American Control Conference. *Submitted.* [204]

2. A. Goshtasbi, B.L. Pence, J. Chen, J.R. Waldecker, S. Hirano, and T. Ersal. "*Soft Sensor for Real-Time Monitoring of Automotive PEM Fuel Cell Systems.*" 236th

Meeting of the Electrochemical Society, 2019. [200]

3. A. Goshtasbi, J. Chen, J.R. Waldecker, S. Hirano, and T. Ersal. "*Optimal Experimental Design for Parameter Identification of PEM Fuel Cell Models.*" 236th Meeting of the Electrochemical Society, 2019. [207]

4. A. Goshtasbi, and T. Ersal. "*Degradation-Conscious Control for PEM Fuel Cell Systems.*" 236th Meeting of the Electrochemical Society, 2019. [210]

5. A. Goshtasbi, and T. Ersal. "*LQ-MPC design for degradation-conscious control of PEM fuel cells.*" 2019 American Control Conference. IEEE, 2019. [208]

6. A. Goshtasbi, J. Chen, J.R. Waldecker, S. Hirano, and T. Ersal. "*On Parameterizing PEM Fuel Cell Models.*" 2019 American Control Conference. IEEE, 2019. [206]

7. A. Goshtasbi, B. L. Pence, and T. Ersal. "*A Real-Time Pseudo-2D Bi-Domain Model of PEM Fuel Cells for Automotive Applications.*" ASME 2017 Dynamic Systems and Control Conference. American Society of Mechanical Engineers, 2017. [198]

8. A. Goshtasbi, B. L. Pence, and T. Ersal. "*1+1D Non-Isothermal and Two-Phase Transient Model of PEM Fuel Cells for Real-Time Estimation and Control.*" 229th Meeting of the Electrochemical Society, 2016. [199]

6.2.2 Journal Publications

1. A. Goshtasbi, and T. Ersal. "*Degradation-Conscious Control for Enhanced Lifetime of Automotive Polymer Electrolyte Membrane Fuel Cells.*" 2019, *Submitted.* [202]

2. A. Goshtasbi, J. Chen, J.R. Waldecker, S. Hirano, and T. Ersal. "*Effective Parameterization of PEM Fuel Cell Models - Part II: Robust Parameter Subset Selection,*

Robust Optimal Experimental Design, and Multi-Step Parameter Identification Algorithm." 2019, *Submitted*. [205]

3. A. Goshtasbi, J. Chen, J.R. Waldecker, S. Hirano, and T. Ersal. "*Effective Parameterization of PEM Fuel Cell Models - Part I: Sensitivity Analysis and Parameter Identifiability.*" 2019, *Submitted*. [203]

4. A. Goshtasbi, B.L. Pence, J. Chen, M.A. DeBolt, C. Wang, J.R. Waldecker, S. Hirano, and T. Ersal. "*A Mathematical Model toward Real-Time Monitoring of Automotive PEM Fuel Cells.*" 2019, *Submitted*. [202]

5. A. Goshtasbi, B. L. Pence, and T. Ersal. "*Computationally Efficient Pseudo-2D non-isothermal modeling of Polymer Electrolyte Membrane Fuel Cells with Two-Phase Phenomena.*" Journal of The Electrochemical Society 163.13 (2016): F1412-F1432. [201]

6.3 Outlook

This dissertation is an initial contribution to model-based control of PEM fuel cells towards the objective of performance and durability enhancement and enabling the widespread adoption of the technology in the transportation sector. Future research can build on the foundation laid out in this work with potential advances on several fronts. Below, some important future research directions are highlighted.

6.3.1 Fuel Cell Modeling

Capturing the most salient physics with high computational efficiency is expected to remain an active area of research. Data-driven modeling of the PEM fuel cell system appears to be a particularly fertile ground for improvements in this regard. Two important

future directions can be envisioned. First, experimental fuel cell performance data can be used to construct data-driven models. This is especially useful when large historical datasets are available (as is the case with test fleet data) and can lead to significant savings in time and capital investments to develop models from first principles. Recent advances in physics-aware data-driven modeling [371, 372] are of particular interest as the main governing physical laws can be incorporated into the data-driven modeling framework. Moreover, data-driven modeling approaches can also be used to complement existing physics-based models for improved prediction accuracy.

The second important area in data-driven modeling is the use of such data-driven techniques to develop surrogate models. This is expected to be a key enabler of future high-fidelity and efficient simulations for PEM fuel cells. Such data-driven techniques can be used to model the physical phenomena across multiple time and length scales (*i.e.*, multi-scale modeling) [373], which continues to be a major challenge in fuel cell research. Moreover, surrogate models can be developed to allow for online computations of critical conditions inside a fuel cell stack on embedded hardware, that would otherwise require significant computational power.

6.3.2 Model Parameterization

Effective identification of model parameters is expected to remain a major hurdle for large-scale physics-based models of fuel cells. Several improvements to the identification framework proposed in this dissertation can be envisioned. First, improved sampling of the parameter and operating condition spaces can lead to more efficient and accurate analyses. Second, the proposed framework considers the problems of parameter subset selection and experimental design sequentially, *i.e.*, a subset of parameters is first selected for identification and the experiments are designed for this selected subset. It is expected that an algorithm that finds the optimal subset of parameters and experimental conditions

simultaneously can potentially lead to improved identification results. This approach was not pursued in this dissertation, as the resulting optimization problem could not be solved effectively and the algorithms would find a sub-optimal solution that was worse than the solution obtained with the sequential method. Novel algorithmic approaches could address this challenge and improve the parameter subset selection and optimal experimental design for identification. Lastly, this dissertation only considers point estimates for the parameters. However, inferring parameter distributions with statistical methods is expected to be more informative. This dissertation does not pursue this route due to the associated computational cost. Future reduction in cost of simulating the models and the statistical algorithms could render this feasible.

6.3.3 Degradation-Conscious Control

Given the durability challenges of PEM fuel cells and the shortcomings of material-based solutions, system-level mitigation strategies are expected to play a key role in extending fuel cell lifetime. While the degradation-conscious control framework proposed in this dissertation is an initial step towards developing such system-level strategies, future work should improve it in several ways to ensure robust implementation in practice.

First and foremost, the proposed framework relies on full-state feedback. While the model may be used to provide such feedback, this method is not robust to modeling mismatch. Therefore, the framework must be augmented with observers to allow for output feedback implementation. Robust observers such as sliding mode [368] and high-gain observers [374] are of particular interest in this regard. Alternatively, moving horizon estimation [375] can be utilized in conjunction with the MPC framework to allow for output feedback implementation [376].

Additionally, the demonstrated nominal robustness of the proposed control framework may not be sufficient for practical implementation with output feedback. Therefore, a

robust MPC [367] framework should be considered to ensure successful implementation. The added computational cost of such a framework would be a potential concern and calls for further improvements on both the system modeling and control formulation fronts. Moreover, additional research is required to better understand different fuel cell stressors and develop reliable lifetime indicators that can be used to extend the stack's longevity.

Lastly, the proposed framework relies on local linearization of a nonlinear model for MPC design. This offers significant computational advantages, but also results in sub-optimal solution as the system nonlinearities are not effectively taken into account. While a nonlinear MPC formulation is not suitable due to significant computational cost, the recent advances on using Koopman operator theory in conjunction with MPC [377] appear to offer a solution by allowing development of linear models that capture the nonlinear system behavior globally. Therefore, further focus on this area is warranted to ensure a linear MPC framework can be utilized to obtain the true optimal solution.

Appendix A

Model Parameter Values Used for Simulations

Complete lists of model parameters used for simulation studies of Chapters 2 and 5 are provided below in Tables A1 and A2, respectively. Any parameter that is used in Chapter 5 but not reported in Table A2 remains identical to its value in Table A1. Moreover, the anode and cathode parameters are assumed to be the same unless noted otherwise. The description for each parameter can be found in the nomenclature and the text of the dissertation. We also note that the particular choice of units for model parameters is based on common practices and is made for convenience. For example, the layer thicknesses are reported in μm whereas the channel dimensions are reported in cm.

Table A1: Model parameters used for simulation case studies of Section 2.4.

Symbol	Units	Value/Eq.
Structural parameters		
D_{h}	[cm]	0.06
h_{CH}	[cm]	0.04
w_{CH}	[cm]	0.10
w_{LN}	[cm]	0.05

δ_{mb}	[μm]	20
δ_{CL}	[μm]	3/6 for an/ca
δ_{MPL}	[μm]	60
δ_{GDL}	[μm]	140
$\varepsilon_{\mathrm{CL}}$	[−]	Eq. 2.33
$\varepsilon_{\mathrm{MPL}}$	[−]	0.55
$\varepsilon_{\mathrm{GDL}}$	[−]	0.72

Physical constants

F	[C/mol]	96485
H_{H_2}	[atm $\cdot$ m^3/mol]	4.5×10^{-2}
M_{H_2}	[g/mol]	2
M_{H_2O}	[g/mol]	18
M_{N_2}	[g/mol]	28
M_{O_2}	[g/mol]	32
R	[J/(mol $\cdot$ K)]	8.314

Physical properties and local variables

$c_{H_2}^{\mathrm{ref}}$	[mol/cm^3]	4×10^{-5}
$c_{O_2}^{\mathrm{ref}}$	[mol/cm^3]	4×10^{-5}
$E_{\mathrm{act,mb}}$	[kJ/mol]	15
$E_{\mathrm{act,an}}$	[kJ/mol]	10
$E_{\mathrm{act,ca}}$	[kJ/mol]	67
$E_{\mathrm{rev,PtO}}$	[V]	0.81
E_{PtO}	[kJ/mol]	10
EW	[g/mol]	1000
$f_{RH,a}$	[−]	0.5
$f_{RH,b}$	[−]	2

$f_{RH,c}$	$[-]$	0.7
h_{conv}	$[\text{W}/(\text{cm}^2 \cdot \text{K})]$	0.4
$i_{0,\text{an}}^{\text{ref}}$	$[\text{A}/\text{cm}^2]$	0.05
$i_{0,\text{ca}}^{\text{ref}}$	$[\text{A}/\text{cm}^2]$	2×10^{-7}
$K_{\text{abs,CL}}$	$[\text{cm}^2]$	1×10^{-11}
$K_{\text{abs,MPL}}$	$[\text{cm}^2]$	3×10^{-11}
$K_{\text{abs,GDL}}$	$[\text{cm}^2]$	10×10^{-11}
$K_{\text{l,rel}}$	$[-]$	s^5
k_{PtO}	$[1/\text{s}]$	0.0128
$k_{\text{evp/cnd,CL}}$	$[1/\text{s}]$	50000
$k_{\text{evp/cnd,MPL}}$	$[1/\text{s}]$	1000
$k_{\text{evp/cnd,GDL}}$	$[1/\text{s}]$	500
$k_{T,\text{CL}}$	$[\text{W}/(\text{m} \cdot \text{K})]$	0.3
$k_{T,\text{MPL}}$	$[\text{W}/(\text{m} \cdot \text{K})]$	0.15
$k_{T,\text{GDL}}$	$[\text{W}/(\text{m} \cdot \text{K})]$	0.5
$k_{T,\text{mb}}$	$[\text{W}/(\text{m} \cdot \text{K})]$	Table 2.4
k_1	$[-]$	8.5
k_2	$[-]$	5.4
k_3	$[-]$	5.4
k_{cross}	$[-]$	1
n_v	$[-]$	2.5
n_e	$[-]$	1.1
R_{elec}	$[\Omega \cdot \text{cm}^2]$	0.025
Sh	$[-]$	2.693
α_{an}	$[-]$	2
α_{ca}	$[-]$	0.7

α_{PtO}	[−]	0.5
ε_{g}	[−]	$(1-s)\varepsilon$
ε_{l}	[−]	$s\varepsilon$
γ_{an}	[−]	1.0
γ_{ca}	[−]	1.0
κ_{res}	[S/cm]	0.001
κ_0	[S/cm]	0.35
μ_{l}	[Pa · s]	4.05×10^{-4}
Π_{HOR}	[V]	$0.013\frac{T}{298}$
Π_{ORR}	[V]	$0.24\frac{T}{298}$
φ	[−]	0.35
ρ_{l}	[g/cm^3]	0.997
$(\rho c_p)_{\mathrm{g}}$	[J/(cm^3 · K)]	0.00125
$(\rho c_p)_{\mathrm{l}}$	[J/(cm^3 · K)]	4.2
$(\rho c_p)_{\mathrm{s}}$	[J/(cm^3 · K)]	2
σ_{l}	[N/m]	0.0644
θ_{CL}	[−]	97
θ_{MPL}	[−]	135
θ_{GDL}	[−]	115
ω	[kJ/mol]	3
$\xi_{\mathrm{diff,mb}}$	[−]	1

Catalyst structural parameters

a_c	[cm^2/cm^3]	$\frac{3\varepsilon_{\mathrm{c}}}{r_{\mathrm{c}}}(r_{\mathrm{c}}+\delta_{\mathrm{ion}})^2$
a_{Pt}	[cm^2/cm^3]	$\frac{ECSA \cdot L_{\mathrm{Pt}}}{\delta_{\mathrm{CL}}}$
$ECSA$	[(m^2/g)$_{\mathrm{Pt}}$]	70
IC	[−]	1.0/1.3 for an/ca

L_{c}	[mg/cm^2]	$\frac{L_{\mathrm{Pt}}(1-wt\%)}{wt\%}$
L_{Pt}	[mg/cm^2]	0.1/0.2 for an/ca
n_{Brugg}	[−]	1.5
r_{c}	[nm]	40
r_{Pt}	[nm]	$\frac{3}{\rho_{\mathrm{Pt}} \cdot ECSA}$
$wt\%$	[−]	0.4
x	[−]	1
ε_{c}	[−]	Eq. 2.30
$\varepsilon_{\mathrm{Pt}}$	[−]	Eq. 2.31
$\varepsilon_{\mathrm{ion}}$	[−]	Eq. 2.32
ρ_{c}	[g/cm^3]	1.95
ρ_{Pt}	[g/cm^3]	21.45
ρ_{ion}	[g/cm^3]	1.9

Table A2: Model parameters used in Chapter 5.

Symbol	Units	Value/Eq.
Constant inputs		
St_{H_2}	[−]	1.5
Physical constants		
$M_{\mathrm{a,atm}}$	[g/mol]	28.9647
Structural parameters		
A_{cool}	[cm^2]	280
A_{fc}	[cm^2]	280
A_{T}	[cm^2]	17.5
d_{c}	[cm]	22.86

D_{h}	[cm]	0.03
J_{cp}	$[\mathrm{kg} \cdot \mathrm{m}^2]$	5×10^{-5}
n_{cell}	[−]	380
V_{sm}	$[\mathrm{m}^3]$	0.02
V_{ca}	$[\mathrm{m}^3]$	0.01
δ_{mb}	[μm]	20
δ_{CL}	[μm]	5.5/6.7 for an/ca
δ_{MPL}	[μm]	30
δ_{GDL}	[μm]	160
$\varepsilon_{\mathrm{CL}}$	[−]	0.35
$\varepsilon_{\mathrm{MPL}}$	[−]	0.45
$\varepsilon_{\mathrm{GDL}}$	[−]	0.65

Physical properties and local variables

C_{D}	[−]	0.0124
EW	[g/mol]	1000
h_{conv}	$[\mathrm{W}/(\mathrm{cm}^2 \cdot \mathrm{K})]$	0.2
$i_{0,\mathrm{an}}^{\mathrm{ref}}$	$[\mathrm{A}/\mathrm{cm}^2]$	0.1
$i_{0,\mathrm{ca}}^{\mathrm{ref}}$	$[\mathrm{A}/\mathrm{cm}^2]$	1×10^{-7}
$k_{T,\mathrm{CL}}$	$[\mathrm{W}/(\mathrm{m} \cdot \mathrm{K})]$	0.25
$k_{T,\mathrm{MPL}}$	$[\mathrm{W}/(\mathrm{m} \cdot \mathrm{K})]$	0.15
$k_{T,\mathrm{GDL}}$	$[\mathrm{W}/(\mathrm{m} \cdot \mathrm{K})]$	0.4
k_{PtO}	[1/s]	0.0128
k_t	$[\mathrm{N} \cdot \mathrm{m}/\mathrm{A}]$	0.0153
k_v	[V/(rad/s)]	0.0153
$k_{\mathrm{ca,in}}$	$[\mathrm{kg}/(\mathrm{s} \cdot \mathrm{Pa})]$	3.63×10^{-6}
n_v	[−]	2.5

n_e	[−]	1.6
R_{elec}	$[\Omega \cdot \text{cm}^2]$	0.05
R_{cm}	$[\Omega]$	0.82
U_{c}	[m/s]	Ref. [174]
x_{O_2}	[−]	0.233
α_{an}	[−]	2
α_{ca}	[−]	0.6
η_{cm}	[−]	98%
η_{cp}	[V]	Ref. [174]
γ_{an}	[−]	0.5
γ_{ca}	[−]	0.8
γ	[−]	1.4
μ_{l}	$[\text{Pa} \cdot \text{s}]$	4.05×10^{-4}
φ	[−]	0.35
ρ_{l}	$[\text{g/cm}^3]$	0.997
ρ_{ion}	$[\text{g/cm}^3]$	1.9
σ_{l}	[N/m]	0.0644

Catalyst structural parameters

$ECSA$	$[(\text{m}^2/\text{g})_{\text{Pt}}]$	55/70 for an/ca
IC	[−]	1.1/0.9 for an/ca
L_{Pt}	$[\text{mg/cm}^2]$	0.15/0.2 for an/ca
$wt\%$	[−]	0.35

Bibliography

[1] M. M. Mench, *Fuel cell engines*. John Wiley & Sons, 2008.

[2] United States Department of Energy, "Fuel cell technologies office multi-year research, development, and demonstration plan." `https://www.energy.gov/sites/prod/files/2017/05/f34/fcto_myrdd_fuel_cells.pdf`, May 2017. [Online; accessed 25-Nov-2017].

[3] A. Z. Weber, R. L. Borup, R. M. Darling, P. K. Das, T. J. Dursch, W. Gu, D. Harvey, A. Kusoglu, S. Litster, M. M. Mench, *et al.*, "A critical review of modeling transport phenomena in polymer-electrolyte fuel cells," *Journal of The Electrochemical Society*, vol. 161, no. 12, pp. F1254–F1299, 2014.

[4] R. Borup, J. Meyers, B. Pivovar, Y. S. Kim, R. Mukundan, N. Garland, D. Myers, M. Wilson, F. Garzon, D. Wood, *et al.*, "Scientific aspects of polymer electrolyte fuel cell durability and degradation," *Chemical reviews*, vol. 107, no. 10, pp. 3904–3951, 2007.

[5] M. Eikerling and A. Kulikovsky, *Polymer electrolyte fuel cells: physical principles of materials and operation*. CRC Press, 2014.

[6] T. Yoshida and K. Kojima, "Toyota MIRAI fuel cell vehicle and progress toward a future hydrogen society," *The Electrochemical Society Interface*, vol. 24, no. 2, pp. 45–49, 2015.

[7] C. Gittleman, A. Kongkanand, D. Masten, and W. Gu, "Materials research and development priorities for low cost automotive PEM fuel cells," *Current Opinion in Electrochemistry*, 2019.

[8] M. S. Saha, D. K. Paul, B. A. Peppley, and K. Karan, "Fabrication of catalyst-coated membrane by modified decal transfer technique," *Electrochemistry Communications*, vol. 12, no. 3, pp. 410–413, 2010.

[9] M. K. Debe, "Novel catalysts, catalysts support and catalysts coated membrane methods," *Handbook of fuel cells*, 2010.

[10] T. F. Fuller and J. Newman, "Experimental determination of the transport number of water in Nafion 117 membrane," *Journal of The Electrochemical Society*, vol. 139, no. 5, pp. 1332–1337, 1992.

[11] T. E. Springer, T. Zawodzinski, and S. Gottesfeld, "Polymer electrolyte fuel cell model," *Journal of the electrochemical society*, vol. 138, no. 8, pp. 2334–2342, 1991.

[12] D. M. Bernardi and M. W. Verbrugge, "Mathematical model of a gas diffusion electrode bonded to a polymer electrolyte," *AIChE journal*, vol. 37, no. 8, pp. 1151–1163, 1991.

[13] S. Kim and M. Mench, "Investigation of temperature-driven water transport in polymer electrolyte fuel cell: Thermo-osmosis in membranes," *Journal of Membrane Science*, vol. 328, no. 12, pp. 113 – 120, 2009.

[14] A. Kusoglu and A. Z. Weber, "New insights into perfluorinated sulfonic-acid ionomers," *Chemical Reviews*, vol. 117, no. 3, pp. 987–1104, 2017.

[15] A. Z. Weber, "Gas-crossover and membrane-pinhole effects in polymer-electrolyte fuel cells," *Journal of the Electrochemical Society*, vol. 155, no. 6, pp. B521–B531, 2008.

[16] M. Inaba, "Chemical degradation of perfluorinated sulfonic acid membranes," in *Polymer Electrolyte Fuel Cell Durability*, pp. 57–69, Springer, 2009.

[17] G. Ding, M. H. Santare, A. M. Karlsson, and A. Kusoglu, "Numerical evaluation of crack growth in polymer electrolyte fuel cell membranes based on plastically dissipated energy," *Journal of Power Sources*, vol. 316, pp. 114–123, 2016.

[18] A. Kusoglu and A. Z. Weber, "A mechanistic model for pinhole growth in fuel-cell membranes during cyclic loads," *Journal of The Electrochemical Society*, vol. 161, no. 8, pp. E3311–E3322, 2014.

[19] M. N. Silberstein and M. C. Boyce, "Constitutive modeling of the rate, temperature, and hydration dependent deformation response of Nafion to monotonic and cyclic loading," *Journal of Power Sources*, vol. 195, no. 17, pp. 5692–5706, 2010.

[20] M. Inaba, T. Kinumoto, M. Kiriake, R. Umebayashi, A. Tasaka, and Z. Ogumi, "Gas crossover and membrane degradation in polymer electrolyte fuel cells," *Electrochimica Acta*, vol. 51, no. 26, pp. 5746–5753, 2006.

[21] C. Lim, L. Ghassemzadeh, F. Van Hove, M. Lauritzen, J. Kolodziej, G. Wang, S. Holdcroft, and E. Kjeang, "Membrane degradation during combined chemical and mechanical accelerated stress testing of polymer electrolyte fuel cells," *Journal of Power Sources*, vol. 257, pp. 102–110, 2014.

[22] A. Kusoglu, M. Calabrese, and A. Z. Weber, "Effect of mechanical compression on chemical degradation of Nafion membranes," *ECS Electrochemistry Letters*, vol. 3, no. 5, pp. F33–F36, 2014.

[23] A. Kusoglu and A. Z. Weber, "Electrochemical/mechanical coupling in ion-conducting soft matter," *The journal of physical chemistry letters*, vol. 6, no. 22, pp. 4547–4552, 2015.

[24] H. Wang, H. Li, and X.-Z. Yuan, *PEM fuel cell failure mode analysis*, vol. 1. CRC Press, 2011.

[25] M. M. Mench, E. C. Kumbur, and T. N. Veziroglu, *Polymer electrolyte fuel cell degradation*. Academic Press, 2011.

[26] F. N. Büchi, M. Inaba, and T. J. Schmidt, *Polymer electrolyte fuel cell durability*. Springer, 2009.

[27] Y. Singh, F. P. Orfino, M. Dutta, and E. Kjeang, "3D visualization of membrane failures in fuel cells," *Journal of Power Sources*, vol. 345, pp. 1–11, 2017.

[28] S. Shi, A. Z. Weber, and A. Kusoglu, "Structure/property relationship of Nafion XL composite membranes," *Journal of Membrane Science*, vol. 516, pp. 123–134, 2016.

[29] B. Kienitz, J. Kolde, S. Priester, C. Baczkowski, and M. Crum, "Ultra-thin reinforced ionomer membranes to meet next generation fuel cell targets," *ECS Transactions*, vol. 41, no. 1, pp. 1521–1530, 2011.

[30] E. Endoh, "Development of highly durable PFSA membrane and MEA for PEMFC under high temperature and low humidity conditions," *ECS Transactions*, vol. 16, no. 2, pp. 1229–1240, 2008.

[31] S. M. Stewart, R. L. Borup, M. S. Wilson, A. Datye, and F. H. Garzon, "Ceria and doped ceria nanoparticle additives for polymer fuel cell lifetime improvement," *ECS Transactions*, vol. 64, no. 3, pp. 403–411, 2014.

[32] A. M. Baker, L. Wang, W. B. Johnson, A. K. Prasad, and S. G. Advani, "Nafion membranes reinforced with ceria-coated multiwall carbon nanotubes for improved mechanical and chemical durability in polymer electrolyte membrane fuel cells," *The Journal of Physical Chemistry C*, vol. 118, no. 46, pp. 26796–26802, 2014.

[33] C. Lim, A. S. Alavijeh, M. Lauritzen, J. Kolodziej, S. Knights, and E. Kjeang, "Fuel cell durability enhancement with cerium oxide under combined chemical and mechanical membrane degradation," *ECS Electrochemistry Letters*, vol. 4, no. 4, pp. F29–F31, 2015.

[34] M. Hasan, A. Goshtasbi, J. Chen, M. H. Santare, and T. Ersal, "Model-based analysis of PFSA membrane mechanical response to relative humidity and load cycling in PEM fuel cells," *Journal of The Electrochemical Society*, vol. 165, no. 6, pp. F3359–F3372, 2018.

[35] R. Singh, P. Sui, K. Wong, E. Kjeang, S. Knights, and N. Djilali, "Modeling the effect of chemical membrane degradation on PEMFC performance," *Journal of The Electrochemical Society*, vol. 165, no. 6, pp. F3328–F3336, 2018.

[36] M. K. Debe, "Electrocatalyst approaches and challenges for automotive fuel cells," *Nature*, vol. 486, no. 7401, p. 43, 2012.

[37] R. Jinnouchi, K. Kudo, N. Kitano, and Y. Morimoto, "Molecular dynamics simulations on O2 permeation through nafion ionomer on platinum surface," *Electrochimica Acta*, vol. 188, pp. 767–776, 2016.

[38] K. Kudo, R. Jinnouchi, and Y. Morimoto, "Humidity and temperature dependences of oxygen transport resistance of Nafion thin film on platinum electrode," *Electrochimica Acta*, vol. 209, pp. 682–690, 2016.

[39] M. Sabharwal, L. Pant, A. Putz, D. Susac, J. Jankovic, and M. Secanell, "Analysis of catalyst layer microstructures: From imaging to performance," *Fuel Cells*, vol. 16, no. 6, pp. 734–753, 2016.

[40] S. J. Normile and I. V. Zenyuk, "Imaging ionomer in fuel cell catalyst layers with synchrotron nano transmission X-ray microscopy," *Solid State Ionics*, vol. 335, pp. 38–46, 2019.

[41] F. C. Cetinbas, R. K. Ahluwalia, N. Kariuki, V. De Andrade, D. Fongalland, L. Smith, J. Sharman, P. Ferreira, S. Rasouli, and D. J. Myers, "Hybrid approach combining multiple characterization techniques and simulations for microstructural analysis of proton exchange membrane fuel cell electrodes," *Journal of Power Sources*, vol. 344, pp. 62–73, 2017.

[42] F. C. Cetinbas, R. K. Ahluwalia, N. N. Kariuki, and D. J. Myers, "Agglomerates in polymer electrolyte fuel cell electrodes: Part I. Structural characterization," *Journal of The Electrochemical Society*, vol. 165, no. 13, pp. F1051–F1058, 2018.

[43] J. Jankovic, S. Zhang, A. Putz, M. S. Saha, and D. Susac, "Multiscale imaging and transport modeling for fuel cell electrodes," *Journal of Materials Research*, vol. 34, no. 4, pp. 579–591, 2019.

[44] A. Kongkanand and M. F. Mathias, "The priority and challenge of high-power performance of low-platinum proton-exchange membrane fuel cells," *The journal of physical chemistry letters*, vol. 7, no. 7, pp. 1127–1137, 2016.

[45] V. Yarlagadda, M. K. Carpenter, T. E. Moylan, R. S. Kukreja, R. Koestner, W. Gu, L. Thompson, and A. Kongkanand, "Boosting fuel cell performance with accessible carbon mesopores," *ACS Energy Letters*, vol. 3, no. 3, pp. 618–621, 2018.

[46] A. Z. Weber and A. Kusoglu, "Unexplained transport resistances for low-loaded fuel-cell catalyst layers," *Journal of Materials Chemistry A*, vol. 2, no. 41, pp. 17207–17211, 2014.

[47] T. Muzaffar, T. Kadyk, and M. Eikerling, "Tipping water balance and the Pt loading effect in polymer electrolyte fuel cells: a model-based analysis," *Sustainable Energy & Fuels*, vol. 2, no. 6, pp. 1189–1196, 2018.

[48] T. W. Patterson and R. M. Darling, "Damage to the cathode catalyst of a PEM fuel cell caused by localized fuel starvation," *Electrochemical and Solid-State Letters*, vol. 9, no. 4, pp. A183–A185, 2006.

[49] J. P. Meyers and R. M. Darling, "Model of carbon corrosion in PEM fuel cells," *Journal of the Electrochemical Society*, vol. 153, no. 8, pp. A1432–A1442, 2006.

[50] J. Chen, J. Hu, and J. R. Waldecker, "A comprehensive model for carbon corrosion during fuel cell start-up," *Journal of The Electrochemical Society*, vol. 162, no. 8, pp. F878–F889, 2015.

[51] R. M. Darling and J. P. Meyers, "Kinetic model of platinum dissolution in PEMFCs," *Journal of the Electrochemical Society*, vol. 150, no. 11, pp. A1523–A1527, 2003.

[52] H. Zhang, H. Haas, J. Hu, S. Kundu, M. Davis, and C. Chuy, "The impact of potential cycling on PEMFC durability," *Journal of The Electrochemical Society*, vol. 160, no. 8, pp. F840–F847, 2013.

[53] R. K. Ahluwalia, S. Arisetty, J.-K. Peng, R. Subbaraman, X. Wang, N. Kariuki, D. J. Myers, R. Mukundan, R. Borup, and O. Polevaya, "Dynamics of particle growth and electrochemical surface area loss due to platinum dissolution," *Journal of The Electrochemical Society*, vol. 161, no. 3, pp. F291–F304, 2014.

[54] P. Schneider, C. Sadeler, A.-C. Scherzer, N. Zamel, and D. Gerteisen, "Fast and reliable state-of-health model of a PEM cathode catalyst layer," *Journal of The Electrochemical Society*, vol. 166, no. 4, pp. F322–F333, 2019.

[55] B. K. Hong, P. Mandal, J.-G. Oh, and S. Litster, "On the impact of water activity on reversal tolerant fuel cell anode performance and durability," *Journal of Power Sources*, vol. 328, pp. 280–288, 2016.

[56] P. Mandal, B. K. Hong, J.-G. Oh, and S. Litster, "Understanding the voltage reversal behavior of automotive fuel cells," *Journal of Power Sources*, vol. 397, pp. 397–404, 2018.

[57] J. P. Meyers, "Modeling of catalyst structure degradation in PEM fuel cells," in *Modeling and Numerical Simulations*, pp. 249–271, Springer, 2008.

[58] S. Kim and M. M. Mench, "Investigation of temperature-driven water transport in polymer electrolyte fuel cell: Phase-change-induced flow," *Journal of The Electrochemical Society*, vol. 156, no. 3, pp. B353–B362, 2009.

[59] A. Weber and M. Hickner, "Modeling and high-resolution-imaging studies of water-content profiles in a polymer-electrolyte-fuel-cell membrane-electrode assembly," *Electrochimica Acta*, vol. 53, no. 26, pp. 7668–7674, 2008.

[60] I. V. Zenyuk, D. Y. Parkinson, L. G. Connolly, and A. Z. Weber, "Gas-diffusion-layer structural properties under compression via X-ray tomography," *Journal of Power Sources*, vol. 328, pp. 364–376, 2016.

[61] I. V. Zenyuk, D. Y. Parkinson, G. Hwang, and A. Z. Weber, "Probing water distribution in compressed fuel-cell gas-diffusion layers using X-ray computed tomography," *Electrochemistry Communications*, vol. 53, pp. 24–28, 2015.

[62] J. Zhou, S. Shukla, A. Putz, and M. Secanell, "Analysis of the role of the microporous layer in improving polymer electrolyte fuel cell performance," *Electrochimica Acta*, vol. 268, pp. 366–382, 2018.

[63] H. K. Atiyeh, K. Karan, B. Peppley, A. Phoenix, E. Halliop, and J. Pharoah, "Experimental investigation of the role of a microporous layer on the water transport and performance of a PEM fuel cell," *Journal of Power Sources*, vol. 170, no. 1, pp. 111–121, 2007.

[64] A. Z. Weber and J. Newman, "Effects of microporous layers in polymer electrolyte fuel cells," *Journal of the Electrochemical Society*, vol. 152, no. 4, pp. A677–A688, 2005.

[65] R. O'hayre, S.-W. Cha, F. B. Prinz, and W. Colella, *Fuel cell fundamentals*. John Wiley & Sons, 2016.

[66] T. Hasegawa, H. Imanishi, M. Nada, and Y. Ikogi, "Development of the fuel cell system in the Mirai FCV," tech. rep., SAE Technical Paper, 2016.

[67] J. B. Siegel, *Experiments and Modeling of PEM Fuel Cells for Dead-Ended Anode Operation.* PhD thesis, University of Michigan, 2010.

[68] J. Chen, *Degradation, Efficiency, and Equilibrium of a Dead-Ended Anode Fuel Cell.* PhD thesis, University of Michigan, 2013.

[69] R. K. Ahluwalia and X. Wang, "Fuel cell systems for transportation: Status and trends," *Journal of power sources*, vol. 177, no. 1, pp. 167–176, 2008.

[70] P. Choi and R. Datta, "Sorption in proton-exchange membranes an explanation of Schroeders paradox," *Journal of the Electrochemical Society*, vol. 150, no. 12, pp. E601–E607, 2003.

[71] M. H. Eikerling and P. Berg, "Poroelectroelastic theory of water sorption and swelling in polymer electrolyte membranes," *Soft matter*, vol. 7, no. 13, pp. 5976–5990, 2011.

[72] C. W. Monroe, T. Romero, W. Mérida, and M. Eikerling, "A vaporization-exchange model for water sorption and flux in Nafion," *Journal of Membrane Science*, vol. 324, no. 1-2, pp. 1–6, 2008.

[73] R. Anderson, L. Zhang, Y. Ding, M. Blanco, X. Bi, and D. P. Wilkinson, "A critical review of two-phase flow in gas flow channels of proton exchange membrane fuel cells," *Journal of Power Sources*, vol. 195, no. 15, pp. 4531–4553, 2010.

[74] S. G. Kandlikar, E. J. See, and R. Banerjee, "Modeling two-phase pressure drop along PEM fuel cell reactant channels," *Journal of The Electrochemical Society*, vol. 162, no. 7, pp. F772–F782, 2015.

[75] L. M. Pant, S. K. Mitra, and M. Secanell, "A generalized mathematical model to study gas transport in PEMFC porous media," *International Journal of Heat and Mass Transfer*, vol. 58, no. 1-2, pp. 70–79, 2013.

[76] A. Z. Weber and J. Newman, "Modeling gas-phase flow in porous media," *International Communications in Heat and Mass Transfer*, vol. 32, no. 7, pp. 855–860, 2005.

[77] A. Z. Weber, R. M. Darling, and J. Newman, "Modeling two-phase behavior in PEFCs," *Journal of the Electrochemical Society*, vol. 151, no. 10, pp. A1715–A1727, 2004.

[78] A. Z. Weber, "Improved modeling and understanding of diffusion-media wettability on polymer-electrolyte-fuel-cell performance," *journal of Power Sources*, vol. 195, no. 16, pp. 5292–5304, 2010.

[79] J. Hinebaugh, J. Gostick, and A. Bazylak, "Stochastic modeling of polymer electrolyte membrane fuel cell gas diffusion layers–Part 2: A comprehensive substrate

model with pore size distribution and heterogeneity effects," *International Journal of Hydrogen Energy*, vol. 42, no. 24, pp. 15872–15886, 2017.

[80] J. Liu and M. Eikerling, "Model of cathode catalyst layers for polymer electrolyte fuel cells: The role of porous structure and water accumulation," *Electrochimica Acta*, vol. 53, no. 13, pp. 4435–4446, 2008.

[81] J. Liu, J. Gazzarri, and M. Eikerling, "Model-based ex situ diagnostics of water fluxes in catalyst layers of polymer electrolyte fuel cells," *Fuel Cells*, vol. 13, no. 2, pp. 134–142, 2013.

[82] L. Hao, K. Moriyama, W. Gu, and C.-Y. Wang, "Modeling and experimental validation of Pt loading and electrode composition effects in PEM fuel cells," *Journal of The Electrochemical Society*, vol. 162, no. 8, pp. F854–F867, 2015.

[83] T. Suzuki, K. Kudo, and Y. Morimoto, "Model for investigation of oxygen transport limitation in a polymer electrolyte fuel cell," *Journal of Power Sources*, vol. 222, pp. 379–389, 2013.

[84] M. Moore, P. Wardlaw, P. Dobson, J. Boisvert, A. Putz, R. Spiteri, and M. Secanell, "Understanding the effect of kinetic and mass transport processes in cathode agglomerates," *Journal of the Electrochemical Society*, vol. 161, no. 8, pp. E3125–E3137, 2014.

[85] T. Mashio, H. Iden, A. Ohma, and T. Tokumasu, "Modeling of local gas transport in catalyst layers of PEM fuel cells," *Journal of Electroanalytical Chemistry*, vol. 790, pp. 27–39, 2017.

[86] L. Hao, K. Moriyama, W. Gu, and C.-Y. Wang, "Three dimensional computations and experimental comparisons for a large-scale proton exchange membrane fuel cell," *Journal of The Electrochemical Society*, vol. 163, no. 7, pp. F744–F751, 2016.

[87] K. Promislow, P. Chang, H. Haas, and B. Wetton, "Two-phase unit cell model for slow transients in polymer electrolyte membrane fuel cells," *Journal of The Electrochemical Society*, vol. 155, no. 7, pp. A494–A504, 2008.

[88] J. B. Siegel, S. V. Bohac, A. G. Stefanopoulou, and S. Yesilyurt, "Nitrogen front evolution in purged polymer electrolyte membrane fuel cell with dead-ended anode," *Journal of the Electrochemical Society*, vol. 157, no. 7, pp. B1081–B1093, 2010.

[89] A. Goshtasbi, P. García-Salaberri, J. Chen, K. Talukdar, D. G. Sanchez, and T. Ersal, "Through-the-membrane transient phenomena in PEM fuel cells: A modeling study," *Journal of The Electrochemical Society*, vol. 166, no. 7, 2019.

[90] I. V. Zenyuk, P. K. Das, and A. Z. Weber, "Understanding impacts of catalyst-layer thickness on fuel-cell performance via mathematical modeling," *Journal of the Electrochemical Society*, vol. 163, no. 7, pp. F691–F703, 2016.

[91] J. Zhou, A. Putz, and M. Secanell, "A mixed wettability pore size distribution based mathematical model for analyzing two-phase flow in porous electrodes I. Mathematical model," *Journal of The Electrochemical Society*, vol. 164, no. 6, pp. F530–F539, 2017.

[92] G. A. Futter, P. Gazdzicki, K. A. Friedrich, A. Latz, and T. Jahnke, "Physical modeling of polymer-electrolyte membrane fuel cells: Understanding water management and impedance spectra," *Journal of Power Sources*, vol. 391, pp. 148–161, 2018.

[93] J. T. Pukrushpan, H. Peng, and A. G. Stefanopoulou, "Control-oriented modeling and analysis for automotive fuel cell systems," *Journal of dynamic systems, measurement, and control*, vol. 126, no. 1, pp. 14–25, 2004.

[94] B. A. McCain, A. G. Stefanopoulou, and I. V. Kolmanovsky, "A dynamic semi-analytic channel-to-channel model of two-phase water distribution for a unit fuel

cell," *IEEE Transactions on Control Systems Technology*, vol. 17, no. 5, pp. 1055–1068, 2009.

[95] D. A. McKay, J. B. Siegel, W. Ott, and A. G. Stefanopoulou, "Parameterization and prediction of temporal fuel cell voltage behavior during flooding and drying conditions," *Journal of Power Sources*, vol. 178, no. 1, pp. 207–222, 2008.

[96] M. Zaglio, A. Wokaun, J. Mantzaras, and F. Büchi, "1D-modelling and experimental study of the PEFC dynamic behaviour at load increase," *Fuel Cells*, vol. 11, no. 4, pp. 526–536, 2011.

[97] C. Ziegler, H. M. Yu, and J. Schumacher, "Two-phase dynamic modeling of PEMFCs and simulation of cyclo-voltammograms," *Journal of The Electrochemical Society*, vol. 152, no. 8, pp. A1555–A1567, 2005.

[98] J. Golbert and D. R. Lewin, "Model-based control of fuel cells::(1) regulatory control," *Journal of power sources*, vol. 135, no. 1-2, pp. 135–151, 2004.

[99] H. Meng, "Multi-dimensional liquid water transport in the cathode of a PEM fuel cell with consideration of the micro-porous layer (MPL)," *International Journal of Hydrogen Energy*, vol. 34, no. 13, pp. 5488–5497, 2009.

[100] A. Z. Weber, "Effective diffusion-medium thickness for simplified polymer-electrolyte-fuel-cell modeling," *Electrochimica Acta*, vol. 54, no. 2, pp. 311–315, 2008.

[101] A. Z. Weber and J. Newman, "Using a quasi-potential transformation for modeling diffusion media in polymer-electrolyte fuel cells," *SIAM Journal on Applied Mathematics*, vol. 70, no. 2, pp. 488–509, 2009.

[102] D. R. Baker, D. A. Caulk, K. C. Neyerlin, and M. W. Murphy, "Measurement of oxygen transport resistance in PEM fuel cells by limiting current methods," *Journal of The Electrochemical Society*, vol. 156, no. 9, pp. B991–B1003, 2009.

[103] M. Zaglio, J. Roth, A. Wokaun, J. Mantzaras, and F. N. Büchi, "Transient bi-domain 1D PEFC model," *ECS Electrochemistry Letters*, vol. 1, no. 1, pp. F1–F3, 2012.

[104] G.-S. Kim, P. Sui, A. Shah, and N. Djilali, "Reduced-dimensional models for straight-channel proton exchange membrane fuel cells," *Journal of Power Sources*, vol. 195, no. 10, pp. 3240–3249, 2010.

[105] L. M. Pant, M. R. Gerhardt, N. Macauley, R. Mukundan, R. L. Borup, and A. Z. Weber, "Along-the-channel modeling and analysis of PEFCs at low stoichiometry: Development of a 1+2D model," *Electrochimica Acta*, p. 134963, 2019.

[106] H. Wu, P. Berg, and X. Li, "Steady and unsteady 3D non-isothermal modeling of PEM fuel cells with the effect of non-equilibrium phase transfer," *Applied Energy*, vol. 87, no. 9, pp. 2778–2784, 2010.

[107] T. Silverman, J. Meyers, and J. Beaman, "Dynamic thermal, transport and mechanical model of fuel cell membrane swelling," *Fuel Cells*, vol. 11, no. 6, pp. 875–887, 2011.

[108] A. Kongkanand and P. K. Sinha, "Load transients of nanostructured thin film electrodes in polymer electrolyte fuel cells," *Journal of the Electrochemical Society*, vol. 158, no. 6, pp. B703–B711, 2011.

[109] J. X. Wang, T. E. Springer, and R. R. Adzic, "Dual-pathway kinetic equation for the hydrogen oxidation reaction on Pt electrodes," *Journal of the Electrochemical Society*, vol. 153, no. 9, pp. A1732–A1740, 2006.

[110] N. Subramanian, T. Greszler, J. Zhang, W. Gu, and R. Makharia, "Pt-oxide coverage-dependent oxygen reduction reaction (ORR) kinetics," *Journal of The Electrochemical Society*, vol. 159, no. 5, pp. B531–B540, 2012.

[111] J. X. Wang, J. Zhang, and R. R. Adzic, "Double-trap kinetic equation for the oxygen reduction reaction on Pt (111) in acidic media," *The Journal of Physical Chemistry A*, vol. 111, no. 49, pp. 12702–12710, 2007.

[112] M. Moore, A. Putz, and M. Secanell, "Investigation of the ORR using the double-trap intrinsic kinetic model," *Journal of the Electrochemical Society*, vol. 160, no. 6, pp. F670–F681, 2013.

[113] M. Markiewicz, C. Zalitis, and A. Kucernak, "Performance measurements and modelling of the ORR on fuel cell electrocatalysts–the modified double trap model," *Electrochimica Acta*, vol. 179, pp. 126–136, 2015.

[114] B. Jayasankar and K. Karan, "O2 electrochemistry on Pt: A unified multi-step model for oxygen reduction and oxide growth," *Electrochimica Acta*, vol. 273, pp. 367–378, 2018.

[115] K. Neyerlin, H. A. Gasteiger, C. K. Mittelsteadt, J. Jorne, and W. Gu, "Effect of relative humidity on oxygen reduction kinetics in a PEMFC," *Journal of The Electrochemical Society*, vol. 152, no. 6, pp. A1073–A1080, 2005.

[116] H. Xu, Y. Song, H. R. Kunz, and J. M. Fenton, "Effect of elevated temperature and reduced relative humidity on ORR kinetics for PEM fuel cells," *Journal of The Electrochemical Society*, vol. 152, no. 9, pp. A1828–A1836, 2005.

[117] H. Xu, H. R. Kunz, and J. M. Fenton, "Analysis of proton exchange membrane fuel cell polarization losses at elevated temperature 120 C and reduced relative humidity," *Electrochimica Acta*, vol. 52, no. 11, pp. 3525–3533, 2007.

[118] Y. Liu, M. W. Murphy, D. R. Baker, W. Gu, C. Ji, J. Jorne, and H. A. Gasteiger, "Proton conduction and oxygen reduction kinetics in PEM fuel cell cathodes: effects of ionomer-to-carbon ratio and relative humidity," *Journal of The Electrochemical Society*, vol. 156, no. 8, pp. B970–B980, 2009.

[119] J. Chlistunoff and B. Pivovar, "Effects of ionomer morphology on oxygen reduction on Pt," *Journal of The Electrochemical Society*, vol. 162, no. 8, pp. F890–F900, 2015.

[120] Y. Furuya, H. Iden, T. Mashio, A. Ohma, and K. Shinohara, "Effect of ionomer coverage on pt-based catalyst on ORR activity," in *Meeting Abstracts*, no. 40, pp. 1522–1522, The Electrochemical Society, 2012.

[121] K. Shinozaki, Y. Morimoto, B. S. Pivovar, and S. S. Kocha, "Suppression of oxygen reduction reaction activity on Pt-based electrocatalysts from ionomer incorporation," *Journal of Power Sources*, vol. 325, pp. 745–751, 2016.

[122] K. T. Cho, A. Turhan, J. H. Lee, J. S. Brenizer, A. K. Heller, L. Shi, and M. M. Mench, "Probing water transport in polymer electrolyte fuel cells with neutron radiography," *Nuclear Instruments and Methods in Physics Research Section A: Accelerators, Spectrometers, Detectors and Associated Equipment*, vol. 605, no. 1-2, pp. 119–122, 2009.

[123] M. Hickner, N. Siegel, K. Chen, D. Hussey, D. Jacobson, and M. Arif, "Understanding liquid water distribution and removal phenomena in an operating PEMFC via neutron radiography," *Journal of The Electrochemical Society*, vol. 155, no. 3, pp. B294–B302, 2008.

[124] D. S. Hussey, D. Spernjak, A. Z. Weber, R. Mukundan, J. Fairweather, E. L. Brosha, J. Davey, J. S. Spendelow, D. L. Jacobson, and R. L. Borup, "Accurate measurement

of the through-plane water content of proton-exchange membranes using neutron radiography," *Journal of Applied Physics*, vol. 112, no. 10, p. 104906, 2012.

[125] T. Suzuki, Y. Tabuchi, S. Tsushima, and S. Hirai, "Measurement of water content distribution in catalyst coated membranes under water permeation conditions by magnetic resonance imaging," *international journal of hydrogen energy*, vol. 36, no. 9, pp. 5479–5486, 2011.

[126] J. Eller, T. Rosén, F. Marone, M. Stampanoni, A. Wokaun, and F. N. Büchi, "Progress in in-situ X-ray tomographic microscopy of liquid water in gas diffusion layers of PEFC," *Journal of The Electrochemical Society*, vol. 158, no. 8, pp. B963–B970, 2011.

[127] A. Kusoglu, M. A. Modestino, A. Hexemer, R. A. Segalman, and A. Z. Weber, "Subsecond morphological changes in Nafion during water uptake detected by small-angle X-ray scattering," *ACS Macro Letters*, vol. 1, no. 1, pp. 33–36, 2011.

[128] M. Fumagalli, S. Lyonnard, G. Prajapati, Q. Berrod, L. Porcar, A. Guillermo, and G. Gebel, "Fast water diffusion and long-term polymer reorganization during Nafion membrane hydration evidenced by time-resolved small-angle neutron scattering," *The Journal of Physical Chemistry B*, vol. 119, no. 23, pp. 7068–7076, 2015.

[129] W. K. Epting and S. Litster, "Microscale measurements of oxygen concentration across the thickness of diffusion media in operating polymer electrolyte fuel cells," *Journal of Power Sources*, vol. 306, pp. 674–684, 2016.

[130] T. A. Greszler, D. Caulk, and P. Sinha, "The impact of platinum loading on oxygen transport resistance," *Journal of The Electrochemical Society*, vol. 159, no. 12, pp. F831–F840, 2012.

[131] F. Jiang and C.-Y. Wang, "Numerical modeling of liquid water motion in a polymer electrolyte fuel cell," *international journal of hydrogen energy*, vol. 39, no. 2, pp. 942–950, 2014.

[132] M. Grötsch and M. Mangold, "A two-phase PEMFC model for process control purposes," *Chemical engineering science*, vol. 63, no. 2, pp. 434–447, 2008.

[133] F. Mueller, J. Brouwer, S. Kang, H.-S. Kim, and K. Min, "Quasi-three dimensional dynamic model of a proton exchange membrane fuel cell for system and controls development," *Journal of Power Sources*, vol. 163, no. 2, pp. 814–829, 2007.

[134] S. Philipps and C. Ziegler, "Computationally efficient modeling of the dynamic behavior of a portable PEM fuel cell stack," *Journal of Power Sources*, vol. 180, no. 1, pp. 309–321, 2008.

[135] P. Noiying, M. Hinaje, P. Thounthong, S. Raël, and B. Davat, "Using electrical analogy to describe mass and charge transport in PEM fuel cell," *Renewable energy*, vol. 44, pp. 128–140, 2012.

[136] A. Headley, V. Yu, R. Borduin, D. Chen, and W. Li, "Development and experimental validation of a physics-based PEM fuel cell model for cathode humidity control design," *IEEE/ASME Transactions on Mechatronics*, vol. 21, no. 3, pp. 1775–1782, 2016.

[137] A. A. Kulikovsky, *Analytical modelling of fuel cells*. Elsevier, 2010.

[138] G. Napoli, M. Ferraro, F. Sergi, G. Brunaccini, and V. Antonucci, "Data driven models for a PEM fuel cell stack performance prediction," *International Journal of Hydrogen Energy*, vol. 38, no. 26, pp. 11628–11638, 2013.

[139] B. A. McCain, *Modeling and Analysis for Control of Reactant and Water Distributions in Fuel Cells*. PhD thesis, University of Michigan, 2008.

[140] D. Gerteisen, T. Heilmann, and C. Ziegler, "Modeling the phenomena of dehydration and flooding of a polymer electrolyte membrane fuel cell," *Journal of Power Sources*, vol. 187, no. 1, pp. 165–181, 2009.

[141] B. Carnes, D. Spernjak, G. Luo, L. Hao, K. S. Chen, C.-Y. Wang, R. Mukundan, and R. L. Borup, "Validation of a two-phase multidimensional polymer electrolyte membrane fuel cell computational model using current distribution measurements," *Journal of Power Sources*, vol. 236, pp. 126–137, 2013.

[142] J. Zhou, D. Stanier, A. Putz, and M. Secanell, "A mixed wettability pore size distribution based mathematical model for analyzing two-phase flow in porous electrodes II. Model validation and analysis of micro-structural parameters," *Journal of The Electrochemical Society*, vol. 164, no. 6, pp. F540–F556, 2017.

[143] S. K. Babu, H. T. Chung, P. Zelenay, and S. Litster, "Modeling electrochemical performance of the hierarchical morphology of precious group metal-free cathode for polymer electrolyte fuel cell," *Journal of The Electrochemical Society*, vol. 164, no. 9, pp. F1037–F1049, 2017.

[144] N. Zamel and X. Li, "Effective transport properties for polymer electrolyte membrane fuel cells–with a focus on the gas diffusion layer," *Progress in energy and combustion science*, vol. 39, no. 1, pp. 111–146, 2013.

[145] O. S. Burheim, G. A. Crymble, R. Bock, N. Hussain, S. Pasupathi, A. Du Plessis, S. le Roux, F. Seland, H. Su, and B. G. Pollet, "Thermal conductivity in the three layered regions of micro porous layer coated porous transport layers for the PEM fuel cell," *international journal of hydrogen energy*, vol. 40, no. 46, pp. 16775–16785, 2015.

[146] H. Sadeghifar, N. Djilali, and M. Bahrami, "Effect of polytetrafluoroethylene (PTFE) and micro porous layer (MPL) on thermal conductivity of fuel cell gas diffusion layers: Modeling and experiments," *Journal of Power Sources*, vol. 248, pp. 632–641, 2014.

[147] B. Carnes and N. Djilali, "Systematic parameter estimation for PEM fuel cell models," *Journal of Power Sources*, vol. 144, no. 1, pp. 83–93, 2005.

[148] P. Dobson, C. Lei, T. Navessin, and M. Secanell, "Characterization of the PEM fuel cell catalyst layer microstructure by nonlinear least-squares parameter estimation," *Journal of the Electrochemical Society*, vol. 159, no. 5, pp. B514–B523, 2012.

[149] T. C. Yau, P. Sauriol, X. T. Bi, and J. Stumper, "Experimental determination of water transport in polymer electrolyte membrane fuel cells," *Journal of the Electrochemical Society*, vol. 157, no. 9, pp. B1310–B1320, 2010.

[150] N. Lin, X. Xie, R. Schenkendorf, and U. Krewer, "Efficient global sensitivity analysis of 3D multiphysics model for Li-ion batteries," *Journal of The Electrochemical Society*, vol. 165, no. 7, pp. A1169–A1183, 2018.

[151] C. Edouard, M. Petit, C. Forgez, J. Bernard, and R. Revel, "Parameter sensitivity analysis of a simplified electrochemical and thermal model for Li-ion batteries aging," *Journal of Power Sources*, vol. 325, pp. 482–494, 2016.

[152] L. Zhang, C. Lyu, G. Hinds, L. Wang, W. Luo, J. Zheng, and K. Ma, "Parameter sensitivity analysis of cylindrical LiFePO4 battery performance using multi-physics modeling," *Journal of The Electrochemical Society*, vol. 161, no. 5, pp. A762–A776, 2014.

[153] A. P. Schmidt, M. Bitzer, Á. W. Imre, and L. Guzzella, "Experiment-driven electrochemical modeling and systematic parameterization for a lithium-ion battery cell," *Journal of Power Sources*, vol. 195, no. 15, pp. 5071–5080, 2010.

[154] J. C. Forman, S. J. Moura, J. L. Stein, and H. K. Fathy, "Genetic identification and fisher identifiability analysis of the Doyle–Fuller–Newman model from experimental cycling of a LiFePO4 cell," *Journal of Power Sources*, vol. 210, pp. 263–275, 2012.

[155] A. Sharma and H. K. Fathy, "Fisher identifiability analysis for a periodically-excited equivalent-circuit lithium-ion battery model," in *American Control Conference*, pp. 274–280, IEEE, 2014.

[156] A. M. Bizeray, J.-H. Kim, S. R. Duncan, and D. A. Howey, "Identifiability and parameter estimation of the single particle lithium-ion battery model," *IEEE Transactions on Control Systems Technology*, no. 99, pp. 1–16, 2018.

[157] S. M. M. Alavi, A. Mahdi, S. J. Payne, and D. A. Howey, "Identifiability of generalized randles circuit models," *IEEE Transactions on Control Systems Technology*, vol. 25, no. 6, pp. 2112–2120, 2016.

[158] J. C. Forman, S. J. Moura, J. L. Stein, and H. K. Fathy, "Genetic parameter identification of the Doyle-Fuller-Newman model from experimental cycling of a LiFePO4 battery," in *Proceedings of the 2011 American Control Conference*, pp. 362–369, IEEE, 2011.

[159] X. Lin and A. G. Stefanopoulou, "Analytic bound on accuracy of battery state and parameter estimation," *Journal of The Electrochemical Society*, vol. 162, no. 9, pp. A1879–A1891, 2015.

[160] N. W. Brady, C. A. Gould, and A. C. West, "Quantitative parameter estimation, model selection, and variable selection in battery science," *Journal of The Electrochemical Society*, vol. 167, no. 1, p. 013501, 2020.

[161] S. Park, D. Kato, Z. Gima, R. Klein, and S. Moura, "Optimal experimental design for parameterization of an electrochemical lithium-ion battery model," *Journal of The Electrochemical Society*, vol. 165, no. 7, pp. A1309–A1323, 2018.

[162] A. Pozzi, G. Ciaramella, S. Volkwein, and D. M. Raimondo, "Optimal design of experiments for a lithium-ion cell: parameters identification of an isothermal single particle model with electrolyte dynamics," *Industrial & Engineering Chemistry Research*, vol. 58, no. 3, pp. 1286–1299, 2018.

[163] J. Forman, J. Stein, and H. Fathy, "Optimization of dynamic battery parameter characterization experiments via differential evolution," in *American Control Conference*, pp. 867–874, IEEE, 2013.

[164] M. J. Rothenberger, D. J. Docimo, M. Ghanaatpishe, and H. K. Fathy, "Genetic optimization and experimental validation of a test cycle that maximizes parameter identifiability for a Li-ion equivalent-circuit battery model," *Journal of Energy Storage*, vol. 4, pp. 156–166, 2015.

[165] T. Quaiser and M. Mönnigmann, "Systematic identifiability testing for unambiguous mechanistic modeling–application to jak-stat, map kinase, and nf-κ b signaling pathway models," *BMC systems biology*, vol. 3, no. 1, p. 50, 2009.

[166] D. P. Howsmon and J. Hahn, "Regularization techniques to overcome overparameterization of complex biochemical reaction networks," *IEEE life sciences letters*, vol. 2, no. 3, pp. 31–34, 2016.

[167] K. A. McLean and K. B. McAuley, "Mathematical modelling of chemical processesobtaining the best model predictions and parameter estimates using identifiability and estimability procedures," *The Canadian Journal of Chemical Engineering*, vol. 90, no. 2, pp. 351–366, 2012.

[168] A. Vahidi, A. Stefanopoulou, and H. Peng, "Current management in a hybrid fuel cell power system: A model-predictive control approach," *IEEE Transactions on Control Systems Technology*, vol. 14, no. 6, pp. 1047–1057, 2006.

[169] J. Golbert and D. R. Lewin, "Model-based control of fuel cells (2): Optimal efficiency," *Journal of power sources*, vol. 173, no. 1, pp. 298–309, 2007.

[170] J. Luna, S. Jemei, N. Yousfi-Steiner, A. Husar, M. Serra, and D. Hissel, "Nonlinear predictive control for durability enhancement and efficiency improvement in a fuel cell power system," *Journal of Power Sources*, vol. 328, pp. 250–261, 2016.

[171] B. A. McCain, A. G. Stefanopoulou, and J. B. Siegel, "Controllability and observability analysis of the liquid water distribution inside the gas diffusion layer of a unit fuel cell model," *Journal of Dynamic Systems, Measurement, and Control*, vol. 132, no. 6, p. 061303, 2010.

[172] R. Methekar, V. Prasad, and R. Gudi, "Dynamic analysis and linear control strategies for proton exchange membrane fuel cell using a distributed parameter model," *Journal of Power Sources*, vol. 165, no. 1, pp. 152–170, 2007.

[173] A. Pilloni, A. Pisano, and E. Usai, "Observer-based air excess ratio control of a PEM fuel cell system via high-order sliding mode," *IEEE Transactions on Industrial Electronics*, vol. 62, no. 8, pp. 5236–5246, 2015.

[174] J. T. Pukrushpan, A. G. Stefanopoulou, and H. Peng, *Control of fuel cell power systems: principles, modeling, analysis and feedback design*. Springer Science & Business Media, 2004.

[175] F. D. Bianchi, C. Kunusch, C. Ocampo-Martinez, and R. S. Sánchez-Peña, "A gain-scheduled LPV control for oxygen stoichiometry regulation in pem fuel cell systems," *IEEE Transactions on Control Systems Technology*, vol. 22, no. 5, pp. 1837–1844, 2013.

[176] J. Sun and I. V. Kolmanovsky, "Load governor for fuel cell oxygen starvation protection: A robust nonlinear reference governor approach," *IEEE Transactions on Control Systems Technology*, vol. 13, no. 6, pp. 911–920, 2005.

[177] A. Vahidi, I. Kolmanovsky, and A. Stefanopoulou, "Constraint management in fuel cells: A fast reference governor approach," in *American Control Conference, 2005. Proceedings of the 2005*, pp. 3865–3870, IEEE, 2005.

[178] A. Vahidi, I. Kolmanovsky, and A. Stefanopoulou, "Constraint handling in a fuel cell system: A fast reference governor approach," *IEEE Transactions on Control Systems Technology*, vol. 15, no. 1, pp. 86–98, 2006.

[179] A. Vahidi and W. Greenwell, "A decentralized model predictive control approach to power management of a fuel cell-ultracapacitor hybrid," in *2007 American Control Conference*, pp. 5431–5437, IEEE, 2007.

[180] M. Schultze and J. Horn, "Modeling, state estimation and nonlinear model predictive control of cathode exhaust gas mass flow for PEM fuel cells," *Control Engineering Practice*, vol. 49, pp. 76–86, 2016.

[181] C. Ziogou, E. N. Pistikopoulos, M. C. Georgiadis, S. Voutetakis, and S. Papadopoulou, "Empowering the performance of advanced NMPC by multiparametric

programming – An application to a PEM fuel cell system," *Industrial & Engineering Chemistry Research*, vol. 52, no. 13, pp. 4863–4873, 2013.

[182] C. Ziogou, S. Papadopoulou, M. C. Georgiadis, and S. Voutetakis, "On-line nonlinear model predictive control of a PEM fuel cell system," *Journal of Process Control*, vol. 23, no. 4, pp. 483–492, 2013.

[183] M. A. Danzer, S. J. Wittmann, and E. P. Hofer, "Prevention of fuel cell starvation by model predictive control of pressure, excess ratio, and current," *Journal of Power Sources*, vol. 190, no. 1, pp. 86–91, 2009.

[184] C. Hähnel, V. Aul, and J. Horn, "Power control for efficient operation of a PEM fuel cell system by nonlinear model predictive control," *IFAC-PapersOnLine*, vol. 48, no. 11, pp. 174–179, 2015.

[185] V. Tsourapas, J. Sun, and A. Stefanopoulou, "Control oriented analysis of a hybrid solid oxide fuel cell and gas turbine system," *Journal of fuel cell science and technology*, vol. 6, no. 4, p. 041008, 2009.

[186] V. Tsourapas, J. Sun, and A. Stefanopoulou, "Incremental step reference governor for load conditioning of hybrid fuel cell and gas turbine power plants," *IEEE Transactions on Control Systems Technology*, vol. 17, no. 4, pp. 756–767, 2009.

[187] Y. Wang, S. J. Moura, S. G. Advani, and A. K. Prasad, "Power management system for a fuel cell/battery hybrid vehicle incorporating fuel cell and battery degradation," *International Journal of Hydrogen Energy*, vol. 44, no. 16, pp. 8479–8492, 2019.

[188] D. A. McKay, A. G. Stefanopoulou, and J. Cook, "A controllable membrane-type humidifier for fuel cell applications Part I: Operation, modeling and experimental

validation," *Journal of Fuel Cell Science and Technology*, vol. 7, no. 5, p. 051006, 2010.

[189] D. A. McKay, A. G. Stefanopoulou, and J. Cook, "A controllable membrane-type humidifier for fuel cell applicationsPart II: Controller design, analysis and implementation," *Journal of Fuel Cell Science and Technology*, vol. 8, no. 1, p. 011004, 2011.

[190] C. Damour, M. Benne, B. Grondin-Perez, M. Bessafi, D. Hissel, and J.-P. Chabriat, "Polymer electrolyte membrane fuel cell fault diagnosis based on empirical mode decomposition," *Journal of Power Sources*, vol. 299, pp. 596–603, 2015.

[191] F. D. Bianchi, C. Ocampo-Martinez, C. Kunusch, and R. S. Sánchez-Pena, "Fault-tolerant unfalsified control for PEM fuel cell systems," *IEEE Transactions on Energy Conversion*, vol. 30, no. 1, pp. 307–315, 2014.

[192] M. B. Burkholder, N. S. Siefert, and S. Litster, "Nonlinear analysis of voltage dynamics in a polymer electrolyte fuel cell due to two-phase channel flow," *Journal of Power Sources*, vol. 267, pp. 243–254, 2014.

[193] M. B. Burkholder and S. Litster, "Stabilization of polymer electrolyte fuel cell voltage with reduced-order Lyapunov exponent feedback and corrective pressure perturbations," *Journal of Power Sources*, vol. 275, pp. 408–418, 2015.

[194] J. Luna, E. Usai, A. Husar, and M. Serra, "Enhancing the efficiency and lifetime of a proton exchange membrane fuel cell using nonlinear model-predictive control with nonlinear observation," *IEEE transactions on industrial electronics*, vol. 64, no. 8, pp. 6649–6659, 2017.

[195] H. A. Gasteiger, S. S. Kocha, B. Sompalli, and F. T. Wagner, "Activity benchmarks and requirements for Pt, pt-alloy, and non-Pt oxygen reduction catalysts for PEMFCs," *Applied Catalysis B: Environmental*, vol. 56, no. 1-2, pp. 9–35, 2005.

[196] R. L. Borup, J. R. Davey, F. H. Garzon, D. L. Wood, and M. A. Inbody, "PEM fuel cell electrocatalyst durability measurements," *Journal of Power Sources*, vol. 163, no. 1, pp. 76–81, 2006.

[197] R. M. Darling and J. P. Meyers, "Mathematical model of platinum movement in PEM fuel cells," *Journal of the Electrochemical Society*, vol. 152, no. 1, pp. A242–A247, 2005.

[198] A. Goshtasbi, B. L. Pence, and T. Ersal, "A real-time pseudo-2D bi-domain model of PEM fuel cells for automotive applications," in *ASME 2017 Dynamic Systems and Control Conference*, pp. V001T25A001–V001T25A001, American Society of Mechanical Engineers, 2017.

[199] A. Goshtasbi, B. Pence, and T. Ersal, "1+ 1d non-isothermal and two-phase transient model of PEM fuel cells for real-time estimation and control," in *Meeting Abstracts*, no. 45, pp. 2220–2220, The Electrochemical Society, 2016.

[200] A. Goshtasbi, B. Pence, J. Chen, J. Waldecker, S. Hirano, and T. Ersal, "Soft sensor for real-time monitoring of automotive PEM fuel cell systems," in *Meeting Abstracts*, no. 33, pp. 1461–1461, The Electrochemical Society, 2019.

[201] A. Goshtasbi, B. L. Pence, and T. Ersal, "Computationally efficient pseudo-2D non-isothermal modeling of polymer electrolyte membrane fuel cells with two-phase phenomena," *Journal of The Electrochemical Society*, vol. 163, no. 13, pp. F1412–F1432, 2016.

[202] A. Goshtasbi, B. L. Pence, J. Chen, M. A. DeBolt, C. Wang, J. R. Waldecker, S. Hirano, and T. Ersal, "A mathematical model toward real-time monitoring of automotive PEM fuel cells," Submitted.

[203] A. Goshtasbi, J. Chen, J. R. Waldecker, S. Hirano, and T. Ersal, "Effective parameterization of PEM fuel cell models: I. Sensitivity analysis and parameter identifiability," Submitted.

[204] A. Goshtasbi, J. Chen, J. R. Waldecker, S. Hirano, and T. Ersal, "Robust parameter subset selection and optimal experimental design for effective parameterization of PEM fuel cell models," in *2020 American Control Conference*, IEEE, Submitted.

[205] A. Goshtasbi, J. Chen, J. R. Waldecker, S. Hirano, and T. Ersal, "Effective parameterization of PEM fuel cell models: II. Robust parameter subset selection, robust optimal experimental design, and multi-step identification algorithm," Submitted.

[206] A. Goshtasbi, J. Chen, J. R. Waldecker, S. Hirano, and T. Ersal, "On parameterizing PEM fuel cell models," in *2019 American Control Conference (ACC)*, pp. 903–908, IEEE, 2019.

[207] A. Goshtasbi, J. Chen, J. Waldecker, S. Hirano, and T. Ersal, "Optimal experimental design for parameter identification of PEM fuel cell models," in *Meeting Abstracts*, no. 32, pp. 1384–1384, The Electrochemical Society, 2019.

[208] A. Goshtasbi and T. Ersal, "LQ-MPC design for degradation-conscious control of PEM fuel cells," in *2019 American Control Conference (ACC)*, pp. 1555–1560, IEEE, 2019.

[209] A. Goshtasbi and T. Ersal, "Degradation-conscious control for enhanced lifetime of automotive polymer electrolyte membrane fuel cells," Submitted.

[210] A. Goshtasbi and T. Ersal, "Degradation-conscious control for PEM fuel cell systems," in *Meeting Abstracts*, no. 33, pp. 1494–1494, The Electrochemical Society, 2019.

[211] C. D. Rahn and C.-Y. Wang, *Battery systems engineering*. John Wiley & Sons, 2013.

[212] E. Birgersson, M. Noponen, and M. Vynnycky, "Analysis of a two-phase non-isothermal model for a PEFC," *Journal of the Electrochemical Society*, vol. 152, no. 5, pp. A1021–A1034, 2005.

[213] J. Benziger, E. Kimball, R. Mejia-Ariza, and I. Kevrekidis, "Oxygen mass transport limitations at the cathode of polymer electrolyte membrane fuel cells," *AIChE Journal*, vol. 57, no. 9, pp. 2505–2517, 2011.

[214] V. Liso, S. S. Araya, A. C. Olesen, M. P. Nielsen, and S. K. Kær, "Modeling and experimental validation of water mass balance in a PEM fuel cell stack," *International Journal of Hydrogen Energy*, 2015.

[215] Q. Duan, H. Wang, and J. Benziger, "Transport of liquid water through Nafion membranes," *Journal of Membrane Science*, vol. 392, pp. 88–94, 2012.

[216] S. Ge, X. Li, B. Yi, and I.-M. Hsing, "Absorption, desorption, and transport of water in polymer electrolyte membranes for fuel cells," *Journal of the Electrochemical Society*, vol. 152, no. 6, pp. A1149–A1157, 2005.

[217] O. Burheim, P. Vie, J. Pharoah, and S. Kjelstrup, "Ex situ measurements of through-plane thermal conductivities in a polymer electrolyte fuel cell," *Journal of Power Sources*, vol. 195, no. 1, pp. 249–256, 2010.

[218] R. Vetter and J. O. Schumacher, "Experimental parameter uncertainty in PEM fuel cell modeling. Part I: Scatter in material parameterization," *arXiv preprint arXiv:1811.10091*, 2018.

[219] I. V. Zenyuk, A. Lamibrac, J. Eller, D. Y. Parkinson, F. Marone, F. N. Buchi, and A. Z. Weber, "Investigating evaporation in gas diffusion layers for fuel cells with X-ray computed tomography," *The Journal of Physical Chemistry C*, vol. 120, no. 50, pp. 28701–28711, 2016.

[220] J. Zhou, D. Stanier, A. Putz, and M. Secanell, "A mixed wettability pore size distribution based mathematical model for analyzing two-phase flow in porous electrodes II. Model validation and analysis of micro-structural parameters," *Journal of The Electrochemical Society*, vol. 164, no. 6, pp. F540–F556, 2017.

[221] R. Marek and J. Straub, "Analysis of the evaporation coefficient and the condensation coefficient of water," *International Journal of Heat and Mass Transfer*, vol. 44, no. 1, pp. 39–53, 2001.

[222] A. L. Buck, "New equations for computing vapor pressure and enhancement factor," *Journal of applied meteorology*, vol. 20, no. 12, pp. 1527–1532, 1981.

[223] A. Z. Weber and J. Newman, "Coupled thermal and water management in polymer electrolyte fuel cells," *Journal of The Electrochemical Society*, vol. 153, no. 12, pp. A2205–A2214, 2006.

[224] M. Leverett, "Capillary pressure in porous solids," *Transactions of the AIME*, vol. 142, pp. 152–169, 1941.

[225] P. A. Mateo Villanueva, "A mixed wettability pore size distribution model for the analysis of water transport in PEMFC materials," Master's thesis, University of Alberta, 2013.

[226] R. J. Balliet and J. Newman, "Cold start of a polymer-electrolyte fuel cell II. Development of a two-dimensional model," *Journal of the Electrochemical Society*, vol. 158, no. 8, pp. B927–B938, 2011.

[227] P. A. García-Salaberri, I. V. Zenyuk, A. D. Shum, G. Hwang, M. Vera, A. Z. Weber, and J. T. Gostick, "Analysis of representative elementary volume and through-plane regional characteristics of carbon-fiber papers: diffusivity, permeability and electrical/thermal conductivity," *International Journal of Heat and Mass Transfer*, vol. 127, pp. 687–703, 2018.

[228] Q. Zhao, P. Majsztrik, and J. Benziger, "Diffusion and interfacial transport of water in Nafion," *The Journal of Physical Chemistry B*, vol. 115, no. 12, pp. 2717–2727, 2011.

[229] M. B. Satterfield and J. Benziger, "Non-fickian water vapor sorption dynamics by Nafion membranes," *The Journal of Physical Chemistry B*, vol. 112, no. 12, pp. 3693–3704, 2008.

[230] D. T. Hallinan Jr and Y. A. Elabd, "Diffusion of water in Nafion using time-resolved fourier transform infrared- attenuated total reflectance spectroscopy," *The Journal of Physical Chemistry B*, vol. 113, no. 13, pp. 4257–4266, 2009.

[231] A. Kongkanand, "Interfacial water transport measurements in Nafion thin films using a quartz-crystal microbalance," *The Journal of Physical Chemistry C*, vol. 115, no. 22, pp. 11318–11325, 2011.

[232] A. Kusoglu, A. Kwong, K. T. Clark, H. P. Gunterman, and A. Z. Weber, "Water uptake of fuel-cell catalyst layers," *Journal of The Electrochemical Society*, vol. 159, no. 9, pp. F530–F535, 2012.

[233] A. Kusoglu and A. Z. Weber, "Water transport and sorption in Nafion membrane," in *Polymers for Energy Storage and Delivery: Polyelectrolytes for Batteries and Fuel Cells*, ch. 11, pp. 175–199, 2012.

[234] T. J. Silverman, J. P. Meyers, and J. J. Beaman, "Modeling water transport and swelling in polymer electrolyte membranes," *Journal of The Electrochemical Society*, vol. 157, no. 10, pp. B1376–B1381, 2010.

[235] Y.-H. Lai, G. W. Fly, and S. Clapham, "In-situ membrane hydration measurement of proton exchange membrane fuel cells," *Journal of Power Sources*, vol. 274, pp. 324–337, 2015.

[236] L. Onishi, J. Prausnitz, and J. Newman, "Modeling Nafion: Water diffusion and polymer relaxation," *ECS Transactions*, vol. 16, no. 50, pp. 139–153, 2009.

[237] M. Zaglio, *Model Based Transient Analysis of Polymer Electrolyte Fuel Cells*. PhD thesis, ETH Zurich, 2011.

[238] C. Mittelsteadt and H. Liu, "Conductivity, permeability, and ohmic shorting of ionomeric membranes," *Handbook of Fuel Cells*, 2010.

[239] P. Mangiagli, C. Ewing, K. Xu, Q. Wang, and M. Hickner, "Dynamic water uptake of flexible ion-containing polymer networks," *Fuel Cells*, vol. 9, no. 4, pp. 432–438, 2009.

[240] A. Kusoglu, B. L. Kienitz, and A. Z. Weber, "Understanding the effects of compression and constraints on water uptake of fuel-cell membranes," *Journal of the Electrochemical Society*, vol. 158, no. 12, pp. B1504–B1514, 2011.

[241] S. Jomori, N. Nonoyama, and T. Yoshida, "Analysis and modeling of PEMFC degradation: Effect on oxygen transport," *Journal of Power Sources*, vol. 215, pp. 18–27, 2012.

[242] S. Jomori, K. Komatsubara, N. Nonoyama, M. Kato, and T. Yoshida, "An experimental study of the effects of operational history on activity changes in a PEMFC," *Journal of The Electrochemical Society*, vol. 160, no. 9, pp. F1067–F1073, 2013.

[243] J. P. Owejan, J. E. Owejan, and W. Gu, "Impact of platinum loading and catalyst layer structure on PEMFC performance," *Journal of The Electrochemical Society*, vol. 160, no. 8, pp. F824–F833, 2013.

[244] Y. Ono, T. Mashio, S. Takaichi, A. Ohma, H. Kanesaka, and K. Shinohara, "The analysis of performance loss with low platinum loaded cathode catalyst layers," *Ecs Transactions*, vol. 28, no. 27, pp. 69–78, 2010.

[245] Y. Ono, A. Ohma, K. Shinohara, and K. Fushinobu, "Influence of equivalent weight of ionomer on local oxygen transport resistance in cathode catalyst layers," *Journal of The Electrochemical Society*, vol. 160, no. 8, pp. F779–F787, 2013.

[246] M.-J. Choo, K.-H. Oh, J.-K. Park, and H.-T. Kim, "Analysis of oxygen transport in cathode catalyst layer of low-Pt-loaded fuel cells," *ChemElectroChem*, vol. 2, no. 3, pp. 382–388, 2015.

[247] A. Chowdhury, C. J. Radke, and A. Z. Weber, "Transport resistances in fuel-cell catalyst layers," *ECS Transactions*, vol. 80, no. 8, pp. 321–333, 2017.

[248] N. Nonoyama, S. Okazaki, A. Z. Weber, Y. Ikogi, and T. Yoshida, "Analysis of oxygen-transport diffusion resistance in proton-exchange-membrane fuel cells," *Journal of The Electrochemical Society*, vol. 158, no. 4, pp. B416–B423, 2011.

[249] N. Ramaswamy and S. Kumaraguru, "Materials and design selection to improve high current density performance in PEMFC," *ECS Transactions*, vol. 85, no. 13, pp. 835–842, 2018.

[250] E. Sadeghi, A. Putz, and M. Eikerling, "Hierarchical model of reaction rate distributions and effectiveness factors in catalyst layers of polymer electrolyte fuel cells," *Journal of the Electrochemical Society*, vol. 160, no. 10, pp. F1159–F1169, 2013.

[251] Q. Wang, M. Eikerling, D. Song, and Z. Liu, "Structure and performance of different types of agglomerates in cathode catalyst layers of PEM fuel cells," *Journal of Electroanalytical Chemistry*, vol. 573, no. 1, pp. 61–69, 2004.

[252] M. Secanell, K. Karan, A. Suleman, and N. Djilali, "Multi-variable optimization of PEMFC cathodes using an agglomerate model," *Electrochimica Acta*, vol. 52, no. 22, pp. 6318–6337, 2007.

[253] H. Liu, W. K. Epting, and S. Litster, "Gas transport resistance in polymer electrolyte thin films on oxygen reduction reaction catalysts," *Langmuir*, vol. 31, no. 36, pp. 9853–9858, 2015.

[254] E. M. Davis, C. M. Stafford, and K. A. Page, "Elucidating water transport mechanisms in Nafion thin films," *ACS Macro Letters*, vol. 3, no. 10, pp. 1029–1035, 2014.

[255] S. A. Eastman, S. Kim, K. A. Page, B. W. Rowe, S. Kang, C. L. Soles, and K. G. Yager, "Effect of confinement on structure, water solubility, and water transport in Nafion thin films," *Macromolecules*, vol. 45, no. 19, pp. 7920–7930, 2012.

[256] S. C. DeCaluwe, A. M. Baker, P. Bhargava, J. E. Fischer, and J. A. Dura, "Structure-property relationships at Nafion thin-film interfaces: Thickness effects on hydration and anisotropic ion transport," *Nano energy*, vol. 46, pp. 91–100, 2018.

[257] A. Ohma, T. Mashio, K. Sato, H. Iden, Y. Ono, K. Sakai, K. Akizuki, S. Takaichi, and K. Shinohara, "Analysis of proton exchange membrane fuel cell catalyst layers

for reduction of platinum loading at Nissan," *Electrochimica Acta*, vol. 56, no. 28, pp. 10832–10841, 2011.

[258] S. Holdcroft, "Fuel cell catalyst layers: a polymer science perspective," *Chemistry of materials*, vol. 26, no. 1, pp. 381–393, 2013.

[259] R. M. Darling, "A hierarchical model for oxygen transport in agglomerates in the cathode catalyst layer of a polymer-electrolyte fuel cell," *Journal of The Electrochemical Society*, vol. 165, no. 9, pp. F571–F580, 2018.

[260] F. C. Cetinbas, S. G. Advani, and A. K. Prasad, "A modified agglomerate model with discrete catalyst particles for the PEM fuel cell catalyst layer," *Journal of The Electrochemical Society*, vol. 160, no. 8, pp. F750–F756, 2013.

[261] F. C. Cetinbas, S. G. Advani, and A. K. Prasad, "An improved agglomerate model for the PEM catalyst layer with accurate effective surface area calculation based on the sphere-packing approach," *Journal of The Electrochemical Society*, vol. 161, no. 6, pp. F803–F813, 2014.

[262] A. Kulikovsky, "A physically–based analytical polarization curve of a PEM fuel cell," *Journal of The Electrochemical Society*, vol. 161, no. 3, pp. F263–F270, 2014.

[263] H. Iden and A. Ohma, "An in-situ technique for analyzing ionomer coverage in catalyst layers," *Journal of Electroanalytical Chemistry*, vol. 693, pp. 34–41, 2013.

[264] K. Malek, T. Mashio, and M. Eikerling, "Microstructure of catalyst layers in PEM fuel cells redefined: a computational approach," *Electrocatalysis*, vol. 2, no. 2, p. 141, 2011.

[265] K. Malek, M. Eikerling, Q. Wang, T. Navessin, and Z. Liu, "Self-organization in catalyst layers of polymer electrolyte fuel cells," *The Journal of Physical Chemistry C*, vol. 111, no. 36, pp. 13627–13634, 2007.

[266] A. Srouji, L. Zheng, R. Dross, D. Aaron, and M. Mench, "The role of water management on the oxygen transport resistance in polymer electrolyte fuel cell with ultra-low precious metal loading," *Journal of Power Sources*, vol. 364, pp. 92–100, 2017.

[267] A. Kulikovsky, "How important is oxygen transport in agglomerates in a PEM fuel cell catalyst layer?," *Electrochimica Acta*, vol. 130, pp. 826–829, 2014.

[268] R. B. Bird, W. E. Stewart, and E. N. Lightfoot, *Transport phenomena*. John Wiley & Sons, 2007.

[269] E. L. Cussler, *Diffusion: mass transfer in fluid systems*. Cambridge university press, 2009.

[270] S. A. Vilekar and R. Datta, "The effect of hydrogen crossover on open-circuit voltage in polymer electrolyte membrane fuel cells," *Journal of Power Sources*, vol. 195, no. 8, pp. 2241–2247, 2010.

[271] C. K. Mittelsteadt and H. Liu, "Conductivity, permeability, and ohmic shorting of ionomeric membranes," *Handbook of Fuel Cells*, 2009.

[272] R. Ahluwalia and X. Wang, "Buildup of nitrogen in direct hydrogen polymer-electrolyte fuel cell stacks," *Journal of Power Sources*, vol. 171, no. 1, pp. 63–71, 2007.

[273] U. M. Ascher, *Numerical methods for evolutionary differential equations*, vol. 5. Siam, 2008.

[274] K. Neyerlin, W. Gu, J. Jorne, A. Clark, and H. A. Gasteiger, "Cathode catalyst utilization for the ORR in a PEMFC analytical model and experimental validation," *Journal of The Electrochemical Society*, vol. 154, no. 2, pp. B279–B287, 2007.

[275] E. Padgett, N. Andrejevic, Z. Liu, A. Kongkanand, W. Gu, K. Moriyama, Y. Jiang, S. Kumaraguru, T. E. Moylan, R. Kukreja, *et al.*, "Connecting fuel cell catalyst nanostructure and accessibility using quantitative cryo-STEM tomography," *Journal of The Electrochemical Society*, vol. 165, no. 3, pp. F173–F180, 2018.

[276] F. C. Cetinbas, R. K. Ahluwalia, N. N. Kariuki, V. De Andrade, and D. J. Myers, "Effects of porous carbon morphology, agglomerate structure and relative humidity on local oxygen transport resistance," *Journal of The Electrochemical Society*, vol. 167, no. 1, p. 013508, 2020.

[277] K. A. Hoffmann and S. T. Chiang, "Computational fluid dynamics volume I," *Engineering Education System*, 2000.

[278] S. C. Chapra, R. P. Canale, *et al.*, *Numerical methods for engineers*. Boston: McGraw-Hill Higher Education,, 2010.

[279] R. Alink and D. Gerteisen, "Coupling of a continuum fuel cell model with a discrete liquid water percolation model," *International Journal of Hydrogen Energy*, vol. 39, no. 16, pp. 8457–8473, 2014.

[280] A. Szymkiewicz, *Modelling water flow in unsaturated porous media: Accounting for nonlinear permeability and material heterogeneity*. Springer Science & Business Media, 2012.

[281] Y. Shi *et al.*, "Particle swarm optimization: developments, applications and resources," in *Proceedings of the 2001 congress on evolutionary computation (IEEE Cat. No. 01TH8546)*, vol. 1, pp. 81–86, IEEE, 2001.

[282] R. Bellman and K. J. Åström, "On structural identifiability," *Mathematical Biosciences*, vol. 7, no. 3-4, pp. 329–339, 1970.

[283] E. J. Dickinson and G. Hinds, "The Butler-Volmer equation for polymer electrolyte membrane fuel cell (PEMFC) electrode kinetics: A critical discussion," *Journal of The Electrochemical Society*, vol. 166, no. 4, pp. F221–F231, 2019.

[284] R. Vetter and J. O. Schumacher, "Experimental parameter uncertainty in PEM fuel cell modeling. Part II: Sensitivity analysis and importance ranking," *arXiv preprint arXiv:1811.10093*, 2018.

[285] S. Arisetty, Y. Liu, W. Gu, and M. Mathias, "Modeling platinum oxide growth of PEMFC cathode catalysts," *ECS Transactions*, vol. 69, no. 17, pp. 273–289, 2015.

[286] K. Nishida, T. Hosotani, and M. Asa, "Evaluation of two water transports through electrolyte membrane of polymer electrolyte fuel cell based on water visualization and current measurement," *Fuel Cells*, vol. 19, no. 1, pp. 60–70, 2019.

[287] P. Berg, K. Promislow, J. S. Pierre, J. Stumper, and B. Wetton, "Water management in PEM fuel cells," *Journal of the Electrochemical Society*, vol. 151, no. 3, pp. A341–A353, 2004.

[288] A. Thomas, G. Maranzana, S. Didierjean, J. Dillet, and O. Lottin, "Thermal effect on water transport in proton exchange membrane fuel cell," *Fuel Cells*, vol. 12, no. 2, pp. 212–224, 2012.

[289] N. Ge, R. Banerjee, D. Muirhead, J. Lee, H. Liu, P. Shrestha, A. Wong, J. Jankovic, M. Tam, D. Susac, *et al.*, "Membrane dehydration with increasing current density at high inlet gas relative humidity in polymer electrolyte membrane fuel cells," *Journal of Power Sources*, vol. 422, pp. 163–174, 2019.

[290] K. Godfrey and J. DiStefano, "Chapter 1 - identifiability of model parameters," in *Identifiability of Parametric Models* (E. WALTER, ed.), pp. 1 – 20, Pergamon, 1987.

[291] H. Miao, X. Xia, A. S. Perelson, and H. Wu, "On identifiability of nonlinear ODE models and applications in viral dynamics," *SIAM review*, vol. 53, no. 1, pp. 3–39, 2011.

[292] L. Ljung and T. Glad, "On global identifiability for arbitrary model parametrizations," *Automatica*, vol. 30, no. 2, pp. 265–276, 1994.

[293] X. Xia and C. H. Moog, "Identifiability of nonlinear systems with application to HIV/AIDS models," *IEEE transactions on automatic control*, vol. 48, no. 2, pp. 330–336, 2003.

[294] A. F. Villaverde and J. R. Banga, "Structural properties of dynamic systems biology models: Identifiability, reachability, and initial conditions," *Processes*, vol. 5, no. 2, p. 29, 2017.

[295] A. F. Villaverde, N. Tsiantis, and J. R. Banga, "Full observability and estimation of unknown inputs, states and parameters of nonlinear biological models," *Journal of the Royal Society Interface*, vol. 16, no. 156, p. 20190043, 2019.

[296] M. Rodriguez-Fernandez, J. A. Egea, and J. R. Banga, "Novel metaheuristic for parameter estimation in nonlinear dynamic biological systems," *BMC bioinformatics*, vol. 7, no. 1, p. 483, 2006.

[297] D. Zhao, M. Dou, D. Zhou, and F. Gao, "Study of the modeling parameter effects on the polarization characteristics of the pem fuel cell," *International Journal of Hydrogen Energy*, vol. 41, no. 47, pp. 22316–22327, 2016.

[298] C. Min, Y. He, X. Liu, B. Yin, W. Jiang, and W. Tao, "Parameter sensitivity examination and discussion of PEM fuel cell simulation model validation: Part II: Results of sensitivity analysis and validation of the model," *Journal of power sources*, vol. 160, no. 1, pp. 374–385, 2006.

[299] X.-D. Wang, J.-L. Xu, and D.-J. Lee, "Parameter sensitivity examination for a complete three-dimensional, two-phase, non-isothermal model of polymer electrolyte membrane fuel cell," *International journal of hydrogen energy*, vol. 37, no. 20, pp. 15766–15777, 2012.

[300] D. Zhou, T. T. Nguyen, E. Breaz, D. Zhao, S. Clénet, and F. Gao, "Global parameters sensitivity analysis and development of a two-dimensional real-time model of proton-exchange-membrane fuel cells," *Energy conversion and management*, vol. 162, pp. 276–292, 2018.

[301] B. Laoun, M. W. Naceur, A. Khellaf, and A. M. Kannan, "Global sensitivity analysis of proton exchange membrane fuel cell model," *International Journal of Hydrogen Energy*, vol. 41, no. 22, pp. 9521–9528, 2016.

[302] D. V. Raman, J. Anderson, and A. Papachristodoulou, "Delineating parameter unidentifiabilities in complex models," *Physical Review E*, vol. 95, no. 3, p. 032314, 2017.

[303] A. Saltelli, M. Ratto, T. Andres, F. Campolongo, J. Cariboni, D. Gatelli, M. Saisana, and S. Tarantola, *Global sensitivity analysis: the primer*. John Wiley & Sons, 2008.

[304] Y. Chu and J. Hahn, "Parameter set selection via clustering of parameters into pairwise indistinguishable groups of parameters," *Industrial & Engineering Chemistry Research*, vol. 48, no. 13, pp. 6000–6009, 2008.

[305] M. Rodriguez-Fernandez, P. Mendes, and J. R. Banga, "A hybrid approach for efficient and robust parameter estimation in biochemical pathways," *Biosystems*, vol. 83, no. 2-3, pp. 248–265, 2006.

[306] E. Kumbur, K. Sharp, and M. Mench, "Validated leverett approach for multiphase flow in PEFC diffusion media i. hydrophobicity effect," *Journal of the Electrochemical Society*, vol. 154, no. 12, pp. B1295–B1304, 2007.

[307] A. Lamibrac, J. Roth, M. Toulec, F. Marone, M. Stampanoni, and F. Büchi, "Characterization of liquid water saturation in gas diffusion layers by X-ray tomographic microscopy," *Journal of The Electrochemical Society*, vol. 163, no. 3, pp. F202–F209, 2016.

[308] S. M. Moosavi, M. Niffeler, J. Gostick, and S. Haussener, "Transport characteristics of saturated gas diffusion layers treated with hydrophobic coatings," *Chemical Engineering Science*, vol. 176, pp. 503–514, 2018.

[309] Q. Meyer, S. Ashton, P. Boillat, M. Cochet, E. Engebretsen, D. P. Finegan, X. Lu, J. J. Bailey, N. Mansor, R. Abdulaziz, *et al.*, "Effect of gas diffusion layer properties on water distribution across air-cooled, open-cathode polymer electrolyte fuel cells: a combined ex-situ x-ray tomography and in-operando neutron imaging study," *Electrochimica Acta*, vol. 211, pp. 478–487, 2016.

[310] P. A. García-Salaberri, J. T. Gostick, I. V. Zenyuk, G. Hwang, M. Vera, and A. Z. Weber, "On the limitations of volume-averaged descriptions of gas diffusion layers in the modeling of polymer electrolyte fuel cells," *ECS Transactions*, vol. 80, no. 8, pp. 133–143, 2017.

[311] S. Lee, H. Jeong, B. Ahn, T. Lim, and Y. Son, "Parametric study of the channel design at the bipolar plate in PEMFC performances," *International journal of hydrogen energy*, vol. 33, no. 20, pp. 5691–5696, 2008.

[312] S. G. Goebel, "Impact of land width and channel span on fuel cell performance," *Journal of Power Sources*, vol. 196, no. 18, pp. 7550–7554, 2011.

[313] S. Kim and M. Mench, "Investigation of temperature-driven water transport in polymer electrolyte fuel cell: phase-change-induced flow," *Journal of The Electrochemical Society*, vol. 156, no. 3, pp. B353–B362, 2009.

[314] R. S. Fu, J. S. Preston, U. Pasaogullari, T. Shiomi, S. Miyazaki, Y. Tabuchi, D. S. Hussey, and D. L. Jacobson, "Water transport across a polymer electrolyte membrane under thermal gradients," *Journal of The Electrochemical Society*, vol. 158, no. 3, pp. B303–B312, 2011.

[315] A. Thomas, G. Maranzana, S. Didierjean, J. Dillet, and O. Lottin, "Measurements of electrode temperatures, heat and water fluxes in PEMFCs: conclusions about transfer mechanisms," *Journal of The Electrochemical Society*, vol. 160, no. 2, pp. F191–F204, 2013.

[316] K. S. Brown and J. P. Sethna, "Statistical mechanical approaches to models with many poorly known parameters," *Physical review E*, vol. 68, no. 2, p. 021904, 2003.

[317] R. N. Gutenkunst, J. J. Waterfall, F. P. Casey, K. S. Brown, C. R. Myers, and J. P. Sethna, "Universally sloppy parameter sensitivities in systems biology models," *PLoS computational biology*, vol. 3, no. 10, p. e189, 2007.

[318] C. Tönsing, J. Timmer, and C. Kreutz, "Cause and cure of sloppiness in ordinary differential equation models," *Physical Review E*, vol. 90, no. 2, p. 023303, 2014.

[319] O.-T. Chis, A. F. Villaverde, J. R. Banga, and E. Balsa-Canto, "On the relationship between sloppiness and identifiability," *Mathematical biosciences*, vol. 282, pp. 147–161, 2016.

[320] A. White, M. Tolman, H. D. Thames, H. R. Withers, K. A. Mason, and M. K. Transtrum, "The limitations of model-based experimental design and parame-

ter estimation in sloppy systems," *PLoS computational biology*, vol. 12, no. 12, p. e1005227, 2016.

[321] M. Secrier, T. Toni, and M. P. Stumpf, "The ABC of reverse engineering biological signalling systems," *Molecular BioSystems*, vol. 5, no. 12, pp. 1925–1935, 2009.

[322] R. Brun, P. Reichert, and H. R. Künsch, "Practical identifiability analysis of large environmental simulation models," *Water Resources Research*, vol. 37, no. 4, pp. 1015–1030, 2001.

[323] B. F. Lund and B. A. Foss, "Parameter ranking by orthogonalizationApplied to nonlinear mechanistic models," *Automatica*, vol. 44, no. 1, pp. 278–281, 2008.

[324] A. Miller, *Subset selection in regression*. Chapman and Hall/CRC, 2002.

[325] Y. Chu, Z. Huang, and J. Hahn, "Improving prediction capabilities of complex dynamic models via parameter selection and estimation," *Chemical Engineering Science*, vol. 64, no. 19, pp. 4178–4185, 2009.

[326] Y. Chu and J. Hahn, "Generalization of a parameter set selection procedure based on orthogonal projections and the d-optimality criterion," *AIChE Journal*, vol. 58, no. 7, pp. 2085–2096, 2012.

[327] Y. Chu and J. Hahn, "Parameter set selection for estimation of nonlinear dynamic systems," *AIChE Journal*, vol. 53, no. 11, pp. 2858–2870, 2007.

[328] K. A. McLean, S. Wu, and K. B. McAuley, "Mean-squared-error methods for selecting optimal parameter subsets for estimation," *Industrial & Engineering Chemistry Research*, vol. 51, no. 17, pp. 6105–6115, 2012.

[329] C. P. Kitsos, *Optimal experimental design for non-linear models: theory and applications*. Springer Science & Business Media, 2014.

[330] L. Pronzato, "Optimal experimental design and some related control problems," *Automatica*, vol. 44, no. 2, pp. 303–325, 2008.

[331] L. Pronzato and É. Walter, "Robust experiment design via stochastic approximation," *Mathematical Biosciences*, vol. 75, no. 1, pp. 103–120, 1985.

[332] L. Pronzato and É. Walter, "Robust experiment design via maximin optimization," *Mathematical Biosciences*, vol. 89, no. 2, pp. 161–176, 1988.

[333] S. Asprey and S. Macchietto, "Designing robust optimal dynamic experiments," *Journal of Process Control*, vol. 12, no. 4, pp. 545–556, 2002.

[334] R. Schenkendorf, X. Xie, M. Rehbein, S. Scholl, and U. Krewer, "The impact of global sensitivities and design measures in model-based optimal experimental design," *Processes*, vol. 6, no. 4, p. 27, 2018.

[335] R. C. Aster, B. Borchers, and C. H. Thurber, *Parameter estimation and inverse problems*. Elsevier, 2018.

[336] C. Kravaris, J. Hahn, and Y. Chu, "Advances and selected recent developments in state and parameter estimation," *Computers & chemical engineering*, vol. 51, pp. 111–123, 2013.

[337] L. N. Trefethen and D. Bau III, *Numerical linear algebra*, vol. 50. Siam, 1997.

[338] E. Walter, *Identifiability of parametric models*. Elsevier, 2014.

[339] S. R. Weijers and P. A. Vanrolleghem, "A procedure for selecting best identifiable parameters in calibrating activated sludge model no. 1 to full-scale plant data," *Water science and technology*, vol. 36, no. 5, pp. 69–79, 1997.

[340] W. Dai, L. Bansal, J. Hahn, and D. Word, "Parameter set selection for dynamic systems under uncertainty via dynamic optimization and hierarchical clustering," *AIChE Journal*, vol. 60, no. 1, pp. 181–192, 2014.

[341] K. Z. Yao, B. M. Shaw, B. Kou, K. B. McAuley, and D. Bacon, "Modeling ethylene/butene copolymerization with multi-site catalysts: parameter estimability and experimental design," *Polymer Reaction Engineering*, vol. 11, no. 3, pp. 563–588, 2003.

[342] M. Fink, A. Attarian, and H. Tran, "Subset selection for parameter estimation in an HIV model," in *PAMM: Proceedings in Applied Mathematics and Mechanics*, vol. 7, pp. 1121501–1121502, Wiley Online Library, 2007.

[343] T. H. Cormen, C. E. Leiserson, R. L. Rivest, and C. Stein, *Introduction to algorithms*. MIT press, 2009.

[344] T. Hastie, R. Tibshirani, J. Friedman, and J. Franklin, "The elements of statistical learning: data mining, inference and prediction," *The Mathematical Intelligencer*, vol. 27, no. 2, pp. 83–85, 2005.

[345] G. S. Harzer, J. N. Schwämmlein, A. M. Damjanović, S. Ghosh, and H. A. Gasteiger, "Cathode loading impact on voltage cycling induced PEMFC degradation: A voltage loss analysis," *Journal of The Electrochemical Society*, vol. 165, no. 6, pp. F3118–F3131, 2018.

[346] R. L. Borup and A. Z. Weber, "FC-PAD: Fuel cell performance and durability consortium," in *Annual Merit Review Proceedings*, U.S. Department of Energy, 2019.

[347] S. Kumaraguru, "Durable high power membrane electrode assembly with low Pt loading," in *Annual Merit Review Proceedings*, U.S. Department of Energy, 2017.

[348] M. Hasan and M. H. Santare, "Characterizing durability of PFSA membranes of PEM fuel cell based on numerical fatigue crack propagation," in *Meeting Abstracts*, no. 34, pp. 1522–1522, The Electrochemical Society, 2019.

[349] Y.-H. Lai, K. M. Rahmoeller, J. H. Hurst, R. S. Kukreja, M. Atwan, A. J. Maslyn, and C. S. Gittleman, "Accelerated stress testing of fuel cell membranes subjected to combined mechanical/chemical stressors and cerium migration," *Journal of The Electrochemical Society*, vol. 165, no. 6, pp. F3217–F3229, 2018.

[350] M. Krstic and A. Smyshlyaev, *Boundary control of PDEs: A course on backstepping designs*, vol. 16. SIAM, 2008.

[351] L. Chisci, P. Falugi, and G. Zappa, "Gain-scheduling MPC of nonlinear systems," *International Journal of Robust and Nonlinear Control: IFAC-Affiliated Journal*, vol. 13, no. 3-4, pp. 295–308, 2003.

[352] T. Keviczky and G. J. Balas, "Receding horizon control of an F-16 aircraft: A comparative study," *Control Engineering Practice*, vol. 14, no. 9, pp. 1023–1033, 2006.

[353] P. Falcone, F. Borrelli, H. E. Tseng, J. Asgari, and D. Hrovat, "Linear time-varying model predictive control and its application to active steering systems: Stability analysis and experimental validation," *International Journal of Robust and Nonlinear Control: IFAC-Affiliated Journal*, vol. 18, no. 8, pp. 862–875, 2008.

[354] K. W. Suh, *Modeling, analysis and control of fuel cell hybrid power systems*. PhD thesis, The University of Michigan, 2006.

[355] N. S. Khattra, Z. Lu, A. M. Karlsson, M. H. Santare, F. C. Busby, and T. Schmiedel, "Time-dependent mechanical response of a composite PFSA membrane," *Journal of Power Sources*, vol. 228, pp. 256–269, 2013.

[356] M. P. Rodgers, L. J. Bonville, H. R. Kunz, D. K. Slattery, and J. M. Fenton, "Fuel cell perfluorinated sulfonic acid membrane degradation correlating accelerated stress testing and lifetime," *Chemical reviews*, vol. 112, no. 11, pp. 6075–6103, 2012.

[357] D. S. Bernstein, *Matrix mathematics: theory, facts, and formulas*. Princeton University Press, 2009.

[358] G. Pannocchia and J. B. Rawlings, "The velocity algorithm LQR: a survey," *Technical Report 2001-01, TWMCC*, 2001.

[359] G. Betti, M. Farina, and R. Scattolini, "A robust MPC algorithm for offset-free tracking of constant reference signals," *IEEE Transactions on Automatic Control*, vol. 58, no. 9, pp. 2394–2400, 2013.

[360] C. Gohrle, A. Schindler, A. Wagner, and O. Sawodny, "Design and vehicle implementation of preview active suspension controllers," *IEEE Transactions on Control Systems Technology*, vol. 22, no. 3, pp. 1135–1142, 2013.

[361] S. Di Cairano and I. V. Kolmanovsky, "Automotive applications of model predictive control," in *Handbook of Model Predictive Control*, pp. 493–527, Springer, 2019.

[362] F. Borrelli, A. Bemporad, and M. Morari, *Predictive control for linear and hybrid systems*. Cambridge University Press, 2017.

[363] A. Bemporad, M. Morari, V. Dua, and E. N. Pistikopoulos, "The explicit linear quadratic regulator for constrained systems," *Automatica*, vol. 38, no. 1, pp. 3–20, 2002.

[364] J. A. E. Andersson, J. Gillis, G. Horn, J. B. Rawlings, and M. Diehl, "CasADi – A software framework for nonlinear optimization and optimal control," *Mathematical Programming Computation*, vol. 11, no. 1, pp. 1–36, 2019.

[365] B. Stellato, G. Banjac, P. Goulart, A. Bemporad, and S. Boyd, "OSQP: An operator splitting solver for quadratic programs," *ArXiv e-prints*, Nov. 2017.

[366] S. Boyd, N. Parikh, E. Chu, B. Peleato, J. Eckstein, *et al.*, "Distributed optimization and statistical learning via the alternating direction method of multipliers," *Foundations and Trends in Machine Learning*, vol. 3, no. 1, pp. 1–122, 2011.

[367] D. Mayne, "Robust and stochastic model predictive control: Are we going in the right direction?," *Annual Reviews in Control*, vol. 41, pp. 184–192, 2016.

[368] Y. Shtessel, C. Edwards, L. Fridman, and A. Levant, *Sliding mode control and observation*. Springer, 2014.

[369] M. Albaba, Y. Yildiz, N. Li, I. Kolmanovsky, and A. Girard, "Stochastic driver modeling and validation with traffic data," in *2019 American Control Conference*, pp. 4198–4203, IEEE, 2019.

[370] A. Sciarretta and A. Vahidi, *Energy-Efficient Driving of Road Vehicles: Toward Cooperative, Connected, and Automated Mobility*. Springer, 2019.

[371] N. B. Erichson, M. Muehlebach, and M. W. Mahoney, "Physics-informed autoencoders for Lyapunov-stable fluid flow prediction," *arXiv preprint arXiv:1905.10866*, 2019.

[372] Y. Zhu, N. Zabaras, P.-S. Koutsourelakis, and P. Perdikaris, "Physics-constrained deep learning for high-dimensional surrogate modeling and uncertainty quantification without labeled data," *Journal of Computational Physics*, vol. 394, pp. 56–81, 2019.

[373] G. Teichert, A. Natarajan, A. Van der Ven, and K. Garikipati, "Machine learning materials physics: Integrable deep neural networks enable scale bridging by learning

free energy functions," *Computer Methods in Applied Mechanics and Engineering*, vol. 353, pp. 201–216, 2019.

[374] H. H. Khalil, *High-gain observers in nonlinear feedback control*, vol. 31. SIAM, 2017.

[375] C. V. Rao, J. B. Rawlings, and J. H. Lee, "Constrained linear state estimationa moving horizon approach," *Automatica*, vol. 37, no. 10, pp. 1619–1628, 2001.

[376] D. A. Copp and J. P. Hespanha, "Simultaneous nonlinear model predictive control and state estimation," *Automatica*, vol. 77, pp. 143–154, 2017.

[377] M. Korda and I. Mezić, "Linear predictors for nonlinear dynamical systems: Koopman operator meets model predictive control," *Automatica*, vol. 93, pp. 149–160, 2018.